

https://dspace.org/

Fischer–Tropsch synthesis: application of clinoptilolite (natural zeolite) as catalyst support

Chikati, Roick

2024
https://hdl.handle.net/10539/37372

Downloaded from a DSpace repository. https://dspace.org/



Fischer–Tropsch synthesis: Application of Clinoptilolite (natural zeolite) as catalyst support

---

ROICK CHIKATI

A thesis submitted to the School of Chemical and Metallurgical Engineering, Faculty of Engineering and the Built Environment, University of the Witwatersrand, Johannesburg, in fulfillment of the requirements for the Degree of Doctor of Philosophy.

January, 2023

DECLARATION

I declare that this thesis is my own unaided work. It is being submitted for the Degree of Doctor of Philosophy to the University of the Witwatersrand, Johannesburg. It has not been submitted before for any degree or examination to any other University.

…… on this ……day of ……

(*Candidate*)

ABSTRACT

In this study, clinoptilolite (a naturally occurring zeolite) was used as catalyst support in Fischer Tropsch Synthesis (FTS). Prior to its use, raw clinoptilolite was crushed sieved to yield different particle sizes (-212 to +150 μm; -150 to +106 μm; -106 to +75 μm; -75 to +53 μm; -53 to +38 μm; -38 to +25 μm; and less than -25 μm). Seven 10% wt cobalt catalyst supported on different size classes of clinoptilolite were prepared using the incipient wetness impregnation method. A thorough investigation was done on the characteristics of cobalt supported on clinoptilolite particles of different sizes using TPR, XRD, XRF, BET and SEM techniques. It has been demonstrated that these techniques provide insight on the effect of the support particle size, and this could be used as a quality control tool to evaluate the efficacy of the preparation method. Temperature-programmed reduction (TPR) was used to examine the non-isothermal reduction of cobalt oxide using 5% hydrogen in argon at three distinct heating rates (5, 10, 15 ^{o}C/min). When using the Kissinger model, it was discovered that the activation energy (Ea), varied from 102.45 to 254.01 kJ/mol, depending on the support particle size of the catalyst. The lowest activation energy being achieved with a support particle size in the -212 to +150 μm range. Reducing the catalyst reduction temperature has significance in FTS, since it drastically reduces the sum of money spent on the energy input required for reduction. XRD, XRF and SEM confirmed the phases making up the catalyst, loading of the catalyst and the particle size distribution respectively. It is worth noting that though differences exist between different size classes, no clear trend was obtained for any of the BET parameters.

For this study, three size classes were investigated as the support for an FT catalyst: -75 to +53 μm; -53 to +38 μm; less than -25 μm. Using a fixed bed reactor at 220 ^{o}C and 10.85 bar(abs), the maximum CO conversion obtained was 44.97% when using the -53 to +38 μm size class (-78 to +53 μm size class giving 32.06 %, and < 25 μm giving 31.29 % CO conversion). At the conditions studied, methane selectivity ranged between 14.95 and 16.97% for the support class size studied, while C_2-C_4 selectivity ranged between 14.55 and 19.01%, and C_{5+} selectivity ranged between 66.04 and 70.29 %. Statistical analysis done on the FT results obtained, one-way analysis of variance (ANOVA) and post-hoc Bonferroni adjustment indicated that utilization of different support size classes had an effect on CO conversion. An innovative data simulation technique based on response surface methodology (RSM) was used as part of the

design of experiments (DOE) to thoroughly investigate the effect of the various operating FTS conditions for both cobalt and Iron based catalysts. These discoveries might be have valuable implications for the design of a catalyst that can be used in the coal/biomass to liquid process.

DEDICATION

Mommy

ACKNOWLEDGEMENTS

To begin, I would like to express my gratitude to GCC for the financial support; without it, the completion of this project would not have been feasible. I would like to express my sincere appreciation to my supervisors, Professor D Nkazi and Dr. J. Gorimbo, for granting me the opportunity to pursue postgraduate studies at the University of Witwatersrand's Department of Chemical and Metallurgical Engineering. In particular, I would like to thank Prof. Nkazi for his guidance and Dr. Gorimbo for his mentorship. I'd like to express my gratitude to my family for all of the love.

PRESENTATIONS AND PUBLICATIONS

As noted below, some of the data in this thesis has been written in paper format for submission to scholarly journals. This section provides an overview of some of the data that were presented (orally and in poster form).

Conference presentations

- Joshua Gorimbo, **Roick Chikati**. Adsorption of Cadmium, Nickel, and Lead on Modified Clinoptilolite: Equilibrium, Kinetic and Selectivity Studies, American Institute of Chemical Engineers (AIChE) annual meeting, 31 October 2018, David L. Lawrence Convention Center, USA, (ISBN: 978-0-8169-1108-0).

- **Roick Chikati**, Diakua Nkazi, Iron Supported on Clinoptilolite (natural zeolites) As a Low-Temperature Fischer–Tropsch Synthesis Catalyst, American Institute of Chemical Engineers (AIChE) annual meeting, 31 October 2018, David L. Lawrence Convention Center, USA, (ISBN: 978-0-8169-1112-7).

- **Roick Chikati**, Joshua Gorimbo, Diakanua Nkazi, Application of Natural Zeolites As Support in Low-Temperature Fischer-Tropsch Synthesis, American Institute of Chemical Engineers (AIChE) annual meeting, 20 August 2020, 2020 Virtual Spring Meeting and 16th GCPS (ISBN: 978-0-8169-1113-4).

Published Manuscripts

- Chikati, R., Okonye, L., Nkazi, D. and **Gorimbo, J. (2021).** Commercial Technologies for Biodiesel Production. In Biodiesel Technology and Applications (eds Inamuddin, M.I. Ahamed, R. Boddula and M. Rezakazemi), Scrivener Publishing, (pp.195-213), Wiley, https://doi.org/10.1002/9781119724957.ch6

- Chikati, C., Otun, K.O., Nkazi, D. and **Gorimbo, J. (2021).** Non-Edible Feedstock for Biodiesel Production. In Biodiesel Technology and Applications (eds Inamuddin, M.I. Ahamed, R. Boddula and M. Rezakazemi) Scrivener Publishing. (pp. 283- 302), Wiley, https://doi.org/10.1002/9781119724957.ch10

Table of Contents

DECLARATION ..... **II**

ABSTRACT ..... **III**

DEDICATION ..... **IV**

ACKNOWLEDGEMENTS ..... **VI**

PRESENTATIONS AND PUBLICATIONS ..... **VII**

List of Figures XIII

List of Tables ..... **XVI**

LIST OF ABBREVIATIONS, NOMENCLATURES AND SYMBOLS ..... **XVII**

CHAPTER 1: BACKGROUND AND INTRODUCTION **1**

1.1. INTRODUCTION **1**
1.2. RESEARCH JUSTIFICATION **7**
1.3. ACADEMIC AND INDUSTRIAL JUSTIFICATION **7**
1.4. AIM AND SCOPE **7**
1.5. DISSERTATION OUTCOME **8**
1.6. DISSERTATION OUTLINE **8**

CHAPTER 2: LITERATURE REVIEW **13**

2.1. INTRODUCTION **13**
2.2. COBALT CATALYST PREPARATION METHODS **14**
2.3. PRONENESS OF COBALT CATALYST TO OXIDATION **25**
2.4. THE EFFECT OF COBALT – SUPPORT INTERACTION **28**
2.5. CRYSTALLITE SIZE DETERMINATION TECHNIQUES **29**
2.6. CRYSTALLITE SIZE MEASUREMENT TECHNIQUES **30**
2.6.1. CRYSTALLITE CHARACTERISATION 30
2.6.2. TEM APPLICATION IN DETERMINING CRYSTALLITE SIZE 31
2.6.3. XRD 33
2.6.4. H_2 CHEMISORPTION 37
2.7. COBALT CATALYST REDUCTION **42**
2.8. THERMODYNAMICS OF CO-BASED CATALYSTS **45**
2.9. PORE SIZE **46**
2.10. PROMOTERS **47**

2.11. CONCLUDING REMARKS 48

CHAPTER 3: EXPERIMENTAL METHODOLOGY 60

3.1. INTRODUCTION 60
3.2. CATALYST PREPARATION 60
3.2.1. SUPPORT PREPARATION 61
3.2.2. CATALYST SYNTHESIS 62
3.3. CATALYST CHARACTERISATION 62
3.3.1. X-RAY DIFFRACTION 62
3.3.2. SEM-ENERGY DISPERSIVE SPECTROSCOPY 63
3.3.3. X-RAY FLUORESCENCE SPECTROMETRY 64
3.3.4. DETERMINATION OF PARTICLES SIZES USING THE MALVERN MASTERSIZER 3000 66
3.3.5. BRUNAUER-EMMETT-TELLER 68
3.3.6. TEMPERATURE-PROGRAMMED REDUCTION STUDIES 69
3.4. EXPERIMENTAL SET-UP 69
3.4.1. TUBULAR FIXED BED REACTOR 71
3.5. TUBULAR FIXED BED REACTOR ISOTHERMAL TEST 72
3.6. CATALYST EVALUATION IN THE FTS REACTION 73
3.6.1. GASES USED 74
3.7. FTS PRODUCT STORAGE 75
3.8. CALCULATIONS 75

CHAPTER 4: CLINOPTILOLITE-SUPPORTED COBALT CRYSTALLITE AS FISCHER-TROPSCH CATALYST: EFFECT OF SUPPORT PARTICLE SIZE 81

4.1. INTRODUCTION 81
4.2. EXPERIMENTAL 83
4.2.1. PREPARATION OF 10WT%CO/CLINO CATALYST 83
4.3. MATERIAL CHARACTERIZATION 84
4.3.1. X-RAY DIFFRACTION 84
4.3.2. X-RAY FLUORESCENCE SPECTROMETRY 84
4.3.3. SCANNING ELECTRON SPECTROSCOPY-ENERGY DISPERSIVE SPECTROSCOPY 84
4.3.4. DETERMINATION OF PARTICLE SIZE USING A MALVERN MASTERSIZER 3000 ANALYZER 85
4.3.5. TPR STUDIES 85
4.4. RESULTS AND DISCUSSION 86
4.4.1. X-RAY DIFFRACTION MEASUREMENTS 86
4.4.2. DISCUSSION OF SEM AND PSD 88
4.4.3. EFFECT OF HEATING RATE ON TPR PROFILE 91
4.4.4. DEGREE OF REDUCTION OF DIFFERENT PARTICLE SIZES OF CATALYST 93
4.4.5. ACTIVATION ENERGY CALCULATIONS 95
4.4.6. EVALUATION OF SURFACE AREA AND PORE VOLUME USING NITROGEN ADSORPTION 98
4.5. CONCLUSION 102

CHAPTER 5: OPTIMIZATION AND EVALUATION OF THE DISTRIBUTION OF FISCHER-TROPSCH PRODUCTS OVER A COBALT-BASED CATALYST UTILIZING DESIGN EXPERT SOFTWARE 107

5.1. INTRODUCTION 108
5.2. EXPERIMENTAL 109
5.2.1. CATALYST PREPARATION 109
5.2.2. MATERIAL CHARACTERIZATION 110
5.2.3. EVALUATION OF FT PERFORMANCE 111
5.2.4. FTS CALCULATIONS 112
5.3. CATALYST CHARACTERIZATION 113
5.3.1. DOE USING RSM 113
5.3.2. DESCRIPTIVE STATISTICS AND MODEL FITTING 118
5.4. RESULTS AND DISCUSSION 118
5.4.1. MODEL FITTING AND ANALYSIS OF VARIANCE 121
5.4.2. MODEL OF SELECTIVITY FOR C_1 123
5.4.3. MODEL OF SELECTIVITY FOR C_2-C_4 128
5.4.4. MODEL OF SELECTIVITY FOR C_{5+} 132
5.5. DETERMINING OPTIMUM CONDITIONS 138
5.6. CONCLUSION 139

CHAPTER 6: EFFECT ON SUPPORT PARTICLE SIZE IN FISCHER-TROPSCH SYNTHESIS: THE USE OF NATURAL CLINOPTILOLITE AS SUPPORT 145

6.1. INTRODUCTION 146
6.2. EXPERIMENTAL SECTION 147
6.5. SYNTHESIS OF 10WT%COBALT ON CLINOPTILOLITE (10WT%CO/CLINO FOR NOMENCLATURE) 147
6.2. MATERIAL CHARACTERIZATION 148
6.2.1. X-RAY DIFFRACTION 148
6.2.2. X-RAY FLUORESCENCE SPECTROMETRY 149
6.2.3. SCANNING ELECTRON SPECTROSCOPY-ENERGY DISPERSIVE SPECTROSCOPY 149
6.2.4. MALVERN MASTERSIZER 3000 USED TO MEASURE PARTICLE SIZE 149
6.2.5. TEMPERATURE PROGRAMMED REDUCTION STUDY 150
6.2.6. EVALUATION OF FT PERFORMANCE 151
6.2.7. FTS CALCULATIONS 151
6.3. RESULTS AND DISCUSSION 153
6.3.1. X-RAY DIFFRACTION MEASUREMENTS 153
6.3.2. SCANNING ELECTRON MICROSCOPE AND PARTICLE SIZE DISTRIBUTION DISCUSSION 155
6.3.3. EFFECT OF HEATING RATES ON TPR PROFILES 160
6.3.4. DEGREE OF REDUCTION OF DIFFERENT CATALYST PARTICLE SIZES 161
6.3.5. ACTIVATION ENERGY CALCULATIONS 163
6.3.6. SURFACE AREA AND PORE VOLUME EVALUATION USING NITROGEN ADSORPTION 165
6.3.7. EFFECT OF TOS ON CO CONVERSATION 168
6.3.8. STATISTICAL ANALYSIS 174
6.4. CONCLUSION 178

CHAPTER 7: OPTIMIZATION AND SCREENING OF IRON-SUPPORTED ON CLINOPTILOLITE AS A LOW-TEMPERATURE FISCHER-TROPSCH SYNTHESIS CATALYST 185

7.1. INTRODUCTION 185
7.1.1. IRON-BASED CATALYST 187
7.2. EXPERIMENTAL 193
7.2.1. CATALYST PREPARATION 193
7.2.2. CATALYST CHARACTERIZATION 194
7.2.3. CATALYTIC TESTING 195
7.2.4. DESIGN OF EXPERIMENT USING RSM 197
7.2.5. DESCRIPTIVE STATISTICS AND MODEL FITTING 198
7.3. RESULTS AND DISCUSSION 198
7.3.1. NORMAL PROBABILITY PLOT OF EFFECTS 199
7.4. EFFECT OF OPERATIONAL PARAMETERS (H_2/CO, TEMPERATURE, PRESSURE AND GHSV) 205
7.4.1. EFFECT OF H_2:CO ON HYDROCARBON SELECTIVITY 206
7.4.2. EFFECT OF TEMPERATURE ON HYDROCARBON SELECTIVITY 209
7.4.3. EFFECT OF PRESSURE ON HYDROCARBON SELECTIVITY 212
7.4.4. EFFECT OF GHSV ON HYDROCARBON SELECTIVITY 215
7.4.5. ADEQUACY OF THE MODEL DEVELOPED 218
7.4.6. MODEL OF SELECTIVITY FOR C_2-C_4 223
7.4.7. MODEL OF SELECTIVITY FOR C_{5+}-C_∞ 227
7.4.8. DETERMINING OPTIMUM CONDITIONS 230
7.5. CONCLUSION 231

CHAPTER 8: CONCLUSION AND RECOMMENDATIONS 238

8.1. CONCLUSION 238
8.1.1. DEBUNKING THE EFFECT OF CRYSTALLITE / PARTICLE SIZE IN COBALT-BASED FISHER-TROPSCH SYNTHESIS 238
8.1.2. EXPERIMENTAL SECTION 239
8.1.3. CLINOPTILOLITE-SUPPORTED COBALT CRYSTALLITE AS FISCHER-TROPSCH CATALYST: EFFECT OF SUPPORT PARTICLE SIZE 240
8.1.4. OPTIMIZATION AND EVALUATION OF THE DISTRIBUTION OF FISCHER-TROPSCH PRODUCTS OVER A COBALT-BASED CATALYST UTILIZING DESIGN EXPERT SOFTWARE 241
8.1.5. EFFECT ON SUPPORT PARTICLE SIZE IN FISCHER-TROPSCH SYNTHESIS: THE USE OF NATURAL CLINOPTILOLITE AS SUPPORT 242
8.1.6. OPTIMIZATION AND SCREENING OF IRON SUPPORTED ON CLINOPTILOLITE AS A LOW-TEMPERATURE FISCHER- TROPSCH SYNTHESIS CATALYST 243
8.2. RECOMMENDATIONS 243

List of Figures

Figure 1.1 (a) Timeline of the number of scientific journal publications per year, (b) number of journal publication by country. Keyword used in the search "Fischer Tropsch.....2
Figure 1.2 : Bibliometric map of keywords created with VOSviewer software based on the 6299 most cited articles in 2016 and 2022.....3
Figure 1.3: Particle with more crystallites with a range of sizes. The crystallite size from XRD can be compared with some imaging technique mostly Transmission electron microscopy (TEM). 5
Figure 2.1: The increase in cobalt crystallite size on CH4 selectivity: 220 °C, H2/CO = 2, 1 bar (Bezemer et al., 2006); 210 °C, H2/CO=2, 1 bar (Den Breejen et al., 2009); 220 °C, H2/CO=2, 1 bar (Martínez et al., 2003); 239 °C, H2/CO=2, 1 bar (Wang et al. 2012). 19
Figure 2.2: Depiction of the relationship between C5+ selectivity and cobalt crystallite size. Source: Reproduced from Borg et al. (2008) Borg et al. (2008) with permission from [Elsevier]. Copyright [2022].....20
Figure 2.3: Three-dimensional (3-D) plot showing the effect of crystallite size and pressure on C1 selectivity (%). 3-D plot generated using Design-Expert 13 22
Figure 2.4: 3-D plot showing the effect of crystallite size and pressure on C2 – C4 selectivity (%). 3-D plot generated using Design-Expert 13.....23
Figure 2.5: 3-D plot showing the effect of crystallite size and pressure on C5 selectivity (%). 3-D plot generated using Design-Expert 13.....24
Figure 2.6: Theoretical study of the effect of PH2O/PH2 and PCO2/PCO on cobalt catalyst. 27
Figure 2.7: Images obtained from TEM and the corresponding cobalt crystallite size distribution of a reduced catalyst. Crystallite size decreases from a>b>c, and metallic cobalt crystallites are dispersed almost homogeneously with a narrow size distribution Cheng. 32
Figure 2.8: Diffraction curves of a model particles with a cubic shape and a cubic unit cell structure. Particle size measurements are given in nm. Source: (Vorokh, 2018). 36
Figure 2.9: The pattern represents the TCD signal resulting from Co3O4 reduction in hydrogen for a cobalt-based catalyst (Gorimbo et al., 2020).....44
Figure 2.10: Prototypical G-H attainable region of Co reduction system (vertices A, B and C) shows the G-H AR boundary vertices (Gorimbo et al., 2020).....46
Figure 3.1: Stages through which the as-received zeolitic material went when preparing the catalyst, including size reduction, followed by size separation. A spinning riffler ensured that the most representative sample of each class size was obtained. 62
Figure 3.2: Photograph of what an XRD machine looks like. A Rigaku Ultima IV machine was used to do the clinoptilolite analysis.....63
Figure 3.3: SEM-energy dispersive spectroscopy TESCAN (Vega 3XMU) 64
Figure 3.4: XRF – Rigaku ZSX Primus II.....65
Figure 3.5: The Malvern Mastersizer 3000 67
Figure 3.6: Laboratory scale flow diagram FT rig with three parallel fixed reactors.....70
Figure 3.7: Photograph and diagram of the disassembled reactor used in this experiment....72
Figure 3.8: Profile of the central temperature of the reactors (measured from the thermopot) 73
Figure 4.1: XRD patterns for the different size classes of the clinoptilolite particles.....86
Figure 4.2: PSD determined using a Malvern Master Sizer 3000 analyzer.....89

Figure 4.3: TPR profile of different catalyst size classes 77
Figure 4.4: TPR at a heating rate of 5, 10 and 15oC. All the different particle sizes are reported. 92
Figure 4.5: DOR of the catalyst at different ramping rates 94
Figure 4.6: Line graph showing DOR of the catalyst at different ramping rates.....94
Figure 4.7: A plot of In β/(T_m^2) versus 1/T_m for all the different clinoptilolite class sizes 96
Figure 4.8: Physisorption isotherms and BJH pore size distribution for cobalt supported on clinoptilolite particles of different sizes.....99
Figure 5.1: Normal probability plot of residuals - C1 selectivity.....119
Figure 5.2: Normal probability plot of residuals - C2-C4 selectivity.....120
Figure 5.3: Normal probability plot of residuals - C5+ selectivity.....121
Figure 5.4: Effect of temperature on C1 selectivity at (a) a low temperature - 200 oC; (b) a high temperature - 270 oC 125
Figure 5.5: Effect of pressure on C1 selectivity at: (a) a low pressure - 5 bar (g); (b) a high pressure - 20 bar (g) 127
Figure 5.6: Effect of temperature on C2-C4 selectivity at: (a) a low-temperature - 200 oC; (b) a high-temperature - 270 oC 130
Figure 5.7: Effect of pressure on C2-C4 selectivity at: (a) a low pressure - 5 barg; (b) a high pressure - 20 bar.....131
Figure 5.8: Effect of temperature on C5+ selectivity at: (a) a low temperature - 200 oC; (b) a high temperature - 270 oC 133
Figure 5.9: Effect of pressure on C5+ selectivity at: (a) a low-pressure; (b) a high-pressure 137
Figure 5.10: Optimized design parameters for the proposed FT process 138
Figure 6.1: X-ray diffraction patterns for each clinoptilolite particle size classes 154
Figure 6.2: PSD analyzed using a Malvern Mastersizer 3000.....156
Figure 6.3: A micrograph captured with a SEM shows 300x magnification of clinoptilolite particles. It shows particles of various sizes and shapes that fall within the particle size range parameters. 157
Figure 6.4: TPR profile of Co-catalyst supported on different size classes of clinoptilolite. 159
Figure 6.5: Temperature reduction was programmed at three heating rates (5, 10 and 15oC/min) for three catalysts with varying support sizes.....160
Figure 6.6: DOR of catalysts at different ramping rates 162
Figure 6.7: Plot of In β/(T_m^2) versus 1/T_m for all the different clinoptilolite size classes 164
Figure 6.8: Physisorption isotherms and BJH pore size distribution for cobalt supported on clinoptilolite with particles of different sizes.....167
Figure 6.9: CO conversion of cobalt catalysts supported on clinoptilolite particles of different size classes 168
Figure 7.1: Flow scheme of the FT rig with a fixed bed reactor (only one reactor used).....196
Figure 7.2: Normal probability residual plot: (a) CH4 selectivity; (b) C2-C4 selectivity; (c) C5+-C∞ selectivity 202
Figure 7.3: Residual versus predicted value: (a) CH4 selectivity; (b) C2-C4 selectivity; (c) C5+-C∞ selectivity 205

Figure 7.4: Effect of H2:CO on hydrocarbon selectivity: (a) CH4 selectivity; (b) C2-C4 selectivity; (c) C5+-C∞ selectivity 208
Figure 7.5: Effect of temperature on hydrocarbon selectivity: (a) CH4 selectivity; (b) C2-C4 selectivity; (c) C5+-C∞ selectivity. 211
Figure 7.6: Effect of pressure on hydrocarbon selectivity: (a) CH4 selectivity; (b) C2-C4 selectivity; (c) C5+-C∞ selectivity. 214
Figure 7.7: GHSV effect on hydrocarbon selectivity: (a) CH4 selectivity; (b) C2-C4 selectivity; (c) C5+-C∞ selectivity 217
Figure 7.8: RSM representation of CH4 selectivity vs reaction parameters 222
Figure 7.9: RSM representation of C2-C4 selectivity in terms of various reaction parameters 226
Figure 7.10: RSM representation of C5+-C∞ selectivity for various reaction parameters ..229
Figure 7.11: Optimized design parameters for the proposed FT process 230

List of Tables

Table 2.1: Effect of cobalt crystallite size on different supports in FTS 16
Table 2.2: Cobalt crystallite size determined by TEM, H2 chemisorption and XRD 38
Table 2.3: Analysis of Variance (ANOVA): Single Factor 39
Table 2.4: Bonferroni post hoc test 40
Table 3.1: Feed components and the calibration gases employed in the investigation, as well as the mole percentages 74
Table 3.2: Response factors for hydrocarbon products 77
Table 4.1: Cobalt loading and crystalline size determination 87
Table 4.2: Measurements of different particle size classes done using SEM 88
Table 4.3: TPR profile of different catalyst size classes 90
Table 4.4: DOR (%)of the catalyst at different heating rates and with different particle sizes 95
Table 4.5: Activation energy calculated using the Kissinger equation 97
Table 4.6: BET analysis of the Co/Clino catalyst 100
Table 5.1: DOE reaction parameters and limits 114
Table 5.2: Experimental responses and predicted responses obtained by means of RSM 101
Table 5.3: ANOVA for the fitted models of responses 109
Table 5.5: Product generation at optimal conditions 126
Table 6.1: Cobalt loading and crystalline size determination 155
Table 6.2: Particle size measurements for various size classes and measurements performed using SEM 155
Table 6.3: Peak reduction temperatures for different catalyst size classes 159
Table 6.4: DOR (%) at different heating rates used for the catalysts with different sizes of particle 162
Table 6.5: Activation energy calculated using the Kissinger equation 164
Table 6.6: BET analysis of Co/Clino catalyst 167
Table 6.7: The calculated values for CO conversion, CO rate and cobalt catalyst activity supported on different size of support. 169
Table 6.8: Comparison of the effect of Co crystallite size, experimental conditions and product selectivity 171
Table 6.9: Anova: Single Factor 175
Table 6.10: t-Test, Two Sample, assuming Equal Variance 176
Table 7.1: Comparison of FT process parameters 186
Table 7.2: Comparative analysis of research conducted using Fe and zeolites 190
Table 7.3: DOE reaction parameters and limits 197
Table 7.4: Experimental responses and predicted responses using RSM 198
Table 7.5: ANOVA for the fitted models of responses 218
Table 7.6: Significance of predicted models 219

LIST OF ABBREVIATIONS, NOMENCLATURES AND SYMBOLS

Abs	Absolute
Afrox	African Oxygen Limited
AIChE	American Institute of Chemical Engineers
ANOVA	Analysis of Variance
ASF	Anderson–Schultz–Flory
BET	Brunauer–Emmett–Teller
BTL	Biomass to liquid
Co	Cobalt
CO	Carbon monoxide
CSTR	Continuous stirred-tank reactor
CTL	Coal to liquid
DOE	Design of experiments
Ea	Activation energy
FBR	Fixed bed reactor
Fe	Iron
FFD	Fixed fluidized bed reactor
FID	Flame ionisation detector
FR	Flow rate
FT	Fischer Tropsch
FTS	Fischer Tropsch synthesis
GC	Gas chromatograph
GTL	Gas to liquid

H_2	Hydrogen
HTFT	High temperature Fischer Tropsch
ID	Internal diameter
mL/min	Millilitre per minute
mol/min	Mole per minute
N	Carbon number
N2	Nitrogen
NTP	Normal temperature and pressure
OD	Outside diameter
P	Pressure
PS	particle size
PSD	Particle size distribution
P&ID	Piping and instrumentation diagram
RSM	Response surface methodology
Syn	Syngas
SA	Surface area
SASOL	South African Coal, Oil and Gas Corporation
SEM	Scanning electron microscopy
SOP	Standard Operating Procedure
T	Temperature
TCD	Thermal conductivity detector
TEM	Transmission electron microscopy
TGA	Thermo gravimetric analysis
TOS	Time on stream

TPR	Temperature-programmed reduction
UHP	Ultra high purity
VOS	Visualisation of similarity
WGS	Water-gas shift
Wn	Mass fraction of the species with carbon number n
XRD	X-ray diffraction
α	Chain growth probability
μm	Micrometre

Chapter 1: Background and Introduction

1.1. Introduction

The Earth has entered a new geological age known as the "Anthropocene," which follows the relatively stable Holocene epoch and comes after it in the geological timescale (Malhi, 2017). The fact that people have profoundly altered the chemical composition of the atmosphere through a range of activities, including industrialisation, is a defining characteristic of the epoch that we are living in now, which is referred to as the Anthropocene. This new development has given rise to a wide range of worries and problems in relation to climate change and global warming.

Since Fischer Tropsch (FT) technology is a significant contributor to climate change, studies into ways to lessen the impact of the technology are warranted. After FT technology was first developed in the 1920s, the number of scholarly articles published in this area slowly but steadily increased. There was only one article published in 1929, but after 1968, when interest began to rise, there was a steady growth (**see Figure 1.1a**). An all-time high of 818 articles was reached in 2008, and since then, the number of papers produced has been gradually declining.

Since the invention of the technology in the early 1920s, there have been **1,632 papers** written about it as of the date of a recent search (**31 September 2022**), which used the phrase "Fischer Tropsch" in both Elsevier's Scopus and Google scholar search engines (**see Figure 1a**). The vast majority of the study has been carried out in industrialized nations (**see Figure 1b**), with the United States of America and China being at the forefront of the field.

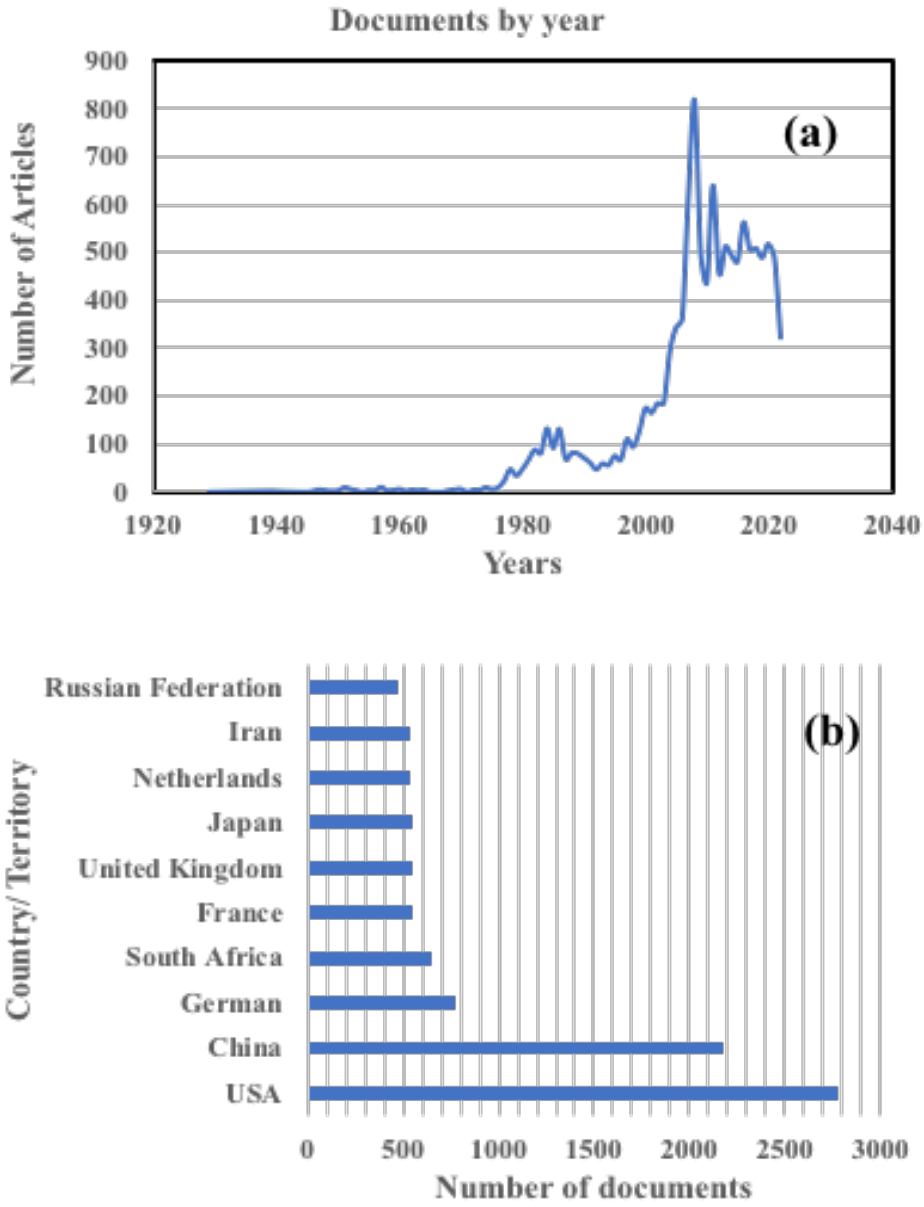

Figure 1.1 (a) Timeline of the number of scientific journal publications per year, (b) number of journal publication by country. Keyword used in the search "Fischer Tropsch

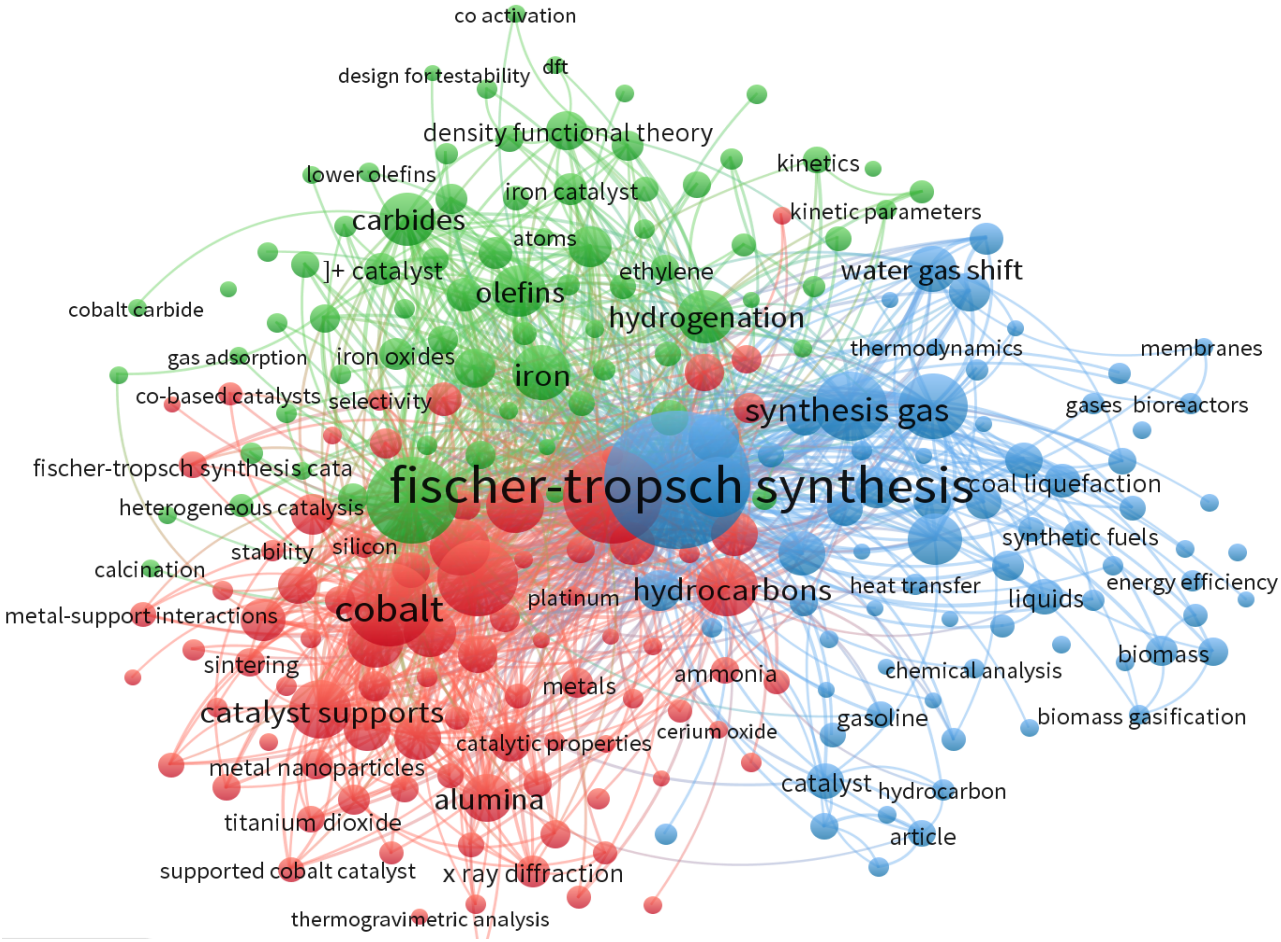

Figure 1.2 : Bibliometric map of keywords created with VOSviewer software based on the 6299 most cited articles in 2016 and 2022.

A bibliometric map of keywords derived from the 6299 publications that were cited the most in 2016 and 2022 was produced by VOSviewer (VOS stands for *visualisation of similarity*) (**Figure 1.2**). The size of the circles is related to the number of times that specific keywords appeared in the research articles that corresponded to the Fischer Tropsch synthesis (FTS) investigations, while the colors were used to categorize the topics with similar concept. The VOSViewer bibliometric tool grouped these articles into three research clusters: Cluster 1 (green): deals with the study of iron catalysts, kinetics and the reactions involved, Cluster 2 (red): focuses more on cobalt catalyst and supports used, Cluster 3 (blue): deals with the energy efficiency and the reactions involved for example water gas shift and biomass gasification. The clusters in **Figure 1.2** illustrate how researchers are seeking to improve iron- and cobalt-based catalysts. The kind of support that is utilized in the production of a catalyst is an important component since it has an effect on how effective the catalyst is and how the products are

distributed. The investigation of new, more cost-effective supports in FTS is not only crucial for the improvement of the processes, but it is also necessary.

Since their discovery, zeolites—a type of microporous crystalline material, have been used in the chemical industry as catalysts, adsorbents, and ion exchangers (Li & Yu, 2021). Naturally occurring zeolites are hydrated aluminosilicate minerals made of three dimensional framework of silica (SiO_4) and alumina (AlO_4) (Marantos, I., Christidis, G. E., & Ulmanu, 2012). Only clinoptilolite, a specific form of zeolite, is currently being mined in South Africa. South African clinoptilolite has a molecular formula $(Na_{1.25}K_{1.6})(Ca_{0.49}Mg_{0.43})(Al_{5.14}Fe_{0.31})(Si_{25.67}Ti_{0.04})O_{62}$ corresponding to a silica content of 77.24%, alumina 13.30%, hematite 0.23% , manganese oxide 0.04%, magnesium oxide 0.86%, Calcium oxide 1.40%, sodium oxide 1.94, potassium oxide 3.78% and titania 0.14% (Gorimbo., 2011). To date, Fischer-Tropsch synthesis (FTS) is conducted on the catalysts mainly Fe, Co, supported on SiO_2, Al_2O_3 and TiO_2 which are the primary components of the natural Clinoptilolite.

Since natural zeolites possess exceptional physical and chemical properties, scientists are eager to investigate their possible use as a catalyst. Among zeolite's many benefits are its low cost, wide availability, and low impact on the environment (Bish & Ming, 1955; Eroglu et al., 2017; Wahono et al., 2020).

Natural zeolites were used as catalyst supports in the conversion of ethanol to gasoline, and a high conversion rate of up to 80–90% was achieved with the aromatics as the main product (Kristiani et al., 2017). In a study by Vrbková et al. (2021), chloroacetic acid-treated montmorillonite was used as a catalyst in the isomerization of carvone to carvacrol. In the study the total conversion of carvone and the selectivity to carvacrol of 95.5% was achieved (Vrbková et al., 2021). Natural zeolite from Pacitan Indonesia, was used as catalyst support for transesterification of palm oil to biodiesel, by varying several process variables the researchers were able to get a yield of 95.09% biodiesel (Kusuma et al., 2013)**.** The natural Zr-Zeolite catalyst was tested on the glycerol acetylation with acetic acids for triacetin production, positive results were obtained with triacetin selectivity and glycerol conversion at 26% and 94.3%, respectively (Cahyono et al., 2016).

The use of natural zeolite as a support in FTS is a bit of an afterthought in the literature, despite having an open-framework structure, therefore the current effort intends to address the potential for their application. Synthetic zeolites have been applied in FT reaction such as ZSM-5 (Javed et al., 2020; Kang et al., 2008; Klerk, 2008; Martínez et al., 2007).

Before employing natural zeolite as a support, the particle size is reduced (with the help of a hammer mill), and then the material is sieved to produce particles of a specific size. In the context of FTS catalysis, the terms "particle size" and "crystallite size" are used synonymously to refer to the metal deposited on the support. In this investigation, a differentiation is made as follows: a particle is defined as a grain of the zeolite support that has been milled and sieved. The size of the metal clusters that have been deposited on these support particles is referred to as the crystallite size (**see Figure 1.3).** XRD detemines crystallite sizes, and SEM determine the sizes of the particles as well as their morphologies.

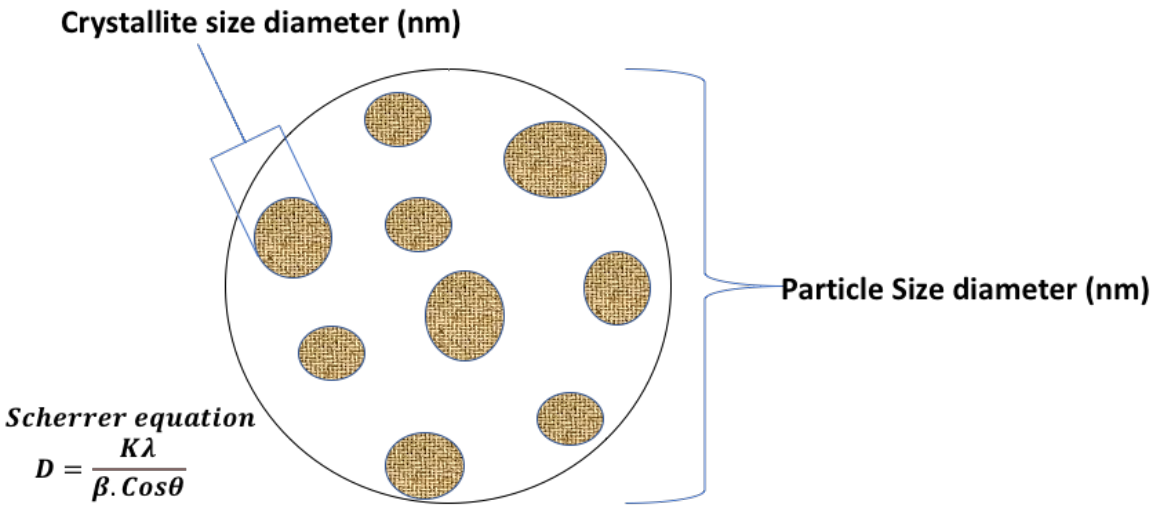

Figure 1.3: Particle with more crystallites with a range of sizes. The crystallite size from XRD can be compared with some imaging technique mostly Transmission electron microscopy (TEM).

Effect of catalyst crystallite size and the type of support has been investigated for different systems, for instance, 1,3-Butadiene Hydrogenation on Pd Catalysts (Decarolis et al., 2018), in methanation reaction (Herranz et al., 2009) and in Fischer−Tropsch reaction (Cheng et al., 2018; Liu et al., 2017). The overarching conclusion that can be drawn from all of these research is that the kind of support and the size of the crystallites both influence the catalytic activity and the product selectivity. Analyzing the crystallite size or particle size is essential for the

process of catalysis because it indicates the size distribution of the particles that make up the catalyst. In the subject of catalysis, there are a few different analytical approaches that may be utilized to quantify the size of the particles.

In catalysis, the search for inexpensive novel materials with open-framework architectures and progressively larger voids is crucial. According to their dimensions (d), the pores of zeolites are categorized as micropores (d < 2 nm), mesopores (2 nm < d < 50 nm), and macropores (d > 50 nm) (Davis, 2002; Li & Yu, 2021). The BET surface area of South African natural clinoptilolite ranged from 65.50 to 33.22 m^2/g, with mesopores varying from 3 to 10 nm (Diale et al., 2011). These characteristics make them promising candidates for use as catalytic support material in FTS. In FTS, the support serves as a carrier for the metal active phase, stabilizes it, and allows access to the active catalyst sites.

Most catalysts consist of crystallite with a diameter between 1 and 50 nm stabilized on chemically inert porous support such as Al_2O_3, SiO_2 or carbon (Cheng et al., 2018; Den Breejen et al., 2009). Crystallite size is not synonymous with particle size, and X-Ray diffraction is sensitive to the crystallite size inside the particles (Monshi et al., 2012). From the well-known Scherrer formula the average crystallite size, D, is given by:

$$D = \frac{K\lambda}{\beta . Cos\theta} \qquad Equation\ 1.1$$

In this equation, D average crystallite size, K is (the Scherrer constant) or K is a constant related to crystallite shape, normally taken as 0.9, λ is the Xray wavelength in nanometers (nm), CuKα=1.5406 angstrom, β is the line broadening at FWHM in radians, and θ is the Bra gg's angle in degrees (Langford & Wilson, 1978; Monshi et al., 2012). The size and location of the metal crystallite deposited on the support material often depend on the nature of the support materials.

1.2. Research justification

The catalyst support is just as crucial as the metals deposited on it since it affects a number of variables, such as the activity, selectivity, stability, and cost of the entire FT process. However, the majority of the catalyst supports utilized in FTS nowadays are manufactured. Natural zeolites (Clinoptilolite, which is mined in South Africa) feature other constituents that are congruent with commercial supports as well as the physico-chemical characteristics of a good support and an appropriate phase makeup. Therefore, it is justified to conduct a thorough inquiry to learn more about naturally supported FT catalysts. Very few researchers have investigated the idea of employing natural zeolites in FTS, which is a substantial gap in the published literature that has both academic and industrial significance.

1.3. Academic and industrial justification

There is a significant amount of potential for the discovery and distribution of new knowledge as a result of the limited knowledge base accessible on natural zeolite applications as supports in FTS catalysis, which is available in the literature. If the price of the catalyst can be brought down, it will be possible to cut significantly into the high costs associated with FTS processing. In order for FT-based operations to be competitive in comparison to crude oil refining and natural gas liquefaction, the question of how to reduce operating costs needs to be investigated. If successful, this might have far-reaching implications for the FT industry. Therefore, there is adequate room for new knowledge to be added to the subject, and there is ample chance to investigate particular facets in sufficient depth for the investigation to have academic and industrial significance.

1.4. Aim and Scope

This thesis will investigate several aspects of catalyst design with the end goal of producing an inexpensive catalyst that is not only highly active and selective but also stable. The scope of this investigation will be restricted to the FTS, the primary objective of which is to generate hydrocarbons through the utilization of a non-convectional catalyst. Used as a support for cobalt catalyst, the natural zeolite will be utilized in this process. We are going to look into the variances that occur when utilizing various support particle sizes, as well as the effects that these differences have on the FTS product distribution. In order to establish the distinctions that are brought about by the utilization of various support particle size classes, a variety of characterization approaches will be utilized. The insights that are gathered from such an

investigation would be utilized in the process of proposing an idea catalyst that possesses the best qualities. An exhaustive analysis of the relevant literature is carried out in order to glean the essential background knowledge required to produce the optimum catalyst with ideal product dispersion.

1.5. Dissertation outcome

It is anticipated that the results of this work will lead to a better knowledge of naturally occurring zeolite supports utilized in FT catalyst, as well as the influence that this will have on the distribution of the product. It is anticipated that the work done on this research project will offer a solid foundation for future study on the use of natural zeolites with and without additional modification in order to build FT catalysts with properties, activity, and selectivity to products that are desirable.

1.6. Dissertation outline

The content of this thesis is broken down into eight sections. This chapter has laid out the foundation for the forthcoming research by providing context, justification, objectives, and a framework for the work to come.

Chapter 2: This chapter provides an overview of the published research on Fischer-Tropsch synthesis. The author pays special attention to the type of support that was utilized and how it affected the behavior of the catalyst. This chapter investigates how the size of the crystallites used in the cobalt-based Fisher-Tropsch synthesis affects the distribution of the products. Therefore, the purpose of this chapter is to set the stage for the subsequent research activity.

Chapter 3: This chapter discusses the experimental equipment and measuring system components used in the investigation, as well as the relevant programs and methods.

Chapter 4: This chapter examines the characterization of cobalt crystallite supported by clinoptilolite as a Fischer-Tropsch catalyst. Focusing specifically on the Effect of support particle size

Chapter 5: This chapter examines the optimization and evaluation of the distribution of Fischer-Tropsch products across a cobalt-based catalyst using the design of experiments (DOE) procedure, a data simulation technique based on the response surface methodology (RSM).

Chapter 6: In this chapter, experiments were done on Fischer-Tropsch Synthesis, and the Effect on support particle size was reported.

Chapter 7: As a low-temperature Fischer-Tropsch synthesis catalyst, iron supported on clinoptilolite has been improved and screened. This study examined whether Iron supported on clinoptilolite may likewise produce positive outcomes.

Chapter 8: The concluding chapter of the thesis provides the key findings of the research covered in the thesis and makes recommendations for additional research.

This thesis, therefore, gives knowledge that is quite useful in regard to the application of natural zeolite in the FTS. The development of the optimal techniques for efficient FT runs and the optimization of performance can be facilitated by this information. The same thesis also contains some suggestions for how future work could be improved.

References

Bish, D. L., & Ming, D. W. (1955). *Natural zeolite: ocurrence, properties, applications* (Vol. 45).

Cahyono, R. B., Mufrodi, Z., Hidayat, A., & Budiman, A. (2016). Acetylation of glycerol for triacetin production using Zr-natural zeolite catalyst. *ARPN Journal of Engineering and Applied Sciences*, *11*(8), 5194–5197.

Cheng, Q., Tian, Y., Lyu, S., Zhao, N., Ma, K., Ding, T., Jiang, Z., Wang, L., Zhang, J., Zheng, L., Gao, F., Dong, L., Tsubaki, N., & Li, X. (2018). Confined small-sized cobalt catalysts stimulate carbon-chain growth reversely by modifying ASF law of Fischer–Tropsch synthesis. *Nature Communications*, *9*(1), 1–9. https://doi.org/10.1038/s41467-018-05755-8

Davis, M. E. (2002). Ordered porous materials for Emerging Applications. *Nature*, *417*(June), 813–821.

Decarolis, D., Lezcano-Gonzalez, I., Gianolio, D., & Beale, A. M. (2018). Effect of Particle Size and Support Type on Pd Catalysts for 1,3-Butadiene Hydrogenation. *Topics in Catalysis*, *61*(3–4), 162–174. https://doi.org/10.1007/s11244-018-0887-4

Den Breejen, J. P., Radstake, P. B., Bezemer, G. L., Bitter, J. H., Frøseth, V., Holmen, A., & De Jong, K. P. (2009). On the origin of the cobalt particle size effects in Fischer-Tropsch catalysis. *Journal of the American Chemical Society*, *131*(20), 7197–7203. https://doi.org/10.1021/ja901006x

Diale, P. P., Muzenda, E., & Zimba, J. (2011). A Study of South African Natural Zeolites Properties and Applications. *Proceedings of the World Congress on Engineering and Computer Science*, *2194*(1), 698–703.

Eroglu, N., Emekci, M., & Athanassiou, C. G. (2017). Applications of natural zeolites on agriculture and food production. *Journal of the Science of Food and Agriculture*, *97*(11), 3487–3499. https://doi.org/10.1002/jsfa.8312

Gorimbo, J. (2011). *Effect of the Homoionic form of Clinoptilolite on Ni2+ Adsorption isotherms: A thermodynamic study, Msc Dissertation, University of the Witwatersrand*

Herranz, T., Deng, X., Cabot, A., Guo, J., & Salmeron, M. (2009). Influence of the Cobalt

Particle Size in the CO Hydrogenation Reaction Studied by In Situ X-Ray Absorption Spectroscopy. *The Journal of Physical Chemistry B*, *113*(31), 10721–10727. https://doi.org/10.1021/jp901602s

Javed, M., Cheng, S., Zhang, G., Amoo, C. C., Wang, J., Lu, P., Lu, C., Xing, C., Sun, J., & Tsubaki, N. (2020). A facile solvent-free synthesis strategy for Co-imbedded zeolite-based Fischer-Tropsch catalysts for direct gasoline production. *Chinese Journal of Catalysis*, *41*(4), 604–612. https://doi.org/10.1016/S1872-2067(19)63436-4

Kang, S. H., Bae, J. W., Prasad, P. S. S., & Jun, K. W. (2008). Fischer-Tropsch synthesis using zeolite-supported iron catalysts for the production of light hydrocarbons. *Catalysis Letters*, *125*(3–4), 264–270. https://doi.org/10.1007/s10562-008-9586-2

Klerk, A. De. (2008). Hydroprocessing peculiarities of Fischer – Tropsch syncrude. *Catalysis Today*, *130*, 439–445. https://doi.org/10.1016/j.cattod.2007.10.006

Kristiani, A., Sudiyarmanto, S., Aulia, F., Nurul Hidayati, L., & Abimanyu, H. (2017). Metal supported on natural zeolite as catalysts for conversion of ethanol to gasoline. *MATEC Web of Conferences*, *101*. https://doi.org/10.1051/matecconf/201710101001

Kusuma, R. I., Hadinoto, J. P., Ayucitra, A., Soetaredjo, F. E., & Ismadji, S. (2013). Natural zeolite from Pacitan Indonesia, as catalyst support for transesterification of palm oil. *Applied Clay Science*, *74*, 121–126. https://doi.org/10.1016/j.clay.2012.04.021

Langford, J. ., & Wilson, J. . (1978). Scherrer after Sixty years: A survey and some new results in the determination of crystallite size. *Journal of Applied Crystallography*, *11*, 102–113. https://doi.org/10.1061/9780784479896.140

Li, Y., & Yu, J. (2021). Emerging applications of zeolites in catalysis, separation and host–guest assembly. *Nature Reviews Materials*, *6*(12), 1156–1174. https://doi.org/10.1038/s41578-021-00347-3

Liu, J., Wang, P., Xu, W., & Hensen, E. J. M. (2017). *Particle Size and Crystal Phase Effects in Fischer-Tropsch Catalysts*. *3*, 467–476.

Malhi, Y. (2017). The Concept of the Anthropocene. In *Annual Review of Environment and Resources* (Vol. 42). https://doi.org/10.1146/annurev-environ-102016-060854

Marantos, I., Christidis, G. E., & Ulmanu, M. (2012). Zeolite formation and deposits. In *Handbook of Zeolites* (pp. 28–51).

Martínez, A., Rollán, J., Arribas, M. A., Cerqueira, H. S., Costa, A. F., & Eduardo, E. F. (2007). A detailed study of the activity and deactivation of zeolites in hybrid Co/SiO2-zeolite Fischer-Tropsch catalysts. *Journal of Catalysis*, *249*(2), 162–173. https://doi.org/10.1016/j.jcat.2007.04.012

Monshi, A., Foroughi, M. R., & Monshi, M. R. (2012). Modified Scherrer Equation to Estimate More Accurately Nano-Crystallite Size Using XRD. *World Journal of Nano Science and Engineering*, *02*(03), 154–160. https://doi.org/10.4236/wjnse.2012.23020

Vrbková, E., Šímová, A., Vyskočilová, E., Lhotka, M., & Červený, L. (2021). Acid Treated Montmorillonite—Eco-Friendly Clay as Catalyst in Carvone Isomerization to Carvacrol. *Reactions*, *2*(4), 486–498. https://doi.org/10.3390/reactions2040031

Wahono, S. K., Stalin, J., Addai-Mensah, J., Skinner, W., Vinu, A., & Vasilev, K. (2020). Physico-chemical modification of natural mordenite-clinoptilolite zeolites and their enhanced CO2 adsorption capacity. *Microporous and Mesoporous Materials*, *294*, 109871. https://doi.org/10.1016/j.micromeso.2019.109871

Chapter 2: Literature Review

This chapter examines the relationship between the crystallite size of cobalt and the distribution of products produced by Fischer-Tropsch synthesis (FTS). The ideal range for the average cobalt crystallite diameter is between 6 and 8 nm, and changing the crystallite size above or below this range affects the carbon monoxide (CO) turnover frequency as well as the selectivity of CH_4, C_2-C_4 and C_{5+}. The morphology, size, and metal loading of the support particles can be carefully monitored and adjusted to facilitate the development of a consistent catalyst. For experimental repeatability during FTS applications, it would be ideal if catalyst particles had uniformly sized crystallites. Methods for crystallite characterization and catalyst synthesis are addressed in detail. As the diameter of the cobalt crystallite appears to be a crucial parameter influencing cobalt crystallite oxidation, the thermodynamics of cobalt reduction and oxidation are reported. Design-Expert optimization of the available literature data led to the optimal circumstances for improving FTS's primary target product, C_{5+} selectivity.

2.1. Introduction

In recent years there has been a proliferation of studies on the effect of the size of cobalt crystallite in FTS catalytic systems when tailoring product distribution by controlling both particles and crystallites sizes (Bezemer et al., 2006; Fang et al., 2020; Fischer et al., 2014; Fu et al., 2014; Herranz et al., 2009; Rane et al., 2012; Yang et al., 2016). Different synthesis methods have been employed to yield the required cobalt crystallite size or a specific cobalt diameter on the surface of different supports. For instance, various 10%Co/ITQ-2 model catalysts were synthesised by combining reverse micellar and surface-silylated ITQ-2 delaminated zeolite to yield a Co^0 crystallite size distribution in the 5–11 nm range (Prieto et al., 2009). In another study, cobalt crystallite ranging from 2.6 to 16 nm was prepared using incipient wetness impregnation by controlling the cobalt loading from 1 to 22 wt% and varying the cobalt precursor used ($Co(NO_3)_2xH_2O$ or $Co(CH_3CO_2)_2 \cdot 4\ H_2O$) or the solvent used ($H_2O$ or EtOH) (Den Breejen et al., 2009). Borg et al. (2008) prepared a cobalt catalyst with a crystallite size of 3 to 18 nm by one-step incipient wetness impregnation of alumina supports (γ and α-Al_2O_3) with a variety of cobalt nitrate solutions. The general observation in all these experiments is regarding the intricacies that come with preparing a catalyst with crystallites of a certain size.

The literature shows that different crystallite sizes of the supported cobalt catalyst behave differently during reduction and reaction. Smaller cobalt crystallites (less than 6 nm) are more difficult to reduce than larger crystallites (20–70 nm) (Jacobs et al., 2007). During the FT reaction, cobalt crystallites with a spherical shape and diameter less than 4.4 nm oxidise easily when $pH_2O/pH_2 < 1.5$, according to Van Steen et al. (2005) (Van Steen et al., 2005). This suggests that controlling the size of crystallite is important. The pore size of the support governs the diameter of the Co_3O_4 cobalt crystallite, with small crystallites forming in narrow support pores and large crystallites forming in wide pores (Borg et al., 2007).

The effect of support particle size is equally essential in FTS, as it affects reactant conversion selectivity. Basically, the smaller the support particle size, the larger the specific surface area of support. Soykal et al. (2012) conducted experiments to evaluate the effect of support particle sizes Co/CeO_2 catalysts in ethanol steam reforming. When comparing two support particles of different sizes (μm range and nm range), they observed that particles in the nm range show better ethanol reforming activity and deliver a higher yield of ethylene. The benefit of being highly resistant to coking was observed with catalysts supported on particles in the nm range, whereas larger ceria particles in the μm range were prone to coke formation.

In FTS systems, researchers use a wide range of support particle sizes. For example, in a study done by Tsubaki et al. (2001), from a pellet size of 74±590 μm silica gel, they used support particles small than 149 μm. Den Breejen et al. (2009) used carbon nanofibers with a 90-150 μm fraction. Fu et al. (2014) used carbon nanotubes (CNT) with a particle size of 180−425 μm. Saib et al. (2002) used silica with a particle size of 212–250 μm. Rane et al. (2012) used 53–90 μm of alumina mixed with silicon carbide 75–150 μm. Because of these variations in particle size, further studies are needed to determine the statistical significance of such wide variations in support size. **Table 2.1** gives examples of cobalt crystallite size on the surface of different particle support sizes.

2.2. Cobalt catalyst preparation methods

Several catalyst preparation methods are used for FTS reactions. The different catalysts are made up of an active component (usually transition metals), which are deposited on inert supports, such as titania, silica, alumina and carbon. These supports improve certain properties, such as the stability of the active component. Precipitation and deposition impregnation are the main methods used to prepare the catalyst (Haber, 1991), though other methods specifically

for the FTS reaction exist (Bianchi et al., 2001; Brunner et al., 2015; Hong et al., 2010; Tsubaki et al., 2001). The synthesis method chosen is known to affect catalyst morphology, i.e. crystallite size, pore size distribution, pore-volume, surface area and promoter distribution (Brunner et al., 2015), which eventually affects product distribution.

A review done by Deraz (2018) on the comparative jurisprudence of catalyst preparation methods focused on impregnation and precipitation methods, and clarified the advantages and disadvantages of each technique. Selection of the catalyst preparation method should be defined by the goals of the study. The impregnation method is often chosen because of its simplicity: the procedure is quicker and cheaper than some other methods. and catalyst properties and configuration can be tailored (Deraz, 2018).

Table 2.1: Effect of cobalt crystallite size on different supports in FTS

Support type	Reaction conditions, pressure, temperature, SV	Cobalt (Co) crystallite size	Characterisation method used to measure crystallite size	Remarks (effects in FTS)	Reference
Silica	239.83 °C, H_2/CO = 2). 1 bar	1.4–10.5 nm	TEM	Smaller Co particles (1.4–2.5 nm) are easily oxidised by the water vapour during FTS. A 1.4-2.5 nm particle size results in lower TOF and higher selectivity to CH_4 Larger Co particles in the range 3.5–10.5 nm show no oxidation during FTS. A 3.5-10.5 particle size does not affect TOF and CH_4 selectivity.	(Wang et al., 2012)
Silica	250 °C, H_2/CO = 2:1) 5 bar	3-11nm	TEM	The maximum activity displayed for Co particles of 10–11 nm in size. CO_2 hydrogenation increases with an increase in Co crystallite size from 3 to 11nm. C5+ maximum extent at 11 nm.	(Melaet et al., 2014)
Alumina	210 ºC, H_2/CO = 2.1 20 bar	2–14 nm	XRD, H_2-chemisorption	When increasing the particle size of Co, C5+ selectivity is maximised at a crystallite	(Rane et al., 2012)

	PS = 53–90 μm			size of 8–9 nm. With larger particles, selectivity to C_{5+} decreases before approaching a constant value.	
Alumina	190 °C, H_2/CO = 2, 9.9 bar PS =150–200 μm	2.3-11.7 nm	XRD, TEM	The selectivity of CH_4 varies inversely with a decrease in crystallite size and C_{5+} selectivity.	(Fischer et al., 2013)
Alumina	210 ºC, 20 bar, and H_2/CO = 2.1 PS = 53 and 90 μm	3 to 18 nm	XRD, TEM, XPS	7–8 nm Co particles yielded maximum C_{5+} selectivity. C_{5+} selectivity constant for crystallite sizes larger than 9– 10 nm.	(Borg et al., 2008)
Silica delaminated ITQ-2 zeolite	220 ºC, H_2/CO = 2 20 bar PS = 0.25–0.42 mm	5.6–141 nm	XRD, H_2-chemisorption and (HR)TEM	The activation energies Co_3O_4 reduction to CoO and Co crystallite size dependent, for particles ranging from 5.6 to141 nm,	(Prieto et al., 2009)
Carbon nanofibers	210, 220 and 250 ºC, H_2/CO = 2).1 and 35 bar PS = 0.5-1.0 mm and 150-212 μm	2.6-27 nm	(TEM), EXAFS, XPS and H_2 chemisorption	FTS is not influenced by Co crystallite size > 6 nm at 1 bar and or >8 nm at 35 bar. Both TOF and C_{5+} selectivity decreased when the crystallite size was decreased from 16 to 2.6 nm.	(Bezemer et al., 2006)

Carbon nanofiber	220 °C, H_2/CO = 2).1 and 35 bar PS = 90-150 μm	2.6-16 nm	TEM, H_2-chemisorption	Co particles < 6 nm result in decreased TOF and increased CH4 selectivity	(Den Breejen et al., 2009)
Activated carbon and on CNTs	230 ºC, H_2/CO=2, 20 bar PS=180−425 μm	2.5 – 20.3 nm	XRD, TEM	Co crystallite up to 7 nm displayed higher TOF and C_{5+} selectivity, -for Co crystallite size greater than 7 nm, no effect observed on TOF and C_{5+} selectivity,	(Fu et al., 2014)

----Information not given. PS = particle size.

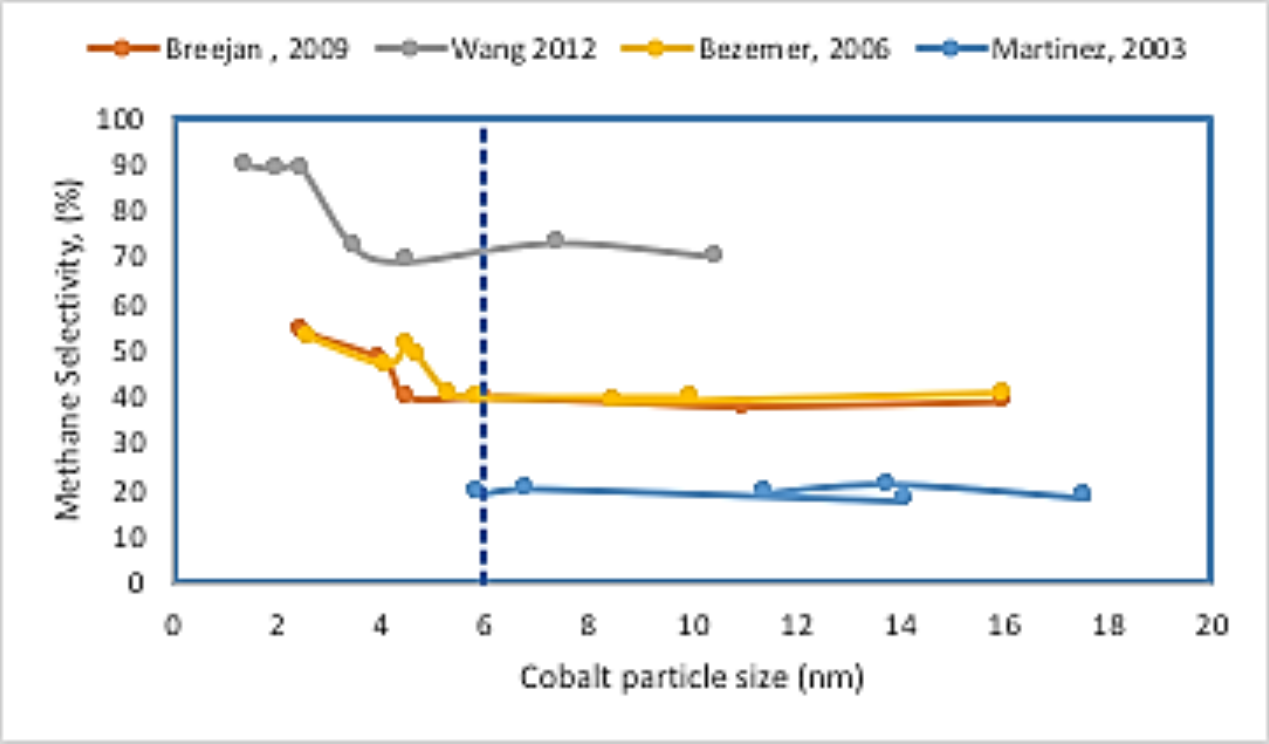

Figure 2.1: The increase in cobalt crystallite size on CH4 selectivity: 220 °C, H2/CO = 2, 1 bar (Bezemer et al., 2006); 210 °C, H2/CO=2, 1 bar (Den Breejen et al., 2009); 220 °C, H2/CO= 2, 1 bar (Martínez et al., 2003); 239 °C, H2/CO= 2, 1 bar (Wang et al. 2012).

Figure 2.1 suggests that CH_4 selectivity is favourable for a cobalt crystallite size less than 6 nm with negligible effect on a larger crystallite size. The methane selectivity shown in **Figure 2.1** differs in magnitude, but more important is the pattern shown and the flattening of the curve after ca.6 nm.

The tabulated literature results (**see Table 2.1**) show that crystallite size affects catalyst activity and product selectivity. Larger cobalt particles (> 7 nm) favour higher TOF and C_{5+} selectivity: for cobalt crystallite ≥7 nm, CH_4 selectivity is suppressed (Fu et al., 2014). In a study carried out by Wang et al. (2012) using steady-state isotopic transient kinetic measurements, it was reported that reduced TOF for Co crystallite <6 nm is attributable to lower intrinsic activity at the small terraces and (to a significant extent) to blocking of edge/corner sites (Wang et al., 2012). The proclivity of small Co crystallite (<6 nm) to favouring high production of CH_4 under FTS conditions is mainly due to higher coverage of surface hydrogen (Den Breejen et al., 2009). It should be noted that turnover rates in FTS are not affected by Co crystallite dispersion and the type of the support used over the accessible dispersion range under typical FTS conditions (Iglesia, 1997b).

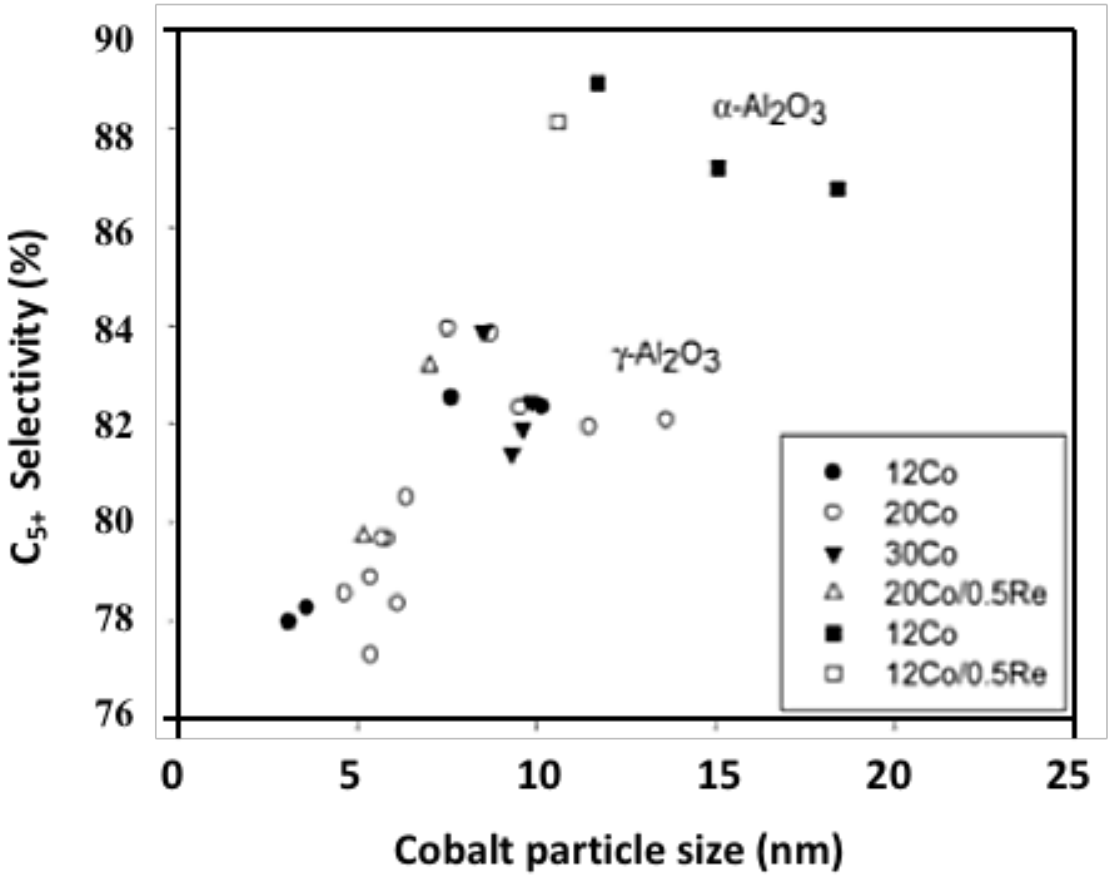

Figure 2.2: Depiction of the relationship between C_{5+} selectivity and cobalt crystallite size. Source: Reproduced from Borg et al. (2008) with permission from [Elsevier]. Copyright [2022].

The activity of the FTS catalyst and its selectivity to desirable C_{5+} hydrocarbons are important production design criteria to consider. **Figure 2.2** shows the relationship of cobalt crystallite size and C_{5+} selectivity. Borg et al. (2008) conducted a series of studies on Co supported on γ-Al_2O_3 and observed that C_{5+} selectivity increases sharply with an increase in crystallite size up to about 7 nm **(see Figure 2.2),** with the optimum crystallite size being about 8 nm. The figure also shows a negligible increase in selectivity for crystallites larger than 9– 10 nm (Borg et al., 2008).

A correlation between CH_4 and C_{5+} selectivity can be deduced from the available literature. Thus, a minimum CH_4 selectivity and maximum C_{5+} selectivity is recorded with larger cobalt crystallites and the opposite is true for smaller sizes. A similar pattern is observed during FTS in a packed bed: when indigenous water accumulates C_{5+} selectivity increases, whereas CH_4 selectivity decreases (Iglesia, 1997a). A study done by Bezemer et al. (2006) supports the view

that TOF and CH_4 selectivity remain unchanged for catalysts with a cobalt crystallite greater than 6.0 nm, while crystallite sizes less than 6 nm result in variations for both selectivity and activity(Bezemer et al., 2006). It can therefore be concluded that the ideal cobalt crystallite size should be greater than 6 nm.

A study done by Bezemer et al. (2006) revealed that the turnover frequency (TOF) for the hydrogenation of CO was not affected by a cobalt crystallite size greater than 6 nm at 1 bar and greater than 8 nm at 35 bar (Bezemer et al., 2006). A number of researchers agree that the TOF which is a surface-specific activity, decreases with a decrease in cobalt crystallite size from about 1 to 7 nm (Den Breejen et al., 2009; Fu et al., 2014). Factors like the type of support used and metal dispersion have been reported not to have an effect on the turnover rate; hence, the activity of the catalyst ought to be proportionate to the number of active sites (Martínez et al., 2003).

The Co_3O_4 crystallite size is influenced significantly by the pore size of the support. A larger pore favours the formation of larger Co_3O_4 crystallites. A study done by Song & Li (2006) indicates that catalysts with a pore size of 6–10 nm produce a moderate Co_3O_4 crystallite diameter, which consequently yields the required selectivity. In a study done by Liu et al. (2007), increasing the pore size of the FTS catalyst from 2.9 to 12.6 nm had a positive effect: catalytic activity, and C_{5+}, C_{12}–C_{18} and C_{18+} selectivity increased and an antagonistic effect on CH_4 selectivity was observed. The higher α values obtained in a study done by Rytter et al. (2018) were attributed to a larger pore size and larger cobalt crystallites, which have a positive effect on CO activation (Rytter et al., 2018). Therefore, pore size is generally a selectivity director. The pore size of the support may control the size of the Co_3O_4 cobalt crystallite, as smaller crystallites form in narrow pores, whereas larger crystallites form in larger pores (Borg et al., 2007).

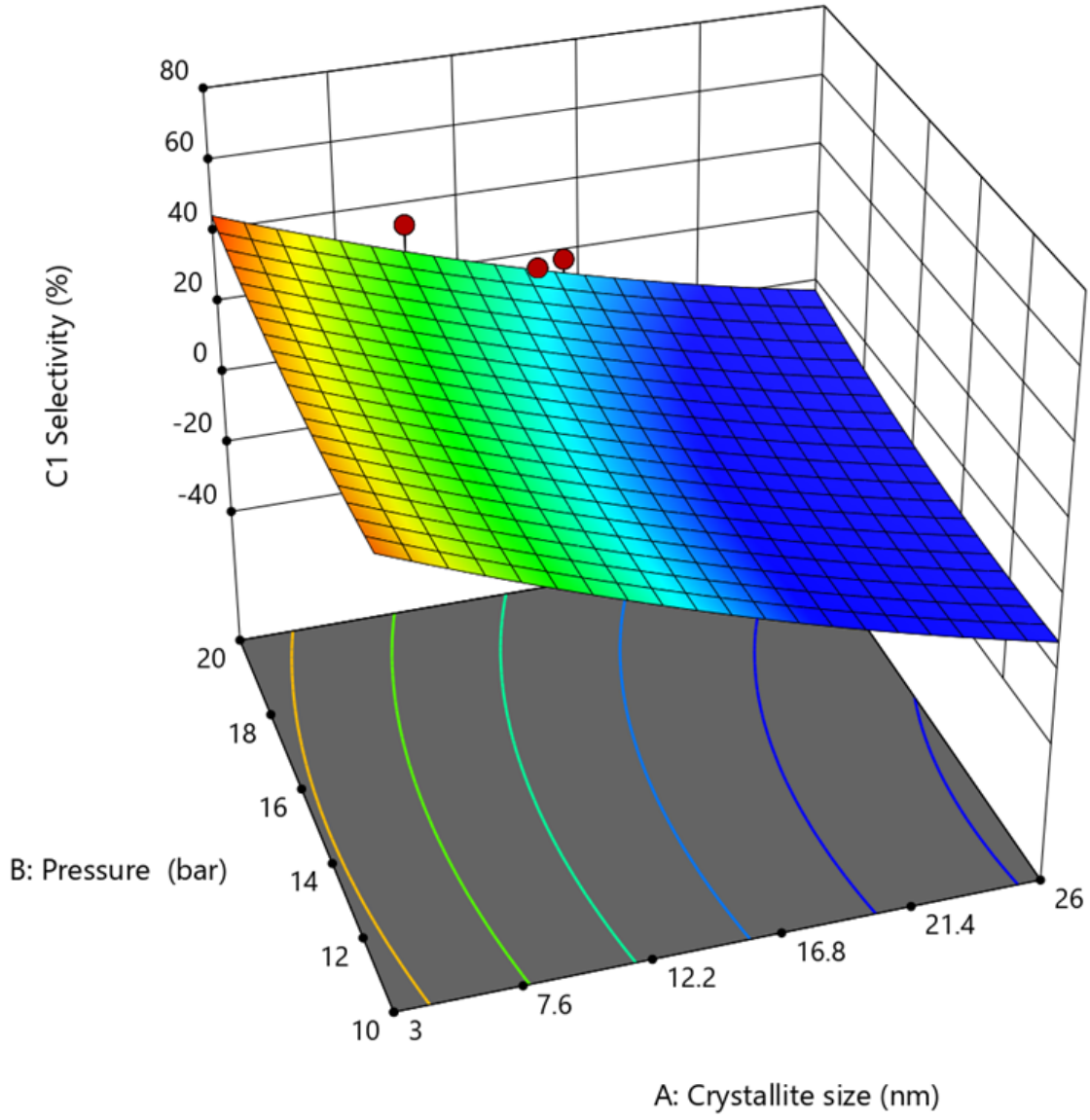

Figure 2.3: Three-dimensional (3-D) plot showing the effect of crystallite size and pressure on C_1 selectivity (%). 3-D plot generated using Design-Expert 13

The data used to construct **Figure 2.3 to Figure 2.5** were extracted from various literature sources (Lira et al., 2008; Martínez et al., 2003; Saib et al., 2002; Song & Li, 2006; Witoon et al., 2011). These sources provided the experimental conditions, catalyst type, catalyst analysis results and product distribution in terms of C_1, C_2-C_4 and C_5 selectivity. Design–Expert 13 was used to generate the 3-D plots. From the data given, smaller cobalt crystallites of less than 12 nm proved to be more selective to methane. Increasing the crystallite size resulted in a decrease in methane selectivity. This observation concurs with the details provided in **Table 2.1**. Increasing pressure has a negligible effect on the conditions given.

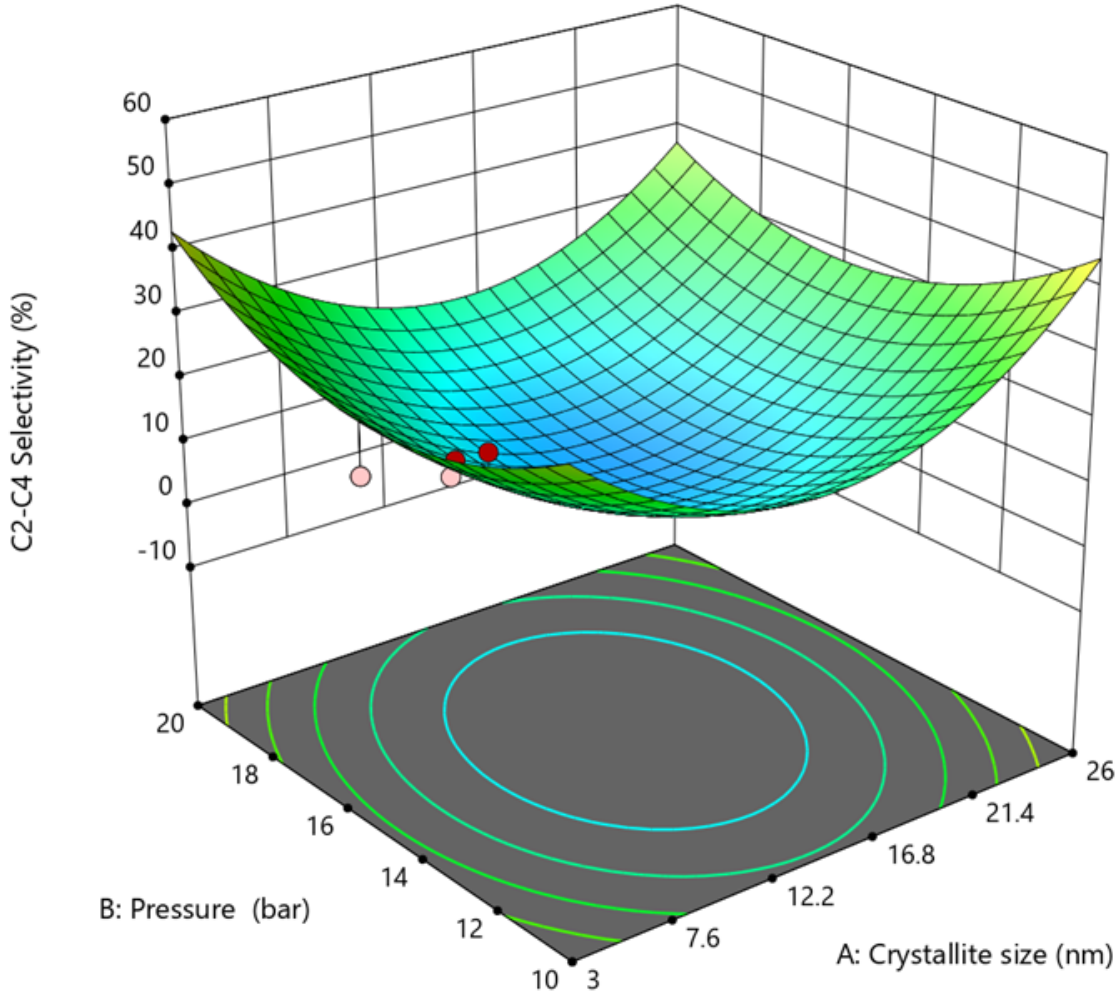

Figure 2.4: 3-D plot showing the effect of crystallite size and pressure on C_2 – C_4 selectivity (%). 3-D plot generated using Design-Expert 13.

C_2 – C_4 selectivity decreases as crystallite size increase from 3 nm to about 15.8 nm, then gradually increases until it reaches 26 nm. Smaller crystallites of 3-7.6 and larger crystallites of 21.4–26 are more selective to C_2-C_4 hydrocarbons. The data for this plot was extracted from various sources (Lira et al., 2008; Martínez et al., 2003; Saib et al., 2002; Song & Li, 2006; Witoon et al., 2011).

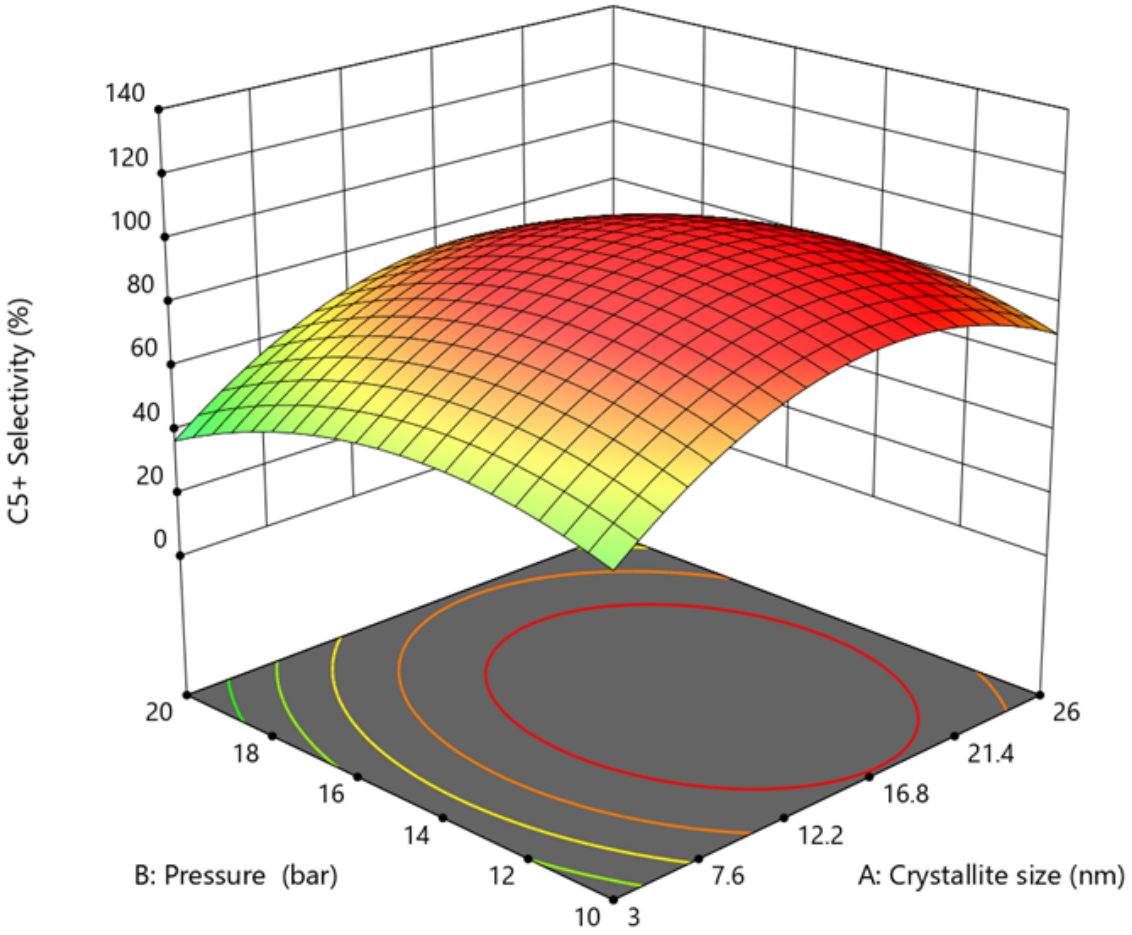

Figure 2.5: 3-D plot showing the effect of crystallite size and pressure on C_{5+} selectivity (%). 3-D plot generated using Design-Expert 13

The effect of pressure and crystallite size produced a dome-shaped distribution, contrary to the pattern observed for C_2-C_4 selectivity (on a carbon basis). Increasing pressure increased C_{5+} to about 16 bar; it then gradually decreased until it reached 20 bar. C_{5+} selectivity increased with an increase in crystallite size until 15.19 nm; it then decreased until it reached 26 nm. The 3-D plot was generated using Design-Expert 13. Analysis of the literature yielded **Figure 2.3 – Figure 2.5** (Lira et al., 2008; Martínez et al., 2003; Saib et al., 2002; Song & Li, 2006; Witoon et al., 2011). Cobalt crystallite size appears to be an important factor that influences product distribution. This novel approach provides insight into selectivity being dependent on pressure and crystallite size in cobalt catalysed FTS.

2.3. Proneness of cobalt catalyst to oxidation

Cobalt catalyst oxidation has been studied extensively as a deactivation mode in FTS (Choudhury et al., 2019; Gorimbo, 2018; Kliewer et al., 2019; Rytter & Holmen, 2015; Van Berge et al., 2000). The literature analysis suggests that, in general, the catalytic properties of small cobalt crystallite differs from that of larger ones in terms of activity, selectivity and deactivation. **Table 2.1** shows that smaller Co particles are easily oxidised by the indigenous water vapour during FTS. A study done by Wang et al. (2012) concludes that with smaller Co crystallite (1.4–2.5 nm), the cobalt metal (Co) was easily oxidised by the indigenous water vapour, which led to reduced TOF and increased CH_4 selectivity. Wang et al (2012) observed that larger Co crystallites of 3.5–10.5 nm are immune to oxidation during FTS and do not affect TOF and CH_4 selectivity.

Thermodynamic analysis done by Van Steen et al. (2005) shows that cobalt crystallites with a spherical shape and measuring < 4.4 nm in diameter are prone to oxidation during FTS (P_{H2O}/P_{H2} < 1.5, *T*) 493 K). The same qualitative observation was recorded by Iglesia (1997), who reported rapid deactivation by oxidation during FTS of cobalt metal crystallite with a diameter less than 5-6 nm. A high P_{H2O}/P_{H2} ratio is needed to re-oxidise bulk cobalt metal, but these ratios are not encountered under normal FTS conditions (Hilmen et al., 1999; Iglesia, 1997a; Van Steen et al., 2005).

Cobalt crystallite size has a significant effect on the activation energy in the stepwise reduction: $Co_3O_4 \rightarrow CoO \rightarrow Co^0$ (Prieto et al., 2009). Thermodynamically, the oxidation of Co^0 by water during FTS is not favoured, but ratio oxidation is observed under very low P_{H2}/P_{H2O}(Van Berge et al., 2000). Cobalt-based catalyst exhibit negligible water-gas shift (WGS) activity, which leads to an increase in H_2O partial pressure during FTS. The issue of crystallite size control is undoubtedly relevant in FTS, as it affects product distribution and catalyst lifetime.

Cobalt oxidation by H_2O and CO_2 is governed by the PH_2/PH_2O and PCO/PCO_2 ratios in the reactor. Cobalt oxidation follows **Equation 2.1** below.

$$Co(s) + \frac{1}{2} O_2(g) = CoO(s) \qquad \text{Equation 2.1}$$

From **equation 2.1**, the minimum oxygen partial pressure required to effect oxidation can be given by **equation 2.2:**

$$\text{Log } PO_2 = -\log K(T) \qquad \text{Equation 2.2}$$

For the oxidation of carbon monoxide, it would be:

$$CO(g) + \frac{1}{2}O_2(g) = CO_2(g) \qquad \text{Equation 2.3}$$

The O_2 partial pressure can be given by **equation 2.4**:

$$\text{Log } \boldsymbol{P}O_2 = 2\log (\boldsymbol{P}CO_2/\boldsymbol{P}_{CO}) - \log K_{co} \qquad \text{Equation 2.4}$$

Equation 2.5 can be used for the oxidation of hydrogen:

$$H_2(g) + \frac{1}{2}O_2(g) = H_2O(g) \qquad \text{Equation 2.5}$$

The oxygen partial pressure can be given by **equation 2.6:**

$$\text{Log } PO_2 = 2\log (\boldsymbol{P}H_2/\boldsymbol{P}H_2O) + \log K_{H2} \qquad \text{Equation 2.6}$$

The oxygen partial pressure corresponds to $\boldsymbol{P}H_2/\boldsymbol{P}H_2O$ and $\boldsymbol{P}CO_2/\boldsymbol{P}_{CO}$ ratios at certain conditions. The plot of O_2 partial pressure versus temperature with different partial pressures of H_2, H_2O, CO and CO_2 can be used to predict the stability of varying cobalt phases. (See **Figure 2.3**.)

Table 2.1: Variation of thermodynamic parameters from 100 – 400°C

	Thermodynamic parameters (range 100-400°C)		
Equation	**Log (Keq)**	**ΔH (kJ)**	**ΔG (kJ)**
$\mathbf{Co(s) + \frac{1}{2}O_2(g) = CoO(s)}$	58.34 to 28.94	-473.83 to -468.00	-416.70 to -372.85

$H_2(g) + \frac{1}{2}O_2(g) = H_2O(g)$	63.04 to 32.64	-485.13 to -490.55	-450.33 to -420.54
$CO(g) + \frac{1}{2}O_2(g) = CO_2(g)$	70.18 to 34.80	-566.70 to -567.05	-501.30 to -448.40

The parameters in **Table 2.1** indicate that all the given reactions are thermodynamically feasible in the temperature ranges given. According to the three equations, the oxygen partial pressure can be related to $\boldsymbol{P}H_2/\boldsymbol{P}H_2O$ and $\boldsymbol{P}CO_2/\boldsymbol{P}_{CO}$ in the reactor at any point during the reaction. From the theoretical calculations of the thermodynamic properties, the oxidation of cobalt catalyst at different $\boldsymbol{P}H_2/\boldsymbol{P}H_2O$, $\boldsymbol{P}CO_2/\boldsymbol{P}_{CO}$ ratios were plotted - see **Figure 2.6.** (The $\boldsymbol{P}H_2/\boldsymbol{P}H_2O$, $\boldsymbol{P}CO_2/\boldsymbol{P}_{CO}$ ratios correspond to a particular partial pressure of O_2.) The thermodynamic calculations for Co^0 oxidation to Co_3O_4 are not presented, as they are approximately four orders of magnitude higher than for Co^0 to CoO.

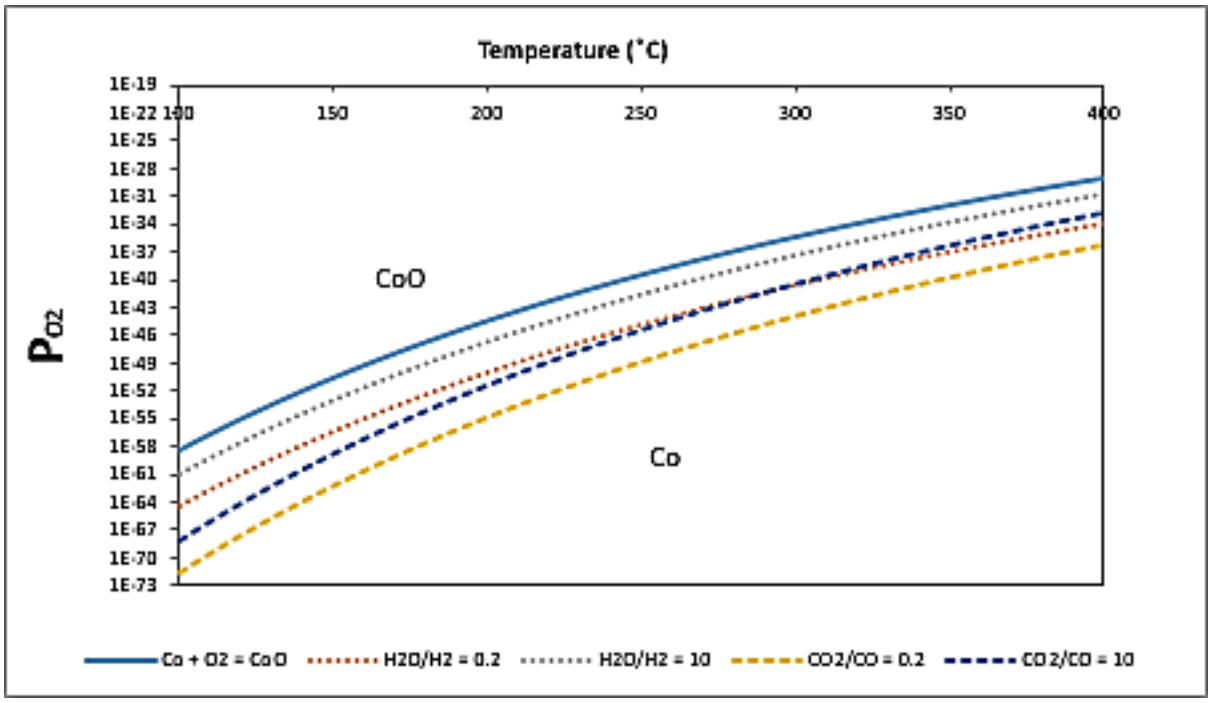

Figure 2.6: Theoretical study of the effect of PH_2O/PH_2 and PCO_2/PCO on cobalt catalyst.

The theoretical calculations show that it is impossible to oxidise the Co-based catalyst under normal FT conditions, as the H_2O/H_2 ratios are usually less than 10. This observation does not agree with many FT practitioners who recorded catalyst oxidation after characterising the spent catalyst. For our theoretical calculations to agree with experimental data, the effects of

cystallite size on thermodynamic properties must be considered. (Here, crystallite size refers to the size of the cobalt metal clusters on the support surface.)

As per **section 2.1**, activity and selectivity can change with changes in crystallite size. Oxidation of cobalt only happens with substantial P_{H2O}/P_{H2} ratios, and these ratios are not encountered under normal FTS conditions, as per Van Steen's calculations (Van Steen et al., 2005). The literature analysis done by Van de Loosdrecht et al. (2007) revealed that, with FTS, P_{H2} ranges from 6.5 to 9.2 bar, and a P_{H2O} between 4.6 and 7.6 bar, corresponding to a P_{H2O}/P_{H2} ratio between 0.5 and 1.2. Cobalt particles of less than 4-5 nm are oxidised if the H_2O/H_2 ratio is 1-1.5 (Van Steen et al., 2005). Schanke et al. (1995) observed no oxidation on 15 and 25 nm particles at a P_{H2O}/P_{H2} of 0.33. Hilmen et al. (1999) experimented with 10 and 16 nm particles using a P_{H2O}/P_{H2} ratio of 10, and observed no Co oxidation. Bian et al. (2003) studied larger Co-crystallites (10 and 29 nm) using a high P_{H2O}/P_{H2} of 6.11 and observed no oxidation. A cobalt particle smaller than 4 nm oxidised at a P_{H2O}/P_{H2} ratio of 0.74 in one study (Iglesia, 1997b). A study done by Jacobs et al. (2003) on a 6 nm Co particle showed that a P_{H2O}/P_{H2} ratio of 0.56 resulted in no oxidation, whereas a P_{H2O}/P_{H2} of 0.60 resulted in oxidation. A study done by Jacobs et al. (2003) showed that, at the same water/hydrogen partial pressure of 0.33, Co- crystallites of less than 6 nm oxidised, whereas the 6 nm crystallites showed no oxidation. Therefore, cobalt oxidation of crystallites less than 6 nm can be avoided by ensuring the correct combination of reactor partial pressure P_{H2O} and P_{H2} .

A study done by Lu (2011) on FT product distribution (using 10%C0/TiO_2) resulted in different P_{H2O}/P_{H2} ratios when using a continuously stirred tank reactor (CSTR) and tubular fixed-bed reactor (TFBR) at H_2/CO = 2 and 20 bar and different pressure. In the study it is shown that the P_{H2O}/P_{H2} ratio increases with temperature. In TFBR, the ratios are significantly higher than in CSTR. The proportions in a CSTR were comparatively lower and tend to approach an asymptote as the temperature is increased to, say, 240 ^oC.

2.4. The effect of cobalt – support interaction

In studying the effect of cobalt crystallite, Bezemer et al. (2006) opined that these type of experiments are better carried out using inert material such as graphitic or carbon-based supports. Oxidic supports, silica and alumina tend to form mixed oxides that are not reduceable

- such as cobalt aluminate or cobalt silicate - which may affect the observations (Li et al., 2002; Van Berge et al., 2000; Wolf et al., 2021).

The strength of cobalt–support interaction has been found to increase in the order $SiO_2 < Al_2O_3 < TiO_2$ (Jacobs et al., 2007; Kliewer et al., 2019; Olusola & Sudip, 2016; Petersen et al., 2019; Yan et al., 2021)**.** Deductions from the literature indicate that strong Co–support interaction of Al_2O_3, and particularly TiO_2, results in increased dispersion and there is a tendency to forming cobalt aluminates and titanates, respectively. This affects the density of the Co^0 surface sites. Comparatively speaking, the interaction of cobalt on a silica support is weaker, which is ideal for complete cobalt oxide reducibility. However, there is a problem with agglomeration of cobalt crystallites during catalyst preparation, which also happens at high temperature during calcination (Martínez et al., 2003). This sintering leads to low Co crystallite dispersion.

2.5. Crystallite size determination techniques

Transmission electron microscopy (TEM), X-ray diffraction (XRD) and H_2-chemisorption are often employed in measuring crystallite size prior to running FTS These analytical techniques often show consistency with crystallite sizes (Bezemer et al., 2006; Den Breejen et al., 2009; Jacobs et al., 2003; Miller et al., 1993; Saib et al., 2010; Schanke et al., 1995), with X-ray absorption studies giving results that are within the experimental error. Powder XRD has been reported to measure millions of crystals and provide the precise size distribution of nano materials (Chauhan, 2014). The terms particle size and crystallite size are often used interchangeably to mean the same thing, but in a material these refer to two distinct properties. Particles are made up of several small crystallites, and nano material properties are dependent on crystallite size, not particle size (Chauhan, 2014).

Due to the principle of measurement, crystallite size calculated with XRD is always smaller than when using the chemisorption method. Crystallite size measured by XRD is smaller than the crystallite size calculated from the results of chemisorption methods. This is expected because the XRD measurements also record dislocations in the crystal structure that are not registered by chemisorption (Geyer et al., 2012). The crystallite size given by TEM analysis agrees with the size derived from XRD traces (Rozita et al., 2010).

Usually, in a minimal particle size regime (nanometer scale), there is close agreement between the TEM and XRD measurements. However, for larger particle size regimes, TEM tends to provide a comparatively larger average particle size than XRD. The discrepancy is attributed to the size that is determined by XRD correlating with the average of the smallest undistorted regions in the material. In contrast, TEM measurements are related to scanned areas separated by more-or-less sharp contours in the micrograph (Rozita et al., 2010).

2.6. Crystallite size measurement techniques

2.6.1. Crystallite characterisation

In FTS, precision catalyst development with defined crystallite size is an area of interest that researchers continue to look at. From the previous sections, it is clear that knowledge of the crystallite size distribution is crucial for interpreting the experimental results of FTS. Various synthetic pathways have been adopted for the preparation of catalysts with uniform good dispersion and controlled crystallite size. Examples include: incipient wetness impregnation (Fu et al., 2014; Gavrilović et al., 2018; Lira et al., 2008; Rytter et al., 2018; Song & Li, 2006; Xiong et al., 2005); the sol-gel technique (Bykova et al., 2012; Liu et al., 2010; Okabe et al., 2004; Sukkathanyawat et al., 2015); the chemical deposition method (Kazemnejad et al., 2019); the precipitation method (Li et al., 2017); the impregnation method (Bian et al., 2003).

Different characterization techniques are used to measure crystallite size accurately. The techniques include TEM, XRD and H_2-chemisoption. Each technique has certain advantages and disadvantages, as there are limitations, given that they are prone to operational and other fundamental uncertainties. So, it is recommended that more than one technique is used to verify agreement if the data. The agreement of the data determined using various methods proves the absence of significant errors in the methods used for each supported metal catalyst. When comparing various experiments that used the XRD Scherrer formula and those that used TEM, it can be concluded that both techniques yielded crystallite size values that are closest for all crystallite sizes less than 60 nm (Vorokh, 2018). Thus, a combination of at least two methods is needed to determine catalyst crystallite size accurately. Work that defines the limitations of various techniques for measuring metal crystallite size has not yet been reported in the case of natural zeolites.

2.6.2. TEM application in determining crystallite size

TEM has been applied to image crystallite size directly on the supported catalyst. However, for accuracy and reproducibility, there is a need for accurate crystallite size distribution analysis. TEM has the advantage of real-space visualisation of nanoparticles. Nevertheless, to ensure accurate results, the operator must still select the correct magnification and have reasonable choices regarding the type of imaging (bright vs dark field) and method of analysis and manual or automated (Pyrz & Buttrey, 2008). These choices have an impact on resolution, the contrast between the background and the particles, the particle population in each image, the efficiency of the analysis and proper background-particle boundary determination (Pyrz & Buttrey, 2008). It is important to note that images visualised at coarse magnifications could clearly show all the particles in that given area, but the reliability of the quantification is severely limited. High magnification imaging results in sampling fewer particles. These limitations contribute to errors or bias in determining the crystallite size of a given sample. Therefore, the statistical significance of the crystallite size determination will be compromised if the particle population is not captured and is not representative of the particle population. Therefore, all variables should be considered, in order to measure particle size distribution with statistical significance and accuracy.

2.6.2.1. TEM limitations

Generally, measuring the crystallite diameter on the supported catalyst and understanding the distribution using TEM can be a challenging exercise. To obtain statistically meaningful data from TEM, many points should be analysed, many particles should be analysed and many crystallites should be measured. Other challenges with TEM image analysis are: the presence of crystallites as clusters at different heights; crystallites that are sometimes embedded in support material; crystallites that overlap; an uneven background. In order to address these issues, Cervera Gontard et al. (2011) invented an image processing algorithm to assist in measuring crystallite size and their distribution using TEM images. The algorithm reportedly allows crystallite to be detected and characterised with greater accuracy than when using other conventional methods (Cervera Gontard et al., 2011). In another study, Fisker et al. (2000) developed an automated image analysis technique built on a deformable ellipse model to

accurately and robustly estimate crystallite size distribution from thousands of crystallites. This method has also proved to be very useful.

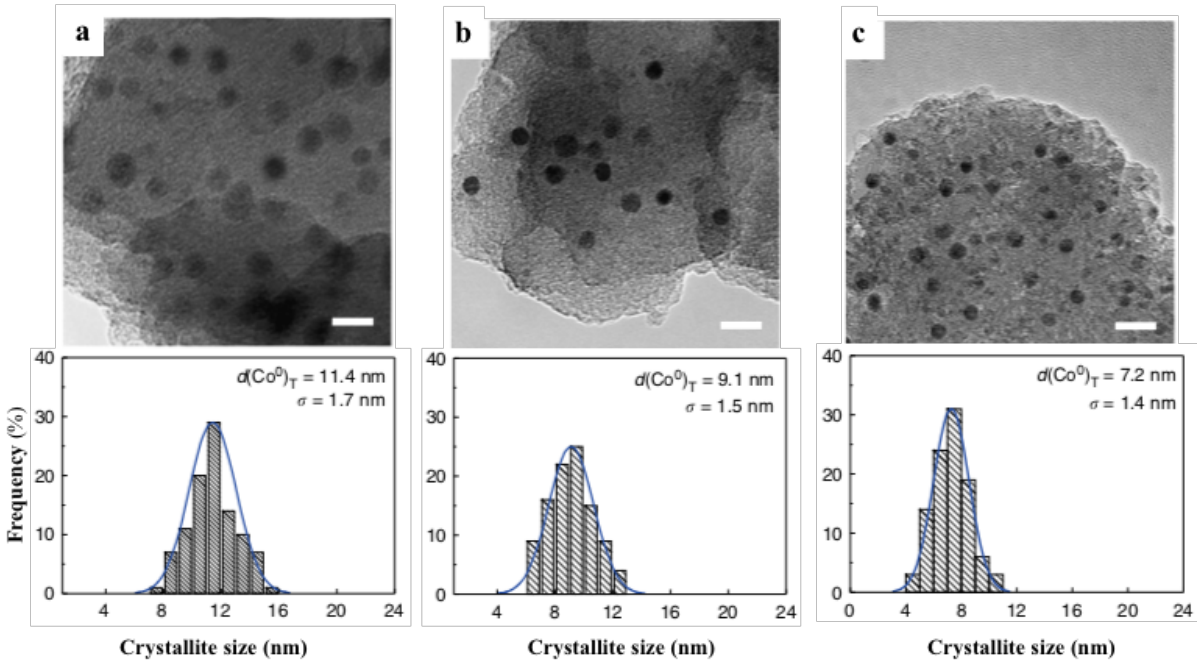

Figure 2.7: Images obtained from TEM and the corresponding cobalt crystallite size distribution of a reduced catalyst. Crystallite size decreases from a>b>c, and metallic cobalt crystallites are dispersed almost homogeneously with a narrow size distribution (modified with permission from Cheng et al., 2018).

Figure 2.7 shows synthesised uniform-sized cobalt crystallites on mesoporous SiO_2 supports. The number of crystallites varies per given area at the same magnification. There is a correlation between crystallite size and selectivity, so the ability to tune the crystallite size controls the selectivity of the products. TEM provides precise information about a small volume of samples, thus sampling techniques need to be representative. The other advantage of TEM is that it can discern crystallite shape and size. Correlation between shape and product selectivity is not mentioned in the available literature. The disadvantages are that TEM sometimes lacks contrast between crystallites and the support, and it is difficult to see tiny particles of 0.5 nm (Mustard & Bartholomew, 1981). In principle, TEM can measure the size of a discrete particle, which can be used to determine particle size average. However, different points or locations need to be imaged to avoid bias and the pictures studied should be representative of the whole sample.

2.6.3. XRD

XRD is another technique that is often used to measure the mean size of crystallites by applying the Scherrer equation to XRD data. The history of applying the Scherrer equation in determining crystallite size is documented in the articles written by Alexander and Klug (1950) and (Langford & Wilson, 1978). The Scherrer equation is the most commonly used modus operandi in FT reported in the literature for extracting crystallite size information from XRD data. The Scherrer Equation, formulated in 1918 to compute the diameter of the crystallite is given in **equation 2.7**.

$$L = \frac{K\lambda}{\beta.cos\theta} \qquad \textbf{Equation 2.7}$$

Where: L is the average crystallite size (crystallite diameter in nanometer (nm)); K is the crystallite shape related constant, normally taken as 0.9 (depending on the shape of the crystallite);

λ is the wavelength of the X-ray, usually in nm; β is the Full Width at Half Maximum (FWHM) at 2θ in radians (β = value of FWHM X π/180), and β varies inversely with crystallite diameter (L); θ is the Bragg angle for the peak at 2θ (in degrees); θ = (2θ/2) FWHM, and θ can be expressed in radians or degrees, since the value of Cosθ corresponds to the same value (Monshi et al., 2012).

2.6.3.1. Uncertainties in calculating crystallite size

The accuracy of the familiar Scherrer Equation is limited by the uncertainties in K (the crystallite shape factor) and β (the pure diffraction broadening) (Alexander & Klug, 1950). In reality, crystallites are not usually uniformly perfect, but have irregular shapes. However, the Scherrer Equation assumes a regular shape for all samples. Although crystallite shape is usually irregular, shapes are often approximated as spheres, triangular prism, cubes, tetrahedra and octahedra, and in some cases include shapes that do not have cubic symmetry (Lele & Anantharaman, 1962; Louër et al., 1972; Wilson AJC, 1969). Special cases of non-cubic

symmetry crystallite shapes that have been considered are parallelepipeds such as needles and plates (Langford & Wilson, 1978).

The K value depends on the determined width, crystallite shape and distribution of the size. The often used values for K (the shape factor) are 0.94 for crystallites that are spherical and 0.89 for some shapes. These values can be approximated to be 1 after rounding off. K varies from 0.62 to 2.08. A detailed discussion of K is given by Langford and Wilson (Langford & Wilson, 1978). The literature survey shows that, when using the Scherrer Equation, the estimates are usually that crystallites are spherical in shape; however, prior analysis using other methods to determine the average crystallite shape can assist in determining the most accurate value of K.

The accuracy of the **Equation 2.7** (the Scherrer crystallite size equation) is restricted partly by the uncertainty regarding the β value, which varies inversely with crystallite size (Alexander & Klug, 1950). FWHM is defined as the diffraction peak width, in radians, at a height halfway between the base and the maxima of the peak (Muniz et al., 2016). FWHM of the broadened line has been criticised for giving unreliable crystallite size values. Therefore, it was proposed that the integral breadth be used together with the Scherrer equation to reduce errors in determining crystallite size (Bushroa et al., 2012). Moreover, the line shape of an XRD pattern is affected by the uneven distribution of crystallite and the wide distribution of size (Bushroa et al., 2012). The Scherrer formula has a lower limit of applicability, which been established. It has been shown that the error when using the Scherrer formula non-linearly increases with a crystallite size less than 4 nm (Vorokh, 2018). In another study, XRD was reported to be insensitive to low metal loading and small particles (<3 nm) (Mustard & Bartholomew, 1981).

2.6.3.2. Crystallite definition

Here, the phrases crystallite size and particle size, and the word size are synonymous with diameter of the crystallite, where the diameter is defined as the length of a straight line traversing through the middle of the mass of the crystallite and ending at the crystallite boundary (Green, 1927; Heywood, 2010). For non-uniform crystallite that cannot be completely defined by a single mean value, a mathematical shape factor for defining the geometric shape can be applied if accuracy is important (Hatch, 1933). Several definitions of

particle size exist in the literature, but the most appropriate is governed by the system being examined and the analysis technique employed (Matyi et al., 1987). For instance, XRD is sensitive to the crystallite size on the surface of or inside any given particle. However, the phrase crystallite size seems more accurate, since individual particles can be made up of many crystallites or domains with non-identical orientations. This distinction is significant if the diameter measured from diffraction broadening is juxtaposed with those obtained from other methods.

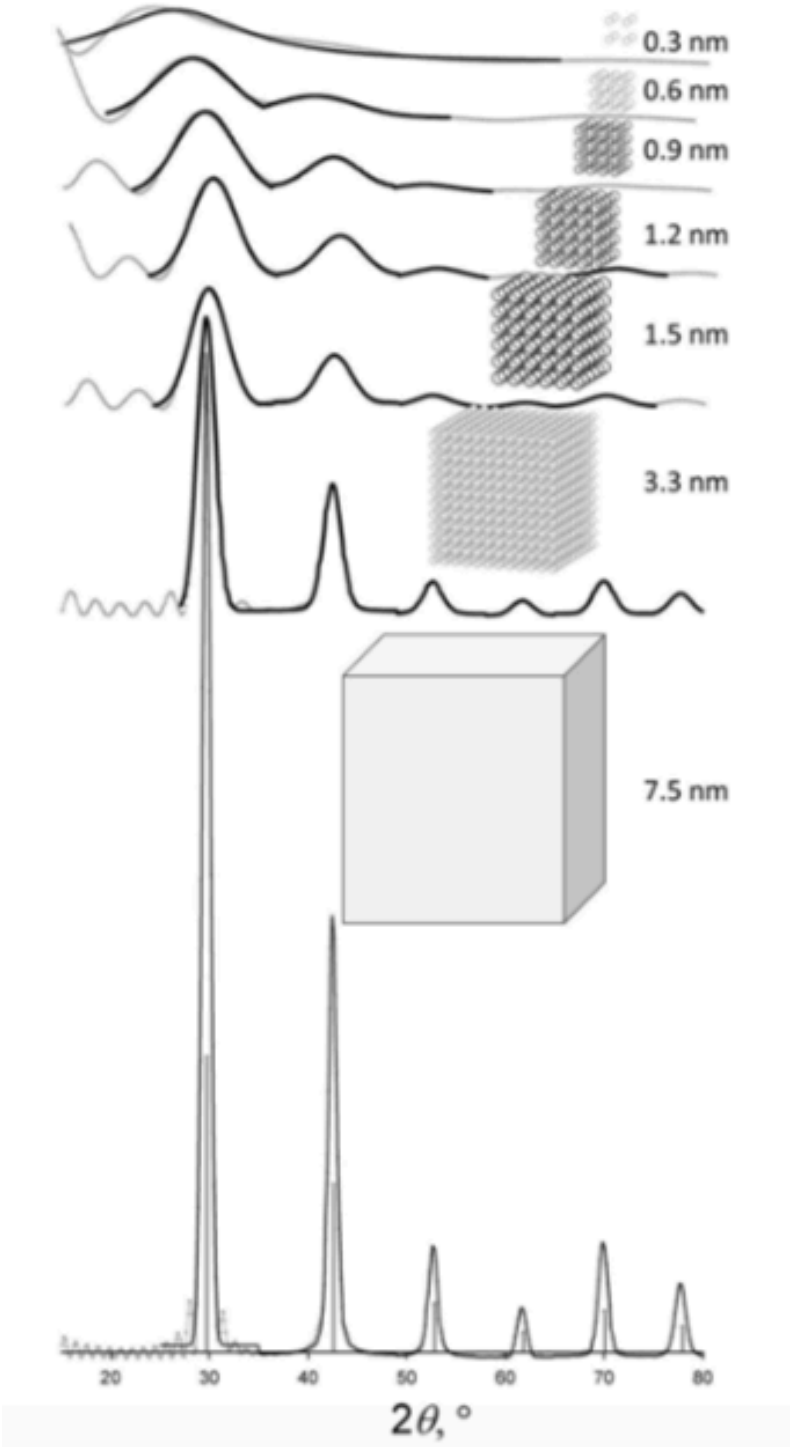

Figure 2.8: Diffraction curves of a model particles with a cubic shape and a cubic unit cell structure. Particle size measurements are given in nm. Source: (Vorokh, 2018).

Figure 2.8 shows that an increase in the size of particles tends to result in narrowing of the peaks to resemble a coarse crystalline material. Smaller particles less than 1.5 nm tend to produce broad peaks synonymous with amorphous substances (Vorokh, 2018). This

phenomenon is observed even if the particles or crystallites are not the same shape and size. The peak width varies with particle or crystallite size, and a narrow peak corresponds with a bigger crystallite diameter. When the peaks are broader, there is a limit to the smallest nanoparticles that can be measured by XRD, (<3 nm) (Mustard & Bartholomew, 1981).

2.6.4. H_2 chemisorption

Many catalyst characterisation studies have utilised H_2 chemisorption as a crystallite size measuring technique (Bezemer et al., 2006; Den Breejen et al., 2009; Prieto et al., 2009; Rane et al., 2012). H_2 chemisorption measurements relate the consumption of H_2 gas molecules to the available surface area of the supported metal crystallites. The relationship that exists between H_2 consumption and the exposed surface area is governed by the chemisorption stoichiometry of the hydrogen-to-metal atom. This technique is useful for small particles when the size is difficult to estimate through electron microscopy or XRD (Almithn & Hibbitts, 2018). The approximation of active crystallite size calculation is a geometrical assumption based on the shape of the crystallite being a regular geometry, with the ideal geometry being a sphere (Webb, 2003).

This analysis makes use of an expression of grain geometry. Using the approximated regular geometry, the size (being the diameter) can then be computed in terms of the volume and area (Webb, 2003). The diameter computed is the average diameter of the active crystallite onto which hydrogen adsorption occurred. The significant economic advantages of using H_2 chemisorption in measuring particle size are that the technique is less expensive than TEM and XRD techniques, it is fairly accurate and it measures particles of all sizes. However, it has disadvantages, as it is easily affected by contamination, there is metal support interaction and adsorption stoichiometry could vary with dispersion or metal loading (Mustard & Bartholomew, 1981). The H_2 chemisorption method also has other inherent difficulties that hinder its effective application, for example, in order for measurement by H_2 chemisorption to make sense, the probe gas should be adsorbed on the surface of the metal as a monolayer and gas desorption should be complete (Matyi et al., 1987).

2.6.4.1. Cobalt crystallite size determined by TEM, H_2 chemisorption and XRD

The crystallite size of cobalt-based catalysts are tabulated in **Table 2.2**. The catalysts were prepared differently by different authors and different analytical methods (TEM, H_2 chemisorption and XRD) were used to determine the crystallite size. When comparing and computing the differences obtained by using two or more methods to determine crystallite size, a statistical approach was used to check if differences exist when certain techniques are used. One-way ANOVA followed by post-hoc Bonferroni correction was used to analyse the results in the literature.

Table 2.2: Cobalt crystallite size determined by TEM, H_2 chemisorption and XRD

	Crystallite determination method (measurements in nm)			**Reference**
Co- based catalyst	**TEM**	**H_2 chemisorption**	**XRD (nm)**	
Co/SiO_2-20	26	19.8	-	(Saib et al., 2002)
Co/SiO_2-40	3	5.9	-	
Co/SiO_2-60	6.7	6	-	
Co/SiO_2-100	6.9	7.3	-	
Co/SiO_2-150	8.3	10.6	-	
Co-silica ID	-	19.9	23.5	(Zhang et al., 2006)
Co-acetic acid	-	14.2	16.1	
Co-ethanol	-	19	22.3	
Co-1-propanol	-	15.6	18.2	
Co-1-butanol	-	14.9	16.5	
30% Co/SiO_2	183	141	125	(Prieto et al., 2009)
10% Co/ITQ(1)	12.8	10.4	12.5	
10% Co/ITQ(2)	8.2	8.9	9.9	
10% Co/ITQ(3)	-	7.3	9.1	
10% Co/ITQ(4)	6.3	5.6	6.8	
10% Co/ITQ(5)	-	-	5.9	
Cat-12 h	11.4	10.6	12.8	

Cat-8h	9.1	8.9	11	(Cheng et al., 2018)
Cat-4h	7.2	7.3	8.9	
Cat-1M	14.3	12.3	13.1	
HDP11	30	25		(Bezemer et al., 2006)
HDP9	14	12.5		
IWN13	7.5	8.5		
IEN4	3.6	4.4		
IWA1	3.7	6.1		
5Co/M	3	-	5	(H. Li et al., 2006)
10Co/M	4.5	-	11	
15Co/M	6.5	-	14	

- Not determined (method not used)

Table 2.3 provides a summary of the one-way ANOVA results that compare different analysis methods used to determine crystallite size. To enable a comparison to be done of the different techniques, a post-hoc Bonferroni correction test was performed, and the results tabulated. As shown in all the ANOVA tables, the *P* values are greater than 0.05 and F is less than Fcrit, which provides strong evidence that the techniques yield almost similar measurements. In layman's terms, the analysis of variance (ANOVA) informs you whether or not there are significant statistical differences between the means of three characterization instruments.

Table 2.3: Analysis of Variance (ANOVA): Single Factor

Summary

Groups	*Count*	*Sum*	*Average*	*Variance*
TEM vs H_2 Chemisorption	18	72.1	4.00555556	92.5923203
TEM vs XRD	11	82.7	7.51818182	285.787636
XRD vs H_2 Chemisorption	14	41.8	2.98571429	14.6551648

ANOVA

Source of variation	*SS*	*df*	*MS*	*F*	*P-value*	*F crit*
Between groups	136.483561	2	68.2417803	0.59052311	0.55879474	3.23172699
Within groups	4622.46295	40	115.561574			
Total	4758.94651	42				

Table 2.4: Bonferroni post hoc test

t-Test: Two-Sample assuming Equal Variance

	TEM vs H_2 chemisorption	*TEM vs XRD*		
Mean	4.00555556	7.51818182		
Variance	92.5923203	285.787636		
Observations	18	11		
Pooled variance	164.146141			
Hypothesized mean Difference	0			
df	27			
t Stat	-0.7163911			
P(T<=t) one-tail	0.2399505			
t Critical one-tail	1.70328845			
P(T<=t) two-tail	0.47990099		0.01666667	FALSE
t Critical two-tail	2.05183052			

t-Test: Two-Sample assuming Equal Variance

	TEM vs H_2 chemisorption	*XRD vs H_2 chemisorption*			
Mean	4.00555556	2.98571429			
Variance	92.5923203	14.6551648			
Observations	18	14			
Pooled variance	58.8195529				
Hypothesized mean Difference	0				
df	30				
t Stat	0.37316165				
P(T<=t) one-tail	0.355826				
t Critical one-tail	1.69726089				
P(T<=t) two-tail	0.711652		0.01666667	False	FALSE
t Critical two-tail	2.04227246				

t-Test: Two-Sample assuming Equal Variance

	TEM vs XRD	*XRD vs H_2 chemisorption*
Mean	7.51818182	2.98571429
Variance	285.787636	14.6551648

Observations	11	14		
Pooled variance	132.538848			
Hypothesized mean Difference	0			
df	23			
t Stat	0.97713251			
P(T<=t) one-tail	0.16933498			
t Critical one-tail	1.71387153			
P(T<=t) two-tail	0.33866996		0.01666667	FALSE
t Critical two-tail	2.06865761			

A one-way ANOVA, followed by a post-hoc Bonferroni correction test, indicated that any of the techniques (TEM, XRD and H_2 chemisorption) can be used to determine crystallite size with P(T <=t) two-tail values all greater that an alpha value of 0.05, even after applying the Bonferroni test (all are above 0.01666667). Any of the techniques discussed can be adopted to give measurements that are of statistical significance, as there are no differences within groups or any combination of techniques.

2.7. Cobalt catalyst reduction

Temperature-programmed reduction (TPR) is a technique applied in FT catalysis, with a catalyst precursor undergoing monitored reduction while the temperature is increased linearly with time. TPR studies of catalysts is a crucial step in FT technology as it produces the active catalyst. The method has been used extensively to study supported and unsupported catalysts to extract qualitative information such as the oxidation state of the reducible species present (Bao et al., 2009; Gorimbo, 2018b; Jacobs et al., 2007; Jozwiak et al., 2007). The technique is highly sensitive to the presence of species in a reducible form and discussions on the sensitivity of the TPR profiles (peak shape, maximum temperature, resolution of reduction steps, etc.)

have been published (Christel et al., 1997; Fierro et al., 1994; Giordano et al., 2000; Malet & Caballero, 1988; Monti & Baiker, 1983).

The TPR technique has been used as a successful fingerprint method for characterising FT catalysts - mainly cobalt and iron. This section will focus on the cobalt-based catalyst in FTS only. Several factors that influence the TPR profile have been studied, and sample weight, hydrogen concentration, carrier flow rate, total hydrogen consumption, and heating rates tend to have a greater degree of influence (Bosch et al., 1984). The conditions reported in the literature differ widely; as a result, it is challenging to compare TPR profiles obtained by different researchers. (See **Figure 2.9**.)

TPR with hydrogen is a commonly used technique for characterising catalysts in FTS reaction. An in-depth understanding of the accurate reduction pathway of the FTS catalyst is an important piece of information. In the case of the cobalt-based catalyst, Co_3O_4 undergoes reduction to Co in two steps, with CoO being the intermediate species regardless of support type (SiO_2, TiO_2, and Al_2O_3) (Jacobs et al., 2007; Kliewer et al., 2019; Xiong et al., 2005). Using hydrogen (H_2) as the reduction gas yields two different reduction regions, as shown in **Figure 2.9**.

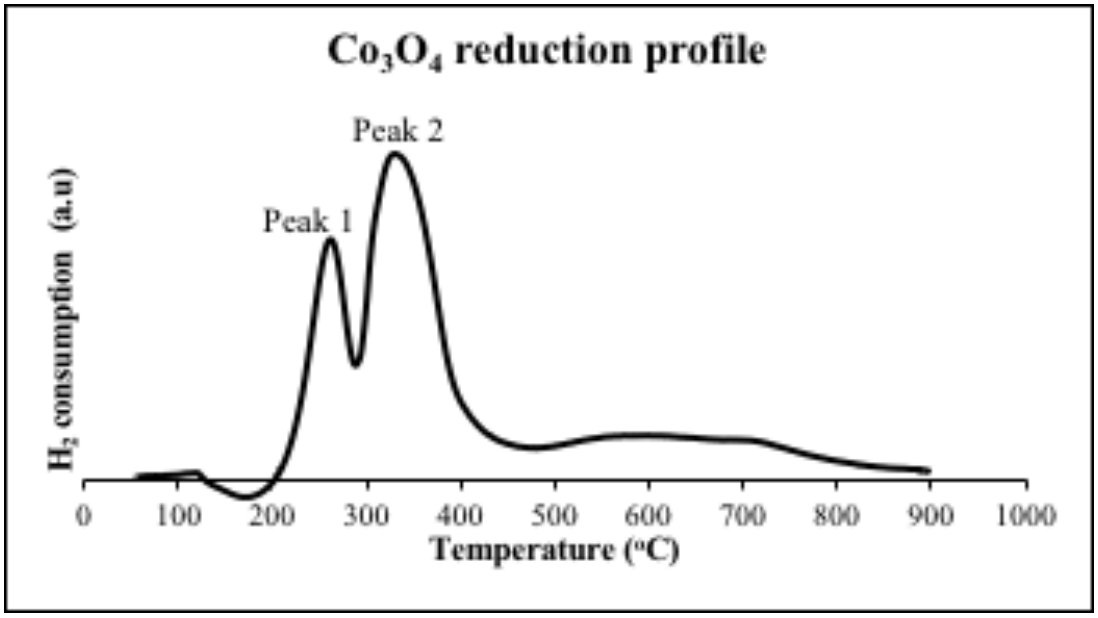

Figure 2.9: The pattern represents the TCD signal resulting from Co_3O_4 reduction in hydrogen for a cobalt-based catalyst (Gorimbo et al., 2020).

Various reducing agents have been used in FTS, including hydrogen, carbon monoxide and syngas (Gorimbo, 2016). In the case of hydrogen, the degree of reduction is determined by monitoring H_2, consumption while increasing the sample temperature at a constant rate. As a result, the reduction profiles are obtained at different temperatures. An elevated temperature is sometimes necessary for reduction, such as when strong metal-support interaction is experienced (Jacobs et al., 2007).

The stoichiometry of **equation 2.8** suggests that 1 mole of Co_3O_4 yields 4 moles of H_2O during reduction.

H_2 -reduction $Co_3O_4 + 4H_2 \rightarrow 3Co + 4H_2O$ Equation 2.8

Co_3O_4 reduction to CoO consumes 1 mole of hydrogen, and it then reduces to metallic Co using 1 mole of H_2 - see **Figure 2.9**.

First peak: $Co_3O_4 + H_2 \rightarrow 3CoO + H_2O$ Equation 2.9

Second peak: $CoO + H_2 \rightarrow Co + H_2O$ Equation 2.10

2.8. Thermodynamics of Co-based catalysts

Gibbs free energy and enthalpy of the reaction system at specific temperature and pressure levels have been used to plot the mass balance-attainable region of the FT system (Gorimbo et al., 2020). Gibbs free energy gives the work potential of the given scenario, while enthalpy presents the minimum reaction energy requirements of the system. So, +ΔH values indicate that work and energy should be supplied to the reaction system, whereas -ΔH values indicate that work and energy are released by the system. Pressure deviations are not considered significant in terms of enthalpy and Gibbs free energy at the temperature levels studied.

$$\Delta H^0 = \Delta H_0^0 + R\int_{T_0}^{T}\frac{\Delta C^0}{R}dT \qquad \text{Equation 2.11}$$

Where ΔH^0 and ΔH_0^0 are heat of formation of the components at temperature T and reference temperature T_0. The heat capacity term at temperature T is given by **equation 2.12**.

$$\frac{\Delta C_P^0}{R} = A + BT + CT^2 + DT^{-2} \qquad \text{Equation 2.12}$$

Where A, B, C and D are heat transfer coefficients. Integrating **equation 2.11 and 2.12** to get ΔH^0 at temperature T gives **equation 2.13**, where: $\text{Ƭ} = \frac{\text{Ƭ}}{T_o}$

$$\Delta H° = \Delta H_o° + R * [\Delta A * T_o * (\text{Ƭ} - 1) + \frac{\Delta B}{2} * {T_o}^2 * (\text{Ƭ}^2 - 1) + \frac{\Delta C}{3} * {T_o}^3 * (\text{Ƭ}^3 - 1) + \frac{\Delta D}{T_o} * (\frac{\text{Ƭ} - 1}{\text{Ƭ}})]$$

Equation 2.13

ΔG at various temperatures can be calculated using **Equation 2.14** (Smith et al., 2018).

$$\Delta G^{\circ}{}_{\text{T}} = \Delta H^{\circ}{}_{\text{o}} - \frac{T}{T_o}(\Delta H^{\circ}{}_{\text{o}} - \Delta G^{\circ}{}_{\text{o}}) + R\int_{T.}^{T}\frac{\Delta \text{Cp}^{\circ}}{R}dT - RT\int_{T.}^{T}\frac{\Delta \text{Cp}^{\circ}}{R}\frac{dT}{T} \qquad \text{Equation 2.14}$$

Where: $\int_{T.}^{T}\frac{\Delta \text{Cp}^{\circ}}{R}dT = \Delta A * T_o * (\text{Ƭ} - 1) + \frac{\Delta B}{2} * \frac{\Delta B}{2} * {T_o}^2 * (\text{Ƭ}^2 - 1) + \frac{\Delta C}{3} * {T_o}^3 * (\text{Ƭ}^3 - 1) + \frac{\Delta D}{\text{To}} * (\frac{\text{Ƭ} - 1}{\text{Ƭ}})$

and $\int_{T.}^{T}\frac{\Delta \text{Cp}^{\circ}}{R}\frac{dT}{T} = \Delta A * ln\text{Ƭ} + [\Delta B T_o + (\Delta C {T_o}^2 + \frac{\Delta \text{D}}{\text{Ƭ}^2 {T_o}^2})(\frac{\text{Ƭ}+1}{2})] * (\text{Ƭ} - 1)$

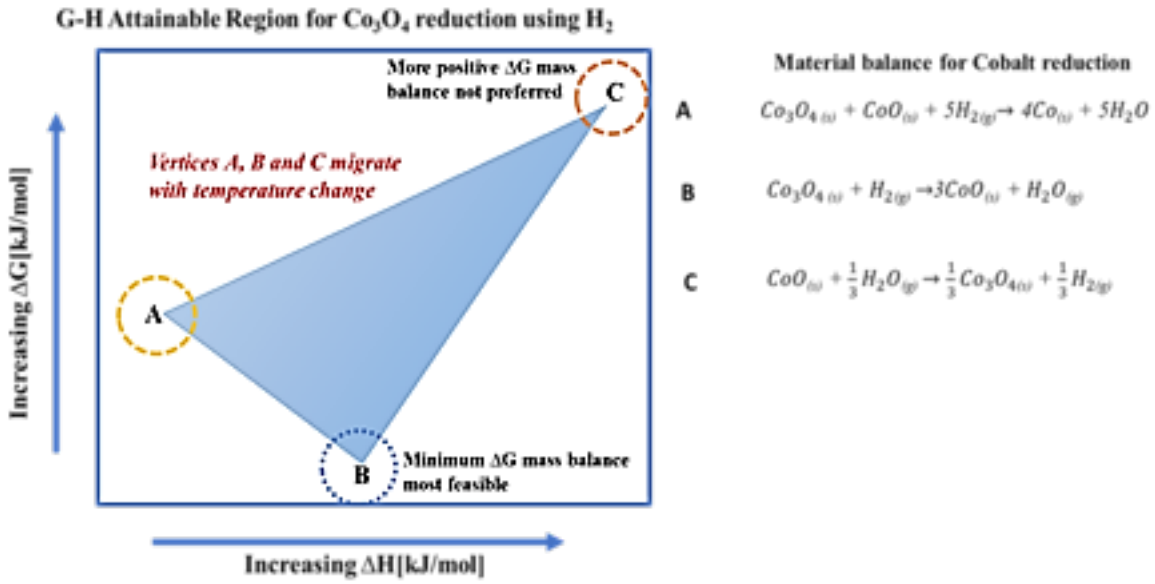

Figure 2.10: Prototypical G-H attainable region of Co reduction system (vertices A, B and C) shows the G-H AR boundary vertices (Gorimbo et al., 2020).

Gorimbo et al. (2020) applied the Attainable Region (AR) approach to cobalt catalyst reduction thermodynamics and depicted the reduction pathway, as shown in **Figure 2.10.** The method entails setting up ideal conditions for Co reduction and focusing on determining minimal G at varying temperatures. **Figure 2.10**, supported by **Figure 2.10** and TAR space diagrams, shows that the reduction of Co_3O_4 often happens through two reaction stages. Peak 1 is assigned to direct reduction of Co_3O_4 to Co and Co_3O_4 to intermediate CoO. Then peak 2 is assigned to the reduction of Co_3O_4 to Co or CoO to Co (Jacobs et al., 2007).

2.9. Pore size

Several catalysts used in FTS are porous, with pores grouped as macropores, mesopores and micropores (Haber, 1991). The surface area, pore volume and pore diameter determined by Brunauer, Emmett and Teller (BET) theory, influences the catalyst activity and product selectivity. These parameters govern reactant diffusion. Porosity relates to the volume percentage occupied by the pores, and the pore-size distribution refers to the pore volume distribution with reference to pore size. Porosity is a key factor in controlling the diffusion of

reactants from the pore mouth through the catalyst pores to the immediate vicinity of the internal catalytic surface and desorption of the products from the surface (Haber, 1991).

The metal crystallite size and the extent of reduction were shown to increase linearly with an increase in the support pore diameter (Iglesia, 1997a). Iglesia (1997) also observed that the metal crystallites form clusters on the surface of the support, and that increasing the support pore diameter resulted in the size of the clusters increasing. If cobalt crystallites form that are bigger than the average pore diameter of the support, they will probably be situated on the external surface of the support. A general observation is that cobalt crystallite distribution on the support is not even, i.e. clusters of various sized crystallites can be observed on the support (Saib et al., 2002).

Xie et al. (2012) used CNT and reported an important phenomenon: Co catalyst crystallites inside CNT reduced more easily than those outside CNT; with crystallites inside the CNT, smaller Co crystallite reduced better than bigger crystallites. Xie et al. (2012) observed that FT catalytic activity was higher for Co crystallite inside the CNT than outside it Xie et al. (2012). Larger pores correspond to the formation of larger Co_3O_4 crystallite with decreased dispersion. Different pore sizes exhibited by supports result in varying CO adsorption properties. Supports with a pore size in the range 6–10 nm have shown to result in better FT activity and more selectivity to the desired C_{5+}. This observation is attributed to moderate crystallite size and CO adsorption on the catalyst (Song & Li, 2006).

2.10. Promoters

In FT, promoters are chemical additives that enhance the physical, chemical and catalytic properties of the catalyst. In a study done by Jacobs et al. (2002), reducing temperature was significantly reduced by incorporating small amounts of Ru and Pt during the synthesis of a cobalt-based catalyst (Jacobs et al., 2002). Adding Mn has been shown to enhance metal cluster dispersion, which results in a smaller average size of cobalt crystallite (Sukkathanyawat et al., 2015). Mn also influences FTS product distribution by promoting the formation of long chain hydrocarbon on a cobalt-supported catalyst (Sukkathanyawat et al., 2015). Findings reported by Morales et al. (2007) indicate that species of MnO cause positive structural and electronic

modification of the catalyst, resulting in improved FT catalytic performance. Morales et al. (2007) also observed that the WGS reaction is catalysed by MnO, which adjusts the H_2/CO ratio and alters overall FT catalytic performance. Alkali metals are also useful as FT catalyst chemical promoters, as they affect activity and selectivity. Performance evaluation of the Co/Al_2O_3 catalysts promoted Li, Na, K, Rb, and Cs resulted in enhanced C_{5+} selectivity (Gholami et al., 2021). Generally, the literature provides definitive evidence that promoters facilitate Co reducibility at a lower reduction temperature than non promoted catalyst. Several detailed reviews on the effect of promoters are available.

2.11. Concluding remarks

The literature analysis indicates that the catalytic properties of small cobalt particles (<6 nm) differ from larger ones (>6 nm) in FT synthesis. Oxidation of cobalt particles less than 6 nm in diameter can be minimized by correctly adjusting the hydrogen and water partial pressure in the FT reactor. The crystallite diameter of cobalt particle size appears to be a parameter of influence in controlling speciation by oxidation of the cobalt catalyst. From the literature surveyed, the general conclusion is that cobalt crystallite size has a significant effect on product selectivity. Cobalt crystallite with a size of <6-8 nm tends to favor the formation of methane and reduce C_{5+} selectivity.

H_2 adsorption is the most convenient, accurate and generally applicable technique for estimating the average crystallite size of several FT catalysts. However, TEM is a precise technique for measuring the average crystallite size and the distribution of the size of the metal catalysts in FT. XRD is widely used in FT to determine particle size, although it is generally insensitive to small metal particles that are <3 nm (Mustard & Bartholomew, 1981).

It is apparent that no single method fully characterises crystallite size and distribution in supported metal catalysts in the absence of inherent theoretical shortcomings, uncertainty in the experimental approach and ambiguity in the interpretation of results. Therefore, it is ideal to use multiple techniques whenever possible, so as to validate the readings obtained.

References

Alexander, L., & Klug, H. P. (1950). Determination of crystallite size with the x-ray spectrometer. *Journal of Applied Physics*, *21*(2), 137–142. https://doi.org/10.1063/1.1699612

Almithn, A. S., & Hibbitts, D. D. (2018). Supra-monolayer coverages on small metal clusters and their effects on H2 chemisorption particle size estimates. *AIChE Journal*, *64*(8), 3109–3120. https://doi.org/10.1002/aic.16110

Bao, A., Liew, K., & Li, J. (2009). Fischer-Tropsch synthesis on CaO-promoted Co/Al2O3 catalysts. *Journal of Molecular Catalysis A: Chemical*, *304*(1–2), 47–51. https://doi.org/10.1016/j.molcata.2009.01.022

Bezemer, G. L., Bitter, J. H., Kuipers, H. P. C. E., Oosterbeek, H., Holewijn, J. E., Xu, X., Kapteijn, F., Van Diilen, A. J., & De Jong, K. P. (2006). Cobalt particle size effects in the Fischer-Tropsch reaction studied with carbon nanofiber supported catalysts. *Journal of the American Chemical Society*, *128*(12), 3956–3964. https://doi.org/10.1021/ja058282w

Bian, G. Z., Fujishita, N., Mochizuki, T., Ning, W. S., & Yamada, M. (2003). Investigations on the structural changes of two Co/SiO2 catalysts by performing Fischer-Tropsch synthesis. *Applied Catalysis A: General*, *252*(2), 251–260. https://doi.org/10.1016/S0926-860X(03)00470-8

Bianchi, C. L., Martini, F., & Moggi, P. (2001). *Co / SiO 2 sol – gel catalysts for Fischer – Tropsch synthesis*. *76*(1), 65–69.

Borg, Ø., Dietzel, P. D. C., Spjelkavik, A. I., Tveten, E. Z., Walmsley, J. C., Diplas, S., Eri, S., Holmen, A., & Rytter, E. (2008). Fischer-Tropsch synthesis: Cobalt particle size and support effects on intrinsic activity and product distribution. *Journal of Catalysis*, *259*(2), 161–164. https://doi.org/10.1016/j.jcat.2008.08.017

Borg, Ø., Eri, S., Blekkan, E. A., Storsæter, S., Wigum, H., Rytter, E., & Holmen, A. (2007). Fischer-Tropsch synthesis over γ-alumina-supported cobalt catalysts: Effect of support variables. *Journal of Catalysis*, *248*(1), 89–100. https://doi.org/10.1016/j.jcat.2007.03.008

Bosch, H., Kip, B. J., Van Ommen, J. G., & Gellings, P. J. (1984). Factors influencing the temperature-programmed reduction profiles of vanadium pentoxide. *Journal of the*

Chemical Society, Faraday Transactions 1: Physical Chemistry Phases, *80*(9), 2479–2488. https://doi.org/10.1039/F19848002479

Brunner, K. M., Huang, B., Woodfield, B. F., & Hecker, W. C. (2015). Iron Fischer-Tropsch catalysts prepared by solvent-deficient precipitation (SDP): Effects of washing, promoter addition step, and drying temperature. *Catalysts*, *5*(3), 1352–1374. https://doi.org/10.3390/catal5031352

Bushroa, A. R., Rahbari, R. G., Masjuki, H. H., & Muhamad, M. R. (2012). Approximation of crystallite size and microstrain via XRD line broadening analysis in TiSiN thin films. *Vacuum*, *86*(8), 1107–1112. https://doi.org/10.1016/j.vacuum.2011.10.011

Bykova, M. V., Ermakov, D. Y., Kaichev, V. V., Bulavchenko, O. A., Saraev, A. A., Lebedev, M. Y., & Yakovlev, V. (2012). Ni-based sol-gel catalysts as promising systems for crude bio-oil upgrading: Guaiacol hydrodeoxygenation study. *Applied Catalysis B: Environmental*, *113–114*, 296–307. https://doi.org/10.1016/j.apcatb.2011.11.051

Cervera Gontard, L., Ozkaya, D., & Dunin-Borkowski, R. E. (2011). A simple algorithm for measuring particle size distributions on an uneven background from TEM images. *Ultramicroscopy*, *111*(2), 101–106. https://doi.org/10.1016/j.ultramic.2010.10.011

Chauhan, A. (2014). Powder XRD Technique and its Applications in Science and Technology. *Journal of Analytical & Bioanalytical Techniques*, *5*(6). https://doi.org/10.4172/2155-9872.1000212

Cheng, Q., Tian, Y., Lyu, S., Zhao, N., Ma, K., Ding, T., Jiang, Z., Wang, L., Zhang, J., Zheng, L., Gao, F., Dong, L., Tsubaki, N., & Li, X. (2018). Confined small-sized cobalt catalysts stimulate carbon-chain growth reversely by modifying ASF law of Fischer–Tropsch synthesis. *Nature Communications*, *9*(1), 1–9. https://doi.org/10.1038/s41467-018-05755-8

Choudhury, H. A., Cheng, X., Afzal, S., Prakash, A. V., Tatarchuk, B. J., & Elbashir, N. O. (2019). Understanding the deactivation process of a microfibrous entrapped cobalt catalyst in supercritical fluid Fischer-Tropsch Synthesis. *Catalysis Today*, *January*. https://doi.org/10.1016/j.cattod.2019.01.031

Christel, L., Pierre, A., & Abel, D. A. M. R. (1997). Temperature programmed reduction studies of nickel manganite spinels. *Thermochimica Acta*, *306*(1–2), 51–59.

https://doi.org/10.1016/s0040-6031(97)00299-2

Den Breejen, J. P., Radstake, P. B., Bezemer, G. L., Bitter, J. H., Frøseth, V., Holmen, A., & De Jong, K. P. (2009). On the origin of the cobalt particle size effects in Fischer-Tropsch catalysis. *Journal of the American Chemical Society*, *131*(20), 7197–7203. https://doi.org/10.1021/ja901006x

Deraz, N. M. (2018). comparative jurisprudence of catalysts preparation methods: I. precipitation and impregnation methods.', J. Ind. Environ. Chem., vol. 2, no. 1, pp. 19–21, 2018.The comparative jurisprudence of catalysts preparation methods: I. precipitation and impregnati. *Journal of Industrial and Environmental Chemistry*, *2*(1), 19–21.

Fang, X., Liu, B., Cao, K., Yang, P., Zhao, Q., Jiang, F., Xu, Y., Chen, R., & Liu, X. (2020). Particle-Size-Dependent Methane Selectivity Evolution in Cobalt-Based Fischer-Tropsch Synthesis. *ACS Catalysis*, *10*(4), 2799–2816. https://doi.org/10.1021/acscatal.9b05371

Fierro, G., Lo Jacono, M., Inversi, M., Porta, P., Lavecchia, R., & Cioci, F. (1994). A study of anomalous temperature-programmed reduction profiles of Cu2O, CuO, and CuO-ZnO catalysts. In *Journal of Catalysis* (Vol. 148, Issue 2, pp. 709–721). https://doi.org/10.1006/jcat.1994.1257

Fischer, N., Van Steen, E., & Claeys, M. (2013). Structure sensitivity of the Fischer-Tropsch activity and selectivity on alumina supported cobalt catalysts. *Journal of Catalysis*, *299*, 67–80. https://doi.org/10.1016/j.jcat.2012.11.013

Fischer, Nico, Clapham, B., Feltes, T., van Steen, E., & Claeys, M. (2014). Size-Dependent Phase Transformation of Catalytically Active Nanoparticles Captured In Situ. *Angewandte Chemie*, *126*(5), 1366–1369. https://doi.org/10.1002/ange.201306899

Fisker, R., Carstensen, J. M., Hansen, M. F., Bødker, F., & Mørup, S. (2000). Estimation of nanoparticle size distributions by image analysis. *Journal of Nanoparticle Research*, *2*(3), 267–277. https://doi.org/10.1023/A:1010023316775

Fu, T., Lv, J., & Li, Z. (2014). Effect of carbon porosity and cobalt particle size on the catalytic performance of carbon supported cobalt fischer-tropsch catalysts. *Industrial and Engineering Chemistry Research*, *53*(4), 1342–1350. https://doi.org/10.1021/ie402128y

Gavrilović, L., Brandin, J., Holmen, A., Venvik, H. J., Myrstad, R., & Blekkan, E. A. (2018). Fischer-Tropsch synthesis—Investigation of the deactivation of a Co catalyst by exposure

to aerosol particles of potassium salt. *Applied Catalysis B: Environmental*, *230*(September 2017), 203–209. https://doi.org/10.1016/j.apcatb.2018.02.048

Geyer, R., Hunold, J., Keck, M., Kraak, P., Pachulski, A., & Schödel, R. (2012). Methods for determining the metal crystallite size of Ni supported catalysts. *Chemie-Ingenieur-Technik*, *84*(1–2), 160–164. https://doi.org/10.1002/cite.201100101

Gholami, Z., Tišler, Z., & Rubáš, V. (2021). Recent advances in Fischer-Tropsch synthesis using cobalt-based catalysts: a review on supports, promoters, and reactors. *Catalysis Reviews - Science and Engineering*, *63*(3), 512–595. https://doi.org/10.1080/01614940.2020.1762367

Giordano, F., Trovarelli, A., De Leitenburg, C., & Giona, M. (2000). A Model for the Temperature-Programmed Reduction of Low and High Surface Area Ceria. *Journal of Catalysis*, *193*(2), 273–282. https://doi.org/10.1006/jcat.2000.2900

Gorimbo, J. (2016). *An experimental and thermodynamic study of iron catalyst activation and deactivation during Fischer Tropsch Synthsis, PhD thesis,* University of the Witwatersrand.

Gorimbo, J. (2018). Use of stability diagrams to predict catalyst speciation during Fischer Tropsch reduction stage: A mini-review. *Catalysis Science and Technology*, *8*(8), 2022–2029. https://doi.org/10.1039/c8cy00228b

Gorimbo, J., Muvhiiwa, R., Llane, E., & Hildebrandt, D. (2020). Cobalt Catalyst Reduction Thermodynamics in Fischer Tropsch: An Attainable Region Approach. *Reactions*, *1*(2), 115–129. https://doi.org/10.3390/reactions1020010

Green, H. (1927). The Effect of Non-uniformity and Particulate Shape on "Average Particle' Size". *Jl. Franklin Inst.*, *204*, 713–729.

Haber, J. (1991). Manual on catalyst characterization. *Pure and Applied Chemistry*, *63*(9), 1227–1246. https://doi.org/10.1351/pac199163091227

Hatch, T. (1933). Determination of “average particle size” from the screen-analysis of non-uniform particulate substances. *Journal of the Franklin Institute*, *215*(1), 27–37. https://doi.org/10.1016/S0016-0032(33)90137-4

Herranz, T., Deng, X., Cabot, A., Guo, J., & Salmeron, M. (2009). Influence of the Cobalt Particle Size in the CO Hydrogenation Reaction Studied by In Situ X-Ray Absorption

Spectroscopy. *The Journal of Physical Chemistry B*, *113*(31), 10721–10727. https://doi.org/10.1021/jp901602s

Heywood, H. (2010). Numerical definitions of particle size and shape. *Journal of the Society of Chemical Industry*, *56*(7), 149–154. https://doi.org/10.1002/jctb.5000560702

Hilmen, A. M., Schanke, D., Hanssen, K. F., & Holmen, A. (1999). Study of the effect of water on alumina supported cobalt Fischer–Tropsch catalysts.pdf. *Applied Catalysis A*, *186*, 169–188.

Hong, J., Chu, W., Ying, Y., Chernavskii, P. A., & Khodakov, A. (2010). Plasma-assisted design of supported cobalt catalysts for Fischer-Tropsch synthesis. In *Studies in Surface Science and Catalysis* (Vol. 175). Elsevier Masson SAS. https://doi.org/10.1016/S0167-2991(10)75036-9

Iglesia, E. (1997a). Design, synthesis, and use of cobalt-based Fischer-Tropsch synthesis catalysts. *Applied Catalysis A: General*, *161*(1–2), 59–78. https://doi.org/10.1016/S0926-860X(97)00186-5

Iglesia, E. (1997b). Fischer-Tropsch synthesis on cobalt catalysts: Structural requirements and reaction pathways. *Studies in Surface Science and Catalysis*, *107*, 153–162. https://doi.org/10.1016/s0167-2991(97)80328-x

Jacobs, G., Das, T. K., Patterson, P. M., Li, J., Sanchez, L., & Davis, B. H. (2003). Fischer-Tropsch synthesis XAFS - XAFS studies of the effect of water on a Pt-promoted Co/Al2O3 catalyst. *Applied Catalysis A: General*, *247*(2), 335–343. https://doi.org/10.1016/S0926-860X(03)00107-8

Jacobs, G., Das, T. K., Zhang, Y., Li, J., Racoillet, G., & Davis, B. H. (2002). Fischer-Tropsch synthesis: Support, loading, and promoter effects on the reducibility of cobalt catalysts. *Applied Catalysis A: General*, *233*(1–2), 263–281. https://doi.org/10.1016/S0926-860X(02)00195-3

Jacobs, G., Ji, Y., Davis, B. H., Cronauer, D., Kropf, A. J., & Marshall, C. L. (2007). Fischer – Tropsch synthesis : Temperature programmed EXAFS / XANES investigation of the influence of support type , cobalt loading , and noble metal promoter addition to the reduction behavior of cobalt oxide particles. *Applied Catalysis A General*, *333*, 177–191. https://doi.org/10.1016/j.apcata.2007.07.027

Jozwiak, W. K., Kaczmarek, E., Maniecki, T. P., Ignaczak, W., & Maniukiewicz, W. (2007). Reduction behavior of iron oxides in hydrogen and carbon monoxide atmospheres. *Applied Catalysis A: General*, *326*(1), 17–27. https://doi.org/10.1016/j.apcata.2007.03.021

Kazemnejad, I., Feizbakhsh, A., Niazi, A., & Tavasoli, A. (2019). Highly dispersed cobalt Fischer–Tropsch synthesis catalysts supported on γ-Al2O3, CNTs, and graphene nanosheet using chemical vapor deposition. *International Journal of Industrial Chemistry*, *10*(4), 321–333. https://doi.org/10.1007/s40090-019-00195-9

Kliewer, C. E., Soled, S. L., & Kiss, G. (2019). Morphological transformations during Fischer-Tropsch synthesis on a titania-supported cobalt catalyst. In *Catalysis Today* (pp. 233–256). https://doi.org/10.1016/j.cattod.2018.05.021

Langford, J. ., & Wilson, J. . (1978). Scherrer after Sixty years: A survey and some new results in the determination of crystallite size. *Journal of Applied Crystallography*, *11*, 102–113. https://doi.org/10.1061/9780784479896.140

Lele, S., & Anantharaman, T. R. (1962). Influence of crystallite shape on particle size broadening of Debye-Scherrer reflections. *Proceedings of the Indian Academy of Sciences*, *2*(1), 261–274.

Li, H., Wang, S., Ling, F., & Li, J. (2006). Studies on MCM-48 supported cobalt catalyst for Fischer-Tropsch synthesis. *Journal of Molecular Catalysis A: Chemical*, *244*(1–2), 33–40. https://doi.org/10.1016/j.molcata.2005.08.050

Li, J., Jacobs, G., Das, T., Zhang, Y., & Davis, B. (2002). Fischer–Tropsch synthesis: effect ofwater on the catalytic properties of a Co/SiO2 catalyst. *Applied Catalysis A*, *236*, 67–76.

Li, Q., Kartikowati, C. W., Horie, S., Ogi, T., Iwaki, T., & Okuyama, K. (2017). Correlation between particle size/domain structure and magnetic properties of highly crystalline Fe3O4 nanoparticles. *Scientific Reports*, *7*(1), 1–4. https://doi.org/10.1038/s41598-017-09897-5

Lira, E., López, C. M., Oropeza, F., Bartolini, M., Alvarez, J., Goldwasser, M., Linares, F. L., Lamonier, J. F., & Pérez Zurita, M. J. (2008). HMS mesoporous silica as cobalt support for the Fischer-Tropsch Synthesis: Pretreatment, cobalt loading and particle size effects.

Journal of Molecular Catalysis A: Chemical, *281*(1–2), 146–153. https://doi.org/10.1016/j.molcata.2007.11.014

Liu, K., Suo, H., Zhang, C., Xu, J., Yang, Y., Xiang, H., & Li, Y. (2010). An active Fischer-Tropsch synthesis FeMo/SiO2 catalyst prepared by a modified sol-gel technique. *Catalysis Communications*, *12*(2), 137–141. https://doi.org/10.1016/j.catcom.2010.09.007

Liu, Y., Fang, K., Chen, J., & Sun, Y. (2007). Effect of pore size on the performance of mesoporous zirconia-supported cobalt Fischer–Tropsch catalysts. *Green Chemistry*, *9*(6), 611–661. https://doi.org/10.1039/b614266d

Louër, D., Weigel, D., & Langford, J. I. (1972). Etude des profils de raies de diffraction des rayons X d'une poudre d'hydroxyde de nickel. *Journal of Applied Crystallography*, *5*(5), 353–359. https://doi.org/10.1107/s0021889872009756

Lu, X. (2011). Fischer Tropsch Synthesis : Towards Understanding. In *Dissertation*. University of the Witwatersrand.

Malet, P., & Caballero, A. (1988). The selection of experimental conditions in temperature-programmed reduction experiments. *Journal of the Chemical Society, Faraday Transactions 1: Physical Chemistry in Condensed Phases*, *84*(7), 2369–2375. https://doi.org/10.1039/F19888402369

Martínez, A., López, C., Márquez, F., & Díaz, I. (2003). Fischer-Tropsch synthesis of hydrocarbons over mesoporous Co/SBA-15 catalysts: The influence of metal loading, cobalt precursor, and promoters. *Journal of Catalysis*, *220*(2), 486–499. https://doi.org/10.1016/S0021-9517(03)00289-6

Matyi, R. J., Schwartz, L. H., & Butt, J. B. (1987). Particle Size, Particle Size Distribution, and Related Measurements of Supported Metal Catalysts. *Catalysis Reviews*, *29*(1), 41–99. https://doi.org/10.1080/01614948708067547

Melaet, G., Lindeman, A. E., & Somorjai, G. A. (2014). Cobalt particle size effects in the fischer-tropsch synthesis and in the hydrogenation of CO2 studied with nanoparticle model catalysts on silica. *Topics in Catalysis*, *57*(6–9), 500–507. https://doi.org/10.1007/s11244-013-0206-z

Miller, J. T., Meyers, B. L., Modica, F. S., Lane, G. S., Vaarkamp, M., & Koningsberger, D.

C. (1993). Hydrogen temperature-programmed desorption (H2 TPD) of supported platinum catalysts. In *Journal of Catalysis* (Vol. 143, Issue 2, pp. 395–408). https://doi.org/10.1006/jcat.1993.1285

Monshi, A., Foroughi, M. R., & Monshi, M. R. (2012). Modified Scherrer Equation to Estimate More Accurately Nano-Crystallite Size Using XRD. *World Journal of Nano Science and Engineering*, *02*(03), 154–160. https://doi.org/10.4236/wjnse.2012.23020

Monti, D. A. M., & Baiker, A. (1983). Temperature-programmed reduction. Parametric sensitivity and estimation of kinetic parameters. *Journal of Catalysis*, *83*(2), 323–335. https://doi.org/10.1016/0021-9517(83)90058-1

Morales, F., de Smit, E., de Groot, F. M. F., Visser, T., & Weckhuysen, B. M. (2007). Effects of manganese oxide promoter on the CO and H2 adsorption properties of titania-supported cobalt Fischer-Tropsch catalysts. *Journal of Catalysis*, *246*(1), 91–99. https://doi.org/10.1016/j.jcat.2006.11.014

Muniz, F. T. L., Miranda, M. A. R., Morilla Dos Santos, C., & Sasaki, J. M. (2016). The Scherrer equation and the dynamical theory of X-ray diffraction. *Acta Crystallographica Section A: Foundations and Advances*, *72*(3), 385–390. https://doi.org/10.1107/S205327331600365X

Mustard, D. G., & Bartholomew, C. H. (1981). Determination of metal crystallite size and morphology in supported nickel catalysts. *Journal of Catalysis*, *67*(1), 186–206. https://doi.org/10.1016/0021-9517(81)90271-2

Okabe, K., Li, X., Wei, M., & Arakawa, H. (2004). Fischer-Tropsch synthesis over Co-SiO2 catalysts prepared by the sol-gel method. *Catalysis Today*, *89*(4), 431–438. https://doi.org/10.1016/j.cattod.2004.01.005

Olusola, O. J., & Sudip, M. (2016). Temperature programme reduction (TPR) studies of cobalt phases in -alumina supported cobalt catalysts. *Journal of Petroleum Technology and Alternative Fuels*, *7*(1), 1–12. https://doi.org/10.5897/jptaf2015.0122

Petersen, A. P., Claeys, M., Kooyman, P. J., & van Steen, E. (2019). Cobalt-based fischer-tropsch synthesis: A kinetic evaluation of metal-support interactions using an inverse model system. *Catalysts*, *9*(10). https://doi.org/10.3390/catal9100794

Prieto, G., Martínez, A., Concepción, P., & Moreno-Tost, R. (2009). Cobalt particle size effects

in Fischer-Tropsch synthesis: structural and in situ spectroscopic characterisation on reverse micelle-synthesised Co/ITQ-2 model catalysts. *Journal of Catalysis*, *266*(1), 129–144. https://doi.org/10.1016/j.jcat.2009.06.001

Pyrz, W. D., & Buttrey, D. J. (2008). Particle size determination using TEM: A discussion of image acquisition and analysis for the novice microscopist. *Langmuir*, *24*(20), 11350–11360. https://doi.org/10.1021/la801367j

Rane, S., Borg, O., Rytter, E., & Holmen, A. (2012). Relation between hydrocarbon selectivity and cobalt particle size for alumina supported cobalt Fischer-Tropsch catalysts. *Applied Catalysis A: General*, *437–438*, 10–17. https://doi.org/10.1016/j.apcata.2012.06.005

Rozita, Y., Brydson, R., & Scott, A. J. (2010). An investigation of commercial gamma-Al 2 O 3 nanoparticles . *Journal of Physics: Conference Series*, *241*, 012096. https://doi.org/10.1088/1742-6596/241/1/012096

Rytter, E., Borg, Ø., Tsakoumis, N. E., & Holmen, A. (2018). Water as key to activity and selectivity in Co Fischer-Tropsch synthesis: Γ-alumina based structure-performance relationships. *Journal of Catalysis*, *365*, 334–343. https://doi.org/10.1016/j.jcat.2018.07.003

Rytter, E., & Holmen, A. (2015). Deactivation and Regeneration of Commercial Type Fischer-Tropsch Co-Catalysts—A Mini-Review. *Catalysts*, *5*(2), 478–499. https://doi.org/10.3390/catal5020478

Saib, A. M., Claeys, M., & Van Steen, E. (2002). Silica supported cobalt Fischer-Tropsch catalysts: Effect of pore diameter of support. *Catalysis Today*, *71*(3–4), 395–402. https://doi.org/10.1016/S0920-5861(01)00466-7

Saib, A. M., Moodley, D. J., Ciobîc, I. M., Hauman, M. M., Sigwebela, B. H., Weststrate, C. J., Niemantsverdriet, J. W., & Van De Loosdrecht, J. (2010). Fundamental understanding of deactivation and regeneration of cobalt Fischer-Tropsch synthesis catalysts. *Catalysis Today*, *154*(3–4), 271–282. https://doi.org/10.1016/j.cattod.2010.02.008

Schanke, D., Hilmen, A. M., Bergene, E., Kinnari, K., Rytter, E., Ådnanes, E., & Holmen, A. (1995). Study of the deactivation mechanism of Al2O3-supported cobalt Fischer-Tropsch catalysts. *Catalysis Letters*, *34*(3–4), 269–284. https://doi.org/10.1007/BF00806876

Smith, J. M., Ness, H. C. Van, Abbott, M. M., & Swihart, M. T. (2018). Introduction to

chemical engineering thermodynamics. In *McGraw Hill Education*. McGraw Hill education. https://doi.org/10.1021/ed027p584.3

Song, D., & Li, J. (2006). Effect of catalyst pore size on the catalytic performance of silica supported cobalt Fischer-Tropsch catalysts. *Journal of Molecular Catalysis A: Chemical*, *247*(1–2), 206–212. https://doi.org/10.1016/j.molcata.2005.11.021

Soykal, I. I., Sohn, H., & Ozkan, U. S. (2012). E ff ect of Support Particle Size in Steam Reforming of Ethanol over Co / CeO 2 Catalysts. *ACS Catalysis*, *2*, 2335–2348.

Sukkathanyawat, H., Tungkamani, S., Phongaksorn, M., Rattana, T., Narataruksa, P., & Yoosuk, B. (2015). Promoter Effect on the Physico-chemical Properties of Cobalt Based Catalyst for CO Hydrogenation. In *Energy Procedia* (Vol. 79). Elsevier B.V. https://doi.org/10.1016/j.egypro.2015.11.505

Tsubaki, N., Zhang, Y., Sun, S., Mori, H., Yoneyama, Y., Li, X., & Fujimoto, K. (2001). A new method of bimodal support preparation and its application in Fischer-Tropsch synthesis. *Catalysis Communications*, *2*(10), 311–315. https://doi.org/10.1016/S1566-7367(01)00055-3

Van Berge, P. J., Van De Loosdrecht, J., Barradas, S., & Van Der Kraan, A. M. (2000). Oxidation of cobalt based Fischer-Tropsch catalysts as a deactivation mechanism. *Catalysis Today*, *58*(4), 321–334. https://doi.org/10.1016/S0920-5861(00)00265-0

van de Loosdrecht, J., Balzhinimaev, B., Dalmon, J. A., Niemantsverdriet, J. W., Tsybulya, S. V., Saib, A. M., van Berge, P. J., & Visagie, J. L. (2007). Cobalt Fischer-Tropsch synthesis: Deactivation by oxidation? *Catalysis Today*, *123*(1–4), 293–302. https://doi.org/10.1016/j.cattod.2007.02.032

Van Steen, E., Claeys, M., Dry, M. E., Van De Loosdrecht, J., Viljoen, E. L., & Visagie, J. L. (2005). Stability of nanocrystals: Thermodynamic analysis of oxidation and re-reduction of cobalt in water/hydrogen mixtures. *Journal of Physical Chemistry B*, *109*(8), 3575–3577. https://doi.org/10.1021/jp045136o

Vorokh, A. S. (2018). Scherrer formula: estimation of error in determining small nanoparticle size. *Nanosystems: Physics, Chemistry, Mathematics*, *9*(3), 364–369. https://doi.org/10.17586/2220-8054-2018-9-3-364-369

Wang, Z. J., Skiles, S., Yang, F., Yan, Z., & Goodman, D. W. (2012). Particle size effects in

Fischer-Tropsch synthesis by cobalt. *Catalysis Today*, *181*(1), 75–81. https://doi.org/10.1016/j.cattod.2011.06.021

Webb, P. a. (2003). Introduction to Chemical Adsorption Analytical Techniques and their Applications to Catalysis. *MIC Technical Publications*, *13*(January), 1–4.

WILSON AJC. (1969). Variance Apparent Particle Sizes for Cylinders, Prisms and Hemispheres. *Journal of Applied Crystallography*, *2*(pt 4), 181–183. https://doi.org/10.1107/S0021889869006893

Witoon, T., Chareonpanich, M., & Limtrakul, J. (2011). Effect of hierarchical meso-macroporous silica supports on Fischer-Tropsch synthesis using cobalt catalyst. *Fuel Processing Technology*, *92*(8), 1498–1505. https://doi.org/10.1016/j.fuproc.2011.03.011

Wolf, M., Fischer, N., & Claeys, M. (2021). Formation of metal-support compounds in cobalt-based Fischer-Tropsch synthesis: A review. *Chem Catalysis*, *1*(5), 1014–1041. https://doi.org/10.1016/j.checat.2021.08.002

Xie, W., Zhang, Y., Liew, K., & Li, J. (2012). Effect of catalyst confinement and pore size on Fischer-Tropsch synthesis over cobalt supported on carbon nanotubes. *Science China Chemistry*, *55*(9), 1811–1818. https://doi.org/10.1007/s11426-012-4727-2

Xiong, H., Zhang, Y., Wang, S., & Li, J. (2005). Fischer-Tropsch synthesis: The effect of Al2O3 porosity on the performance of Co/Al2O3 catalyst. *Catalysis Communications*, *6*(8), 512–516. https://doi.org/10.1016/j.catcom.2005.04.018

Yan, P., Kennedy, E., & Stockenhuber, M. (2021). Natural zeolite supported Ni catalysts for hydrodeoxygenation of anisole. *Green Chemistry*, *23*(13), 4673–4684. https://doi.org/10.1039/d0gc04377j

Yang, J., Frøseth, V., Chen, D., & Holmen, A. (2016). Particle size effect for cobalt Fischer-Tropsch catalysts based on in situ CO chemisorption. *Surface Science*, *648*, 67–73. https://doi.org/10.1016/j.susc.2015.10.029

Zhang, Y., Hanayama, K., & Tsubaki, N. (2006). The surface modification effects of silica support by organic solvents for Fischer-Tropsch synthesis catalysts. *Catalysis Communications*, *7*(5), 251–254. https://doi.org/10.1016/j.catcom.2005.11.008

Chapter 3: Experimental Methodology

3.1. Introduction

In this chapter, the author provides a comprehensive explanation of the laboratory-scale experiments that were carried out in order to collect the results that served as the foundation for the discussions provided in later chapters. The first portion of this explanation provides a summary of the experimental conditions, the gases and catalysts that were used, and the reactors that were chosen for this inquiry. The second half provides an explanation of how the apparatus was set up and a graphic of the procedure and the instrumentation, so that the reader can easily follow the sequence of actions taken in the experiment. The final section describes the processes that must be carried out in order to operate the Fischer Tropsch (FT) system, collect the data, and analyze the data using gas chromatography (GC) instruments. Light hydrocarbons were the primary focus of the study, while liquid and solid hydrocarbons (wax) were also analyzed. Due to analytical restrictions, no mention is made of hydrogen conversion.

During Fischer Tropsch synthesis (FTS), a substantially bigger source of error are encountered, which makes it challenging to reproduce experimental findings. The impact of support particle size is one of the aspects that needs to be looked at. A support with a homogeneous particle size can help maintain uniform loading and help to manage the size of the metal crystallites formed on its surface. The catalyst that is placed into the reactor ought to be an accurate representation of the bulk. It ought to be capable of reproducing the distribution characteristics of the entire batch in terms of particle size or particle shape and loading. In most cases, inability to reproduce FTS results is caused by errors when sampling or manufacturing of the catalyst. These errors can compound and become impossible to rectify, even with accurate product analysis.

3.2. Catalyst Preparation

Cobalt-based catalysts with different particle class sizes were prepared using the incipient wetness impregnation method. Seven class sizes of clinoptilolite support were prepared, i.e.: -212 to +150 μm; -150 to +106 μm; -106 to +75 μm; -75 to +53 μm; -53 to +38 μm; -38 to +25 μm; -25 μm to Pan (Defination: -212 to +150 μm for example means particles go through sieve 212 μm but do no pass through sieve 150 μm. So this range discribes particles between

the 2 sieves sizes). The objective of the study was to investigate the effect of the size of clinoptilolite zeolite particles in FTS.

3.2.1. Support preparation

A ring pulverizer was used to reduce the size of as-received natural zeolite (clinoptilolite) samples that were obtained from Pratley Minerals in Krugersdorp, South Africa. Following pulverization, the powdered zeolite was successively screened through a series of sieves with the following mesh sizes: -212 to +150 μm; -150 to +106 μm; -106 to +75 μm; -75 to +53 μm; -53 to +38 μm; -38 to +25 μm; -25 μm to Pan. The presence of a negative sign in this context indicates that the particle goes through that size sieve; a positive sign indicates that the particle does not go through that size sieve. The class size of the sample was determined based on this information. Representative samples from each class size were obtained with the aid of a spinning riffler.

The stages of support preparation are shown in **Figure 3.1**. Variation within class size exists, hence correct sampling and sample splitting methods need to be used. The most important step is to ensure a support with a uniform particle size and to ensure analysis of a sample that represents the particular class size. The significance of controlling the particle size of the support in catalysis is that there is an increase in the surface area of the particle when the particle size decreases for the same mass.

The term "size reduction" refers to the process by which larger zeolite rocks are broken down into smaller pieces using a variety of machines and processes, such as a jaw crusher, a hammer mill, a ball mills and a ring pulverizer (Hao et al., 2012; Kumar & Yedhu Krishnan, 2020; Veasey & Wills, 1991). As a support for the synthesis of the FTS catalyst, these various zeolite size classes were utilized. The particle size distribution of each class size was analyzed using a scanning electron microscope (SEM). With the vast majority of FT catalysts, a porous, chemically inert substrate like Al_2O_3, SiO_2 or carbon is used to stabilize metal crystallite with a diameter of 1 to 50 nm.

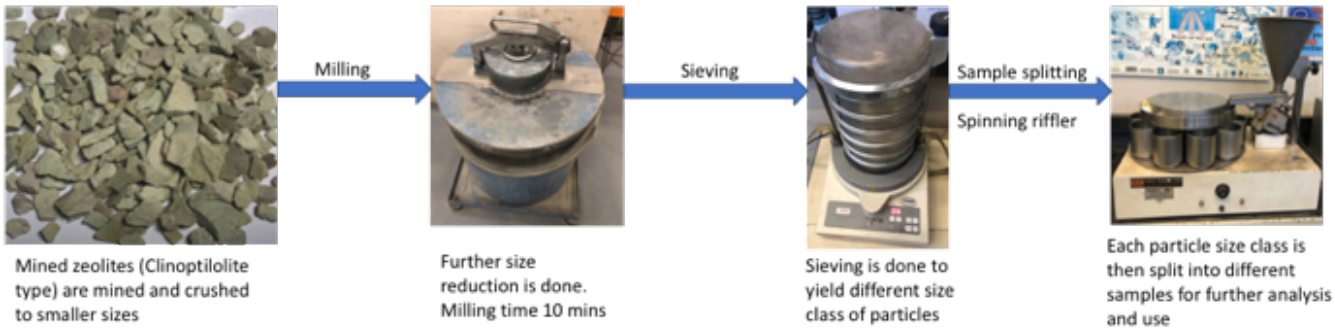

Figure 3.1: Stages through which the as-received zeolitic material went when preparing the catalyst, including size reduction, followed by size separation. A spinning riffler ensured that the most representative sample of each class size was obtained.

3.2.2. Catalyst synthesis

3.2.2.1. Preparation of 10wt%Co/NZeo catalyst

The cobalt (II) nitrate hexahydrate used for the catalyst preparation was purchased from Sigma-Aldrich. 100 g of natural zeolite was measured into a beaker. 54.82 g of cobalt (II) nitrate hexahydrate was measured and dissolved in 70 ml of ethanol (based on the pore volume of the natural zeolite). The solution was stirred in a magnetic stirrer for 30 minutes. Thereafter, the solution was added to the natural zeolite dropwise and stirred in a magnetic stirrer for 1 hour; it was then ultra-sonicated for 30 minutes. The sample was slowly dried at ambient temperature for 24 hours and then dried at 110 ^{o}C for 6 hours. The dried sample was calcined in air at 350 ^{o}C for 6 hours.

3.3. Catalyst characterisation

3.3.1. X-ray diffraction

An x-ray diffraction (XRD) Rigaku Ultima IV instrument was used to gather diffraction patterns of clinoptilolite at a scanning speed of 0.5^{o}/min and from a 10° to a 90° 2-theta angle. The voltage and current of the x-ray source were adjusted to 40 kV and 30 mA settings, respectively. The XRD apparatus features a CuK (=1.54) x-ray generator target with a maximum power of 3 kW and a goniometer that can measure a 2-theta angle from 0° to 162°.

The maximum power of the CuK x-ray generator target is 3 kW. The model that was utilized for XRD spectroscopy is shown in **Figure 3.2**.



Figure 3.2: Photograph of what an XRD machine looks like. A Rigaku Ultima IV machine was used to do the clinoptilolite analysis

3.3.2. SEM-energy dispersive spectroscopy

TESCAN was used for the SEM analysis, and Vega 3X with a tungsten filament served as the electron source. Using secondary detectors and backscatter detectors with a high voltage of 20 kV, the surface morphology of the material was recorded. Vega software was used to capture images at various magnifications. Using Oxford University's INCA software, energy dispersive X-ray spectroscopy (EDS) research was done to identify the chemical makeup of particular areas. The model for this SEM-EDS spectroscopy is shown in **Figure 3.3**.



Figure 3.3: SEM-energy dispersive spectroscopy TESCAN (Vega 3XMU)

3.3.3. X-ray fluorescence spectrometry

Using a Rigaku ZSX Primus II equipped with SQX analysis software, x-ray fluorescence spectrometry (XRF) analysis was carried out to ascertain the elemental composition of the material - pictured in **Figure 3.4**. After weighing and measuring 10 grams of sample, it was mixed with 2 grams of binder, then pelletized using 20 tons of pressure. The resulting pellets were 2.5 millimetres thick and 35 millimetres in diameter. Following the pellet preparation step, the pallets were placed into the spectrometer, in order for the chemical analysis to be done.



Figure 3.4: XRF – Rigaku ZSX Primus II

Clinoptilolite samples of different class sizes were analyzed as received, i.e. without receiving any treatment. The loss on ignition (LOI) of the samples was measured after 30 min at 930°C in air. The borate fusion disc of all the class sizes were prepared; then acquired an XRF scan of the borate fusion disc for the zeolitic material and estimated the composition of the sample with the "Omnian" method from Malvern Panalytical. The mass percentage of the oxides of interest was then determined (Al_2O_3, BaO, CaO, Cr_2O_3, Fe_2O_3, K_2O, MgO, MnO, Na_2O, NiO, P_2O_5, SiO_2, TiO_2 and V_2O_5). The major element method was calibrated with mixtures of pure chemicals (essentially oxides) and with certified reference materials using a fundamental parameters model.

This allowed for all combinations of elements within the range of the calibration, which extends up to:

- 3 mass % Cr_2O_3
- 20 mass % for Na_2O, SO_3, K_2O, V_2O_5, NiO and BaO
- 40 mass % P_2O_5
- 50 mass % for MgO and TiO_2
- 65 mass % MnO
- 90 mass % CaO
- 95 mass % Fe_2O_3
- 100 mass % for Al_2O_3 and SiO_2

The XRF spectrometer used in this work was a Malvern Panalytical MagiX PRO, which is a wavelength-dispersive system.

3.3.4. Determination of particles sizes using the Malvern Mastersizer 3000

Brief equipment description



Figure 3.5: The Malvern Mastersizer 3000

Particle size distribution (PSD) in this work was determined using the Malvern Master Sizer 3000 (picture in **figure 3.5**). This equipment measures particle sizes using laser diffraction. It relies on the inverse relationship between the diffraction angle of light and the size of particles being measured (Bowen, 2002; Fisher et al., 2017; Gazi et al., 2021). The instrument is designed for both wet and dry particle size analysis. In general, the Mastersizer consist of (i) an optical unit whose function is to transmit red and blue laser through the sample and also to generate data from the light scattering pattern as detected by its detectors, (ii) a dispersion unit which can either be wet or dry. The wet unit used in this study is a Hydro LV unit with a capacity to handle 600ml of dispersant i.e., water in our case. It is also used to circulate the water with sample through measurement unit, (iii) a measurement cell which acts as the interface between the dispersion unit and optical unit. It allows the laser to pass through the sample for particle size measurement and (iv) Mastersizer application software with a primary

function of controlling the optical and measurement units in addition to processing the data obtain from scattering pattern.

3.3.4.1. Particle size measuring procedure

To ensure that the particle size distribution (PSD) from the Mastersizer was representative of the sample in our experiments, a statistical sampling procedure needed to be followed. This is especially critical given the small size of samples that was needed to be in the required obscuration range typically between 10 and 20%. In our case, a sample size of approximately 2-3grams was sufficient to get to the correct obscuration. Therefore, the steps taken to subsample such a small mass determine sample representativeness. The procedure followed involved splitting the sample into small subsamples (typically 10grams) by successive splitting using small 10-way rotary splitters. The 10grams was made into a thick paste using water, homogenised manually using a spatula and split further into masses of approximately 2.5 grams using conning and quartering method. The 2.5grams would ensure that the "obscuration" was within range. Obscuration is defined as the optical concentration of the sample.

We developed a Standard Operating Procedure (SOP) as per the procedure highlighted in Mastersizer 3000 manual (Malvern Instruments limited, 2013). Using this developed SOP, actual PSD measurement were then done. For each run, the sub-sample was added into the 600ml of water in Hydro LV while the agitator was running at approximately 2000rpm. The sample was sonicated to deagglomerate the particles during measurement. The SOP was developed such that 3 repeat measurements were done during a cycle and the average PSD and associated statistics calculated. For each sample, 3 repeat measurements were done (from separate 2.5-gram subsamples) to enable comparison and assessment of the accuracy our sample splitting procedure. At the end of each run the system was cleaned automatically and rinsed in preparation for the next run. The PSD data measured as volume distribution was exported as CSV file for processing.

3.3.5. Brunauer-Emmett-Teller

Experiments on adsorption and desorption of nitrogen were carried out at a temperature of -195 °C using a Tristar II, which is manufactured by Micromeritics (USA). The samples were

degassed at 180 °C under nitrogen gas overnight before an experiment was done. Adsorption data collected at relative pressure levels ranging from 0.05 to 0.30 atmospheres were used to calculate the Brunauer-Emmett-Teller (BET) surface areas. After calculating the amount of N_2 vapour that was adsorbed at a relative pressure of 0.99, the total pore volume was determined. Using the Barrett–Joyner–Halenda (BJH) approach, the pore size distributions were determined using the desorption branches of the isotherms as a starting point. the micropore surface area and volume were determined using t-plot data.

3.3.6. Temperature-programmed reduction studies

Temperature-programmed reduction study (TPR) experiments were carried out with a Micromeritics Auto Chem II unit. The catalyst (approximately 50 mg) was placed in a quartz tubular reactor fitted with a thermocouple for continuous temperature measurement. The reactor was heated in a furnace. Before the temperature-programmed reduction measurement, the calcined catalysts were flushed with high-purity argon at 200 °C for 30 min, to remove water or impurities, followed by cooling to ambient temperature. Then, 5% H_2/Ar was switched on, and the temperature was raised from 50 to 850 °C at a rate of 10 °C min^{-1}. Three Brooks mass flow controllers maintained a constant gas flow rate through the reactor of 60 mL/min. A computer was used to make an automatic recording of the TCD signal of the H_2 consumed.

3.4. Experimental set-up

During the investigations, a tubular fixed bed reactor made by Autoclave Engineers was used to conduct FTS reactions. In each of the studies, the feed composition and the analytical system employed were kept consistent throughout. **Figure 3.6** shows the experimental setup used for the FTS experiments. The setup is equipped with gas cylinders with pressure regulators, shut-off valves, mass flow controllers, check-valves, a fixed-bed reactor and a GC. (The key is provided below the flow diagram.)

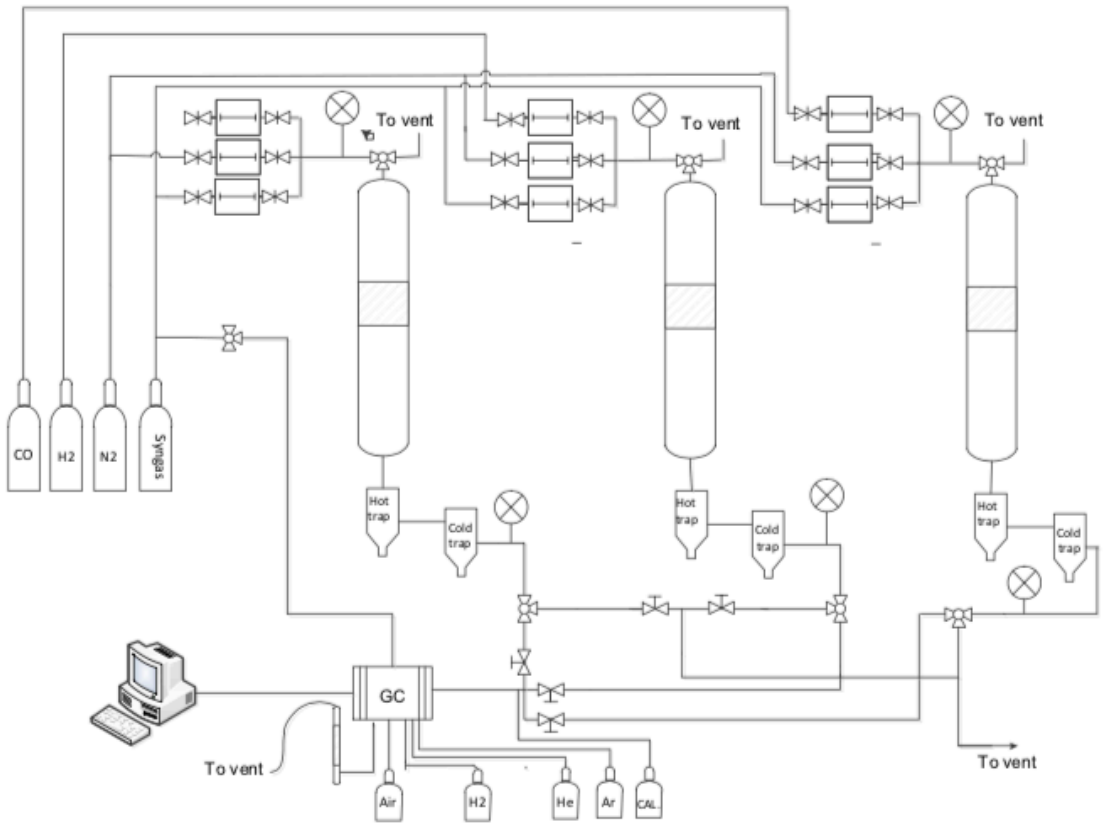

Figure 3.6: Laboratory scale flow diagram FT rig with three parallel fixed reactors



Fixed bed reactor

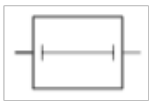

Mass flow controller
Brooks SLA5850



3-way valve
Swagelok



Back pressure regulator



2-way valve
Swagelok

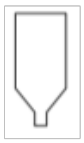

Knock out pots



Non return valve
Swagelok

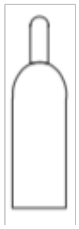

Gas Cylinder

The flow rate of synthesis gas and other gases were controlled by means of a mass flow controller (Brooks flow controller SLA5850 Rev B; maximum pressure - 103 bar). The top portion of the reactor included hot ceramic balls, which ensured the temperature of the syngas was brough up to the level required for the experiment. The products were directed to the product traps at the bottom of the reactor. A high-pressure hot trap was maintained at P = pressure of the reactor and T = 150°C, and the product lines flowing down from the reactor to the trap were heated and insulated to maintain a temperature of 200°C. After each mass balance run, all condensed wax products were removed from the system. At the same time as the wax was collected, the uncondensed stream was sent to the high-pressure cool trap (P=PR, T=25°C) to separate the oil and watery products. A back pressure regulator, which was installed adjacent to the cool trap, regulated the pressure in the reactor and the two traps. Following the back pressure regulator's reduction in pressure, the gaseous stream including the gas phase products and unreacted feed proceeded through sampling loops to an online GC equipped with an ionization detector and thermal conductivity detector (TCD). A TCD equipped with a Porapak Q (1.50 m × 3 mm) packed column was used to analyze H_2, N_2, and CO. A flame ionization detector (FID) equipped with a Porapak Q packed column was used to analyse the hydrocarbons online. The gaseous stream was sent from the sample loops to a bubble meter, and finally to a vent.

Every 2.35 hours, two samples were taken from the gaseous stream using sample valves from the sampling loops. These were analyzed online using the GC. To avoid product condensation, the product tubes between the wax trap and the GC were heated to 150°C. In order to track the temperature of the bed centre during the FTS reaction, one piece of 1/16" OD thermocouple with 1/8" OD thermocouple wells was positioned vertically in the centre of the reactor tube.

GC calibration and product analysis have been described in earlier studies (Gorimbo, 2016; Lu, 2012; Yao, 2011).

3.4.1. Tubular fixed bed reactor

Autoclave Engineers supplied the tubular fixed bed reactor. **Figure 3.7a and 3.7b**, respectively, show the reactor's measurements and technical details.

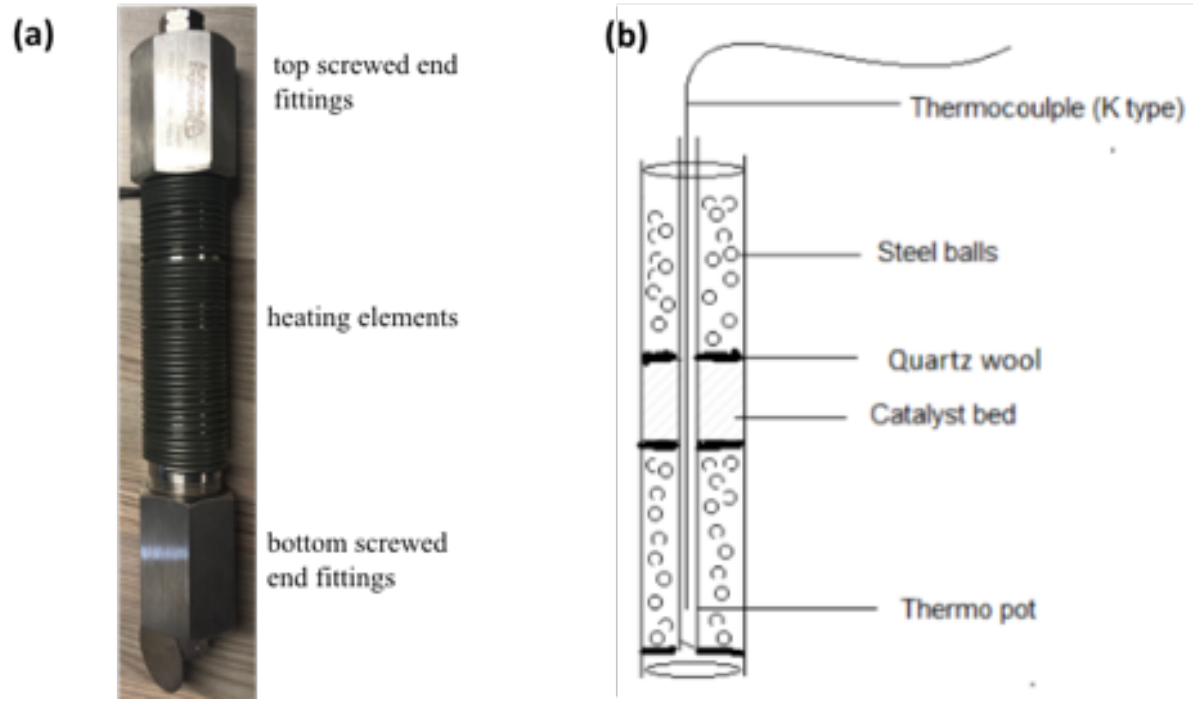

Figure 3.7: Photograph and diagram of the disassembled reactor used in this experiment

The reactor is made of a stainless steel tube (13mm by 300mm Ss316 tubular reactor (650ºC@100Bar, 800ºC@1Bar)). This reactor is used as an integrated reactor and is mounted vertically on the rig. Approximately 1 g of catalyst was loaded into the centre of the tube for the experiments, and stainless steel balls with a diameter of 2-3 mm were used to cover the remaining space. To prevent any of the catalysts from falling off the bed, a very thin coating of quartz wool was placed at either end of the bed. To ensure that the temperature profile of the catalyst bed was flat, the reactor was heated by three independent heating jackets along the axial direction. A thermal blanket was used to prevent heat runaway.

3.5. Tubular fixed bed reactor isothermal test

Since non-isothermal operation could obscure the data and make it difficult to connect the results to the operating conditions, care had to be taken to operate the catalyst bed in an isothermal manner. FTS was studied in a fixed bed reactor with an ID of 13 mm, which is unusually small for such reaction. Measurements were taken of the temperature profile in the centre of the bed before and after the reaction. **Figure 3.8** illustrates this point. To be considered isothermal, there was only a 0.3 ºC difference between the central and wall control

temperatures in the middle of the reactors, where the catalyst bed was located, making the reactor an isothermal system.

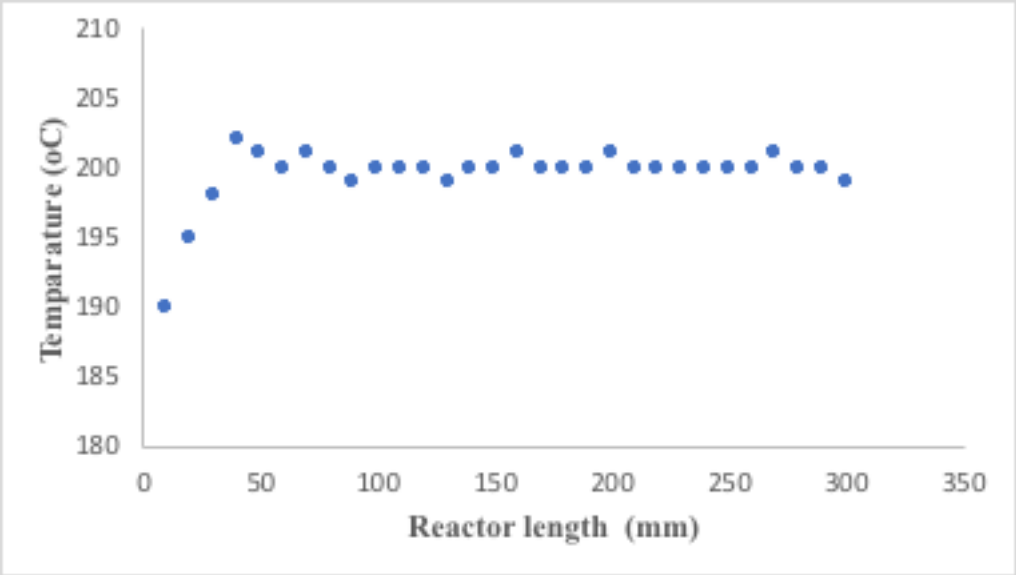

Figure 3.8: Profile of the central temperature of the reactors (measured from the thermopot)

3.6. Catalyst evaluation in the FTS reaction

FTS was performed in a fixed-bed micro-reactor (internal diameter = 1.3 cm; length = 30 cm). A gas cylinder containing syngas - $H_2/CO/N_2$ mixture (~60/30/10 vol. % purity: 99.99) - was used to supply the reactant gas stream to the catalyst at a flow rate of 10 mL/min and 10 bar(g). N_2 was used as an internal standard to ensure accurate mass balance calculations. Three catalysts (1.0 g, ca. 10% Co loading) were reduced in-situ at 350 ℃ in pure hydrogen (ca. 99.99%) for 16 hours. After reduction, the reactor temperature was decreased to ambient temperature under hydrogen flow and then heated up to 220 °C under synthesis gas at a pressure of 10 bar(g). The partial pressure rate of the syngas input for the reactors was $P_{H2} = 6$, $P_{CO} = 3$ and $P_{N2} = 1$ bar, which amounted to 60% H_2, 30% CO and 10% N_2. The flow rate of syngas was determined to be 60 mL(NTP)/min, and the space velocity at normal temperature and pressure was calculated to be 60 mL(NTP)/min/g Co when this flow rate was used.

This work on FTS involved the following general steps: (i) construction of the rig; (ii) characterization of the catalyst; (iii) loading the catalyst into the reactors; (iv) reduction of the catalyst; (v) performance of FT reactions under defined conditions.

3.6.1. Gases used

African Oxygen (AFROX Ltd) supplied the carrier and auxiliary gases (argon, helium, hydrogen and air) used in the GC operations in standard gas cylinders (40 kg). FTS requires ultra-high purity (UHP) grades (> 99.9997 percent) to be used in the laboratory. In this work, the effect on FTS of three distinct sizes of catalyst particles was examined. The FT reactions run all used the same syngas. The H_2, CO, CO_2, N_2, CH_4, C_2H_4 and C_2H_6 gas combination was used by the researcher to calibrate the online GC. **Table 3.1** contains a list of the constituent parts of the syngas and calibration gases.

When using a GC, the gases must be clean, in order to lengthen the lifespan of the column by decreasing the amount of bleed from the stationary phase, preventing column damage, and ensuring low noise and a constant baseline. Impurities, and particularly hydrocarbons, can lead to baseline noise, decreased sensitivity and possibly increased detection limits. Impurities can also cause detection limits to rise.

Table 3.1: Feed components and the calibration gases employed in the investigation, as well as the mole percentages

Component	**Mole percentage (% mol)**	
	Syngas (mole %)	Calibration gas (mole %)
H_2	60	53.2
CO	30	28.8
N_2	10	9.8
CO_2		5.0
CH_4		2.5
C_2H_4		0.2
C_2H_6		0.5

The TCD was calibrated by the author using UHP He and Ar (baseline) gases. The FID used to analyze the sample with the GC was calibrated using Air Instrument Grade (AIG zero), UHP H2 and the carrier gas Ar (baseline) gases. The cylinders had pressure regulators. The high-

pressure lines carried the gases from the cylinders to the FT rig. The system was purged and tested for leaks using nitrogen gas.

3.7. FTS Product Storage

The solid and liquid products were separated and placed in separate glass vials. These were covered with paraffin paper, marked with stickers and placed in a refrigerator in preparation for analysis.

3.8. Calculations

Quantitative analysis was performed on the information that was obtained from the online GC. As an internal reference for the measurements of the TCD data, nitrogen (with a 10 vol percent concentration of N_2) that was present in the syngas feed of the FT tests was used. After completing the initial calculations - i.e. determining the molar flow rate of the various reactants and products - additional calculations were carried out. Using the following equations, the calculations for the mass balance were computed, which included the conversion of the reactants CO. These calculations are similar to those used by previous researchers, while the experimental method used was developed many years ago (Duvenhage, 1994).

The online data gathered was processed statistically. The nitrogen (10 vol percent of N_2) that was present in the syngas feed of the FT tests was used as the internal benchmark for the measurement of the TCD data. Further calculations were carried out after the molar flow rate of the various reactants and products was first established. The following equations were used to calculate the mass balance, which included the conversion of the reactants CO and H_2. These calculations are comparable to those done by earlier scholars (Emma Magdeline Mokoena, 2005; Gorimbo, 2016; Lu, 2011; Phadi, 2012; Yao, 2011), while the experimentation technique has been in use for decades.

$$\% CO = \frac{F_{in}X_{co,in} - F_{out}X_{co,out}}{F_{in}X_{co,in}} \quad (3.1)$$

Where: $X_{co,in}$ denotes the molar fraction of CO in the reactor gas feed; $X_{co,out}$ is the molar fraction of CO in the gas stream exiting the reactor.

The CO consumption rate is determined as follows:

$$r_{co} = \frac{F_{out}X_{co,out} - F_{in}X_{co,in}}{m_{cat}} \quad (3.2)$$

Where: r_{co} is the rate of CO consumption, mol/(min.gcat); m_{cat} is the mass of the catalyst that was used in this reaction is denoted by the variable m cat, which is expressed in grams.

The rate of gas product generation θ_i, mol/(min.gcat) can be calculated as follows:

$$r_{\theta_i} = \frac{F_{out}X_{\theta_{i,out}}}{m_{cat}} \quad (3.3)$$

Where: $X_{\theta_{i,out}}$ represents the molar fraction of θ_i in the gas stream coming out of the reactor exit.

On the basis of moles of carbon, the product selectivity was determined by means of the following calculation:

$$Sel\ (\theta) = \frac{[nC]_\theta}{-r_{co} \times t \times m_{cat}} \quad (3.4)$$

Where: the selectivity of the product θ is denoted by Sel (θ); the number of moles of carbon present in the product is denoted by $[nC]_\theta$.

To correct hydrocarbons based on the known areas of C_2H_4 (olefin) and C_2H_6 (paraffin) in the calibration, the response factors that were published by Dietz (1967) were used. (See **Table 3.2.)** The majority of GCs use either flame ionization or TCDs, although many different kinds of detectors can be used in GCs. Correction factors must be used in order to obtain quantitative findings from the GC trace. The amount of correction is a function of the response of a particular molecule to the detecting instrument (Dietz, 1967).

Table 3.2: Response factors for hydrocarbon products

Carbon number	Olefin	Paraffin
2	1	1
3	0.7	0.74
4	0.55	0.55
5	0.47	0.47
6	0.4	0.4
7	0.35	0.35
8	0.32	0.32
9	0.28	0.28
10	0.24	0.24
11	0.21	0.21
12	0.19	0.19
13	0.18	0.18
14	0.17	0.17
15	0.15	0.15

Olefin/paraffin ratio

The formula that was used to determine the olefin-to-paraffin (O/P) ratio is provided below (equation 4.7). It takes into account the relative molar amount for the same carbon number in the outflow stream.

$$O_n/P_n = N_{C_nH_{2n}}/N_{C_nH_{2n+2}} \quad (3.5)$$

The subsequent parts give an in-depth report of the actual work carried out to evaluate FTS. These accounts can be found in the respective sections. Although both liquid and solid (wax) forms of hydrocarbons were obtained, the main focus of the study was light hydrocarbons, which were monitored exclusively by the online GC. It is important to note that the hydrogen conversion is not given, because of the constraints placed on the analysis.

References

Bowen, P. (2002). Particle size distribution measurement from millimeters to nanometers and from rods to platelets. *Journal of Dispersion Science and Technology*, *23*(5), 631–662. https://doi.org/10.1081/DIS-120015368

Dietz, W. A. (1967). Response Factors for Gas Chromatographic Analyses. *Journal of Chromatographic Science*, *5*(2), 68–71. https://doi.org/10.1093/chromsci/5.2.68

Emma Magdeline Mokoena. (2005). Synthesis and Use of Silica Materials As Supports for the Fischer-Tropsch Reaction. *Philosophy*.

Fisher, P., Aumann, C., Chia, K., O'Halloran, N., & Chandra, S. (2017). Adequacy of laser diffraction for soil particle size analysis. *PLoS ONE*, *12*(5), 1–20. https://doi.org/10.1371/journal.pone.0176510

Gazi, M. Y., Apu, S. I., Sharmili, N., & Rahman, M. Z. (2021). Origin and characterization of clay deposits in the Dupi Tila Formation of the Bengal Basin, Bangladesh. *Solid Earth Sciences*, *6*(3), 313–327. https://doi.org/10.1016/j.sesci.2021.07.001

Gorimbo, J. (2016). *An experimental and thermodynamic study of iron catalyst activation and deactivation during Fischer Tropsch Synthesis, PhD thesis,* University of the Witwatersrand.

Hao, J., Zhang, H., Yang, K., Lu, C., Chen, J., & Li, Y. (2012). Effect of different milling processes on the mineral distribution in a coal powder. *International Journal of Mining Science and Technology*, *22*(2), 237–242. https://doi.org/10.1016/j.ijmst.2011.10.001

Kumar, A., & Yedhu Krishnan, R. (2020). A Review on the Technology of Size Reduction Equipment. *International Journal of ChemTech Research*, *13*(1), 48–54. https://doi.org/10.20902/ijctr.2019.130106

Lu, X. (2011). Fischer Tropsch Synthesis : Towards Understanding. In *Dissertation*. University of the Witwatersrand.

Lu, X. (2012). *Fischer-Tropsch Synthesis: Towards understanding.*

Phadi, T. T. (2012). *Titanium Dioxide-Carbon Spheres Composites for Use As Supports in Cobalt Fischer-Tropsch Synthesis*.

Veasey, T. J., & Wills, B. A. (1991). Review of methods of improving mineral liberation. *Minerals Engineering*, *4*(7–11), 747–752. https://doi.org/10.1016/0892-6875(91)90062-Z

Yao, Y. (2011). Fischer-Tropsch Synthesis Using CO2 -Containing Syngas Mixtures Over Cobalt and Iron Based Catalysts. In *University of the Witwatersrand*.

Chapter 4: Preparation and characterisation of Clinoptilolite-supported cobalt crystallite as Fischer-Tropsch catalyst: Effect of support particle size

This work has been prepared in the form of a paper for future publication. Part of this work was presented at the following conferences:

- *American Institute of Chemical Engineers (AIChE) annual meeting, 20 August 2020, 2020 Virtual Spring Meeting and 16th GCPS (ISBN: 978-0-8169-1113-4).*

Abstract: The effect of particle and crystallite size on supported catalysts is of great interest to industry and researchers, due to the possible applications in Fischer–Tropsch synthesis. Clinoptilolite (a natural zeolite) was explored as a cobalt catalyst support, with special attention being paid to the effect of different support size classes. The catalyst was characterized using XRD, XRF, TPR and BET. Incipient wetness impregnation was used to prepare the powder samples of cobalt on zeolite. Temperature-programmed reduction (TPR) was used to examine the non-isothermal reduction of cobalt oxide using 5% hydrogen in argon at three distinct heating rates (5, 10, 15 ºC/min). The reaction kinetic parameters were identified. When using the Kissinger model, it was discovered that the activation energy (Ea), varied from 102.45 to 254.01 kJ/mol, depending on the particle size of the catalyst. The lowest activation energy is achieved with a support particle size in the 212 to 150 μm range, which indicates that this size of catalyst would be ideal for use in a reduction reaction that takes place at a lower temperature. We conclude that the support plays an important role in catalyst reduction, low Ea, reduces the difficulty of reducing Co_3O_4. These results show unequivocally that particle size matters in terms of the temperature needed for reduction. Reducing the temperature has significance in FTS, since it drastically reduces the sum of money spent on the energy input required for reduction. Therefore, the industrial sector focuses a great deal of attention on lowering the temperature.

4.1. Introduction

Since their discovery, zeolites have been used in the chemical industry as catalysts, adsorbents and ion exchangers. Zeolites belong to a family of microporous crystalline minerals (Li & Yu,

2021). They are hydrated aluminosilicate minerals composed of a three-dimensional silica (SiO_4) and alumina framework (AlO_4). Only clinoptilolite is extracted from South Africa's zeolite mines. Based on the chemical composition of the natural clinoptilolite mined in South Africa, the molecular formula for the natural zeolite is given as $(Na_{1.25}K_{1.6})(Ca_{0.49}Mg_{0.43})(Al_{5.14}Fe_{0.31})(Si_{25.67}Ti_{0.04})O_{62}$. This corresponds to a silica content of 77.24 %, 13.30 % alumina, 0.23 % hematite, 0.04 % manganese oxide, 0.86 % magnesium oxide, 1.40 % calcium oxide, 1.94 % sodium oxide, 3.78 % potassium oxide and 0.14 % titania (Gorimbo et al., 2014; Gorimbo, 2011). All the commonly used supports are contained in this natural clinoptilolite.

Gaining qualitative knowledge about the reducibility of oxidic species, such as metal oxides spread over a support, has been accomplished via temperature-programmed reduction (TPR) (Arnoldy & Moulijn, 1985; Borg et al., 2007; Gorimbo et al., 2020; Li et al., 2006). It has been demonstrated that TPR can provide an accurate picture of the state of a catalyst. Therefore, it has the potential to be used as a device for quality control, with the purpose of evaluating the efficiency of various catalysts and the preparation methods used.

The Kissinger method is one of the main methods used to find kinetic parameters through thermal analysis. Plots of the logarithm of the heating rate versus the inverse of the temperature at the maximum reaction rate in experiments done using a constant heating rate have been used in the research that has been published to determine the apparent activation energy of solid state reactions (Fedorov et al., 2020; Tomić-Tucaković et al., 2012). This research uses the method developed by Kissinger in 1957 (Blaine & Kissinger, 2012), and it is possible to determine the apparent activation energy using the Kissinger approach even without having a comprehensive understanding of the reaction mechanism (Janković et al., 2008).

The Kissinger method is based on a series of experiments in which milligram-scale amounts of reacting material are heated at a various heating rates (β), while the exothermic peak of each reaction is recorded. With each heating rate used, the exothermic peak temperature (T_m) - which is assumed to be a point of constant conversion - is measured. Calculating the pre-exponential factor Z and the activation energy E_a from a plot of $\ln \frac{\beta}{T_m^2}$ versus $\frac{1}{T_m}$, and fitting a straight line allows for the determination of the linear regression coefficients of the least squares method. The intercept and the slope of the plot are used to calculate the pre-exponential factor Z and the activation energy Ea, respectively. The slope of the line is equal to $-\frac{E_a}{R}$, and the intercept

gives $\text{In}\left[\frac{ZR}{E_a}\right]$. Z is the Arrhenius pre-exponential factor; R is the gas constant, which is 8.314 J/mol K; E_a is the activation energy.

Typically, a first order reaction (n = 1) order is considered. The Kissinger equation (**Equation 4.1**) is as follows (Blaine & Kissinger, 2012):

$$\text{In}\frac{\beta}{T_m^2} = \text{In}\left[\frac{ZR}{E_a}\right] - \frac{E_a}{RT_m} \qquad \textbf{Equation 4.1}$$

It was discovered that the particle size of the catalyst support had an effect on the catalytic activity as well as the product selectivity (Harju et al., 2020). Therefore, this study aimed to investigate the effect of the size of the support particle on the behavior of the catalyst. The results obtained enable a discussion of the effect of the size of the catalyst support on the kinetic behavior of the catalyst and the distribution of products. The results also allow for suggestions to be made on optimal particle size for certain products that are to be produced during Fischer–Tropsch synthesis (FTS).

4.2. Experimental

4.2.1. Preparation of 10wt%Co/Clino catalyst

As-received natural zeolite (clinoptilolite) samples obtained from Pratley Minerals in Krugersdorp, South Africa, were reduced in size using a ring pulverizer. After being reduced to a powder form, the zeolites went through a series of sieves with progressively smaller mesh sizes, beginning with a mesh with a range of -212 to +150 μm, then -150 to +106 μm, then -106 to +75 μm; -75 to +53 μm; -53 to +38 μm; -38 to +25 μm and finally a mesh size of less than 25 μm. After that, cobalt was loaded onto each of the distinct clinoptilolite supports. The catalyst is thus referred to as *10wt%Co/Clino*, which denotes that clinoptilolite has been loaded with 10% cobalt metal. Sigma-Aldrich provided the cobalt (II) nitrate hexahydrate that was used to synthesise the catalyst. A beaker was filled with 100 g of pure clinotptilolite. Based on the pore volume of the clinoptilolite support, 54.82 g of cobalt (II) nitrate hexahydrate was measured and dissolved in 70 ml of ethanol. This solution was agitated in a magnetic stirrer for 30 minutes. After that, drops of the solution were added to the clinoptilolite and it was swirled for an hour with a magnetic stirrer, before being ultrasonically sonicated for 30 minutes. The

sample was slowly dried at room temperature for 24 hours, followed by 6 hours of drying at 110 ºC. The dried sample was calcined in air at 350 ºC for six hours.

4.3. Material Characterization

4.3.1. X-ray diffraction

Clinoptilolite diffraction patterns were collected using the XRD Rigaku Ultima IV equipment, at a scanning speed of 0.5 º/min from 10 º to 90 º 2-theta angle. The voltage and current settings of the x-ray source were changed to 40 kV and 30 mA, respectively. A CuK (=1.54) x-ray generator target with a maximum output of 3 kW and a goniometer that can measure 2-theta angles from 0 ° to 162 ° are both included in the XRD equipment. The maximum power of the CuK x-ray generator target is a 3 kW.

4.3.2. X-ray fluorescence spectrometry

An X-ray fluorescence spectrometry (XRF) study of the material was done using a Rigaku ZSX Primus II machine fitted with SQX analysis software. This was done in order to determine the elemental composition of the material. After weighing and measuring 10 grams of sample, combining it with 2 grams of binder and then pelletizing it with 20 tons of pressure, the pellets that were created were 2.5 mm thick and 35 mm in diameter. After completing the pelletization process, the pellets were loaded into the spectrometer, so that chemical analysis could be performed.

4.3.3. Scanning electron spectroscopy-energy dispersive spectroscopy

The scanning electron microscope (SEM) analysis was performed using TESCAN, and the Vega 3X equipment with a tungsten filament was employed as the electron source. The surface morphology of the material was captured using secondary detectors and backscatter detectors with a high voltage of 20 kV. Images were taken using the Vega program at various magnifications. Energy dispersive X-ray spectroscopy (EDS) research was used to determine the chemical composition of specific locations using Oxford University's INCA software.

4.3.4. Determination of particle size using a Malvern Mastersizer 3000 analyzer

Particle size distribution (PSD) was determined using a Malvern Mastersizer 3000 analyzer. It measures particle size using laser diffraction, and relies on the inverse relationship between the diffraction angle of light and the size of the particles being measured (Bowen, 2002; Fisher et al., 2017; Gazi et al., 2021). To ensure that the PSD produced by the Mastersizer was representative of the sample used in the experiments, a statistical sampling procedure had to be followed. This was particularly important given the small size of the samples, which had to be in the required obscuration range - typically between 10 and 20 %. In this study, a sample size of approximately 2-3 grams was sufficient to ensure the correct obscuration. Therefore, the steps taken to sub-sample such a small mass determine the sample's level of representativeness. The procedure followed involved splitting the sample into small sub-samples (typically 10grams) by successive splitting using small 10-way rotary splitters. Water was added to the 10gram sub-sample to make a thick paste, which was homogenised manually using a spatula, then split into masses of approximately 2.5 grams using the conning and quartering method. The 2.5 gram masses ensured that obscuration was within the required range. Obscuration is defined as the optical concentration of the sample.

PSD measurements were then performed using this generated standard operating procedure (SOP). A sub-sample was added to 600 ml of water in Hydro LV for each run, while the agitator was spinning at about 2000 rpm. The sample was sonicated to deagglomerate the particles for measurement. The SOP created required three repeat measurements to be made over the course of a cycle, with the average PSD and related statistics being computed. Three repeat measurements were taken for each sample (from different 2.5-gram sub-samples) to allow comparison and evaluation of the precision of the method used to split the sample.

4.3.5. TPR studies

TPR experiments were conducted using Micromeritics Auto Chem II equipment. The catalyst, which weighed about 100 mg, was put inside a quartz tubular reactor that had a thermocouple installed so that the temperature could be monitored continuously. A furnace was used to provide heat for the reactor. In order to get rid of any water or other contaminants before the

TPR measurements were recorded, the calcined catalysts were flushed with high-purity argon at a temperature of 200 ºC for 30 minutes. They were then allowed to cool to room temperature. After that, a mixture of 5 % H_2/Ar was released into the chamber, and the temperature rose from 50 to 850 ºC at a rate of 10 ºC/min. Three Brooks mass flow controllers were used to regulate the volume of gas that passed through the reactor. A computer was used to automatically record the TCD signal and the amount of H_2 used. The analysis was repeated on the same catalyst at ramping rates of 10 ℃/min and 15 ℃/min to calculate the required activation energy for reduction using the Kissinger equation.

4.4. Results and Discussion

4.4.1. X-ray diffraction measurements

Figure 4.1 depicts the X-ray diffraction (XRD) patterns of cobalt on particles of clinoptilolite of various sizes. As seen in all diffractograms, the clinoptilolite phase dominated, with the heterogenite phase (cobalt representative) detected at intensity peaks positioned at 2theta = 31.05 ◦, 38.35 ◦ , 45.88 ◦ , 56.31 ◦ , 60.48 ◦ and 66.68 ◦. These peaks correspond to the (220), (222), (400), (422), (511) and 440 planes of cobalt oxide crystals, respectively.

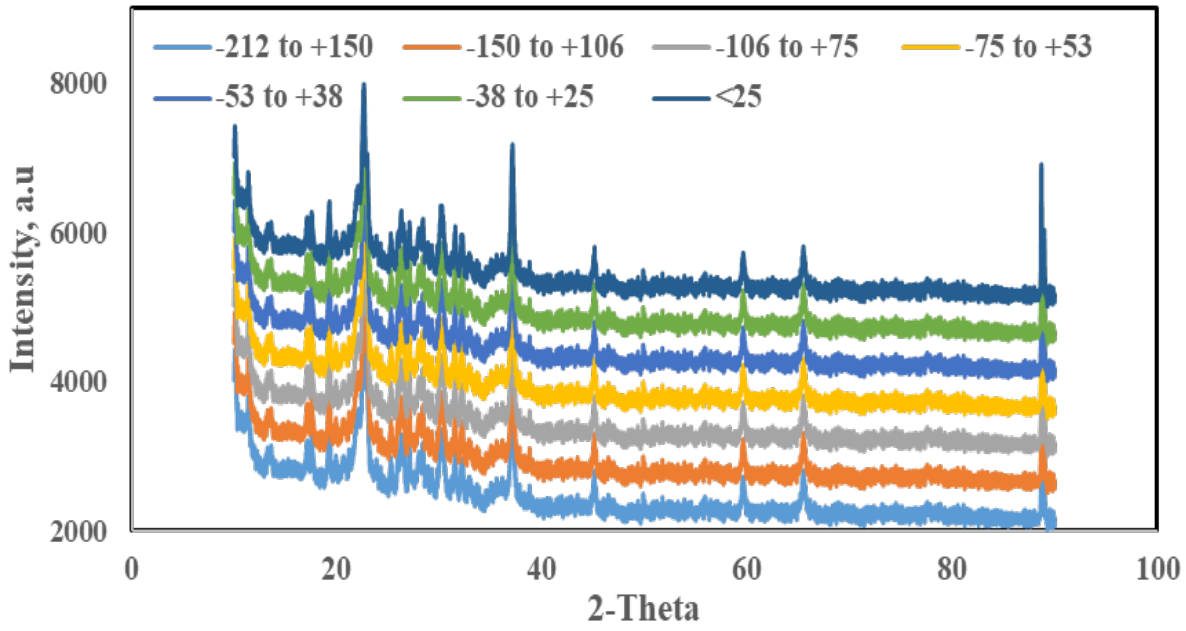

Figure 4.1: XRD patterns for the different size classes of the clinoptilolite particles

The presence of Co_3O_4 crystallites was confirmed by XRD, and the analyzed particle size range did not produce any differences, as was predicted. A few additional lines that represent the clinoptilolite framework are evident at 2-theta values less than 40°,. Different support particle sizes may produce cobalt crystallites of varying sizes; as a result, the width of the XRD peak may increase or decrease according to the crystallite size. The average crystallite size is determined using the Scherrer equation and the half-width of the XRD lines. Though much has been published about determining particle size using XRD and other techniques, the significance of average particle size has not been fully explored in FT-related studies in terms of a catalyst comprised of particles that are irregular in shape and non-uniform in size.

Table 4.1: Cobalt loading and crystalline size determination

(Analysis was done in triplicate for each sample size class.)

Sieve size range ***(μm)***	**% Co content**	**Crystalline size (nm) Co_3O_4**
	XRF	**XRD**
-212 to + 150	10.10 ± 0.12	10.93 ± 0.91
-150 to + 106	10.01 ± 0.02	10.34 ± 1.01
-106 to +75	9.98 ± 0.10	10.01 ± 0.76
-75 to +53	10.23 ± 0.18	8.27 ± 0.44
-53 to +38	9.88 ± 0.98	11.24 ± 1.78
-38 to +25	9.71 ± 0.24	9.22 ± 1.73
<25	9.98 ± 0.12	9.24 ± 2.70

Based on the results of the XRD analysis, the size distribution of the Co_3O_4 that crystallite is supported on various clinoptilolite size classes falls somewhere in the range of 8.27 ± 0.44 to 10.93 ± 0.91 nm (**Table 4.1**). Rietveld refinement was used to estimate the crystallite value from the Scherrer equation. The data tabulated in **Table 4.1** indicates that crystallite size tends to decrease from the 212 – 150 μm size class to less than 25 μm. This could be because of the surface being accessible. According to the results of the statistical analysis provided in our

previous paper ('Debunking the effect of Crystallite/Particle Size in cobalt-based Fisher Tropsch Synthesis'), crystallite size can be determined with equal precision using either transmission electron microscopy (TEM), XRD or hydrogen chemisorption (H_2 Chemisorption).

Saib et al. (2002) measured the diameter of cobalt crystallite using both TEM and H_2 chemisorption, but found no appreciable variations. In two other studies done by Cheng et al. (2018) and Bezemer et al. (2006), the measurements showed the same outcomes. According to Prieto et al. (2009), any piece of equipment can produce reliable data observations of cobalt crystallite using XRD, TEM and H_2 chemisorption. Therefore, using a single method in this investigation was considered acceptable.

4.4.2. Discussion of SEM and PSD

Table 4.2: Measurements of different particle size classes done using SEM

Sieve size range	SEM average size (µm)
-75 to +53 µm	59.52 ± 14.54
-53 to +38 µm	41.45 ± 10.98
-38 to +25 µm	37.38 ± 7.89
>25 µm	13.39 ± 4.92

A scanning electron microscope (SEM) was used to examine the size, shape and cobalt dispersion of the clinoptilolite particles. To make things clearer, discrepancies within these size groups were tested using four successive size classes (see **Table 4.2**). Following the completion of manual measurements, SEM statistical analysis was done. Examples of micrographs taken with a SEM that display clinoptilolite particles at a magnification of 300x are given in **Appendix A**. Two size classes are used to illustrate the measurement of particle size (-38 to +25 µm and -53 to +38 µm). The images show particles of varying shapes and sizes that fall within the dimensions specified for the particle size range.

The micrographs in **Appendix A** were taken at a lower magnification of 300x, which allows the real shapes of the particles to be seen. These micrographs also show that the particle dimensions can vary from the assigned size class by several microns. The literature does not contain any observations of particles that are homogeneous in size or shape; but it does contain observations of irregular and irregularly shaped particles.

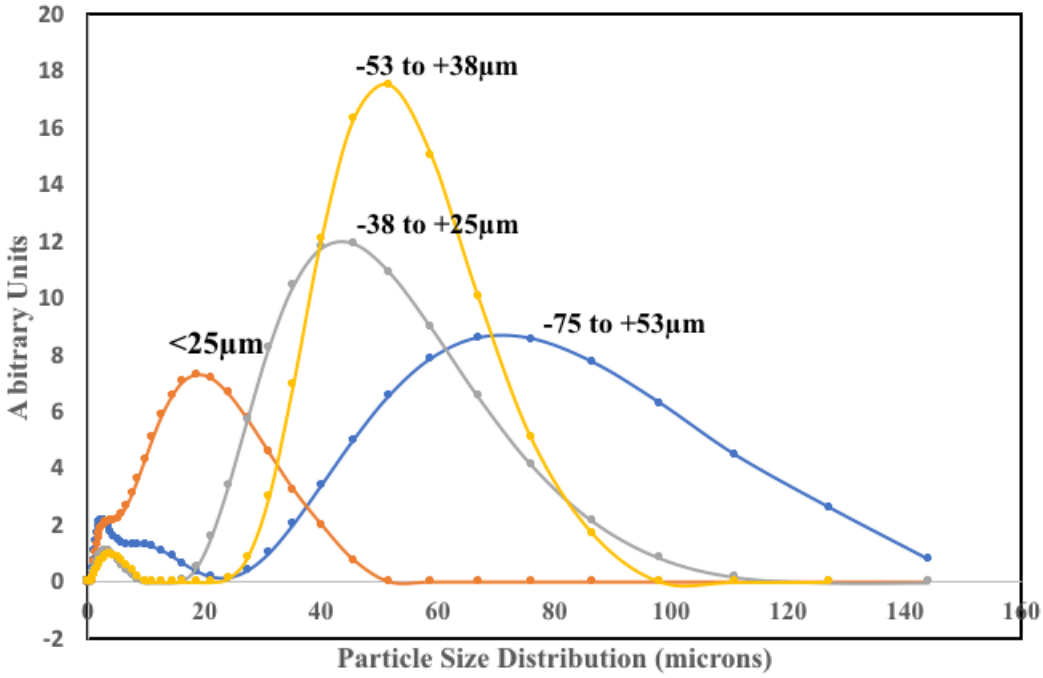

Figure 4.2: PSD determined using a Malvern Master Sizer 3000 analyzer

The seven samples were reduced to just four using the Malvern Master Sizer 3000 analyzer, in order to demonstrate the PSD analysis of the various size classes. The findings are presented in **Figure 4.2**, with the size class used also being specified. Although the average particle size is within the required range, it is difficult to only have particles of a given size class, even though the frequency distribution curves are symmetric. This indicates that coarse and fine particles are present in each class size and that it is difficult to only have particles of a given class size in catalyst sample (see T**able 4.2**). This observation lends credence to the results obtained from the SEM.

Appendix B shows the results of the statistical analysis that was performed to determine whether or not the particles observed with SEM are substantially different. The vast majority of the particles are within the specified range, as shown in **Figure 4.2** (the Malvern result), but the SEM and Malvern measurements that were recorded revealed the existence of particles outside the specified ranges, which introduces the possibility of overlap. In order to remedy this, an Anova single factor test was done to see if there was a statistical difference between these particles. The results show there is. There is a discrepancy between the four distinct size classes since the calculated F value (146.2023) is more than the Fcrit (2.665729). Additionally,

the P-value of 4.66 X 10^{-44} is less than 0.05, which indicates differences within the groups mentioned.

In Fischer Tropsch (FT), the use of moderately-large particles (1–3 mm) is necessary to prevent a high pressure drop (Rytter et al., 2016; Steynberg et al., 2004). Since micro-channel architectures use shorter lengths, the use of small particles (less than 1 mm) is not as problematic for large-scale commercial fixed bed reactors, due to excessive pressure loss (Mandić et al., 2017). Intraparticle transport resistance is reduced when small particles are used, and this is crucial for preserving low CH_4 selectivity (Mandić et al., 2017). As a result, the particle sizes that were investigated in the scenario adopted are suitable, and the experiments conducted were successful.

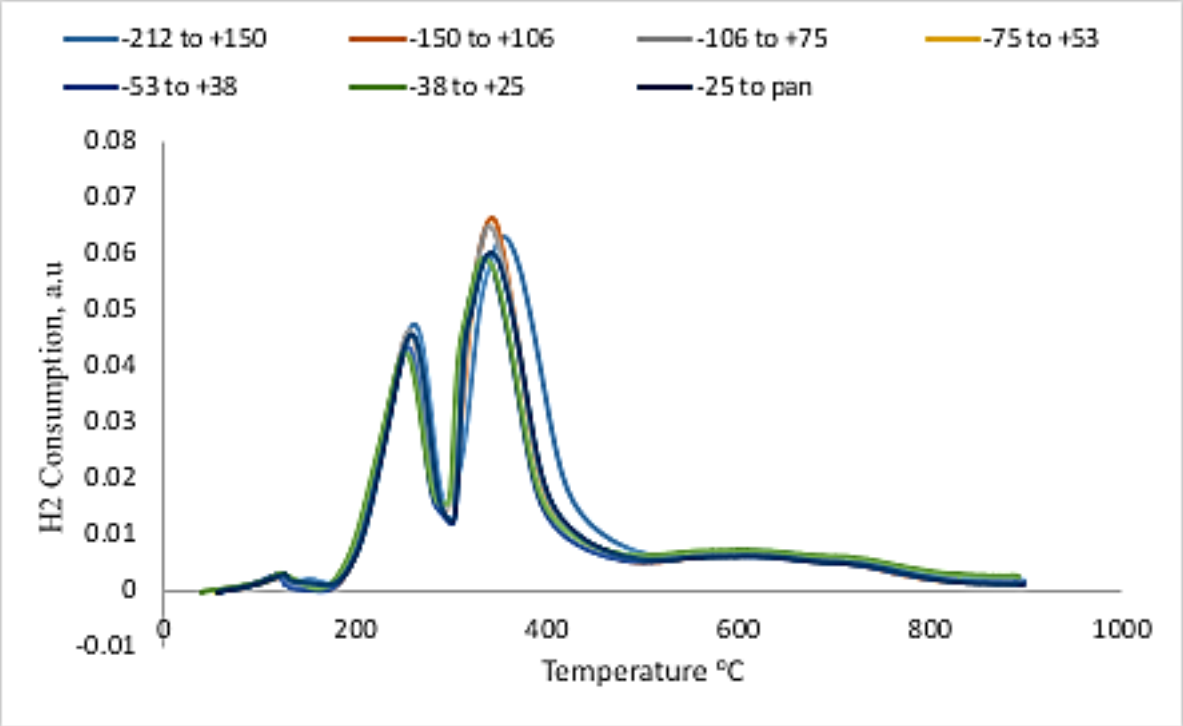

Table 4.3: TPR profile of different catalyst size classes

	Peak Temperature (°C)	
Particle size (µm)	Peak 1	Peak 2
-25 to pan	264.24	353.12

-38 to +25	260.89	344.53
-53 to +38	259.87	343.45
-75 to +53	267.03	349.3
-106 to +75	260.92	347.57
-150 to +106	261.74	348.36
-212 to +150	266.61	363.35

The influence of particle size on the reduction of Co_3O_4 particles was further investigated using TPR. The reduction profiles for the seven catalysts are provided in **Figure 4.3. Table 4.3** shows the reduction peak temperatures of the different size classes.

For the reduction of Co_3O_4, it can be seen that the catalysts provided comparable reduction profiles, albeit with some small displacement of the peaks (**Figure 4.3**). The stepwise reduction of Co_3O_4 to CoO took place at temperatures between 180 and 264 °C, and further reduction of CoO to Co took place at temperatures between 303 and 350 °C. It should be noted that the first and second reduction peaks did not shift backwards or forwards significantly as a result of the different size classes. At a high temperature, there is a decrease in larger particle size, but this only holds true for the size classes -212 to +150 to -106 to +75.

A complete reduction of Co_3O_4 consumes one hydrogen molecule in the first reduction process ($Co_3O_4 + H_2 \rightarrow 3CoO + H_2O$) and three hydrogen molecules in the second reduction process ($3CoO + 3H_2 \rightarrow 3Co + 3H_2O$). The two distinctive peaks that appear at temperatures that are distinct from one another provides evidence that the transformation of CO_3O_4 into Co is a two-stage process that involves the production of a CoO intermediary phase. Other research studies have reported the same characteristic peaks (Borg et al., 2007; Gorimbo et al., 2020; Khodakov et al., 1997; Olusola & Sudip, 2016). Generally. The reduction of the Co/Clino system was found to take place at a notably lower temperature than that reported in other studies (Bao et al., 2009; Lin & Chen, 2004; Prieto et al., 2009).

4.4.3. Effect of heating rate on TPR profile

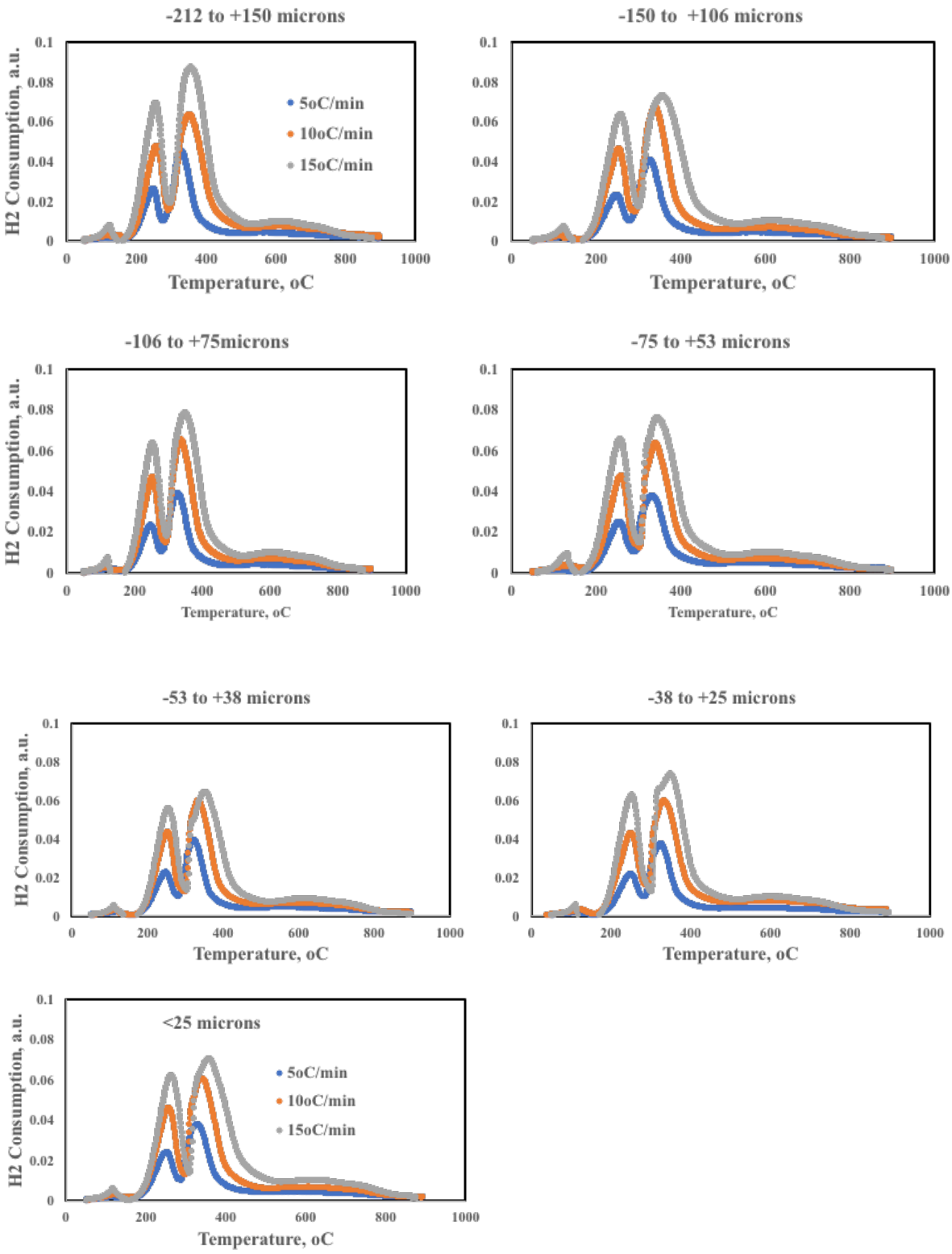

Figure 4.4: TPR at a heating rate of 5, 10 and 15 °C. All the different particle sizes are reported.

The TPR profiles of Co/Clino catalysts were examined at various heating rates. The findings are displayed in **Figure 4.4**. With an increase in heating rate, the first and second peaks on the TPR profiles of all the catalysts migrated to a high temperature (from 5 to 10 and then to 15 ^{o}C). In the investigation done by Vo et al. (2011), the heating rate was increased from 10 to 15 to 20 K/min, and the findings showed the same phenomenon of an increase in reduction temperature with an increase in heating rate.

In order to make the FT process more cost-effective, the focus must be on lowering both the capital and operational costs of a plant. One step in the direction of achieving this goal is lowering the temperature at which the reduction occurs. The operational cost of an FTS plant can also be reduced significantly by creating a catalyst that has a lower reduction temperature and produces desirable products. According to the information provided in **Figure 4.3 and Table 4.3**, a specific size class must be used when manufacturing a catalyst. Additionally, a sufficient number of tests must be conducted in order to select the optimum particle size class and the best heating rate to use during reduction.

4.4.4. Degree of reduction of different particle sizes of catalyst

Figure 4.3 shows the TPR curves. The integrated peak area of the reference Ag_2O was used as a standard to calculate the amount of H_2 consumed for the analyte samples from the integrated values of the curves. The percentage reduction of Co_3O_4 was determined by subtracting the H_2 consumed by the supports alone from the total H_2 consumed. of the calibration data was used to determine the amount of hydrogen used and the degree of reduction (DOR). **Table 4.4**, **Figure 4.5 and Figure 4.6** show the results of these calculations.

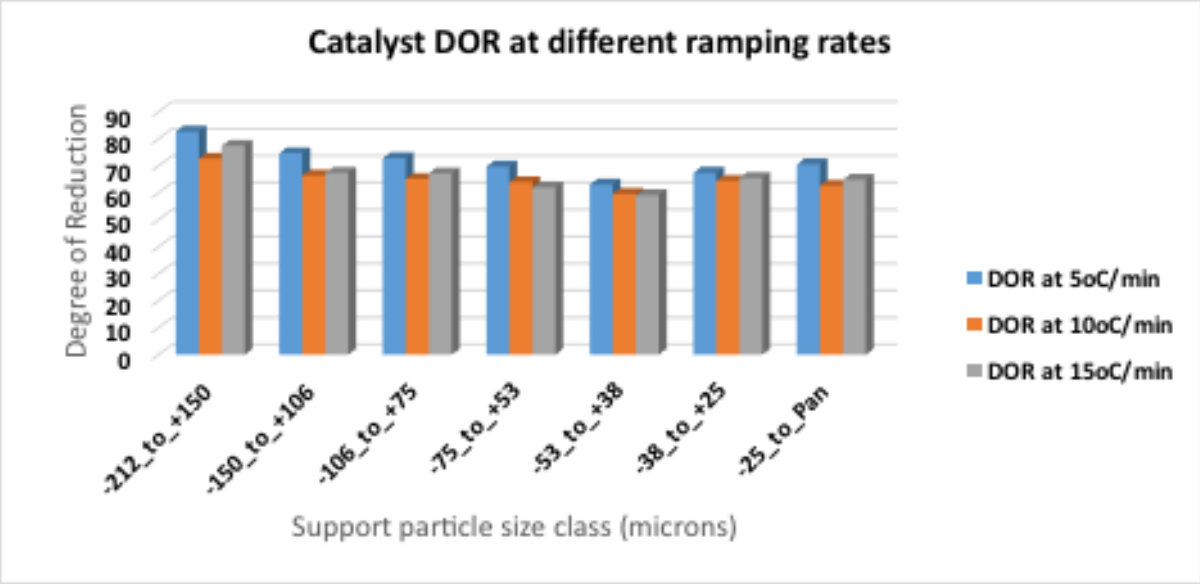

Figure 4.3: DOR of the catalyst at different ramping rates

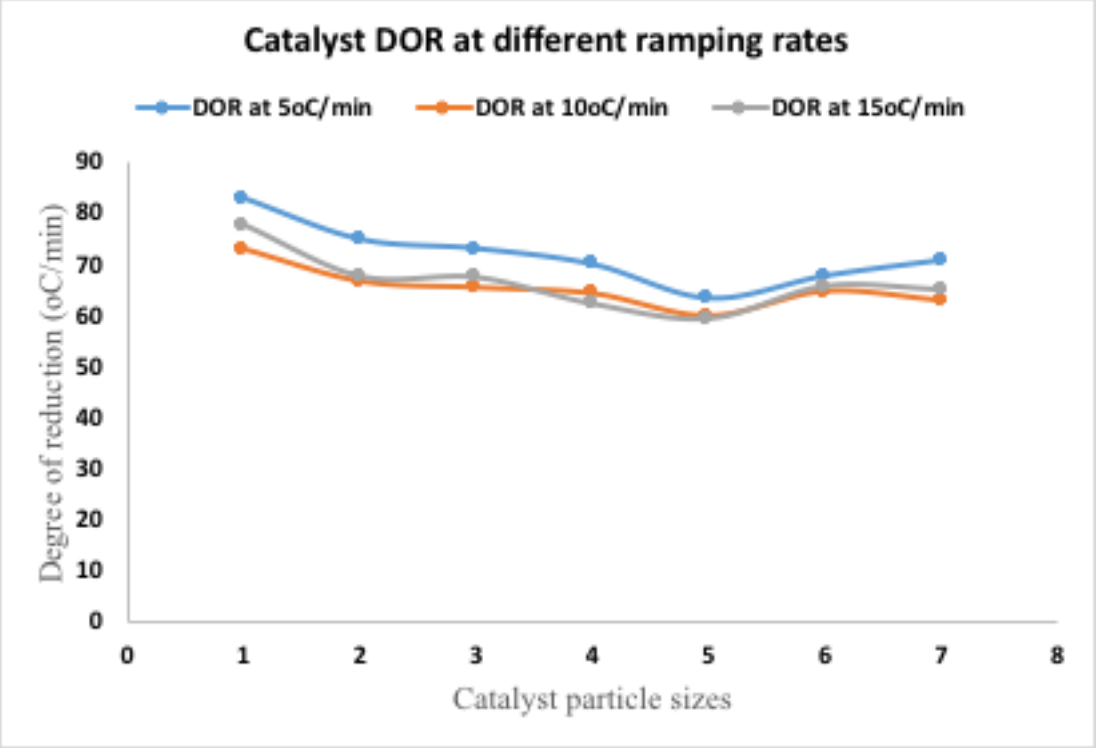

Figure 4.4: Line graph showing DOR of the catalyst at different ramping rates (the number 1-5 are catalyst number with sizes given in Table 4.4).

Table 4.4: DOR (%)of the catalyst at different heating rates and with different particle sizes

Catalyst number	Catalyst size class µm	DOR at 5°C/min	DOR at 10°C/min	DOR at 15°C/min
1	-212 to +150	82.71	72.64	77.42
2	-150 to +106	74.68	66.39	67.42
3	-106 to +75	72.85	65.16	67.20
4	-75 to +53	69.74	63.97	62.02
5	-53 to +38	63.07	59.63	59.17
6	-38 to +25	67.46	64.43	65.50
7	-25 to Pan	70.57	62.65	64.85

At all heating rates, the DOR is seen to decrease as particle size decreases. For instance, in trials carried out at a DOR of 5°C/min, a drop from 82.71 to 63.10 % was observed with particle sizes ranging from 212-150 to 53-38 µm. A further decrease in size increased the degree of reduction. The results cannot be considered definitive for a particle size class size less than 38 microns because the patterns do not remain consistent across all heating rates. However, the DOR dropped across the board with a decrease in particle size from a size class of 212-150 µm down to a particle size of 53-38 µm, regardless of the heating rate. The effect of heating rate on the DOR is equally inconclusive, but the magnitude of the difference between a low heating rate (5 °C/min) and a high heating rate is enormous in comparison. However, the difference between 10 °C/min and 15 °C/min is not that significant.

Below 450 °C, the TPR measurements of cobalt supported on clinoptlilolite particles of different sizes demonstrate that more than 60% of the cobalt is reduced. The results that have been provided indicate that the use of support material of various particle size classes results in a catalyst that possesses a range of attributes. When using a particle size in the range 212 - +150 µm, the best results are obtained in terms of reducibility of the cobalt that is supported by clinoptilolite. It is clear from these observations that the size of the particles has an effect on the temperature required for reduction. Lowering these temperatures is of great importance in the industrial sector, as it results in a large cut in the amount of money spent on the energy input required for reduction.

4.4.5. Activation energy calculations

A comprehensive study was carried out on the kinetics of the reduction of cobalt oxide on clinoptilolite using hydrogen. After choosing the particle size class with the lowest reduction temperature (-53 to +38 µm), peaks at 259.87 and 343.45 °C and a heating rate of 5 °C/min, the values of the local maxima of these peaks were used to estimate the kinetic parameters of the Co_3O_4 reduction reaction. (The values are presented in **Table 4.5.**)

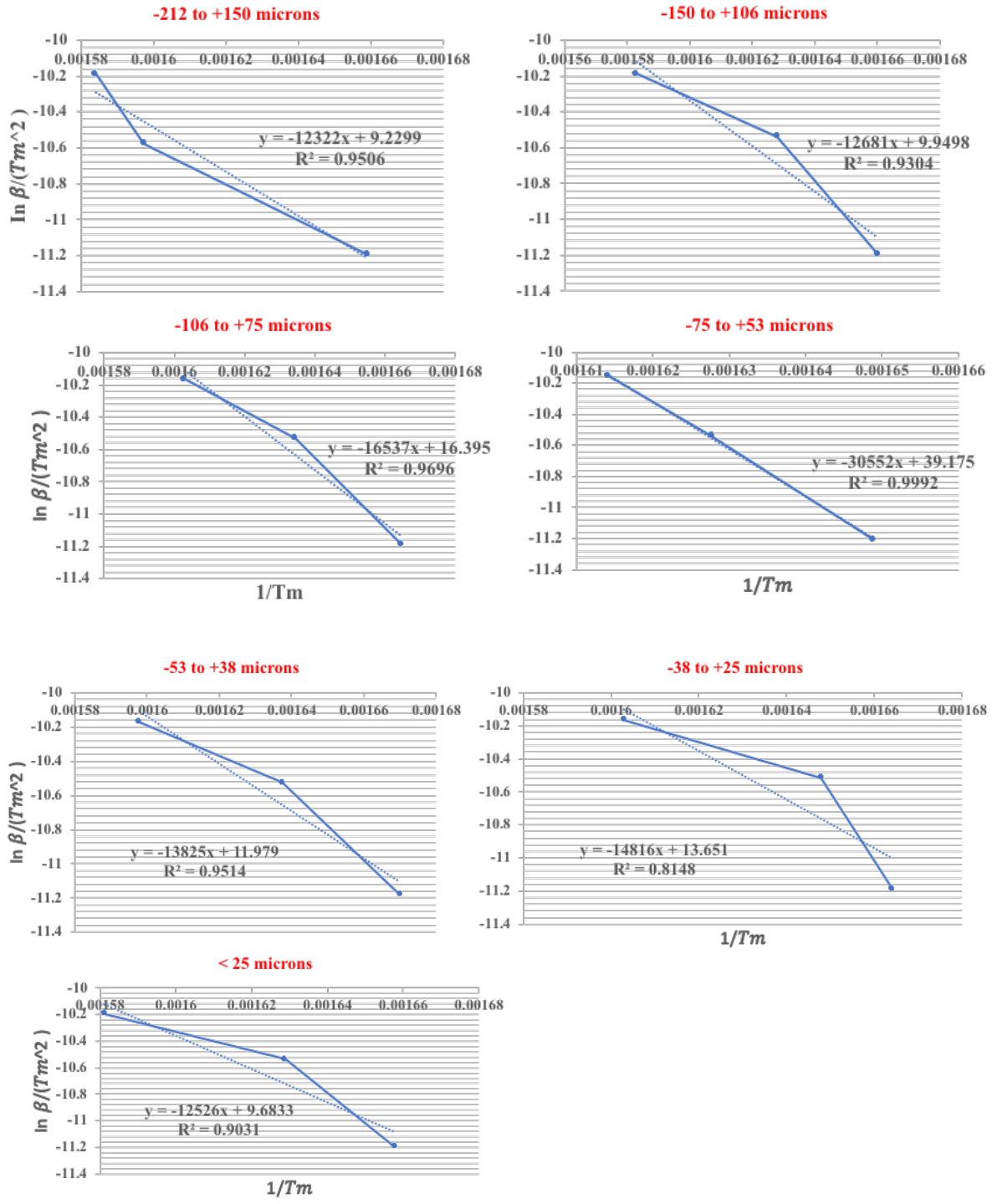

Figure 4.5: A plot of In β/(Tm^2) versus 1/Tm for all the different clinoptilolite class sizes

The linearity of the plot is satisfactory, with a correlation coefficient that is greater than 0.9, except for the particle size class of -38 to +25 µm, which has a coefficient of 0.8148. The activation energy, Ea, for the Co_3O_4 supported on clinoptilolite was determined using this plot; it ranged from 102.44 - 254.00 kJ/mole for particle that were smaller than 212 µm.

Table 4.5: Activation energy calculated using the Kissinger equation

Support catalyst size (µm)	E(i.e. activation energy) kJ/mol
-212 to +150	102.45
-150 to +106	105.43
-106 to +75	137.49
-75 to +53	254.01
-53 to +38	114.94
-38 to +25	123.18
-25 to Pan	104.14

Table 4.6 shows the results of calculations done using the Kissinger technique to determine the apparent activation energy for cobalt supported on clinoptilolite particles of various sizes. The kinetics calculation was done using the Tmax values. It was discovered that the activation energy measured during Co_3O_4 reduction increases when the size of the support particle decreases from -212 to +150 to -75 to +53 µm. The activation energy drops gradually from the particle size class of -75 to +53 to <25 µm. The observed trend almost matches the trend observed for DOR. The reduction of cobalt is optimally performed at a lower activation energy level, which means that the particle size class -212 to +150 µm is the best for this process. Additionally, the best DOR can be found with the same particle size class. This is probably related to changes in the interaction between the cobalt and the support, which could have occurred due to differences in the accessible surface area. When manufacturing a catalyst, the support should typically comprise particles of the same size throughout, as differences in the size of the particles might produce varied behavior.

4.4.6. Evaluation of surface area and pore volume using nitrogen adsorption

Analysis of the porosity of the different catalyst size classes was performed using nitrogen adsorption−desorption analysis. A typical adsorption isotherm obtained at −195 °C of the materials is included in **Figure 4.8**. Analysis of all the isotherms showed that the catalyst material gives a type 11-like adsorption isotherm, with an average pore diameter of 6.6 - 7.2 nm. (See **Table 4.6.)** This indicates that all the particles were mesoporous regardless of class size. Size class did not affect catalyst porosity significantly, as illustrated by the corresponding pore size distribution. (See **Figure 4.8 insert.**) However, it was noted that the average pore diameter is approximately 7mn and the differences are within the experimental error points, which indicates overall consistency among the different experimental data sets. All catalyst materials showed very low BET surface areas, ranging from (18.09 19.01 m^2/g). This obtained surface area is also similar to those previously reported for the same material (Gorimbo et al., 2014; Gorimbo, 2011).

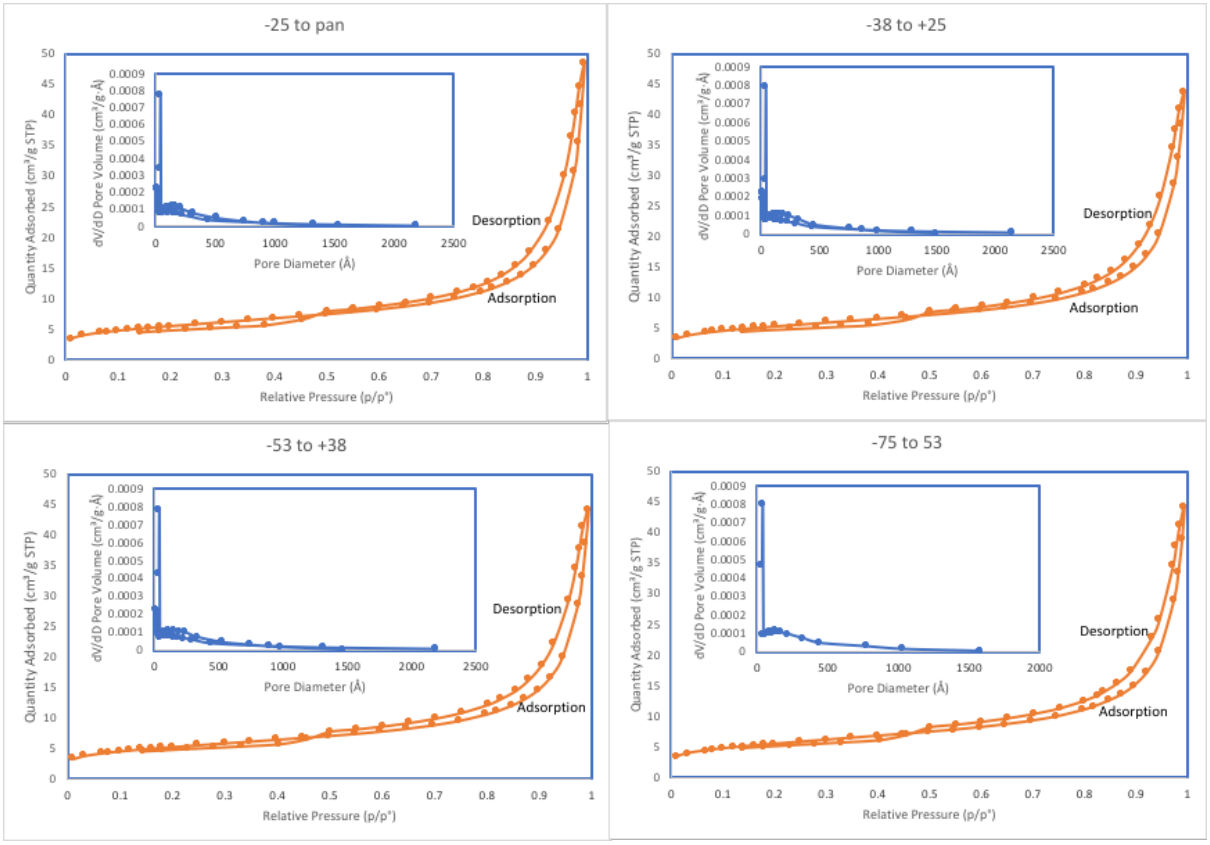

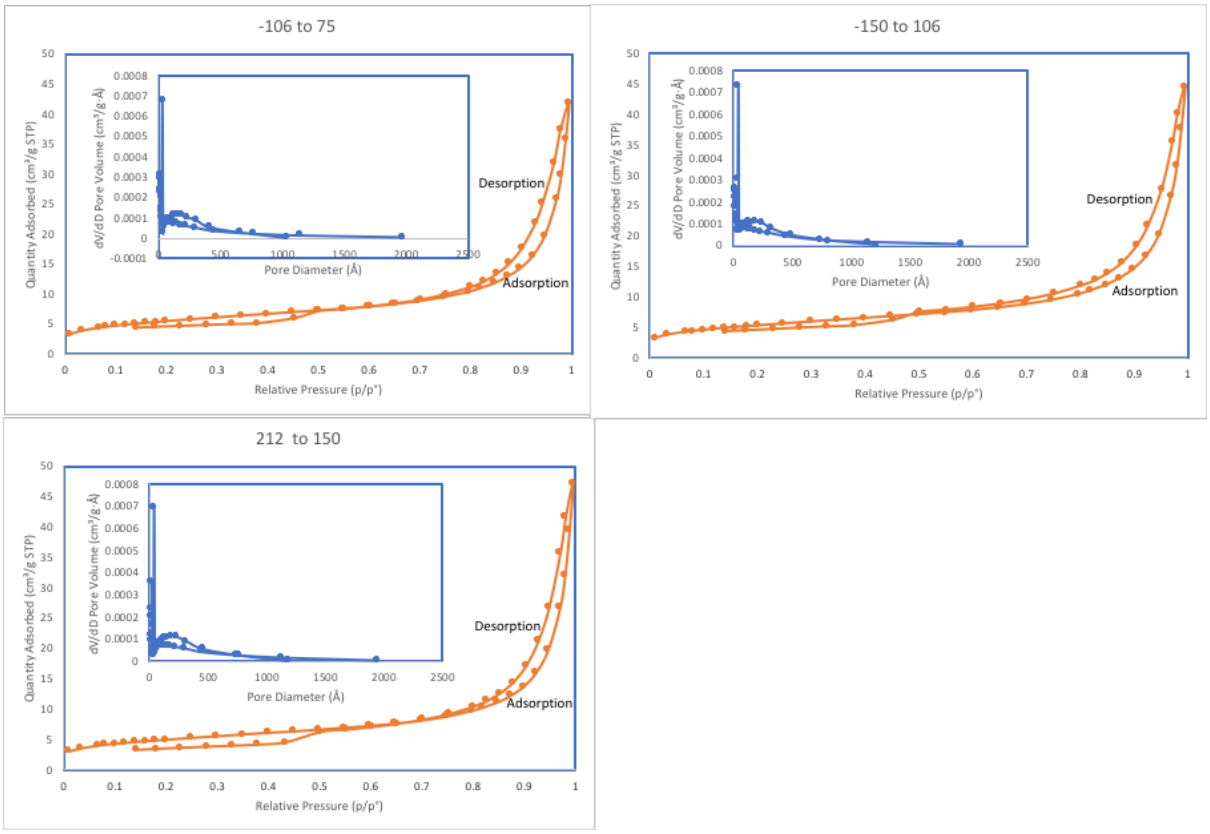

Figure 4.6: Physisorption isotherms and BJH pore size distribution for cobalt supported on clinoptilolite particles of different sizes. (NB: "-25 to pan", "-38 to +25" and "-53 to +38" are the support sizes with a unit given in µm)

Table 4.6: BET analysis of the Co/Clino catalyst (NB: "-25 to pan", "-38 to +25" and "-53 to +38" etc are the support sizes with a unit given in μm).

Support particle size (microns)	25 to pan	38 to 25	53 to 38	75 to 53	106 to 75	150 to 106	212 to 150
Surface area (m^2/g)							
Single point surface area at p/p° = 0.300000000	18.5971	18.1362	17.7749	18.441	18.6221	18.1031	17.0357
BET surface area	18.9175	18.4483	18.0884	18.7979	19.012	18.4496	17.3209
Langmuir surface area	141.8736	133.1885	131.2365	135.141	119.8984	127.7253	124.185
t-Plot Micropore Area	2.5283	2.5166	2.4589	2.0657	1.9738	2.1136	2.5165
t-Plot External Surface Area	16.3892	15.9317	15.6295	16.7322	17.0383	16.336	14.8044
BJH Adsorption cumulative surface area of pores							
between 17.000 Å and 3 000.000 Å diameter	14.779	14.273	13.927	14.897	14.238	14.198	13.237
BJH desorption cumulative surface area of pores							
between 17.000 Å and 3 000.000 Å diameter	17.0177	16.1036	16.1539	16.418	15.1878	16.1543	15.6829
D-H adsorption cumulative surface area of pores							
between 17.000 Å and 3 000.000 Å diameter	14.452	13.962	13.622	14.566	13.921	13.895	12.953
D-H desorption cumulative surface area of pores							

between 17.000 Å and 3 000.000 Å diameter	16.4664	15.6669	15.7298	15.8534	14.8455	15.6653	15.3323
Pore volume (cm³/g)							
Single point adsorption total pore volume of pores							
less than 403.122 Å diameter at p/p° = 0.950000000	0.034268	0.032879	0.032385	0.033369	0.031392	0.032517	0.031727
t-Plot micropore volume	0.001279	0.001282	0.00126	0.001027	0.001011	0.001067	0.00127
BJH adsorption cumulative volume of pores							
between 17.000 Å and 3 000.000 Å diameter	0.072424	0.065187	0.065951	0.066183	0.062038	0.066507	0.070735
BJH desorption cumulative volume of pores							
between 17.000 Å and 3 000.000 Å diameter	0.074293	0.066629	0.06738	0.067289	0.063553	0.068229	0.073301
Pore size (Å)							
Adsorption average pore diameter (4V/A by BET)	72.4585	71.2885	71.6158	71.006	66.0457	70.4981	73.268
BJH adsorption average pore diameter (4V/A)	196.026	182.692	189.419	177.711	174.288	187.363	213.741
BJH desorption average pore diameter (4V/A)	174.625	165.5	166.845	163.94	167.379	168.944	186.957
D-H adsorption average pore diameter (4V/A)	198.928	185.279	192.156	180.295	176.905	190.061	216.963
D-H desorption average pore diameter (4V/A)	179.793	169.952	171.043	168.89	171.96	173.892	192.659

It is worth noting that none of the BET characteristics shown have a clear trend. Therefore, when choosing a support to produce a catalyst, it is crucial to choose a support with a size class that is appropriate for reproducibility. Reproducibility is still a problem with FT, and this variation in particle size could be one of the contributing factors, hence the need to be investigated.

4.5. Conclusion

A thorough investigation was done of the characteristics of cobalt supported on clinoptilolite particles of different sizes using TPR, XRD, XRF, BET and SEM techniques. It has been demonstrated that these techniques provide insight on the effect of the particle size of the support, and this could be used as a quality control tool to evaluate the efficacy of the preparation method.

Reducing the support size improved the reducibility of cobalt oxide (CoO), which lowered both the reduction temperature and the activation energy for Co_3O_4 significantly. The kinetic study confirmed that the support plays an important role in improving catalyst reducibility via the interaction between the catalyst and the support. DOR decreased with a decrease in particle sizes at all heating rates for particle size classes of 212 -150 μm to 53 -38 μm. The magnitude of the difference between a low heating rate (5°C/min) and a high heating rate is comparatively large, however the impact of heating rate on the DOR is also not definitive. There is little difference between 10°C/min and 15°C/min. TPR measurements of cobalt supported on clinoptlilolite show that more than 60% of the cobalt is reduced below 450 °C, regardless of particle size. Based on the data presented, it appears that changing the PSD of the support material can produce a catalyst with a wide variety of characteristics. The best results for reducibility of cobalt supported by clinoptilolite are obtained when using particles that range from 212 to +150 μm.

These observations demonstrate that the temperature needed for reduction depends on the particle size. For the industrial sector, reducing these temperatures is crucial, since it significantly reduces the cost of the input energy needed for reduction. The data presented in this paper indicates that a specific particle size class must be employed when developing a catalyst, and sufficient testing must be done to choose the appropriate particle size class and reduction heating rate.

It is worth noting that no clear trend was obtained for any of the BET parameters, although this is something that has been documented. When choosing a support from which to create a catalyst, it is crucial to select a support from a particular size class, in order to ensure that the results reported here are reproduced accurately. There are issues with reproducibility when using the FTS method, and this is one of the possible factors that contribute to errors that need to be investigated. The issue of compounding of errors needs to be reduced.

References

Arnoldy, P., & Moulijn, J. A. (1985). Temperature-programmed reduction of Co0/Ai203 Catalysts. *Journal of Catalysis*, *93*, 38–54.

Bao, A., Liew, K., & Li, J. (2009). Fischer-Tropsch synthesis on CaO-promoted Co/Al2O3 catalysts. *Journal of Molecular Catalysis A: Chemical*, *304*(1–2), 47–51. https://doi.org/10.1016/j.molcata.2009.01.022

Bezemer, G. L., Bitter, J. H., Kuipers, H. P. C. E., Oosterbeek, H., Holewijn, J. E., Xu, X., Kapteijn, F., Van Diilen, A. J., & De Jong, K. P. (2006). Cobalt particle size effects in the Fischer-Tropsch reaction studied with carbon nanofiber supported catalysts. *Journal of the American Chemical Society*, *128*(12), 3956–3964. https://doi.org/10.1021/ja058282w

Blaine, R. L., & Kissinger, H. E. (2012). Homer Kissinger and the Kissinger equation. *Thermochimica Acta*, *540*, 1–6. https://doi.org/10.1016/j.tca.2012.04.008

Borg, Ø., Eri, S., Blekkan, E. A., Storsæter, S., Wigum, H., Rytter, E., & Holmen, A. (2007). Fischer-Tropsch synthesis over γ-alumina-supported cobalt catalysts: Effect of support variables. *Journal of Catalysis*, *248*(1), 89–100. https://doi.org/10.1016/j.jcat.2007.03.008

Bowen, P. (2002). Particle size distribution measurement from millimeters to nanometers and from rods to platelets. *Journal of Dispersion Science and Technology*, *23*(5), 631–662. https://doi.org/10.1081/DIS-120015368

Cheng, Q., Tian, Y., Lyu, S., Zhao, N., Ma, K., Ding, T., Jiang, Z., Wang, L., Zhang, J., Zheng, L., Gao, F., Dong, L., Tsubaki, N., & Li, X. (2018). Confined small-sized cobalt catalysts stimulate carbon-chain growth reversely by modifying ASF law of Fischer–Tropsch synthesis. *Nature Communications*, *9*(1), 1–9. https://doi.org/10.1038/s41467-018-05755-8

Fedorov, A. V., Kukushkin, R. G., Yeletsky, P. M., Bulavchenko, O. A., Chesalov, Y. A., & Yakovlev, V. A. (2020). Temperature-programmed reduction of model CuO, NiO and mixed CuO–NiO catalysts with hydrogen. *Journal of Alloys and Compounds*, *844*, 156135. https://doi.org/10.1016/j.jallcom.2020.156135

Fisher, P., Aumann, C., Chia, K., O'Halloran, N., & Chandra, S. (2017). Adequacy of laser diffraction for soil particle size analysis. *PLoS ONE*, *12*(5), 1–20. https://doi.org/10.1371/journal.pone.0176510

Gazi, M. Y., Apu, S. I., Sharmili, N., & Rahman, M. Z. (2021). Origin and characterization of clay deposits in the Dupi Tila Formation of the Bengal Basin, Bangladesh. *Solid Earth Sciences*, *6*(3), 313–327. https://doi.org/10.1016/j.sesci.2021.07.001

Gorimbo, J. (2011). *Effect of homoionic form of clinoptilolite on Ni2+ Adsorption isotherms: A thermodynamic study, Msc dissertation, University of the Witwatersrands.*

Gorimbo, J, Muvhiiwa, R., Llane, E., & Hildebrandt, D. (2020). Cobalt catalyst reduction thermodynamics in Fischer Tropsch: An attainable region approach. *Reactions*, *1*(2), 115–129. https://doi.org/10.3390/reactions1020010

Gorimbo, J., Taenzana, B., Kapanji, K., & Jewell, L. L. (2014). Equilibrium ion exchange studies of Ni2+ on homoionic forms of clinoptilolite. *South African Journal of Science*, *110*(5–6), 1–7. https://doi.org/10.1590/sajs.2014/20120027

Harju, H., Pipitone, G., & Lefferts, L. (2020). Influence of the catalyst particle size on the aqueous phase reforming of n-Butanol over Rh/ZrO2. *Frontiers in Chemistry*, *8*(January), 1–13. https://doi.org/10.3389/fchem.2020.00017

Janković, B., Adnadević, B., & Mentus, S. (2008). The kinetic study of temperature-programmed reduction of nickel oxide in hydrogen atmosphere. *Chemical Engineering Science*, *63*(3), 567–575. https://doi.org/10.1016/j.ces.2007.09.043

Khodakov, A. Y., Lynch, J., Bazin, D., Rebours, B., Zanier, N., Moisson, B., & Chaumette, P. (1997). Reducibility of cobalt species in silica-supported Fischer-Tropsch catalysts. *Journal of Catalysis*, *168*(1), 16–25. https://doi.org/10.1006/jcat.1997.1573

Li, H., Wang, S., Ling, F., & Li, J. (2006). Studies on MCM-48 supported cobalt catalyst for Fischer-Tropsch synthesis. *Journal of Molecular Catalysis A: Chemical*, *244*(1–2), 33–40. https://doi.org/10.1016/j.molcata.2005.08.050

Li, Y., & Yu, J. (2021). Emerging applications of zeolites in catalysis, separation and host–guest assembly. *Nature Reviews Materials*, *6*(12), 1156–1174. https://doi.org/10.1038/s41578-021-00347-3

Lin, H. Y., & Chen, Y. W. (2004). The mechanism of reduction of cobalt by hydrogen. *Materials Chemistry and Physics*, *85*(1), 171–175. https://doi.org/10.1016/j.matchemphys.2003.12.028

Mandić, M., Todić, B., Živanić, L., Nikačević, N., & Bukur, D. B. (2017). Effects of catalyst activity, particle size and shape, and process conditions on catalyst effectiveness and methane selectivity for Fischer-Tropsch reaction: A modeling study. *Industrial and Engineering Chemistry Research*, *56*(10), 2733–2745. https://doi.org/10.1021/acs.iecr.7b00053

Olusola, O. J., & Sudip, M. (2016). Temperature programme reduction (TPR) studies of cobalt phases in -alumina supported cobalt catalysts. *Journal of Petroleum Technology and Alternative Fuels*, *7*(1), 1–12. https://doi.org/10.5897/jptaf2015.0122

Prieto, G., Martínez, A., Concepción, P., & Moreno-Tost, R. (2009). Cobalt particle size effects in Fischer-Tropsch synthesis: Structural and in situ spectroscopic characterisation on reverse micelle-synthesised Co/ITQ-2 model catalysts. *Journal of Catalysis*, *266*(1), 129–144. https://doi.org/10.1016/j.jcat.2009.06.001

Rytter, E., Tsakoumis, N. E., & Holmen, A. (2016). On the selectivity to higher hydrocarbons in Co-based Fischer-Tropsch synthesis. *Catalysis Today*, *261*, 3–16. https://doi.org/10.1016/j.cattod.2015.09.020

Saib, A. M., Claeys, M., & Van Steen, E. (2002). Silica supported cobalt Fischer-Tropsch catalysts: Effect of pore diameter of support. *Catalysis Today*, *71*(3–4), 395–402. https://doi.org/10.1016/S0920-5861(01)00466-7

Steynberg, A. P., Dry, M. E., Davis, B. H., & Breman, B. B. (2004). Fischer-Tropsch reactors.

In *Studies in Surface Science and Catalysis* (Vol. 152). Elsevier B.V. https://doi.org/10.1016/s0167-2991(04)80459-2

Tomić-Tucaković, B., Majstorović, D., Jelić, D., & Mentus, S. (2012). Thermogravimetric study of the kinetics of Co 3O 4 reduction by hydrogen. *Thermochimica Acta*, *541*, 15–24. https://doi.org/10.1016/j.tca.2012.04.018

Vo, D. V. N., Nguyen, T. H., Kennedy, E. M., Dlugogorski, B. Z., & Adesina, A. A. (2011). Fischer-Tropsch synthesis: Effect of promoter type on alumina-supported Mo carbide catalysts. *Catalysis Today*, *175*(1), 450–459. https://doi.org/10.1016/j.cattod.2011.04.045

Chapter 5: Optimization and evaluation of the distribution of Fischer-Tropsch products over a cobalt-based catalyst utilizing design expert software

This work has been prepared in the form of a paper for future publication. Part of this work was presented at the following conferences:

- *American Institute of Chemical Engineers (AIChE) annual meeting, 20 August 2020, 2020 Virtual Spring Meeting and 16th GCPS (ISBN: 978-0-8169-1113-4).*

Abstract: Modelling the Fischer-Tropsch synthesis (FTS) system allows researchers to investigate the most efficient parameters while running the system under optimal conditions. As part of the design of experiments (DOE) procedure, a special data simulation method based on response surface methodology (RSM) is utilized to thoroughly analyze the impact of operating circumstances. The objective of this study was to examine the factors that affect the production of C_1, C_2-C_4, and C_{5+} in FTS process, and then optimize the critical factors utilising factorial design and response surface techniques. The parameters evaluated were reaction temperature, reaction pressure and the crystallite size of cobalt. The effects of these factors and their potential for synergy were explored simultaneously using multivariate DOE, with the yield of different hydrocarbon composition selectivity's as the measured responses. In the concept generation phase, optimization was based on the literature consulted, which proved to be an effective method for determining the optimization parameters. The detailed conceptual design included the generation of models using statistical methods and response surface models. Finally, the optimized design was validated using catalysts and parameters obtained during the optimization process, and this were compared to the output recorded in the theoretical modelling. The optimized parameters resulted in performance consistency, with the theoretical model for each group of hydrocarbons being validated by actual experiments. The established models were seen to characterize hydrocarbon distributions accurately and repeatedly over a wide range of reaction conditions (200-270 °C, 5-20 Bar, and 3-26 nm) using a cobalt-based catalyst. According to the detailed quantitative models developed, for higher C_{5+} production, 220 °C, 10 bar_g and 11nm (cobalt crystallite) benchmark parameters were set to produce 19.3 % C_1, 11.4% C_2-C_4 and 69% C_{5+} selectivity's. Comparative analysis showed a 1.9%, 3.9% and 0.3% percentage difference between the theoretical output and the actual output of C_1, C_2-C_4 and C_{5+}, respectively.

5.1. Introduction

Fischer-Tropsch synthesis (FTS) is receiving attention as a potentially game-changing method to cut pollution and make the transition to a more sustainable form of energy (Kuller et al., 2017). FTS transforms carbon monoxide (CO) and hydrogen gas (H_2) into useful hydrocarbons with reduced emissions of burn-off pollutants. This transformation normally takes place at a low pressure and a low temperature, and the stoichiometric ratio of H2 to CO is 2:1. In addition, the pressure and temperature levels used during this operation are normally quite moderate (Dry, 2002; Tijmensen et al., 2002). The utilization of metal catalysts and a variety of supports has been the focus of the vast majority of research on CO and H_2 conversion, which ultimately results in the production of lightweight and heavyweight hydrocarbons. However, it is still difficult to exercise control over the production of required compounds.

Cobalt and iron were considered as the first active catalysts used in the production of hydrocarbons via FTS (Khorashadizadeh et al., 2017). Cobalt catalysts are costly, although relatively cheaper than ruthenium, because they show functionality at lower synthesis pressure and temperatures levels, which means that the higher catalyst cost is counter-balanced by the reduced operating cost (Khodakov et al., 2007). They are also less vulnerable to deactivation (Khodakov et al., 2007). Moreover, cobalt-based catalysts show improved conversion productivity compared to their iron counterparts (Khodakov et al., 2007; Van Steen et al., 2018).

Multiple factors affect the selectivity of Fischer-Tropsch (FT) catalysts, including reaction temperature, reaction pressure, feed composition, catalyst crystallite size (Cheng et al., 2018), residence time (Makhura et al., 2019; Li et al., 2021), flow rate (Ziaei et al., 2020) and reactor type (Makhura et al., 2019). Slight changes in parameters can significantly change the selectivity of FT catalysts. Therefore, these variables should be monitored. Cobalt-based catalysts are preferred for the production of long chain hydrocarbons in low-temperature FT reactions, because of the low water gas shift activity. In addition, cobalt selectively forms linear paraffins (Dry, 2002; Shafer et al., 2019). Cobalt is a relatively expensive metal, so it is important to maximize the available metallic surface area of cobalt in the catalyst while minimizing the amount of cobalt used. This is achieved by dispersing cobalt on high surface area supports. While dispersion is important, operating conditions also have an impact on catalyst selectivity, and it is critical to identify methods of monitoring the catalytic activity of the catalyst.

Response surface methodology (RSM) is a tool used for designing experiments that is oftenly used in the development and optimization of process and synthesis parameters (Sedighi et al., 2016; Khorashadizadeh et al., 2017; Mosayebi et al., 2019; Ziaei et al., 2020). The technique needs minimum experimentation and time, and has proved to be more effective and more cost-effective than conventional methods used to design a synthesis and operation process. Furthermore, the use of Design Expert - a DOE approach - validates the efficiency. Manipulation of individual experimental conditions is traditionally studied using the one-factor-at-a-time (OFAT) approach. This format is time-consuming and tedious (Erbach et al., 2004) compared to the DOE approach, which has the advantage of detecting interaction between the process factors.

The purpose of this study was to look into the interactions between process factors during FT experiments. The investigation also aimed to determine the activity and selectivity of cobalt-based catalysts, with the focus being their role in hydrocarbon generation. The effect of crystallite size on clinoptilolite supports was also investigated. This was done to compare catalytic performances across a variety of operating conditions, the objective being to identify conditions that produce maximum C_{5+} and to identify how changing variables affect C_{5+} production.

5.2. Experimental

5.2.1. Catalyst preparation

5.2.1.1. Synthesis of 10wt%cobalt on clinoptilolite (10wt%Co/Clino for nomenclature)

Natural zeolite (clinoptilolite) samples obtained from Pratley Minerals in Krugersdorp, South Africa, were crushed using ring pulverisers. The powdered zeolite was then passed through a series of sieves with successively decreasing mesh sizes, the size ranges being -212 to +150 μm, then -150 to +106 μm, then -106 to +75 μm, then -75 to +53 μm, then -53 to +38 μm, then -38 to +25 μm, and lastly 25 μm. Only three of the seven clinoptilolite size classes (-75 to +53 μm, -53 to +38 μm, and -25 μm) were chosen for testing for use as a support in the synthesis of a cobalt catalyst. The basis for this decision was determined by preliminary characterisation experiments, which also revealed substantial differences in activation energy levels and particle size. Additionally, the number of samples to be analyzed was constrained by the equipment

used, as the rig employed in this investigation only contained three reactors, which had to run simultaneously.

The correct amount of cobalt was deposited on each individual clinoptilolite support to produce 10 wt%Co/Clino. Sigma-Aldrich supplied the cobalt (II) nitrate hexahydrate required to synthesize the catalyst. A measure of 100g of pure clinoptilolite (of various size classes) was placed in a beaker. Next, 54.82 grams of cobalt (II) nitrate hexahydrate were weighed and diluted in 70 milliliters of ethanol (based on the pore volume of the clinoptilolite support). The solution was stirred with a magnetic stirrer for the allotted period (30 minutes). The solution was then added in drops to the clinoptilolite, which was agitated for an hour with a magnetic stirrer. It was then sonicated ultrasonically for half-an-hour. The sample was allowed to air-dry at room temperature for 24 hours before being heated to 110 °C for 6 hours. The dried sample was calcined in air at 350 ºC for 6 hours.

5.2.2. Material characterization

5.2.2.1. X-ray diffraction

The powder x-ray diffraction (XRD) technique was carried out using a Rigaku Ultima IV X-ray diffractometer at a scanning speed of 0.5 º/min, from 10 º to 90 º 2-theta angle, to obtain the diffraction patterns of the sample. The voltage and current of the x-ray source were set to 40 kV and 30 mA, respectively. A CuK (l=1.54) x-ray generator target with a maximum power of 3 kW and a goniometer that can measure 2-theta angles from 0 ° to 162 ° were included in the XRD apparatus.

5.2.2.2. X-ray fluorescence spectrometry

Using the Rigaku ZSX Primus II with SQX analysis software, X-ray fluorescence spectrometry (XRF) analysis was carried out to ascertain the chemical makeup of the sample. 10 g samples were weighed, combined with 2 g of binder and pelletized under 20 tonnes of pressure to create pellets that were 35 mm in diameter and 2.5 mm thick. After the pellets had been prepared, they were placed in the spectrometer for chemical analysis.

5.2.2.3. Scanning electron spectroscopy-energy dispersive spectroscopy

A TESCAN: Vega 3X was used for the scanning electron microscope (SEM) examination, with an electron source with a tungsten filament being used. The surface morphology of the material was recorded utilising backscatter and secondary detectors at a high voltage of 20 kV. Vega software was used to capture images at various magnifications. The energy dispersive X-ray spectroscopy (EDS) analysis done using Oxford's INCA software determined the chemical composition of the chosen locations.

5.2.2.4. Temperature programmed reduction study

Micromeritics Auto Chem II equipment was used to do the temperature programmed reduction (TPR) experiments. A 50 mg mass of the catalyst was placed inside a quartz tubular reactor, with a thermocouple being used to monitor the temperature of the sample continuously. A furnace was used for heating purpose. The calcined catalyst was flushed with high-purity argon at a temperature of 200 ^{o}C for 30 minutes to remove water and any other impurities before the TPR test was done. It was allowed to cool to room temperature, and a 5% H_2/Ar mixture was then introduced into the chamber, and the temperature increased from 50 to 850 ^{o}C at a rate of 10 ^{o}C/min. The volume of gas passing through the reactor was controlled by three Brooks mass flow controls. The amount of H_2 used and the thermal conductivity detector (TCD) signal were automatically recorded by a computer.

5.2.3. Evaluation of FT performance

A fixed-bed micro-reactor with an internal diameter of 13 mm and a length of 300 mm was used for the FTS. A gas cylinder containing syngas and a mixture of H_2/CO/N_2 (purity: 99.99; 60/30/10 vol. %) was used to feed the reactant gas stream to the FT reactor loaded with the prepared catalyst, using a flow rate of 10 mL/min and pressure of 10 bar(g). In order to achieve precise mass balance calculations, N_2 was used as an internal standard. Three catalysts weighing 1.0 grams with 10% Co loading were reduced in-situ for 16 hours at 350 °C with pure hydrogen (ca. 99.99%).

After the reduction stage, the temperature of the reactor was reduced to ambient temperature under nitrogen flow and then raised to 220 °C under synthesis gas at a pressure of 10.85 bar (abs). A hot trap was installed immediately after the reactor to collect wax. It was kept at 150 °C. The oil and water mixture were collected in a second trap that was held at room

temperature. After the reactor, all the gas lines were kept at 100 °C. A metering valve was used to control the flow, while a bubble meter was used for the flow measurements. Online gas chromatography was used for online analysis of the product stream. A TCD with a Porapak Q packed column (1.50 m long and 3 mm in diameter) was used to evaluate H_2, N_2 and CO. A flame ionization detector (FID) with a Porapak Q packed column was used to analyze the hydrocarbons online.

5.2.4. FTS calculations

Quantitative analysis was performed on the information that was obtained from the online GC. As an internal reference for measuring the TCD data, the nitrogen (with a 10 vol percent concentration of N_2) present in the syngas feed of the FT tests was used. The initial calculations done consisted of determining the molar flow rate of the reactants and products. Additional calculations were then done. The calculations used to determine the mass balance, including the conversion of the reactant CO are similar to those used by previous researchers, while the experimental method used was developed many years ago.

The online data that was gathered was processed statistically. As the internal benchmark for the measurement of the TCD data, N_2 (10 vol percent of N_2) present in the syngas feed of the FT tests was used. Further calculations were done after the molar flow rates of the reactants and products had been established. The equations used to calculate the mass balance, including the conversion of the reactants CO and H_2 are provided below.

$$\% CO = \frac{F_{in}X_{co,in} - F_{out}X_{co,out}}{F_{in}X_{co,in}} \quad (5.1)$$

Where: $X_{co,in}$ denotes the molar fraction of CO in the reactor's gas feed; $X_{co,out}$ is the molar fraction of CO in the gas stream exiting the reactor.

The CO consumption rate is determined as follows:

$$r_{co} = \frac{F_{out}X_{co,out} - F_{in}X_{co,in}}{m_{cat}} \quad (5.2)$$

Where: r_{co} is the rate of CO consumption; mol/(min.gcat), m_{cat} is the mass of the catalyst utilised in this reaction, which is denoted by the variable m cat, and expressed in grams. The rate of gas product generation θ_i, mol/(min.gcat) can be calculated as follows:

$$r_{\theta_i} = \frac{F_{out} X_{\theta_{i,out}}}{m_{cat}} \quad (5.2)$$

Where: $X_{\theta_{i,out}}$ represents the molar fraction of the fraction of θ_i in the gas stream exiting the reactor.

Based on the moles of carbon, the product selectivity was determined using the following calculation:

$$Sel\ (\theta) = \frac{[nC]_\theta}{-r_{co} \times t \times m_{cat}} \quad (5.4)$$

Where: the selectivity of the product θ is denoted by the symbol Sel (θ); the number of moles of carbon present in the product is denoted by the symbol $[nC]_\theta$.

5.3. Catalyst characterization

5.3.1. DOE using RSM

The FT data used as input for DOE were extracted from the literature on cobalt-based catalysts. Using the response surface approach, the effects of numerous independent and dependent variables were examined. The formulation variables and their levels are given in **Table 5.1**. The dependent variables were selectivity of C_1 (%), C_2-C_4 (%) and C_{5+} (%) following FTS over a cobalt-based catalyst. The three independent variables were crystallite size (a), reaction pressure (b) and reaction temperature (c). A design matrix of the investigated responses is provided in **Table 5.2**.

Table 5.1: DOE reaction parameters and limits

Factor	Name	Units	Minimum	Maximum
1	Cobalt crystallite size	nm	3.00	26.0
2	Pressure	Bar	5.00	20.0
3	Temperature	°C	200	270

The effect of the independent variable on responses were modelled as per Montgomery (2013), using the second-order polynomial equation involving independent factors and interaction factors. This was pre-selected based on model analysis, lack of fit and R^2 analysis measured responses. To simulate the effect of the independent factors on crystallite size (a), reaction pressure (b) and reaction temperature (c), the following quadratic mathematical model (**equation 5.5)** was created using optimization design:

$$f = a_0 + \sum_{i=1}^{m} a_i Z_i + \sum_{i=1}^{m} a_{ii} Z_i^2 + \sum_{i<j}^{m} a_{ij} Z_i Z_j \qquad (5.5)$$

Where: f is the response; a_0 is the intercept; a_i, a_{ii}, and a_{ij} are regression coefficients; Z_i and Z_j represent individual effects; quadratic effects are represented by Z^2; interaction effects are represented by Z_iZ_j.

The optimization results were evaluated using ANOVA analysis.

Table 5.2: Experimental responses and predicted responses obtained by means of RSM (Response is the selectivity %)

Data source	Run	Factor 1	Factor 2	Factor 3	Response 1		Response 2		Response 3	
		Crystallite size	Pressure	Temperature	C_1		C_2-C_4		C_{5+}	
		nm	bar	°C	Predicted	Actual	Predicted	Actual	Predicted	Actual
1	1	13.8	20.0	220	19.2	21.3	13.9	15.5	67.9	63.2
	2	17.6	20.0	220	20.5	18.5	13.4	14.8	67.0	66.7
	3	9.50	20.0	220	18.7	14.1	19.9	11.7	62.4	74.2
2	4	5.90	20.0	220	19.2	19.2	29.3	36.6	52.5	44.2
	5	6.80	20.0	220	19.0	20.4	26.6	35.4	55.4	44.2
	6	14.1	20.0	220	19.2	17.9	13.7	19.1	68.1	63.0
3	7	3.00	5.00	250	40.9	40.0	48.3	57.0	11.7	3.00
	8	5.50	5.00	250	35.2	48.0	40.3	34.0	25.4	18.0
	9	8.60	5.00	250	28.7	25.0	33.1	40.0	39.1	35.0
4	10	9.00	10.0	230	17.4	36.4	10.1	3.80	73.5	59.9
	11	13.0	10.0	230	14.4	11.0	5.40	1.80	81.2	87.2
	12	14.3	10.0	230	13.6	11.8	5.00	2.30	82.4	85.9
	13	17.0	10.0	230	12.3	19.3	5.70	3.50	83.0	77.1
5	14	26.0	15.0	200	46.4	44.0	28.6	23.7	26.0	32.3
	15	3.00	15.0	200	22.8	18.7	30.1	20.9	48.0	60.4
	16	6.70	15.0	200	24.4	28.5	18.7	16.7	57.8	54.8

	17	6.90	15.0	200	24.5	19.2	18.2	19.0	58.2	61.8
	18	8.30	15.0	200	25.3	37.6	15.1	18.7	60.5	43.7
6	19	3.00	15.0	220	18.3	12.1	22.9	16.9	59.8	71.0
	20	6.70	15.0	220	16.5	17.5	10.8	13.1	73.7	69.4
	21	6.90	15.0	220	16.4	11.2	10.3	14.8	74.3	74.0
	22	8.30	15.0	220	16.0	13.7	7.00	14.2	78.1	72.1
7	23	6.50	10.0	220	21.3	24.2	19.7	22.4	60.0	53.4
	24	10.0	10.0	220	19.7	16.1	12.9	16.5	68.4	67.4
	25	11.2	10.0	220	19.3	14.4	11.4	15.4	70.3	70.2
	26	7.10	10.0	220	21.0	20.0	18.2	16.2	61.8	63.8
	27	11.0	10.0	220	19.3	17.8	11.6	16.5	70.0	65.7
	28	15.4	10.0	220	18.6	16.1	9.90	11.0	72.5	72.9
8	29	15.0	20.0	270	17.0	17.5	17.2	27.3	65.0	54.3
	30	16.0	20.0	270	15.0	19.0	16.6	11.4	67.6	65.9
	31	16.0	20.0	270	15.0	8.20	16.6	12.6	67.6	78.6
	32	10.0	20.0	270	27.8	35.4	25.1	22.1	46.5	41.7
	33	10.0	20.0	270	27.8	22.2	25.1	30.7	46.5	44.8
9	34	6.20	20.0	220	19.2	28.4	28.4	25.3	53.5	46.3
	35	11.4	20.0	220	18.8	19.5	16.5	15.8	65.7	64.7
	36	13.8	20.0	220	19.2	21.3	13.9	15.5	67.9	63.2
	37	17.6	20.0	220	20.5	18.5	13.4	14.8	67.0	66.7

	38	9.50	20.0	220	18.7	14.1	19.9	11.7	62.4	74.2
	39	5.90	20.0	220	19.2	19.2	29.3	36.6	52.5	44.2
	40	6.80	20.0	220	19.0	20.4	26.6	35.4	55.4	44.2
	41	14.1	20.0	220	19.2	17.9	13.7	19.1	68.1	63.0
10	42	3.00	5.00	250	40.9	40.0	48.3	57.0	11.7	3.00
	43	5.50	5.00	250	35.2	48.0	40.3	34.0	25.4	18.0
	44	8.60	5.00	250	28.7	25.0	33.1	40.0	39.1	35.0
	45	11.0	5.00	250	24.0	5.00	29.6	10.0	47.3	85.0
11	46	11.9	20.0	230	15.9	20.6	14.7	10.7	70.2	68.8
	47	10.8	20.0	230	16.3	13.91	16.5	8.23	68.0	77.66
	48	10.5	20.0	230	16.5	14.94	17.1	9.67	67.3	75.39
	49	10.6	20.0	230	16.4	15.25	16.9	9.67	67.5	75.09
	50	10.4	20.0	230	16.5	17.4	17.3	15.2	67.1	67.42
	51	9.98	20.0	230	16.7	18.47	18.0	16.0	66.1	65.52
12	52	19.7	10.0	240	5.80	10.6	4.50	8.20	90.6	81.2
	53	18.6	10.0	240	6.60	10.7	3.10	8.50	91.2	80.8
	54	18.0	10.0	240	7.10	9.90	2.50	7.50	91.3	82.6
	55	9.20	10.0	240	16.4	15.7	6.40	8.00	78.1	75.8
	56	6.30	10.0	240	20.6	17.9	13.0	10.5	67.4	71.6
	57	4.90	10.0	240	22.7	12.6	17.1	7.80	61.1	79.6

Statistical software was used to optimize the design, create the projected FTS product selectivity and display the effect of the variable parameters on product output, using RSM graphics. The ANOVA data analysis shows the analysis of variance, the significance of the variance test and the first-order coefficient significance test regression equation, all of which were employed to evaluate the reliability of the model.

5.3.2. Descriptive statistics and model fitting

Statistical evaluation of the model included using version 13 of Design Expert for regression analysis of the experimental data to match the equations, while the correlation coefficient (R^2) was used to determine the validity of the resulting model. The significance of the ANOVA equations that were established was also determined using analysis of variance.

5.4. Results and discussion

The results were used to analyse the operating conditions (temperature, pressure and cobalt crystallite size), with the end goal being to identify the optimal operating parameters indicated by the results of the preliminary research. The experimental matrix was used to collect 57 experimental series from 12 different data sources. **Table 5.2** provides the experimental and predicted values for the various experimental settings used that were taken from the published research (Saib et al., 2002; Song and Li, 2006; Lira *et al.*, 2008; Witoon et al., 2011). The actual values for C_1, C_2-C_4 and C_{5+} selectivity acquired by performing actual FTS were compared with the predicted values, with the results showing that they were rather similar. All possible mechanisms of interaction and the reactions of variables were explored using statistical analysis of the results. Prior to determining the statistical significance, the impact of residuals were examined to determine the adequacy of the testing and optimization performed.

The residual values, which represented the discrepancy between the expected results and the ones obtained from optimization. External studentized residuals were used to evaluate the regression assumptions, with all the different normal distributions mapped onto a single standard normal distribution, which makes it easier to note problems with the analysis. The normal probability plots provided in **Figure 5.1, Figure 5.2 and Figure 5.3** show whether or not the residuals followed a normal distribution.

When a sequenced factorial design is used for screening (finding statistically significant factors), high-order interactions can occur (Montgomery, 2013). A normal probability plot based on the coefficient of effects was formed to estimate the important effects based on their amounts and calculate their growing probabilities (Shapiro and Wilk, 1965; Filliben, 1975). A normal probability plot depicts the relationship between actual value evaluations and their accumulative normal probabilities (Montgomery, 2013). **Figure 5.1, Figure 5.2 and Figure 5.3** show the normal probability plots with a straight line of best fit, which indicates that the hypothesis is correct and that the models are adequate to produce the desired products. Another indication of the adequacy of the model is a pattern of experimental points being within the limiting constraints of the line of best fit.

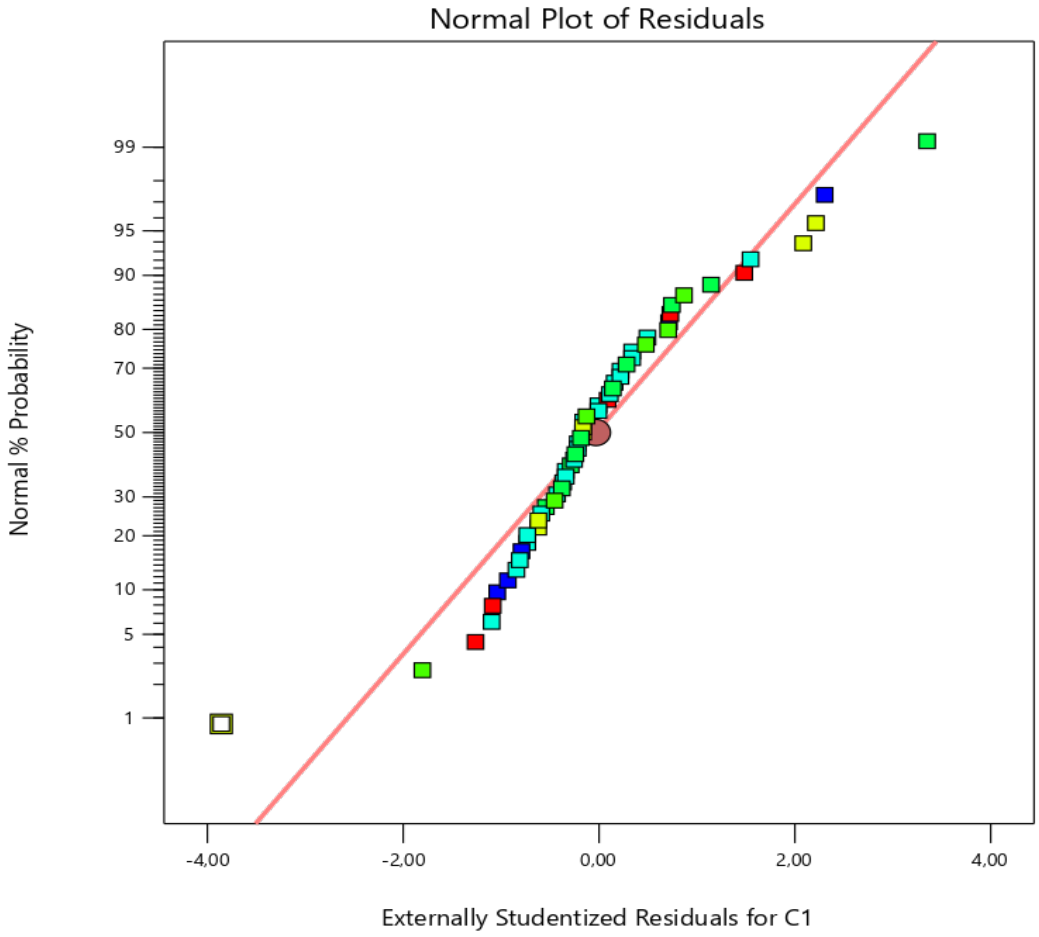

Figure 5.1: Normal probability plot of residuals - C_1 selectivity

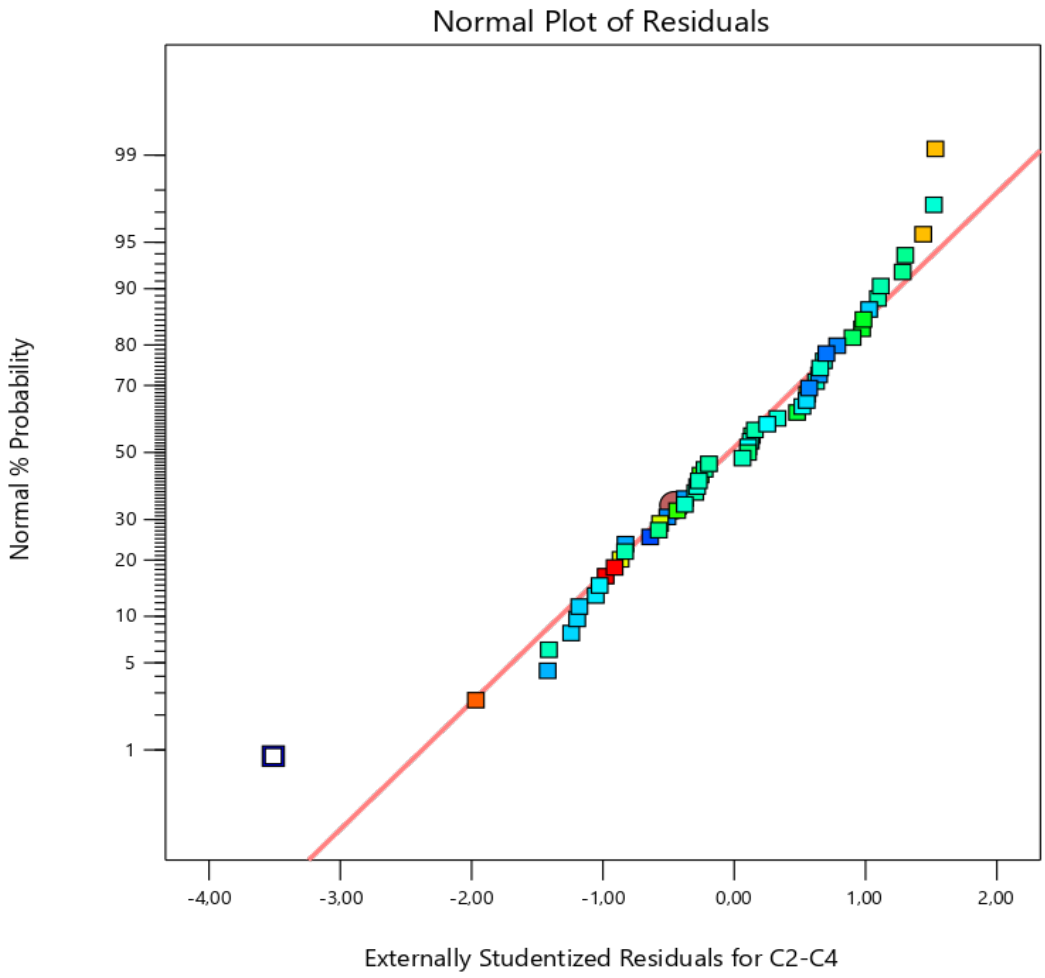

Figure 5.2: Normal probability plot of residuals - C_2-C_4 selectivity

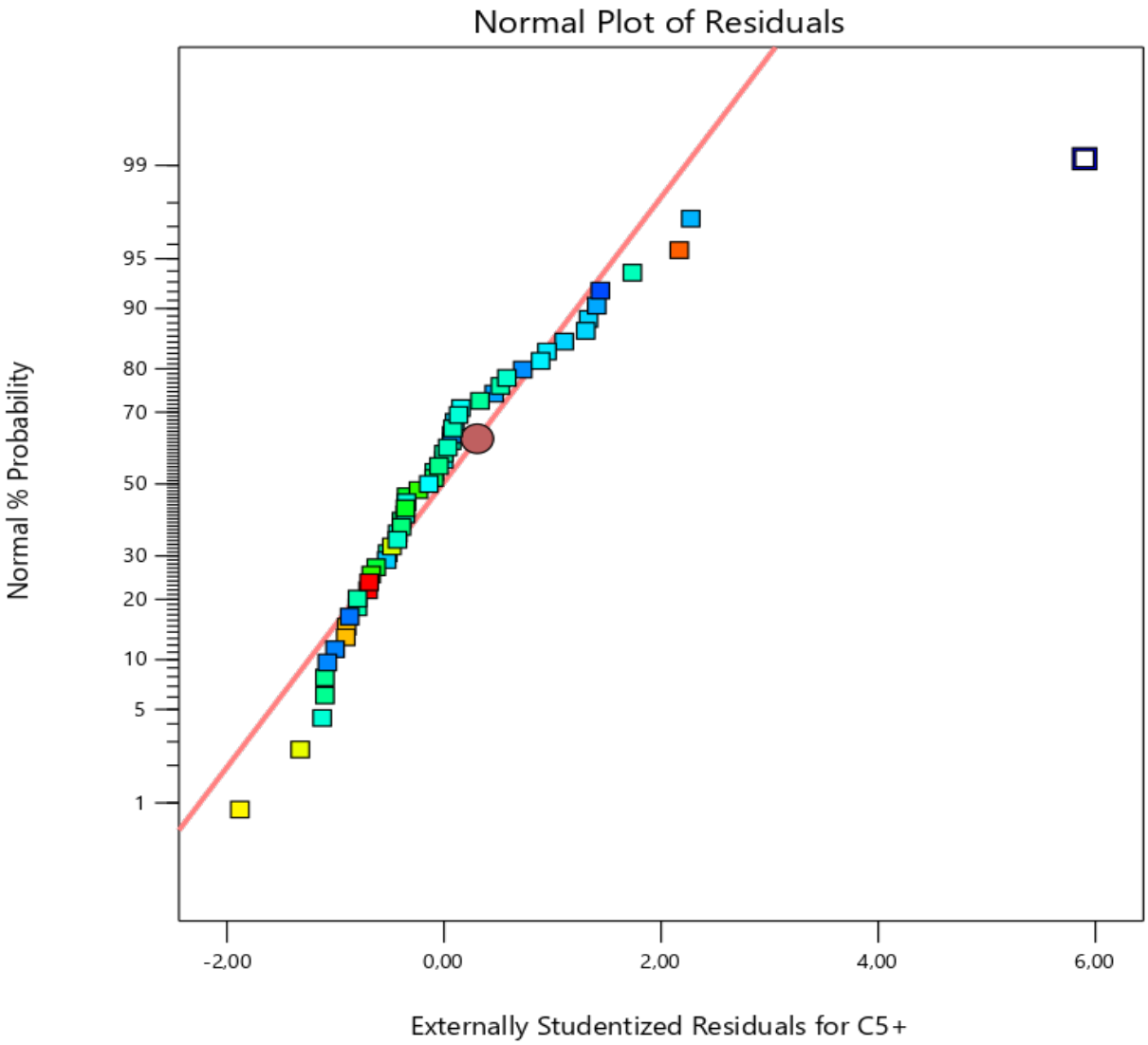

Figure 5.3: Normal probability plot of residuals - C_{5+} selectivity

A one-way ANOVA test was used to determine the statistical significance in describing selectivity behaviour. The statistical significance of the models used as predictive models is indicated by a p-value of less than 0.05 obtained during the ANOVA for C_1, C_2-C_4 and C_{5+}. Furthermore, a strong correlation between model-predicted and experimental results indicates well-fitted, accurate models.

5.4.1. Model fitting and analysis of variance

ANOVA was used to analyze the impact of individual factors and their interactions as well as the statistical significance and goodness of fit of the established second-order quadratic models.

The results are summarized in **Table 5.3**. The P-value must be less than 0.05 in order for the factors to have a crucial effect on the response values (Montgomery, 2013). The ANOVA yielded P-values of 0.001, 0.02 and 0.005 for C_1, C_2-C_4 and C_{5+}, respectively. This indicates that the models are statistically significant at the 95% confidence level. In addition, the magnitude of an independent variable's impact on the response is proportional to the F-value assigned to that variable.

The direct effect of the three variables are only significant for pressure and its effect on C_{5+} selectivity. Temperature has an effect on C_1 and C_{5+}, but the quadratic effects of the terms, i.e., b^2 and c^2, are significant, as indicated by the quadratic terms in the models for C_1 and C_{5+} and also based on the estimated F values and the P-value (0.05). This demonstrates that temperature and pressure have a significant influence on C_1 and C_{5+} selectivity. Furthermore, for C_1 and C_{5+}, the interactive effects of crystallite size and temperature are significant.

Table 5.3: ANOVA for the fitted models of responses.

Model	**C_1**			**C_2-C_4**			**C_{5+}**		
	F-value	**p-value**		**F-value**	**p-value**		**F-value**	**p-value**	
Whole-plot	**4.86**	**0.0011**	**Significant**	**5.46**	**0.0235**	**Significant**	**9.67**	**0.0042**	**Significant**
b	0.5628	0.4569		4.83	0.0595		5.96	0.0326	
c	8.19	0.0063		1.67	0.2561		8.99	0.0363	
bc	0.1907	0.6643		0.6588	0.4513		1.59	0.2576	
b^2	2.17	0.1473		10.92	0.016		16.65	0.004	
c^2	9.41	0.0036		1.76	0.2262		9.42	0.0124	
Sub-plot	**7.11**	**0.0001**	**Significant**	**9.23**	**< 0.0001**	**Significant**	**11.5**	**< 0.0001**	**Significant**
a	3.12	0.0836		1.4	0.2426		3.46	0.0695	
ab	0.5449	0.4641		1.09	0.3017		0.0308	0.8614	
ac	12.9	0.0008		0.8317	0.3671		7.8	0.0078	
a^2	0.6006	0.4422		14.48	0.0005		9.52	0.0035	

a- Crystallite size

b- Reaction pressure

c- Reaction temperature.

The significance of the models shown in **Table 5.3** is further supported by the examination of the R^2 and adjusted R^2 values shown in **Table 5.4**, which show a small percentage difference. These findings show that the test independent variable was in agreement with the model, since the adjusted R^2 takes into account the different independent variables included in the test; the model and R-squared do not do so, but the percentage difference is small.

Table 5.4: Significance of predicted models

Model	Term df	Error df	F-value	p-value	R^2	Adjusted R^2
C_1	5	47	4.86	0.0011	0.6235	0.5315
C_2-C_4	5	6.92	5.46	0.0235	0.7709	0.7150
C_{5+}	5	7.28	9.67	0.0042	0.7851	0.7326

5.4.2. Model of selectivity for C_1

Lowering C_1 selectivity and enhancing C_{5+} selectivity is an essential consideration in the FT process (Yang *et al.*, 2014). After fitting the response data to various models, it was observed that the quadratic model for C_1 selectivity (**equation 5.6)** best explained the data. This indicates the effect of the independent variables.

$$S_{C_1} = \begin{matrix} +538.39143 + 8.87327a - 7.08929b - 4.30395c + 0.035935ab - 0.046370ac + \\ + 0.030586a^2 + 0.144587b^2 + 0.009674c^2 \end{matrix} \quad (1.6)$$

Where:

a- Crystallite size

b- Reaction pressure

c- Reaction temperature.

C_1 production is presumed to be proportional to crystallite size growth; however, the interaction between crystallite size and temperature shows that increasing crystallite size has a negative influence on C_1 production. (See F**igure 5.4a and 5.4b**.) Saib et al. (2002) reveal another factor that shows a correlation between selectivity and pore diameter: at a low temperature (200 °C) and constant pressure, a reduction in crystallite size is accompanied with a decrease in C_1 selectivity; however, at a high temperature (270 °C), the pattern is the opposite. This phenomenon is depicted in **Figure 5.4** and supports the ANOVA findings of this study, which

indicate that the interaction between crystallite size and temperature is significant. Merino *et al.* (2016) explain the phenomenon from the perspective of diffusion and the interaction between reactants and active surfaces. As the reaction progresses, wax accumulates and prevents the reactants from reaching the active site. The activity of Co catalysts during FTS is predominantly determined by the total number of exposed cobalt crystallites. However, CO and H_2 can dissolve and diffuse through the wax to reach the active site (Huang *et al.*, 1988).

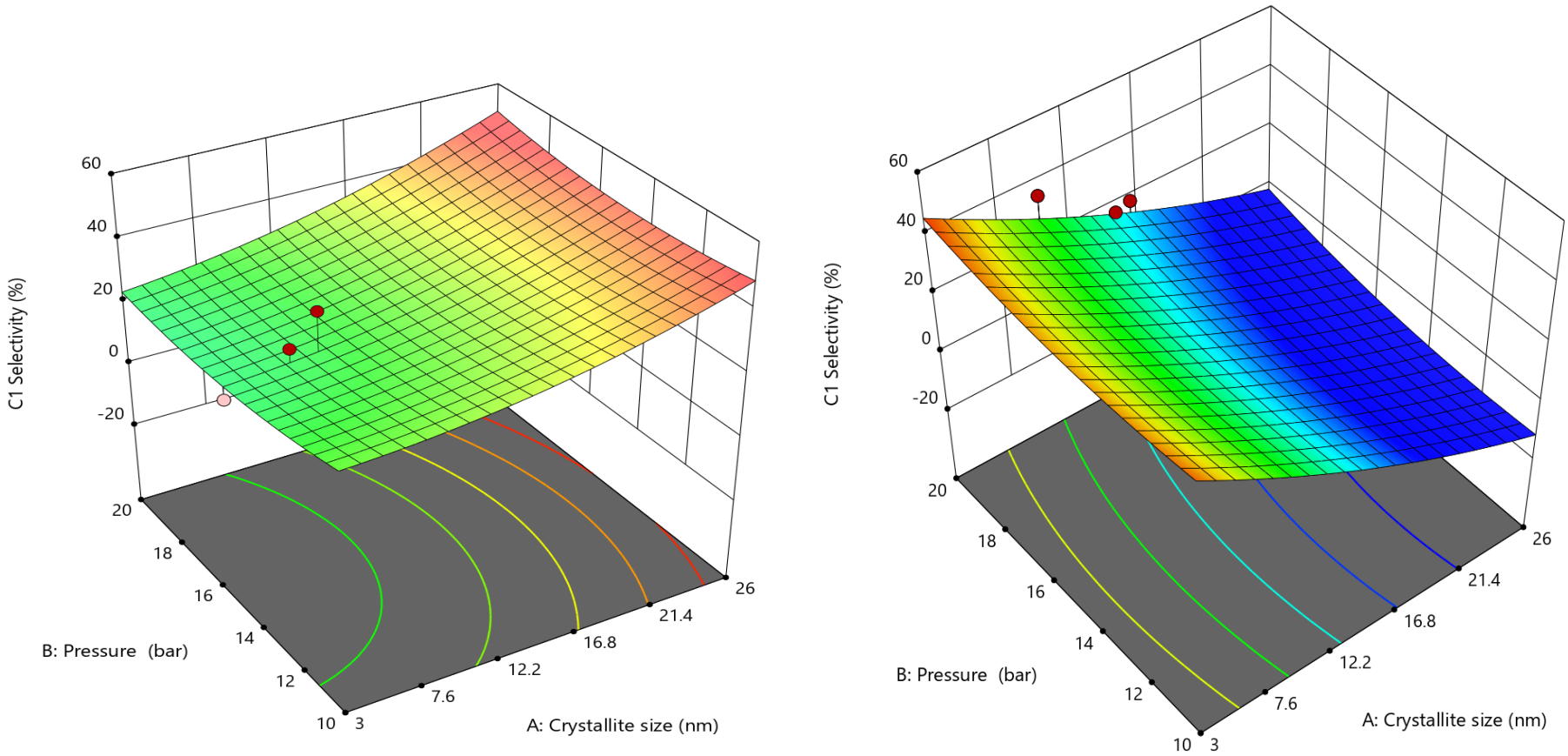

(a) (b)

Figure 5.4: Effect of temperature on C_1 selectivity at (a) a low temperature - 200 ºC; (b) a high temperature - 270 ºC

The dissolution and diffusion of reactants into the pore causes a larger hydrogen concentration inside the porous catalyst and an increase in the H_2/CO ratio since H_2 diffuses considerably more rapidly than CO. This supports the chain termination process and affects product selectivity, which frequently results in high C_1 selectivity. Increasing the reaction temperature causes an increase in the reactant dissolution process, particularly CO, which favours chain propagation. Moreover, smaller crystallite size results in more active sites, according to (Fang *et al.*, 2020). When the crystallite size is reduced, the number of exposed cobalt atoms on the support surface increases, making it easier for CoO to form, which results in high C_1 selectivity (Fang *et al.*, 2020).

An increase in pressure along with an increase in crystallite size resulted in a slight decrease in the production of C_1 molecules at a high temperature of 270 ºC. (See **Figure 5.5**.) A plausible reason before this is that increased pressure in the system forces free-moving molecules to compact together, thus promoting chain propagation. In accordance with Le Chatelier's principle, raising the pressure allows the system to regain equilibrium, which results in a decrease in C_1 and an increase in heavy C_{5+}.

Figure 5.5 shows that at both a high and a low temperature (200 – 270), and regardless of pressure fluctuation, significantly high levels of C_1 are noticed with: a high temperature and a small crystallite size; a low temperature and a large crystallite size. Minimal C_1 generation is noted with a high temperature (270 ºC) and a large crystallite size (26 nm). This shows that temperature had an effect on either conversion to light hydrocarbons or conversion to heavy hydrocarbons.

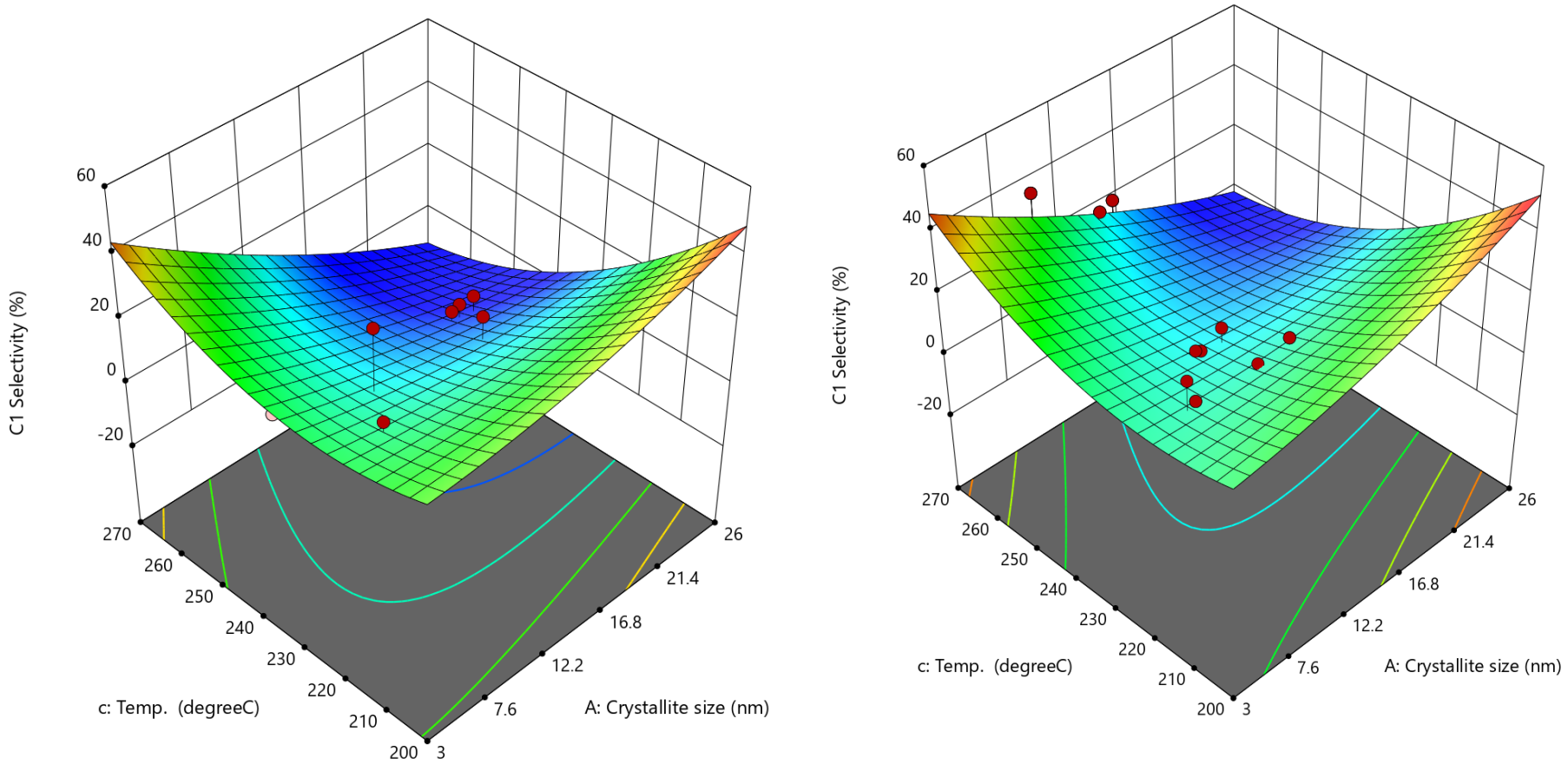

(a) (b)

Figure 5.5: Effect of pressure on C_1 selectivity at: (a) a low pressure - 5 bar (g); (b) a high pressure - 20 bar (g)

5.4.3. Model of selectivity for C_2-C_4

The proportion of low-weight hydrocarbon is expressed as a percentage of C_2-C_4, and has little correlation with individual variables. Crystallite size and pressure affect C_2-C_4 production quadratically on an individual basis. The temperature has a negative impact on C_2-C_4 production. Experimental data analysed using ANOVA showed that: the quadratic effect of crystallite size and pressure had a significant impact on C_2-C_4 generation; the quadratic model had lower R^2 values due to the lack of a fit test and model summary statistics.

The quadratic model was used to investigate the effect of independent factors on C_2-C_4 production, **Equation 5.7** shows the mathematical equation in terms of factors:

$$S_{C_2-C_4} = \begin{matrix} +551.70634 - 2.02503a - 21.32657b - 3.08382c - 0.051173ab - 0.008965ac + 0.035672bc \\ + 0.155881a^2 + 0.486340b^2 + 0.005274c^2 \end{matrix} \quad (5.7)$$

Where:

a- Crystallite size

b- Reaction pressure

c- Reaction temperature.

Even though only the quadratic effect of crystallite size and pressure are significant, the sub-plot ($p < 0.0001$) and the whole plot ($p < 0.05$) are statistically significant, according to the ANOVA results. Crystallite size has a significant quadratic effect on C_2-C_4 formation.

Figure 5.6 illustrates the adverse impact of temperature when the interactions of temperature and crystallite size are taken into consideration. As the temperature rises, the generation of C_2 – C_4 decreases, which demonstrates how temperature can have a negative impact, therefore appropriate conditions needs to be selected. In addition, the interaction between crystallite size and temperature exhibited a negative coefficient, which suggests a relationship to the response that is inversely proportional.

Figure 5.7 shows that an increase in chain propagation of the C_2-C_4 molecules begins to take place when the pressure is increased. Exactly the same behavior can be seen in case of Qiu et al., (2017). During the FT process, cobalt crystallites of a consistently small size adsorb reactants into a confined matrix with high efficiency, which lowers the likelihood of cobalt crystallite clustering and intermediate desorption significantly (Qiu et al., 2017). This, in turn, results in favorable selectivity for heavier hydrocarbons.

It is expected that an increase in pressure would cause the balance to move toward the generation of more viscous products and more C_{5+} products. As less viscous wax favors chain propagation, the subsequent dissolution of CO and H_2 would serve as a wax plasticizer, resulting in an increase in heavy hydrocarbons.

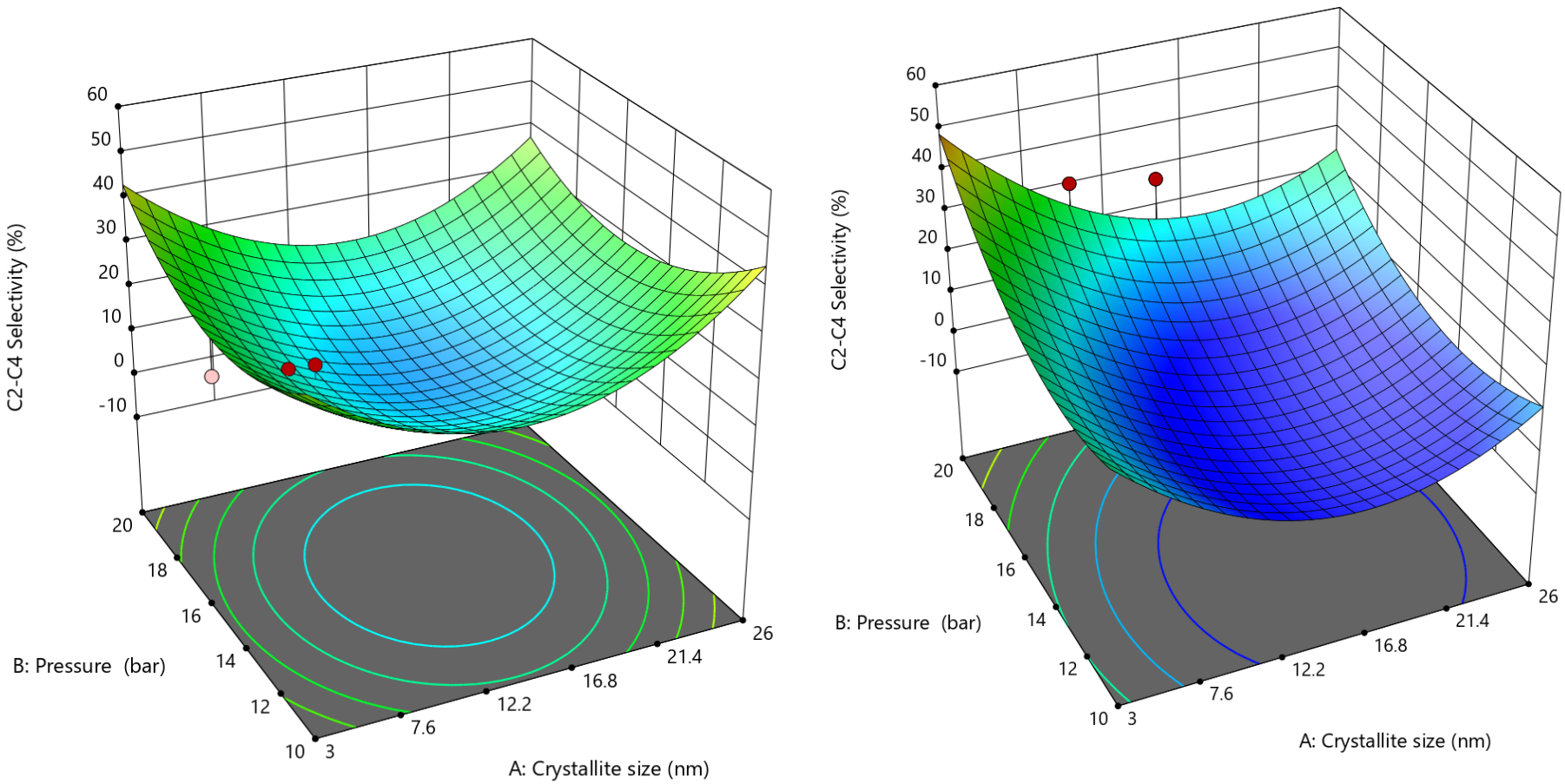

(a) (b)

Figure 5.6: Effect of temperature on C_2-C_4 selectivity at: (a) a low-temperature - 200 ºC; (b) a high-temperature - 270 ºC

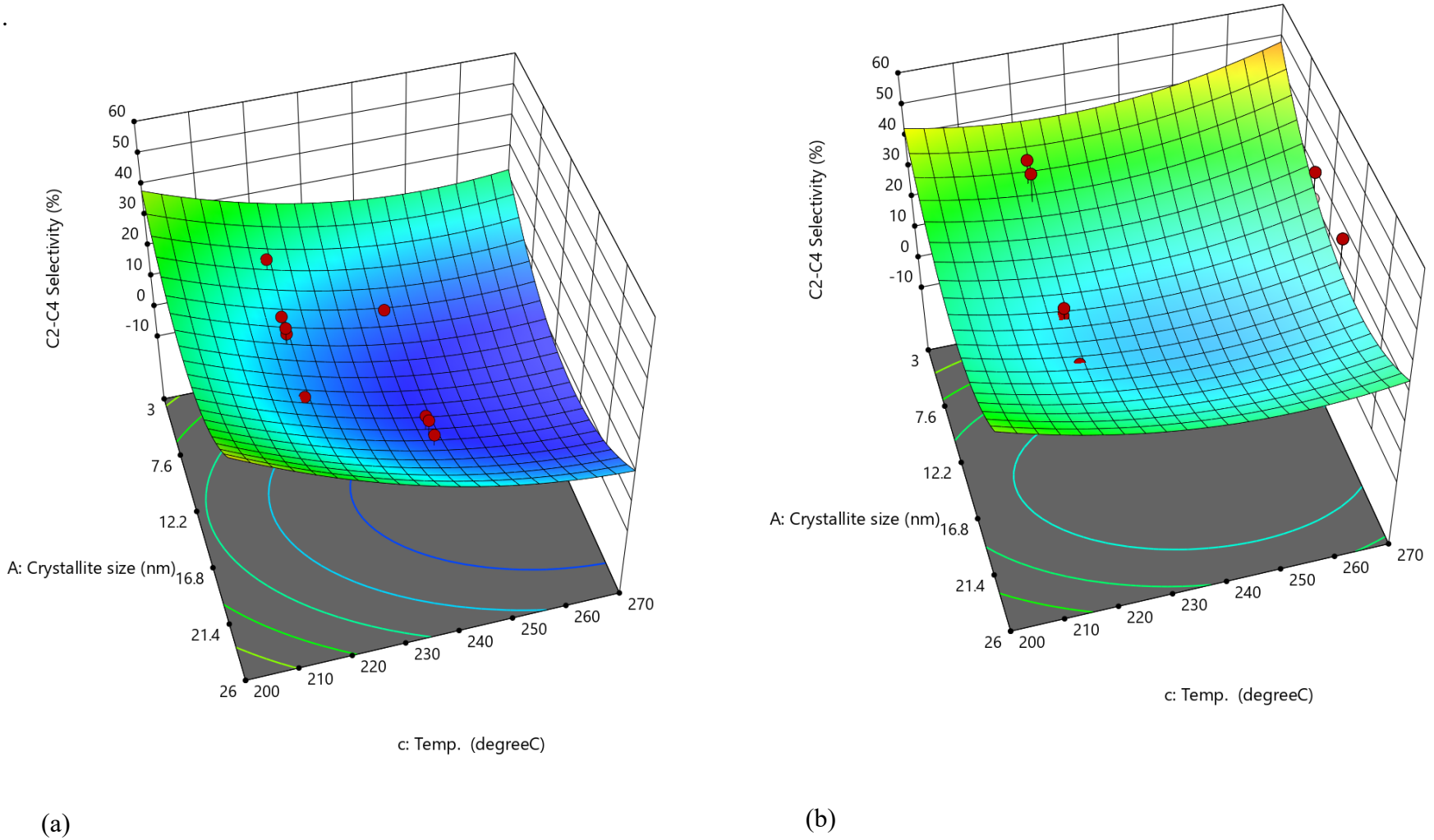

Figure 5.7: Effect of pressure on C_2-C_4 selectivity at: (a) a low pressure - 5 barg; (b) a high pressure - 20 bar

The effect of both temperature and pressure show that the desired product generation (C_2-C_4) is achieved at size extremes of crystallite - whether small or large. In order to produce more C_2-C_4, optimal operation is required at a low pressure (5 bar_g) and a low temperature (200 °C), as the crystallite effect will not be significant. A high temperature is required (270 °C) at a high pressure (20 bar_g), regardless of the size of the crystallite. The study done by Wang et al. (2021) yielded the required products when the cobalt crystallite measured an average 9.9nm, which corresponds to the same range observed on the RSM diagrams in this study. The equilibrium of C_2-C_4 seems to shift as the size of the crystallite is moved from extreme large to extremely low. The three groups of products (C_1, C_2-C_4 and C_{5+}) tend to behave antagonistically, depending on the parameters employed.

5.4.4. Model of selectivity for C_{5+}

The quadratic model was used to examine how the **independent factors (crystallite size, pressure and temperature**) affected the production of C_{5+}. Model terms were deemed significant if the P-value was less than 0.0500. In this scenario, important model terms include b, c, ac, a^2, b^2 and c^2. Model terms with a value less than 0.1000 are considered to be irrelevant. The findings of the ANOVA sub-plot ($p < 0.0001$) and whole-plot ($p < 0.05$) demonstrated their statistical significance. Based on their individual effect, pressure and temperature are both important variables that affect the production of products, and both are significant in their own right.

Equation 5.8 illustrates the mathematical equation in terms of factors:

Model of selectivity for C_{5+}:

$$S_{C_{5+}} = \begin{array}{l} -1015.84237 - 6.70152a + 28.95110b + 7.58213c + 0.014172ab + 0.054825ac \\ - 0.048173bc - 0.187267a^2 - 0.633187b^2 - 0.015316c^2 \end{array} \quad (5.8)$$

Where:

a- Crystallite size (nm)

b- Reaction pressure (bar)

c- Reaction temperature (°C).

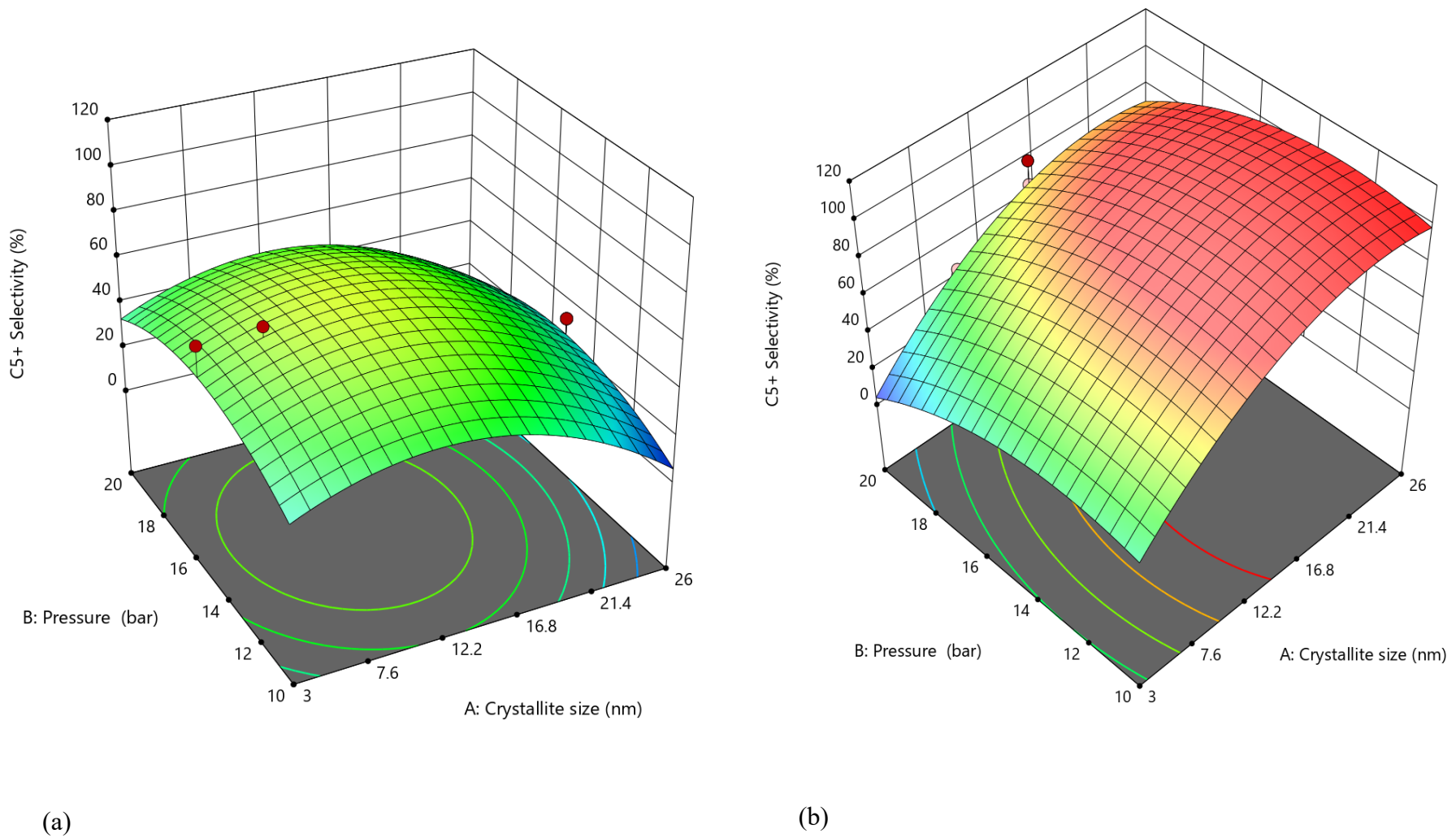

(a) (b)

Figure 5.8: Effect of temperature on C_{5+} selectivity at: (a) a low temperature - 200 ^{o}C; (b) a high temperature - 270 ^{o}C

According to the experimental results, C_{5+} selectivity showed an unusual increase with an increase in temperature. In general, FTS results in heavy products at a low temperature with a high straight-chain paraffin content. A high temperature result in lighter products with a higher straight-chain paraffin content, as well as secondary reactions like chain cessation and short term chain termination. A low temperature increases the wax yield considerably, while reducing light gas output.

When the reaction temperature and crystallite content were increased, the rate of C_{5+} generation increased in an exponential fashion. However, a linear rise in both crystallite content and temperature resulted in an increase in C_{5+} selectivity. Increasing the temperature when there was a low crystallite content resulted in a decrease in the amount of C_{5+} produced. (**See Figure 5.8 a and b**.) Qiu et al. (2017) attributed this to controlled particle size.

Selectivity for C_1 increased with reaction temperature at low crystallite sizes, whereas for C_{5+} increasing temperature enhances productivity with a larger crystallite size. When Qiu et al. (2017) and Liu et al. (2017) findings were compared, small crystallite sizes led to reduced CO hydrogenation activity and enhanced C_1 selectivity, whereas a larger crystallite size favoured C_{5+} products. The most likely rationale is related to fluid properties, specifically the rheological properties of wax in terms of reactant dissolution prior to reaching the reaction surface. With less viscous fluid properties, as a result of temperature change, more CO and H_2 diffuse through the wax, which reduces the chances of chain termination due to hydrogen influx near the active site. This resulted in the chain extension. When increasing the particle size, the catalytic activity increased, while the structural properties remained unchanged. Selectivity to C_{5+} decreased as particle size decreased at 270 ^{o}C. This is consistent with the findings of Wang et al. (2021), who revealed that increasing the size of the cobalt particle improves the turnover frequency for CO conversion, which could be due to increased CO site coverage. This then increases C_{5+} selectivity. Saib et al. (2002) shared the same results.

The viscosity of the reaction tends to rise when pressure is applied. It is hypothesised that the effect is caused by the convective free volume, which decreases when pressure is applied. This causes an increase in internal gas resistance, which raises viscosity and C_{5+} selectivity. The increase in viscosity is dependent on the specific C_{5+} compound. However, the effect of pressure is much smaller than the effect of temperature. The fluids in the process exhibit a minimal viscosity shift at moderate pressure, so the effect of pressure is frequently overlooked. Increased pressure has a greater impact on heavier C_{5+} hydrocarbons, which suggests that

pressure has a greater impact on C_{5+} products than on C_1 and C_2-C_4 Products. The pressure effect can be enhanced by branched waxes, which have more free intrinsic volume. As illustrated in **Figure 5.9,** as pressure increases, so C_{5+} selectivity increases.

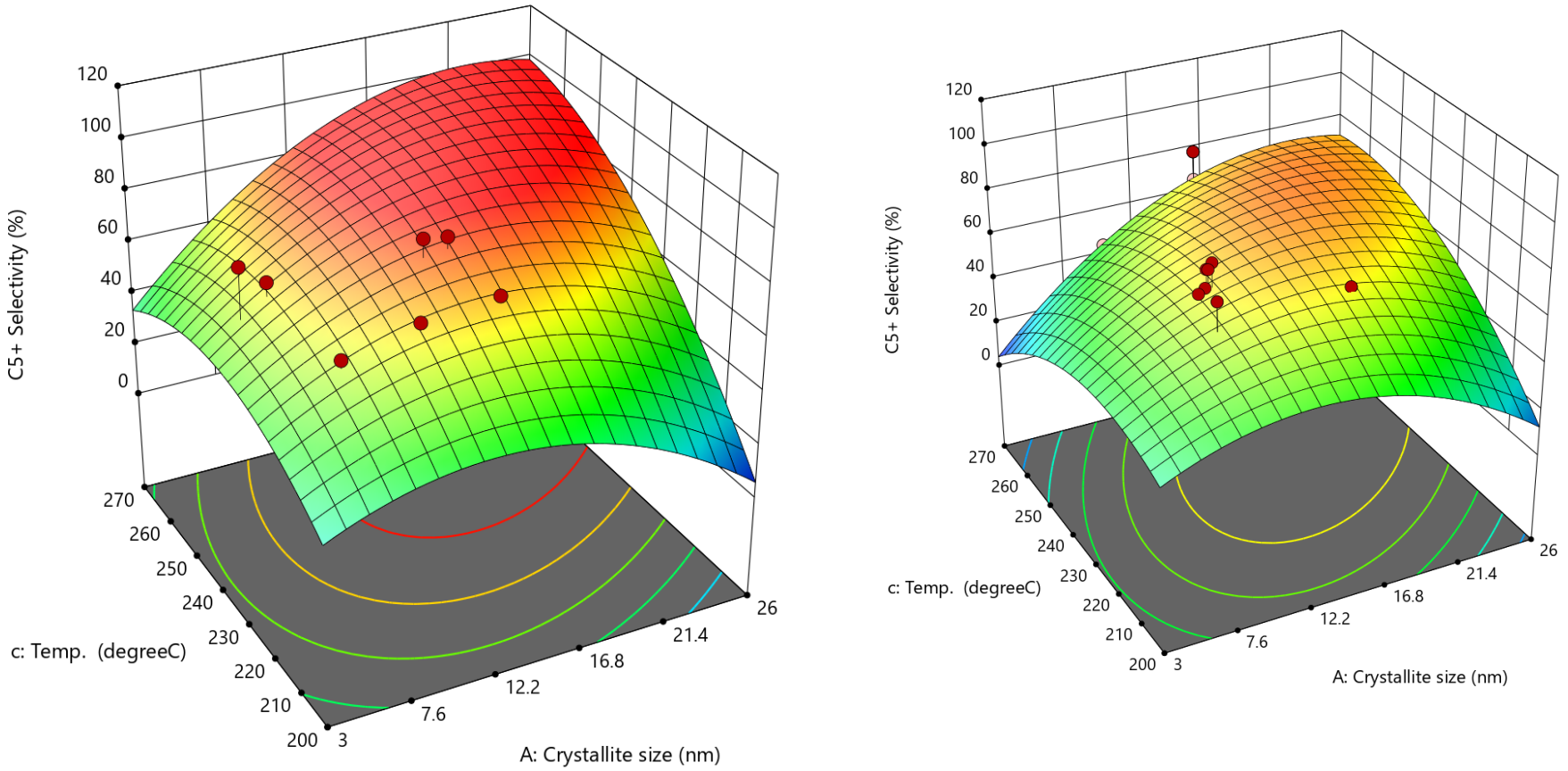

(a) (b)

Figure 5.9: Effect of pressure on C_{5+} selectivity at: (a) a low-pressure; (b) a high-pressure

5.5. Determining optimum conditions

An experiment was carried out with the parameters that were recommended by the model in order to determine whether or not the optimum conditions that were provided by the model were reliable. The conditions proposed for use in the confirmatory experiment were as follows: crystallite size = 11nm; pressure = 10 Bar_g; temperature = 220 °C. **Figure 5.10** illustrates the optimum conditions.

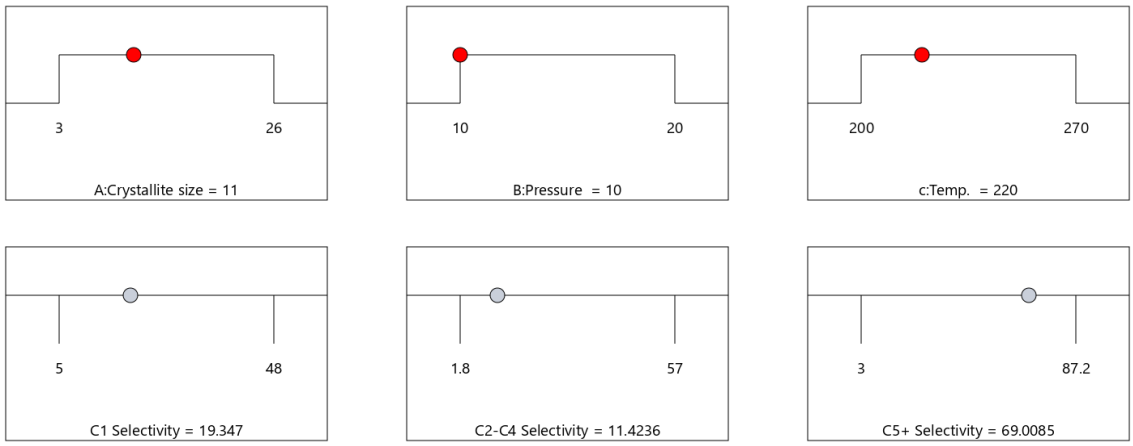

Figure 5.10: Optimized design parameters for the proposed FT process

Of the catalysts manufactured with varying particle sizes for the support, the three with the most similar crystallite size were used, i.e.: -75 to +53 µm; -53 to +38 µm; less than 25 µm. Run 1 represents particles with a catalyst support size class of -75 to +53 mm. Run 2 represents the support size class -53 to +38 µm, and run 3 the support particle size class of less than 25 µm. The results shown are the average of the runs carried out using the same experimental conditions. During optimization, the required set parameters were set so as to prioritize higher C_{5+} generation. As shown in **Table 5.5,** the model can be considered to fit the experimental data under these experimental conditions. It was demonstrated that the optimum conditions for achieving the required high C_{5+} are large crystallites (11 nm), a low temperature (220 ^oC) and a somewhat high pressure (10 bar_g). Furthermore, the optimization process and test runs prove that the experimental design is replicable and reliable enough for use in predicting end products.

Table 5.5: Product generation at optimal conditions

Data Source	Run	Factor 1	Factor 2	Factor 3	Response 1		Response 2		Response 3	
		Crystallite size	Pressure	Temperature	C_1		C_2-C_4		C_{5+}	
		nm	bar	°C	Predicted	Actual	Predicted	Actual	Predicted	Actual
Experiment	1	9.24	10.0	220	19.96	19.79	13.60	14.17	65.99	66.08
	2	9.22	10.0	220	19.97	19.79	13.62	14.19	65.95	66.05
	3	8.27	10.0	220	20.84	20.12	15.17	15.72	63.84	64.21
Model		**11**	**10.0**	**220**	**19.35**	**19.38**	**11.42**	**11.77**	**69.01**	**68.99**

The outcomes of three FTS tests are provided in Table 1.5. An examination and comparison of these findings to the model's optimal values, leads to the conclusion that the results are reliable and that they can be replicated. Therefore, the factors that were selected were validated as being appropriate.

5.6. Conclusion

The phase of optimizing for specific product selectivity is illuminating. Consequently, a straightforward analysis of the output of DOE in respect of the design restrictions exposes the potential for the design to be modified in order to obtain the products that are wanted. The DOE was carried out in order to optimize the effectiveness of the cobalt-based FT catalyst and to ensure that the product groups remained in the required range.

The size of the crystallite, the temperature and the pressure at which the FT reaction takes place all play a role in determining the composition of the final product. Investigations into product distribution and yield expressed as a proportion of total hydrocarbons were carried out using RSM and estimated distribution models, respectively. The effect of system settings and model

parameters on the projected product distribution was therefore identified, and it was established that this distribution is a function of the operating conditions.

The relevance of the parameters investigated in the experiment was determined statistically by plotting the findings of the experiment as probability distributions. When the operating settings were adjusted, there was a discernible shift in the selectivity. As the parameters were altered, there was a corresponding shift in the average number of carbon atoms in the hydrocarbon derivatives. The cobalt crystallite size, temperature and pressure were all found to be statistically significant parameters that have a significant impact on the formation of C_1 optimum, C_2-C_4 and C_{5+}. However, pressure was statistically inconsequential and had no significant impact on the formation of C_1 optimum, C_2-C_4 and C_{5+}.

The significant factors were optimized using RSM, so as to identify the best experimental conditions. The parameters of crystallite size = 11 nm, pressure = 10 Bar and temperature = 220 °C provided the best product distribution under the experimental conditions considered. In order to confirm this, confirmatory tests were conducted using almost identical settings. Optimum conditions were obtained based on the preference of the author, which was maximum C_{5+} output.

The following conclusions were drawn from the results:

- The statistical method chosen, and the experimental design approach used helped to identify the statistically significant and insignificant components under investigation.
- High R^2 values indicate that the model created was able to provide a reasonably accurate response estimate for the system in the area studied.
- Statistical analysis of the normal probability plot showed the significant influence of the parameters and their distribution.
- Under these experimental conditions, the model fits the experimental data quite well. It can be adapted to fit light hydrocarbons, which were not studied in this work, but which were discovered during the process.

References

Cheng, Q. *et al.* (2018) 'Confined small-sized cobalt catalysts stimulate carbon-chain growth reversely by modifying ASF law of Fischer–Tropsch synthesis', *Nature Communications*, 9(1). Available at: https://doi.org/10.1038/s41467-018-05755-8.

Dry, M.E. (2002) 'The Fischer–Tropsch process: 1950–2000', *Catalysis Today*, 71(3–4), pp. 227–241. Available at: https://doi.org/10.1016/S0920-5861(01)00453-9.

Erbach, T., Fan, L. and Kraber, S. (2004) 'How experimental design optimizes assay automation', chromeextension://efaidnbmnnnibpcajpcglclefindmkaj/https://cdnm.statease.com/pubs/optimizeassays.pdf

Fang, X. *et al.* (2020) 'Particle-size-dependent methane selectivity evolution in cobalt-based Fischer-Tropsch Synthesis', *ACS Catalysis*, 10(4), pp. 2799–2816. Available at: https://doi.org/10.1021/acscatal.9b05371.

Filliben, J.J. (1975) 'The probability plot correlation coefficient test for normality', *Technometrics*, pp. 111–117. Available at: https://doi.org/10.1080/00401706.1975.10489279.

Huang, S.H. *et al.* (1988) 'Solubility of synthesis gases in heavy N-paraffins and Fischer-Tropsch wax', *Industrial and Engineering Chemistry Research*, 27(1), pp. 162–169. Available at: https://doi.org/10.1021/ie00073a030.

Khodakov, A.Y., Chu, W. and Fongarland, P. (2007) 'Advances in the development of novel cobalt Fischer-Tropsch catalysts for synthesis of long-chain hydrocarbons and clean fuels', *Chemical Reviews*, 107(5), pp. 1692–1744. Available at: https://doi.org/10.1021/CR050972V/ASSET/CR050972V.FP.PNG_V03.

Khorashadizadeh, M., Atashi, H. and Mirzaei, A.A. (2017) 'Process conditions effects on Fischer–Tropsch product selectivity: Modeling and optimization through a time and cost-efficient scenario using a limited data size', *Journal of the Taiwan Institute of Chemical Engineers*, 80, pp. 709–719. Available at: https://doi.org/10.1016/j.jtice.2017.09.006.

Kuller, M. *et al.* (2017) 'Framing water sensitive urban design as part of the urban form: A critical review of tools for best planning practice', *Environmental Modelling and Software*, 96, pp. 265–

282. Available at: https://doi.org/10.1016/j.envsoft.2017.07.003.

Li, L. *et al.* (2021) 'Wax separated effectively from Fischer-Tropsch wax residue by solvent desorption: Thermodynamic and kinetic analysis', *Applied Sciences (Switzerland)*, 11(16). Available at: https://doi.org/10.3390/APP11167745.

Lira, E. *et al.* (2008) 'HMS mesoporous silica as cobalt support for the Fischer-Tropsch Synthesis: Pretreatment, cobalt loading and particle size effects', *Journal of Molecular Catalysis A: Chemical*, 281(1–2), pp. 146–153. Available at: https://doi.org/10.1016/j.molcata.2007.11.014.

Liu, J.X. *et al.* (2017) 'Particle size and crystal phase effects in Fischer-Tropsch catalysts', *Engineering*, 3(4), pp. 467–476. Available at: https://doi.org/10.1016/J.ENG.2017.04.012.

Makhura, E. *et al.* (2019) 'Effect of the operation parameters on the Fischer Tropsch synthesis process using different reactors', *Procedia Manufacturing*, 35, pp. 349–355. Available at: https://doi.org/10.1016/J.PROMFG.2019.05.051.

Martínez, A. *et al.* (2003) 'Fischer–Tropsch synthesis of hydrocarbons over mesoporous Co/SBA-15 catalysts: The influence of metal loading, cobalt precursor, and promoters', *Journal of Catalysis*, 220(2), pp. 486–499. Available at: https://doi.org/10.1016/S0021-9517(03)00289-6.

Merino, D. *et al.* (2016) 'On the way to a more open porous network of a Co-Re/Al2O3 catalyst for Fischer-Tropsch Synthesis: Pore size and particle size effects on its performance', *Topics in Catalysis*, 59(2–4), pp. 207–218. Available at: https://doi.org/10.1007/s11244-015-0436-3.

Montgomery, D.C. (2013) *Design and Analysis of Experiments*. 8th edn, *Copyright*. Arizona State University.

Mosayebi, A., Nasabi, M. and Abedini, R. (2019) 'Evaluation and modeling of Fischer-Tropsch synthesis in presence of a Co/ZrO2 catalyst', *Petroleum Science and Technology*, 37(23), pp. 2338–2349. Available at: https://doi.org/10.1080/10916466.2018.1522339.

Qiu, T. *et al.* (2017) 'SAPO-34 zeolite encapsulated Fe3C nanoparticles as highly selective Fischer-Tropsch catalysts for the production of light olefins', *Fuel*, 203, pp. 811–816. Available at: https://doi.org/10.1016/j.fuel.2017.05.043.

Saib, A.M., Claeys, M. and Van Steen, E. (2002) 'Silica supported cobalt Fischer-Tropsch

catalysts: Effect of pore diameter of support', *Catalysis Today*, 71(3–4), pp. 395–402. Available at: https://doi.org/10.1016/S0920-5861(01)00466-7.

Sedighi, B., Feyzi, M. and Joshaghani, M. (2016) 'Response surface methodology as an efficient tool for optimizing the Fischer-Tropsch process over a novel Fe-Mn nano catalyst', *RSC Advances*, 6(83), pp. 80099–80105. Available at: https://doi.org/10.1039/c6ra10678a.

Shafer, W.D. *et al.* (2019) 'Fischer–Tropsch: Product selectivity–The fingerprint of synthetic fuels', *Catalysts 2019, Vol. 9, Page 259*, 9(3), p. 259. Available at: https://doi.org/10.3390/CATAL9030259.

Shapiro, S.S. and Wilk, M.B. (1965) 'An analysis of Variance Test for Normality (complete samples)', *Biometrika*, 52(3/4), p. 591. Available at: https://doi.org/10.2307/2333709.

Song, D. and Li, J. (2006) 'Effect of catalyst pore size on the catalytic performance of silica supported cobalt Fischer-Tropsch catalysts', *Journal of Molecular Catalysis A: Chemical*, 247(1–2), pp. 206–212. Available at: https://doi.org/10.1016/j.molcata.2005.11.021.

Tijmensen, M.J.A. *et al.* (2002) 'Exploration of the possibilities for production of Fischer Tropsch liquids and power via biomass gasification', *Biomass and Bioenergy*, 23(2), pp. 129–152. Available at: https://doi.org/10.1016/S0961-9534(02)00037-5.

Van Steen, E. *et al.* (2018) 'Comparing a cobalt-based catalyst with iron-based catalysts for the Fischer-Tropsch XTL-process operating at high conversion', *Applied Catalysis A: General*, 549, pp. 51–59. Available at: https://doi.org/10.1016/J.APCATA.2017.09.019.Wang, H. *et al.* (2021) 'The effect of the particle size on Fischer-Tropsch synthesis for ZSM-5 zeolite supported cobalt-based catalysts.', *Chemical Communications (Cambridge, England)*, 57(99), pp. 13522–13525. Available at: https://doi.org/10.1039/D1CC04844A.

Witoon, T., Chareonpanich, M. and Limtrakul, J. (2011) 'Effect of hierarchical meso-macroporous silica supports on Fischer-Tropsch synthesis using cobalt catalyst', *Fuel Processing Technology*, 92(8), pp. 1498–1505. Available at: https://doi.org/10.1016/j.fuproc.2011.03.011.

Yang, J. *et al.* (2014) 'Fischer-Tropsch synthesis: A review of the effect of CO conversion on methane selectivity', *Applied Catalysis A: General*, 470, pp. 250–260. Available at: https://doi.org/10.1016/j.apcata.2013.10.061.

Zhang, Q. *et al.* (2014) 'Fischer-Tropsch catalysts for the production of hydrocarbon fuels with high selectivity', *ChemSusChem*, 7(5), pp. 1251–1264. Available at: https://doi.org/10.1002/cssc.201300797.

Ziaei, M. *et al.* (2020) 'Maximizing the profitability of integrated Fischer-Tropsch GTL process with ammonia and urea synthesis using response surface methodology', *Journal of CO2 Utilization*, 35, pp. 14–27. Available at: ht

Chapter 6: Effect on support particle size in Fischer-Tropsch Synthesis: The use of natural clinoptilolite as support

This work has been prepared in the form of a paper for future publication.

Abstract: Fischer-Tropsch (FT) coal/biomass-to-liquids projects have require a significant initial investment. The high price of the catalysts used is one area where costs could be reduced. This research explored the possibility of using clinoptilolite as a catalyst support to reduce costs without sacrificing performance. The as-received clinoptilolite was ground and sieved to yield different size classes. For this study, three size classes were investigated as the support for an FT catalyst: -75 to +53 μm; -53 to +38 μm; less than 25 μm. Using a fixed bed reactor, 10% cobalt supported on these various supports was synthesized and evaluated. Experiments carried out in the lab yielded information regarding the effect of particle size on the catalyst used in the Fischer–Tropsch synthesis (FTS). The maximum CO conversion obtained was 44.97% when using the -53 to +38 μm size class. A one-way analysis of variance (ANOVA) was performed, and then a post-hoc Bonferroni adjustment test was carried out, with the goal of determining whether or not the utilization of different support size classes had an effect on CO conversion. The results obtained indicated a significant difference in CO conversion, with P(T <=t) two-tail values ranging from 6.08×10^{-05} to 2.37×10^{-27}. At 220 ^{o}C and 10.85 bar(abs), methane selectivity ranged between 14.95 and 16.97% for the support class size studied, while C_2-C_4 selectivity ranged between 14.55 and 19.01 %, and C_{5+} selectivity ranged between 66.04 and 70.29 %. The acquired product selectivity results are equivalent to those reported in the literature, which validates the use of this support. These discoveries might be have valuable implications for the design of a catalyst that can be used in the coal/biomass to liquid process.

6.1. Introduction

Since their discovery in 1756, zeolites have been put to use in the chemical industry as catalysts, adsorbents, and ion exchangers in a variety of different applications (Li & Yu, 2021). Zeolites are a microporous crystalline mineral family. They are hydrated aluminosilicate minerals that form a three-dimensional framework from alumina (AlO_4) and silica (SiO_4) (Marantos, I., Christidis, G. E., & Ulmanu, 2012). The only type of zeolite that is mined in South Africa is clinoptilolite. The natural clinoptilolite that is mined in South Africa has a chemical composition with the molecular formula $(Na_{1.25}K_{1.6})(Ca_{0.49}Mg_{0.43})(Al_{5.14}Fe_{0.31})(Si_{25.67}Ti_{0.04})O_{62}$. This formula corresponds to a content composition of: 77.24% silica; 13.30% alumina; 0.23% hematite; 0.86% magnesium oxide; 1.40% calcium oxide;1.94%, sodium oxide; 3.78% potassium oxide; 0.14% titania; with the balance being non-essential trace elements (Gorimbo, 2011). Fe and Co catalysts supported on SiO_2, Al_2O_3, and TiO_2 are still commonly used in FTS. These are the primary components of natural clinoptilolite. Due to their exceptional and distinctive physical and chemical characteristics, researchers are attempting to investigate the potential of natural zeolites being used as a catalyst. Zeolites are abundant, affordable and environmentally-friendly, and there are also other benefits (Bish & Ming, 1955; Eroglu et al., 2017; Wahono et al., 2020).

A high conversion rate of up to 80–90% was achieved using natural zeolite as a catalytic support in the conversion of ethanol to gasoline, with aromatics being the principal product produced (Kristiani et al., 2017). Vrbková et al. (2021) used chloroacetic acid-treated montmorillonite as a catalyst to convert carvone into carvacrol. The study reported 95.5% selectivity to carvacrol and complete conversion of carvone (Vrbková et al., 2021). By adjusting a number of process variables, the researchers were able to produce 95.09 % biodiesel using natural zeolite from the Indonesian island of Pacitan as a catalytic support for the transesterification of palm oil to biodiesel (Kusuma et al., 2013). The natural Zr-Zeolite catalyst was also tested on glycerol acetylation with acetic acids for triacetin production, with positive results being obtained for triacetin selectivity and glycerol conversion, i.e. 26% and 94.3%, respectively (Cahyono et al., 2016).

The application of natural zeolites in FTS is uncommon, whereas the use of synthetic zeolites is widespread in other areas of research and industrial applications. Synthetic zeolites like ZSM-5 have been used in the FT process (Javed et al., 2020; Kang et al., 2008; De Klerk, 2008; Martínez et al., 2007).

Despite having an open-framework structure, natural zeolite is a bit of an after-thought in the literature, therefore the current effort intends to address the potential for it being used in the FT process. The current research investigated the feasibility of employing clinoptilolite as an alternative and cost-effective catalyst support in the FT process. The emphasis was on the effect of the size of the support particles on physicochemical properties and catalytic performance under various FT synthesis process conditions.

In FTS, methane is the lightest hydrocarbon product, as it has the highest degree of thermodynamic stability; however, it also has the lowest degree of industrial desirability. As a result, the goal was to develop a catalyst with a low degree of selectivity for methane. In this investigation, the sample groups of products (C_1, C_2-C_4, and C_{5+}) were selected in order to demonstrate how product selectivity depends on the size of the crystallite zeolite support.

6.2. Experimental section

Synthesis of 10wt%cobalt on clinoptilolite (10wt%Co/Clino for nomenclature)

Ring pulverisers were used to reduce the size of natural zeolite (clinoptilolite) samples obtained from Pratley Minerals in Krugersdorp, South Africa. The zeolites were ground to a powder and then passed through a series of sieves with a progressively smaller mesh sizes starting with a range of -212 to +150 μm, then proceeding to those with a range of -150 to +106 μm, then -106 to +75 μm, then -75 to +53 μm, then -53 to +38 μm, then -38 to +25 μm, and finally 25μm. Although it is not possible to use small particles (less than 1 mm) in large-scale industrial fixed bed reactors, due to the severe pressure loss that would result, this limitation is not nearly as significant for laboratory scale reactors because they are shorter in length. Using small particles has a number of benefits, one of which is a reduction in intraparticle transport resistance, which is critical for the maintenance of low CH_4 selectivity (Mandić et al., 2017).

Only three of the seven clinoptilolite size classes were chosen for testing as a support in the development of a cobalt catalyst, i.e.: -75 to +53 μm; -53 to +38 μm; and less than 25 μm. The basis for this decision was determined by preliminary characterisation experiments, which also revealed substantial differences in activation energy levels and particle size. Additionally, the rig used in this study only had three reactors, which had to run simultaneously, this restricted the number of samples that could be tested.

The correct amount of cobalt was deposited onto each of the individual clinoptilolite supports to yield 10%wtCo/Clino. The cobalt (II) nitrate hexahydrate used to synthesise the catalyst was purchased from Sigma-Aldrich. 100g of pure clinoptilolite (of different size classes) was placed in a beaker. 54.82 g of cobalt (II) nitrate hexahydrate was measured and diluted in 70 ml of ethanol (based on the pore volume of the clinoptilolite support). A magnetic stirrer was used to mix the solution for the entirety of the allotted time (30 minutes). Droplets of the solution were then added to the clinoptilolite, and it was stirred with a magnetic stirrer for an hour. It was then sonicated ultrasonically for half-an-hour. The sample was allowed to air dry at ambient temperature for 24 hours before being heated to 110 ºC for the final 6 hours of the drying process. The dried sample was calcined in air at a temperature of 350 ºC degrees for 6 hours.

6.2. Material characterization

6.2.1. X-ray diffraction

Powder XRD was performed with a Rigaku Ultima IV X-ray diffractometer at a scanning speed of 0.5º/min, and the 2-theta angle ranged from 10º to 90º to obtain the diffraction patterns of the sample. The voltage and current of the x-ray source were set to 40 kV and 30 mA, respectively. A CuK (l=1.54) x-ray generator target with a maximum power of 3 kW and a goniometer that can measure 2-theta angles from 0° to 162° were included in the XRD apparatus.

6.2.2. X-ray fluorescence spectrometry

Using the Rigaku ZSX Primus II with SQX analysis software, X-ray fluorescence spectrometry (XRF) analysis was carried out to ascertain the chemical makeup of the sample. 10 g samples were weighed, combined with 2 g of binder and pelletized under 20 tonnes of pressure to create pellets that were 35 mm in diameter and 2.5 mm thick. After the pellets had been prepared, they were placed in the spectrometer for chemical analysis.

6.2.3. Scanning electron spectroscopy-energy dispersive spectroscopy

A TESCAN: Vega 3X was used for SEM examination, with an electron source with a tungsten filament being used. The backscatter and secondary detectors, coupled with a high voltage of 20 kV, were utilized to make an image of the surface morphology of the material. In order to take images at a range of magnifications, the Vega program was utilized. The energy dispersive X-ray spectroscopy (EDS) analysis done using Oxford's INCA software determined the chemical composition of the chosen locations.

6.2.4. Malvern Mastersizer 3000 used to measure particle size

A Malvern Mastersizer 3000 was used in this study to determine the particle size distribution (PSD). With this device, laser diffraction is used to determine particle size. The method is based on the inverse relationship between the diffraction angle of light and the sizer of the particle (Bowen, 2002; Fisher et al., 2017; Gazi et al., 2021). A statistical sampling technique had to be used to ensure that the PSD was truly representative of the samples used in the study. Given the relatively small size of the samples needed to achieve the target obscuration level (usually 10-20%), this was of paramount importance. A sample size of about 2 to 3 grams was used in the experiments, as it was considered adequate for determining the appropriate level of obscuration. Because of this, the procedures used to sub-sample such a small amount determine how representative the sample is.

As part of the method used, the sample was initially divided into a number of smaller sub-samples, each weighing approximately 10 grams. These sub-samples were then successively split using small 10-way rotary splitters.

To ensure consistency, the mixture was homogenized by hand with a spatula after each 10 g sub-sample was transformed into a thick paste with water. The conning and quartering method was then used to divide the paste into portions weighing roughly 2.5 g each. The 2.5-g weight was selected to guarantee that "obscuration" was within the acceptable range. (The term "obscuration" relates to the sample's level of optical concentration.)

The actual PSD measurements were then carried out using the newly developed standard operating procedure (SOP). For each run, the sub-sample was added to the 600 ml of water contained within the Hydro LV, while the agitator was turning at approximately 2000 rpm. Sonication was used on the sample, so that the particles could be measured without being clumped together. The SOP was designed in such a way that three repeat measurements were conducted throughout a cycle, and the average PSD and the related statistics were determined at the end of the cycle. For purposes of comparison and evaluating the precision of the sample splitting procedure, three repeat measurements were taken for each sample (from a variety of sub-samples weighing 2.5 grams). These measurements were taken three times.

6.2.5. Temperature programmed reduction study

Micromeritics Auto Chem II equipment was used to do the temperature programmed reduction (TPR) experiments. A 50 mg sample of the catalyst was placed within a quartz tubular reactor, whose temperature was continually monitored by a thermocouple. A furnace was used for heating purpose. Before the TPR test, the calcined catalyst was flushed with high-purity argon at 200 ^{o}C for 30 minutes to eliminate water and other impurities. It was allowed to cool to room temperature, and a 5% H_2/Ar mixture was then introduced into the chamber, and the temperature increased at a rate of 10 ^{o}C/min from 50 to 850 ^{o}C. Three Brooks mass flow controllers were used to regulate the

amount of gas flowing through the reactor. A computer automatically recorded the quantity of H_2 consumed and the TCD signal.

6.2.6. Evaluation of FT performance

The FTS utilized a fixed-bed microreactor with an interior diameter of 1.6 cm and a length of 25 cm. A gas cylinder containing syngas and a mixture of $H_2/CO/N_2$ (purity: 99.99; 60/30/10 vol. %) was utilised to feed the reactant gas stream to the FT reactor loaded with the prepared catalyst, at a flow rate of 10 mL/min and pressure of 10 bar(g). In order to achieve precise mass balance calculations, N_2 was used as an internal standard. Three catalysts weighing 1.0 grams with 10% Co loading were reduced in-situ for 16 hours at 350 °C with pure hydrogen (ca. 99.99%). After the reduction stage, the temperature of the reactor was lowered to the temperature of the surrounding air while nitrogen was flowing through it. The temperature was then raised to 220 °C while synthesis gas was flowing through it at a pressure of 10.85 bars (abs). The wax collection system consisted of a hot trap that was positioned directly after the reactor. It was kept at 150 °C. The oil and water mixture were collected in a second trap that was held at room temperature. After the reactor, all the gas lines were kept at 100 °C. A metering valve was used to control the flow while a bubble meter was used for the flow measurements. Online gas chromatography was used for online analysis of the product stream. H_2, N_2, and CO were measured using a thermal conductivity detector (TCD) with a Porapak Q packed column (1.50 m long and 3 mm in diameter). To examine the hydrocarbons online, a flame ionization detector (FID) with a Porapak Q packed column was employed.

6.2.7. FTS Calculations

Quantitative analysis was performed on the information that was obtained from the online GC. As an internal reference for the measurements of the TCD data, the nitrogen (with a 10 vol percent concentration of N_2) that was present in the syngas feed of the FT tests was used. Following the completion of the initial calculations, which consisted of determining the molar flow rates of the

reactants and various products, additional calculations were done. The formulas employed to compute the mass balance, including the conversion of the reactant CO are identical to those employed by earlier researchers, while the experimental method used was developed many years ago (Duvenhage, 1994).

The gathered online data was processed statistically. As the internal benchmark for the measurement of the TCD data, nitrogen (10 vol percent of N_2) present in the syngas feed of the FT tests was used. Further calculations were done after the molar flow rates of the reactants and various products had been established. The equations used to calculate the mass balance, including the conversion of the reactants CO and H_2 are provided below. These calculations are comparable to the ones made by earlier scholars (Mokoena, 2005; Gorimbo, 2016; Lu, 2011; Phadi, 2012; Yao, 2011). The experimentation technique has been used for decades.

$$\% CO = \frac{F_{in}X_{co,in} - F_{out}X_{co,out}}{F_{in}X_{co,in}} \quad (6.\ 3)$$

Where: $X_{co,in}$ denotes the CO molar fraction of in the reactor's gas feed; $X_{co,out}$ is the molar fraction of CO in the gas stream exiting the reactor.

The CO consumption rate is determined as follows:

$$r_{co} = \frac{F_{out}X_{co,out} - F_{in}X_{co,in}}{m_{cat}} \quad (64)$$

Where: r_{co} is the rate of CO consumption; mol/(min.gcat), m_{cat} is the number of grams of catalyst utilized in this reaction, and it is represented by the variable m cat.

The rate of production of gas product θ_i, mol/(min.gcat) can be calculated as follows:

$$r_{\theta_i} = \frac{F_{out} X_{\theta_{i,out}}}{m_{cat}} \quad (6.5)$$

Where: $X_{\theta_{i,out}}$ represents the molar fraction of the fraction of θ_i in the gas stream coming out of the reactor exit.

Based on the moles of carbon, the product selectivity was determined using the following calculation:

$$Sel\ (\theta) = \frac{[nC]_\theta}{-r_{co} \times t \times m_{cat}} \quad (6.4)$$

Where: the selectivity of the product θ is represented by the symbol Sel (θ); and $[nC]_\theta$ represent how many moles of carbon are present in the product.

The response factors that were published by Dietz (1967) were utilized in the calibration process in order to make the necessary adjustments to correct for the hydrocarbons areas based on the known areas of C_2H_4 (olefin) and C_2H_6 (paraffin). Most gas chromatographs use either flame ionization (FID) and thermal conductivity detectors (TCD), although there are many different kinds of detectors that can be used in gas chromatographs. In order to acquire quantitative results from the GC trace, correction factors have to be utilized, and the quantity of correction is determined by the response of a specific molecule to the detecting equipment (Dietz, 1967).

6.3. Results and discussion

6.3.1. X-ray diffraction measurements

The XRD patterns of cobalt for the three classes of clinoptilolite particle size tested are shown in Figure 6.1. Cobalt on clinoptilolite was found at intensity peaks located at 2theta = 31.05°, 38.35°, 45.88°, 56.31°, 60.48° and 66.68°, as shown in all the diffractograms. These peaks represent the 220, 222, 400, 422, 511, and 440 planes of cobalt oxide crystals, respectively.

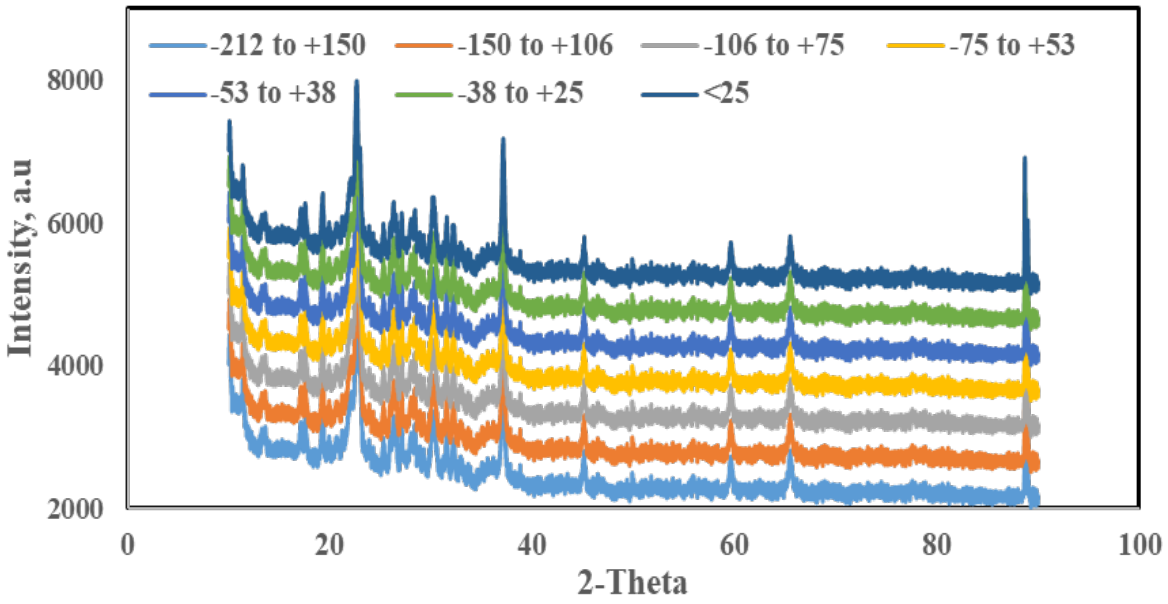

Figure 6.1: X-ray diffraction patterns for each clinoptilolite particle size classes

XRD peaks were used to verify the presence of Co_3O_4 crystallites. The measured particle size range did not generate any variations, as was anticipated. When the value of 2-theta is less than 40 degrees, there are just a few additional lines visible that show the clinoptilolite structure. The cobalt crystallites that form as a result of the use of support particles of different sizes may be different sizes. Consequently, the XRD peak width may widen or narrow, depending on the crystallite size. The Scherrer equation and the half-width of the XRD lines were used to calculate the average size of the crystallites.

Table 6.1: Cobalt loading and crystalline size determination

(Analysis was done in triplicate for each sample size class.)

Sieve size range (µm)	% Co content		Crystalline sizes (nm) Co_3O_4
	XRF	**SEM-EDS**	**XRD**
-75 to +53	10.23 ± 0.18	8.97 ± 0.92	8.27 ± 0.44
-53 to +38	9.88 ± 0.98	9.49 ± 0.73	11.24 ± 1.78
<25	9.98 ± 0.12	9.01 ± 0.42	9.24 ± 2.70

According to the findings of the XRD investigation, the Co_3O_4 crystallite size distribution that is supported on various clinoptilolite size classes falls between 8.27 ± 0.44 and 11.24 ± 1.78 nm. (See Table 6.1). The crystallite value was computed from the Scherrer equation using the Rietveld refinement. Crystallite size showed no trend for the size classes investigated. The statistical analysis of the data obtained from the literature shows that hydrogen chemisorption, X-ray diffraction and transmission electron microscopy (TEM) can all be used to measure crystallite size with identical precision (H_2-Chemisorption). Cobalt crystallite sizes were measured by Saib et al. (2002) using TEM and H_2 chemisorption, but no substantial changes were discovered. Measurements taken in previous research studies done by Cheng et al. (2018) and Bezemer et al. (2006) yielded the same results. The observations done of cobalt crystallites using XRD, TEM and H_2 chemisorption by Prieto et al. (2009) indicate that any piece of equipment can generate reliable outcomes; therefore, using just one method in this inquiry was acceptable.

6.3.2. Scanning electron microscope and particle size distribution discussion

Table 6.2: Particle size measurements for various size classes and measurements performed using SEM

Sieve size range	SEM average size (µm)
-75 to +53 µm	59.52 ± 14.54
-53 to +38 µm	41.45 ± 10.98
<25 µm	13.39 ± 4.92

A SEM was used to examine the size, shape and cobalt dispersion of the clinoptilolite particles. To make things clearer, discrepancies within these size groups were tested using successive size classes. (The size classes are given in Table 6.2). After completing the manual measurements, SEM statistical analysis was performed. Examples of micrographs taken with a SEM, which display clinoptilolite particles at a magnification of 300x, are given in **Figure 6.3**. Two size classes are used to illustrate the measurement of particle size (-38 to +25 µm and -53 to +38 µm). The image depicts particles of varying shapes and sizes that fall within the dimensions specified for the particle size range.

The micrographs in **Figure 6.3** were taken at a lower magnification of 300x, which enables the real forms of the particles to be seen. These micrographs also show that the particle dimensions can vary from the assigned size class by several microns. There are no reported observations of particles that are homogeneous in size or shape; but observations of irregularly-sized and irregularly-shaped particles have been reported.

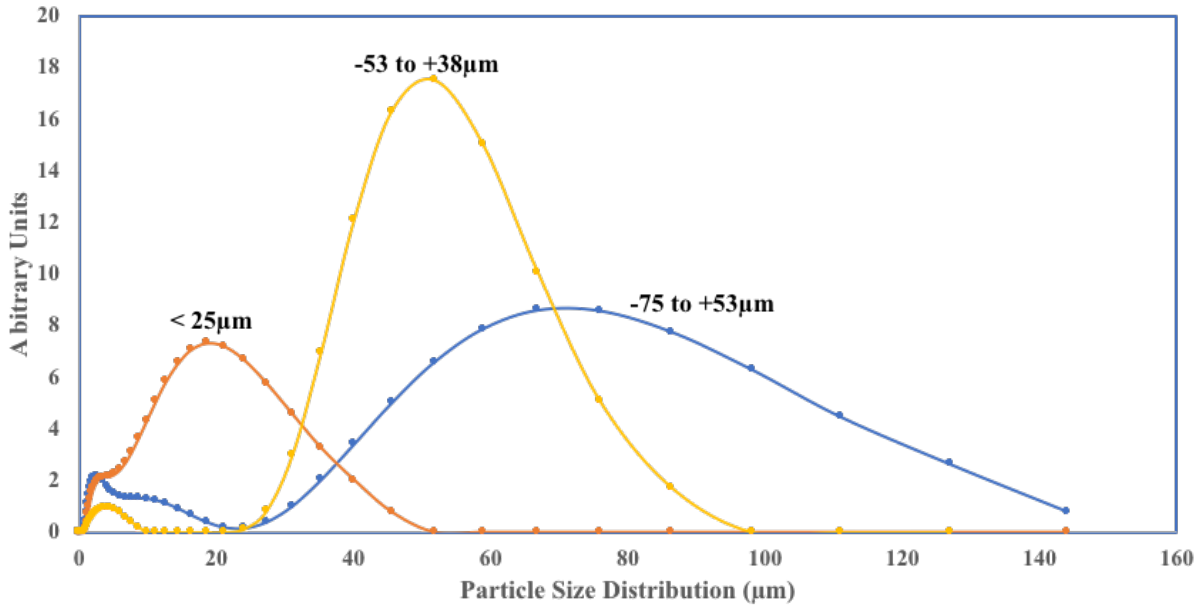

Figure 6.2: PSD analyzed using a Malvern Mastersizer 3000

The PSD analysis of various size classes done using the Malvern Mastersizer 3000 are shown in Figure 6.2. The size class used is also indicated. Even if the average particle size is within the acceptable range and the frequency distribution curves are symmetric, which indicates the presence of tiny coarse particles in each size class, it is difficult to obtain particles of just a single size class. (See Figure 6.3). This observation provides credibility to the SEM results obtained.

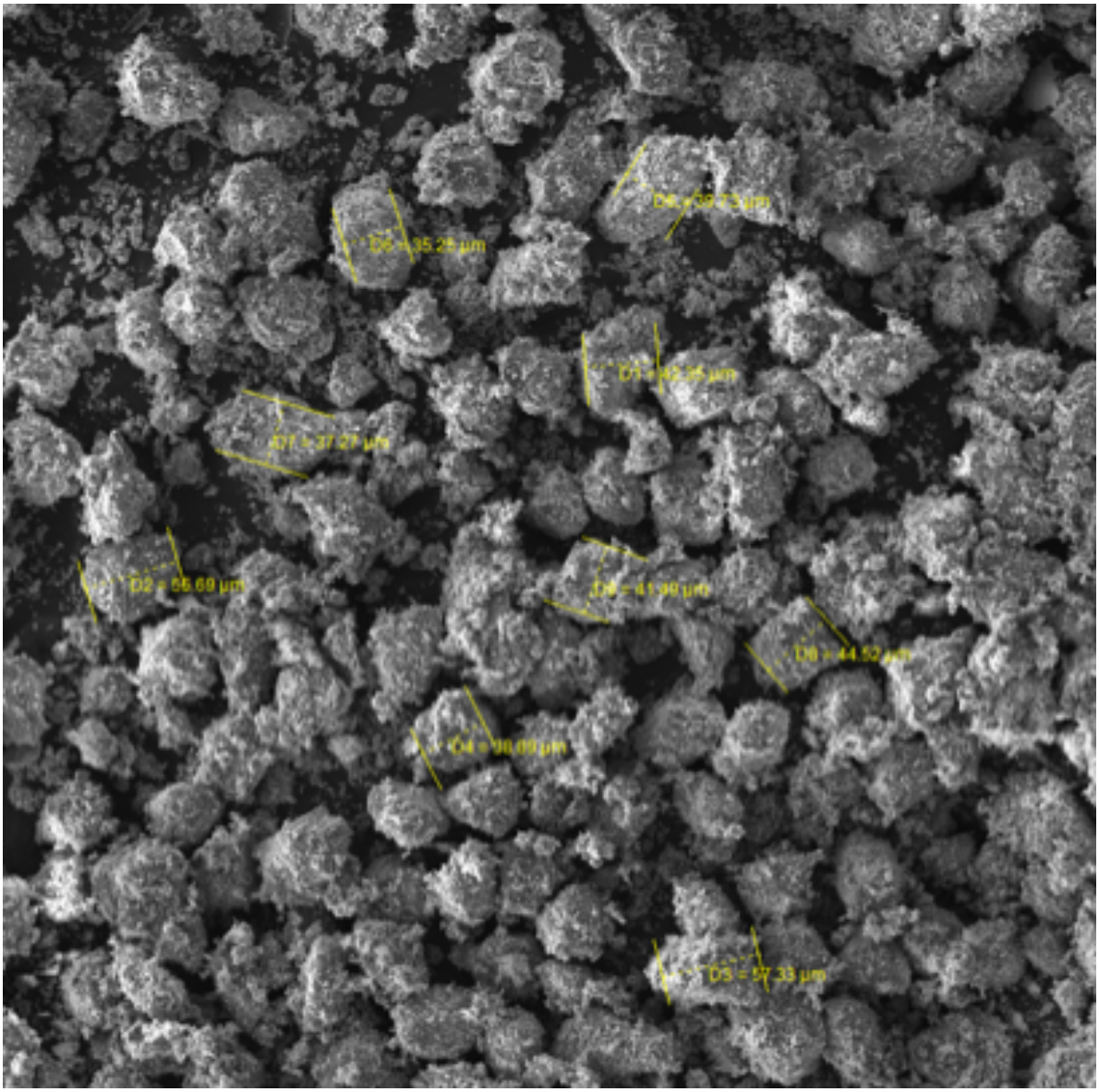

Figure 6.3: A micrograph captured with a SEM shows 300x magnification of clinoptilolite particles. It shows particles of various sizes and shapes that fall within the particle size range parameters.

Using SEM micrographs of particles in the range -53 to +38 μm as an illustrative example, it can be shown that the size and shape of particles vary (See Figure 6.3). This non-uniformity in shape allows larger size particles with a narrow form to slip through a sieve of 53 μm and then likely become stuck in a sieve of 38 μm. After obtaining these micrographs for the various size classes (75-53, 53-38 and 25 μm), statistical analysis was conducted to assess whether or not the SEM-observed particles varied significantly.

As shown in Figure 6.2 and the PSD from the Malvern Mastersizer 3000, most of the particles fall within the desired range. However, both SEM and Malvern tests confirmed the occurrence of particles outside the defined ranges, which increases the possibility of overlap. To address this, we conducted an Anova single factor test to determine whether or not there was a statistical difference between these particles. It indicated that there is. Since the computed F value (146.2023) is more than the Fcrit (2.665729), there is a mismatch between the three different size classes. In addition, the P-value of 4.66×10^{-44}, which is significantly lower than 0.05, demonstrates that there is a difference between the groups.

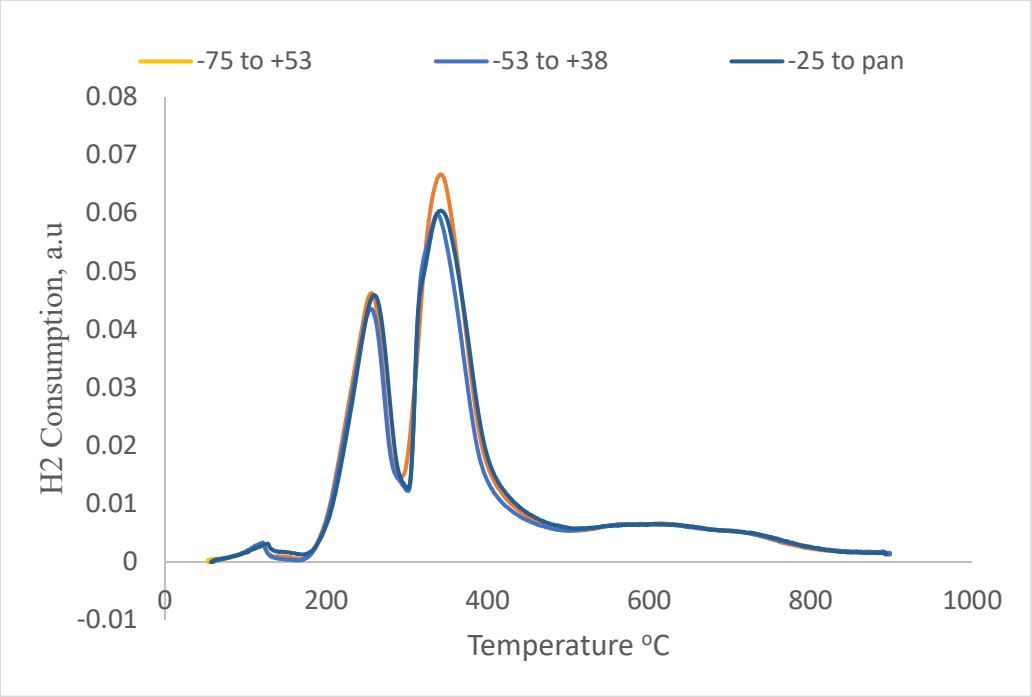

Figure 6.4: TPR profile of Co-catalyst supported on different size classes of clinoptilolite.

Table 6.3: Peak reduction temperatures for different catalyst size classes

	Peak Temperature (°C)	
Particle size (µm)	Peak 1	Peak 2
-25 to pan	264.24	353.12
-53 to +38	259.87	343.45
-75 to +53	267.03	349.3

The effect of particle size on Co_3O_4 reduction was explored further using H_2-TPR. The reduction profiles for the three catalysts are shown in Figure 6.4, while Table 6.3 depicts the peak reduction temperature of several size classes.

The catalysts provided comparable reduction profiles for the reduction of Co_3O_4, albeit with a small displacement of the peaks (see Figure 6.4). Stepwise reduction of Co_3O_4 to CoO took place at temperatures between 180 and 264 °C, and further reduction of CoO to Co took place at

temperatures between 303 and 350 °C. It should be noticed that the first and second reduction peaks did not shift backwards or forwards significantly with the different size classes.

In order to completely reduce cobalt trioxide (Co_3O_4), one H_2 molecule is required for the first reduction process ($Co_3O_4 + H_2 \rightarrow 3CoO + H_2O$), and three H_2 molecules are required for the second reduction process ($3CoO + 3H_2 \rightarrow 3Co + 3H_2O$). The two distinctive peaks that appear at temperatures that are distinct from one another provides evidence that the transformation of CO_3O_4 into Co is a two-stage process that involves the production of a CoO intermediary phase. Other researchers have found the same characteristic peaks (Borg et al., 2007; Gorimbo et al., 2020; Khodakov et al., 1997; Olusola & Sudip, 2016). In this study, the reduction of the Co/Clino system was generally found to take place at notably lower temperatures than in other studies (Bao et al., 2009; Lin & Chen, 2004; Prieto et al., 2009).

6.3.3. Effect of heating rates on TPR profiles

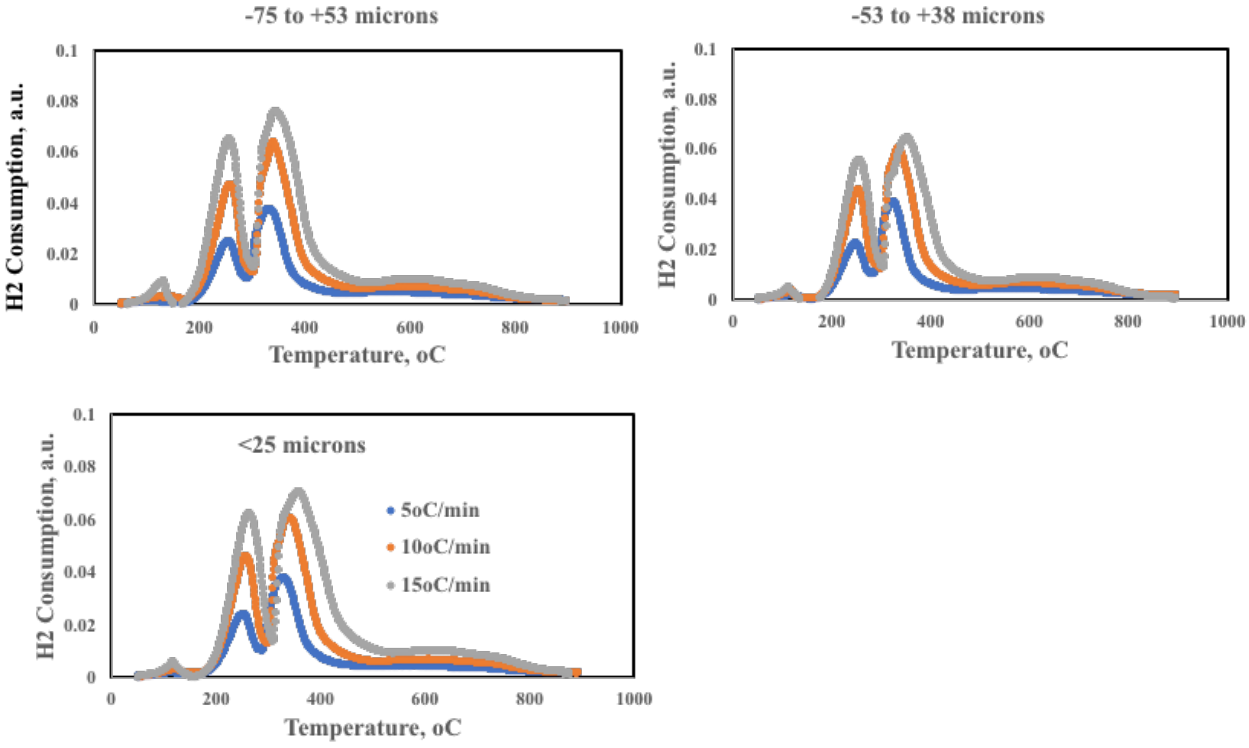

Figure 6.5: Temperature reduction was programmed at three heating rates (5, 10 and 15 °C/min) for three catalysts with varying support sizes.

The TPR profiles of Co/Clino catalysts were examined at various heating rates. The findings are displayed in **Figure 6.5.** With an increase in heating rate, the first and second peaks on the TPR profiles of all the catalysts migrated to a higher temperature, i.e. from 5 to 10 and then to 15 ^{o}C). In the investigation done by Vo et al. (2011), the heating rate was increased from 10 to 15 to 20 K/min, and it was found that the same phenomenon of an increase in reduction temperature with an increase in heating rate was seen.

The emphasis must be on reducing a plant's capital cost as well as its operating cost if the FT process is to become more cost-effective. One step in the direction of achieving this goal is lowering the temperature at which the reduction occurs, as the operational cost of an FTS plant can be decreased significantly by creating a catalyst that has a lower reduction temperature but still produces desirable products. As per the information shown in Figure 6.5 and Table 6.3, a specific size class must be used when manufacturing a catalyst. Additionally, a sufficient number of tests must be conducted in order to select the optimum particle size class and heating rate to be used during reduction.

6.3.4. Degree of reduction of different catalyst particle sizes

Error! Reference source not found. depicts the TPR curves. The integral value of the reference c atalyst Ag_2O was subtracted from the integral value of the curves. The exit gas was analyzed using a thermal conductivity detector (TCD), and the degree of reduction (DOR) (%) was calculated by comparing the matched peak area to that produced by a standard Ag_2O sample. By deducting the H_2 consumption of the supports alone from the total H_2 consumption, the percentage reduction of Co_3O_4 was calculated. Based on calibration data, the amount of hydrogen used and the DOR were determined. **Figure 6.6** and **Table 6.4** show the results of the calculations.

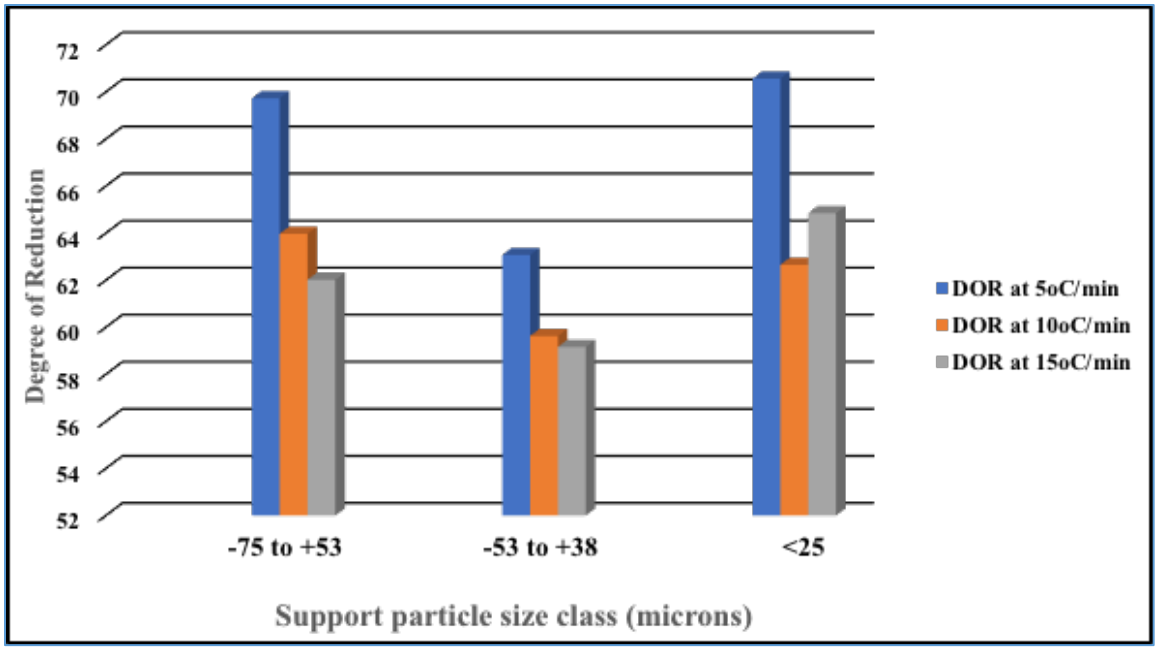

Figure 6.6: DOR of catalysts at different ramping rates

Table 6.4: DOR (%) at different heating rates used for the catalysts with different sizes of particle

Catalyst number	Catalyst size class, **µm**	DOR at 5°C/min	DOR at 10 °C/min	DOR at 15 °C/min
1	-75 to +53	69.74	63.97	62.02
2	-53 to +38	63.07	59.63	59.17
3	-25 to Pan	70.57	62.65	64.85

For particle size groups 1 (-75 to + 53 µm) and 2 (-53 to +38 µm), the DOR decreased with an increase in heating rate. This was not seen with particles less than 25 µm. At temperatures between 5 and 15 °C/min, the most effective reduction was seen with catalyst number 3. Generally, the results cannot be considered definitive for the particle size classes studied, because the patterns do not remain consistent across all heating rates. The effect of heating rate on the DOR is equally inconclusive, but the magnitude of the difference between a low heating rate (5°C/min) and high heating rate is enormous in comparison. The difference between 10 °C/min and 15°C/min is not

that significant. Below 450 ºC, the TPR measurements of cobalt supported on clinoptilolite particles of different sizes demonstrate that more than 59% of the cobalt is reduced. The results that have been provided indicate that the use of support material of various particle size classes results in a catalyst that possesses quite a range of attributes.

When using a particle size less than 75 μm, the best results for the reducibility of cobalt is obtained at a lower heating rate of 5ºC/min. It is clear from these observations that the size of the particles has an effect on the temperature required for reduction. Lowering the temperature is of great importance to the industrial sector, as it results in a reduction in the amount of money spent on the energy input required for reduction.

6.3.5. Activation energy calculations

On the kinetics of hydrogen's reduction of cobalt oxide on clinoptilolite, an extensive investigation was done. Using a heating rate of 5 ºC/min, the values of the local maxima of the peaks were used to compute the kinetic parameters of the Co_3O_4 reduction reaction. (The values are indicated in Error! Reference source not found..)

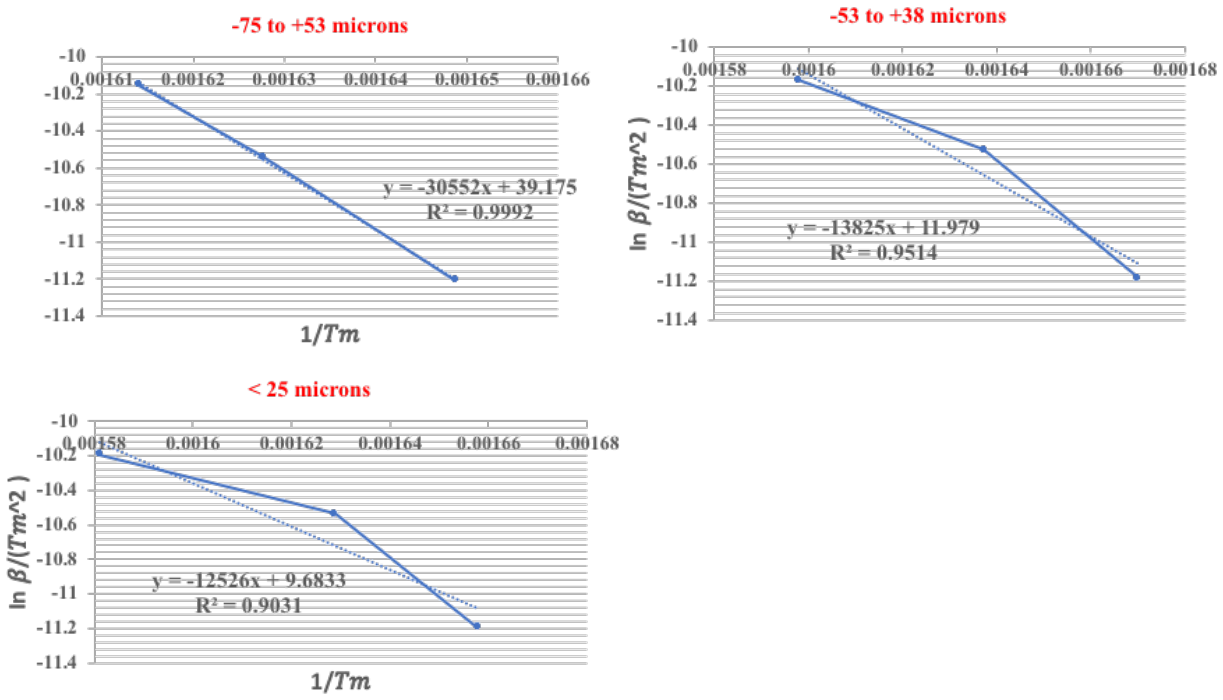

Figure 6.7: Plot of In β/(T_m^2) versus 1/T_m for all the different clinoptilolite size classes

The linearity of the plot is satisfactory, with a correlation coefficient that is greater than 0.95, except for the particle size class less than 25 mm, which has a coefficient of 0.90. Figure 6.7, shows the results of a calculation done using the Kissinger technique to determine the apparent activation energy for cobalt supported on clinoptilolite particles of varying sizes. The kinetics calculation was done using the Tmax values.

Table 6.5: Activation energy calculated using the Kissinger equation

Catalyst	E(i.e. activation energy) kJ/mol
-75 to +53	254.01
-53 to +38	114.94
-25 to Pan	104.14

The activation energy, Ea, for the Co_3O_4 that was supported on clinoptilolite was determined using this plot in **figure 6.7**. It was found that the activation energy measured during Co_3O_4 reduction decreases when the support particle size decreases from -75 to +53 μm to <25 μm. Compared to larger particle sizes (-75 to +53 μm), particles of the support with size less than 25 μm exibited lower activation energy need of 104.14 kilojoules per mole, which is more than 59% less energy required. Reduction of cobalt is performed optimally at lower activation energy levels, which means that the best particle size class for this process is <25 μm. Additionally, the best DOR can be found in the same particle size class at a heating rate of 5°C/min. The observed trend is probably related to changes in the interaction between the cobalt and the support, which could have occurred due to differences in the accessible surface area. When manufacturing a catalyst, the support is typically composed of particles of equal size throughout, as differences in these particle sizes might produce various types of behaviour.

6.3.6. Surface area and pore volume evaluation using nitrogen adsorption

Using nitrogen adsorption and desorption analysis, we were able to determine the levels of porosity present throughout the various catalyst size classes. **Figure 6.8** depicts a typical adsorption isotherm that was produced at a temperature of -195 degrees Celsius. An examination of each of the isotherms reveals that the catalyst material produced an adsorption isotherm of the type 11 variety, with an average pore diameter ranging from 17.77 to 19.60 nanometers (**See Table 6.6**). This indicates that all the particles were mesoporous, regardless of class size. In addition, size class had no significant effect on the porosity of the catalyst, as evidenced by the distribution of pore sizes (**See Figure 6.8 insert**). However, it is noted that the average pore diameter is approximately 18 nm and that the differences are within the experimental error range, which indicates overall consistency among the different experimental data sets. Support materials with a mean pore diameter of 10-15 nm are necessary for the formation of relatively large cobalt crystallites that are ca. 8-10 nm (Van Steen & Town, 2008). All catalyst materials showed a very low BET surface area ranging from (18.09 to 18.92 m^2/g). This obtained surface area is similar to that reported previously for the same material (Gorimbo et al., 2014; Gorimbo, 2011).

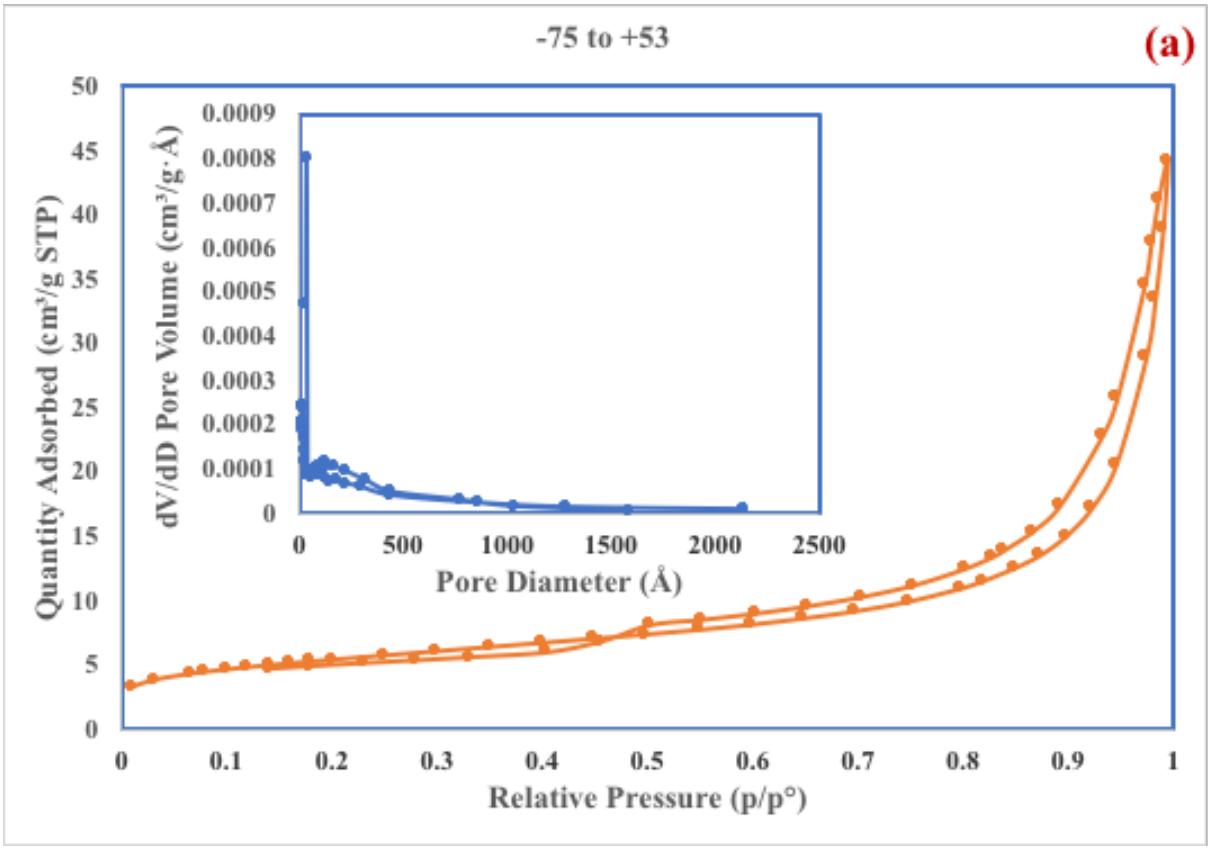
-75 to +53
(a)
Quantity Adsorbed (cm³/g STP)
Relative Pressure (p/p°)
dV/dD Pore Volume (cm³/g·Å)
Pore Diameter (Å)

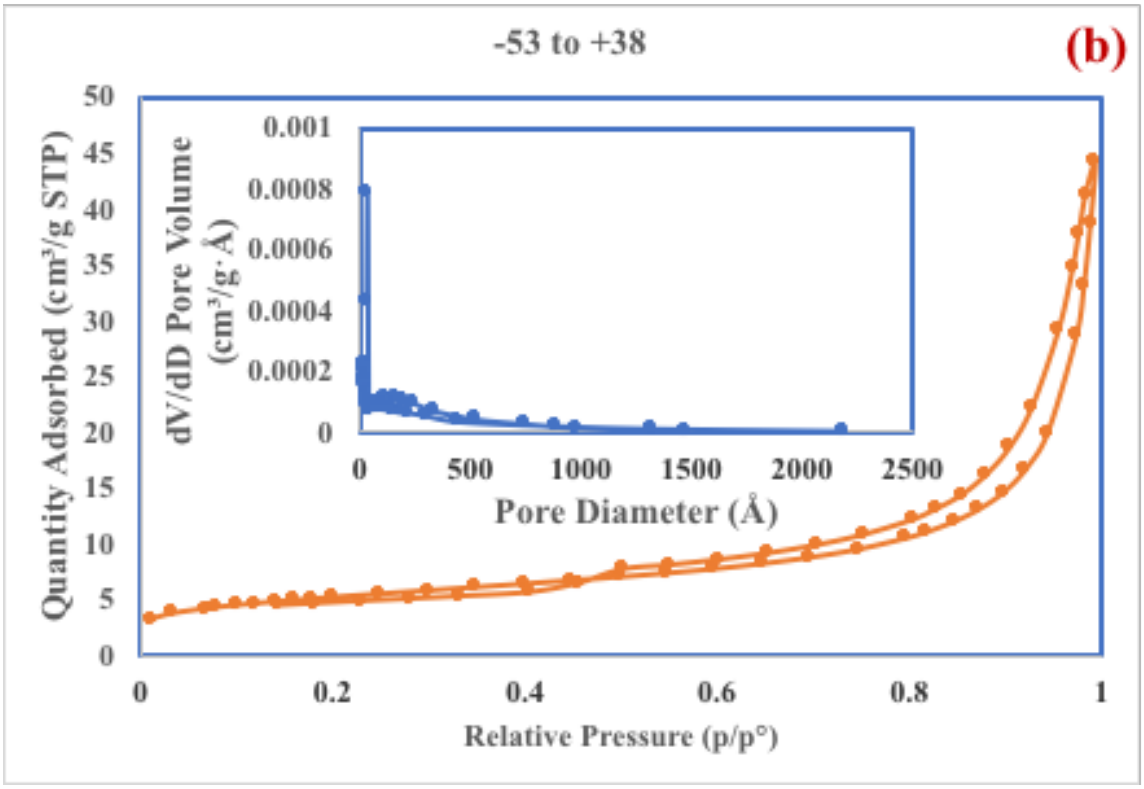
-53 to +38
(b)
Quantity Adsorbed (cm³/g STP)
Relative Pressure (p/p°)
dV/dD Pore Volume (cm³/g·Å)
Pore Diameter (Å)

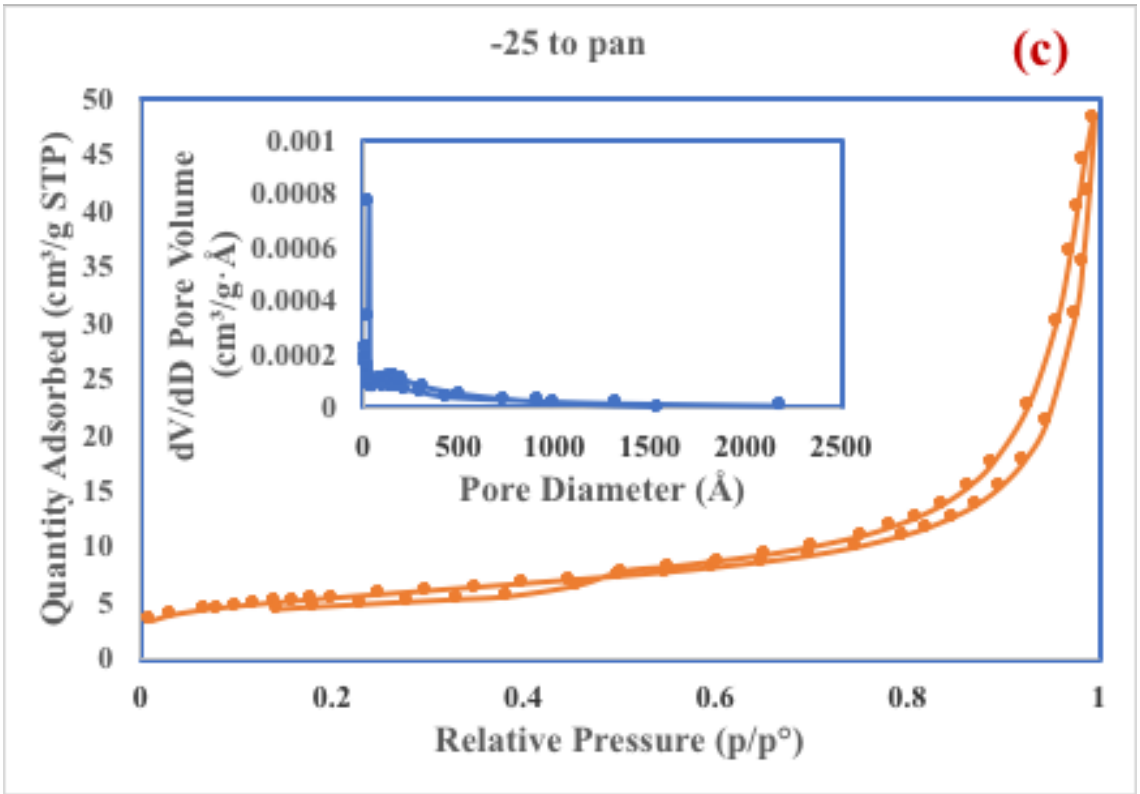

Figure 6.8: Physisorption isotherms and BJH pore size distribution for cobalt supported on clinoptilolite with particles of different sizes

Table 6.6: BET analysis of Co/Clino catalyst

Catalyst support size class, µm	**<25**	**-53 to +38**	**-75 to + 53**
BET surface area (m²/g)	18.92	18.09	18.80
BJH adsorption average pore diameter (4V/A):(nm)	19.60	18.94	17.77

It is worth noting that none of the BET characteristics shown has a clear trend. Therefore, when choosing a support to produce a catalyst, it is crucial to choose a support with a size class that is suited to reproducibility. FT has difficulty with reproducibility, and this could be one of the contributing factors that need to be investigated. Error compounding must be minimized.

6.3.7. Effect of TOS on CO conversation

In this particular investigation, the synthesis was performed at a temperature of 220 °C for approximately 56.5 hours time on stream (TOS) at a constant pressure of 10.85 bar (abs) and a flow rate of 10 mL/min. The outcomes of these studies are presented in **Figure 6.9** below. The data indicate that all three catalysts have a relatively high CO conversion level.

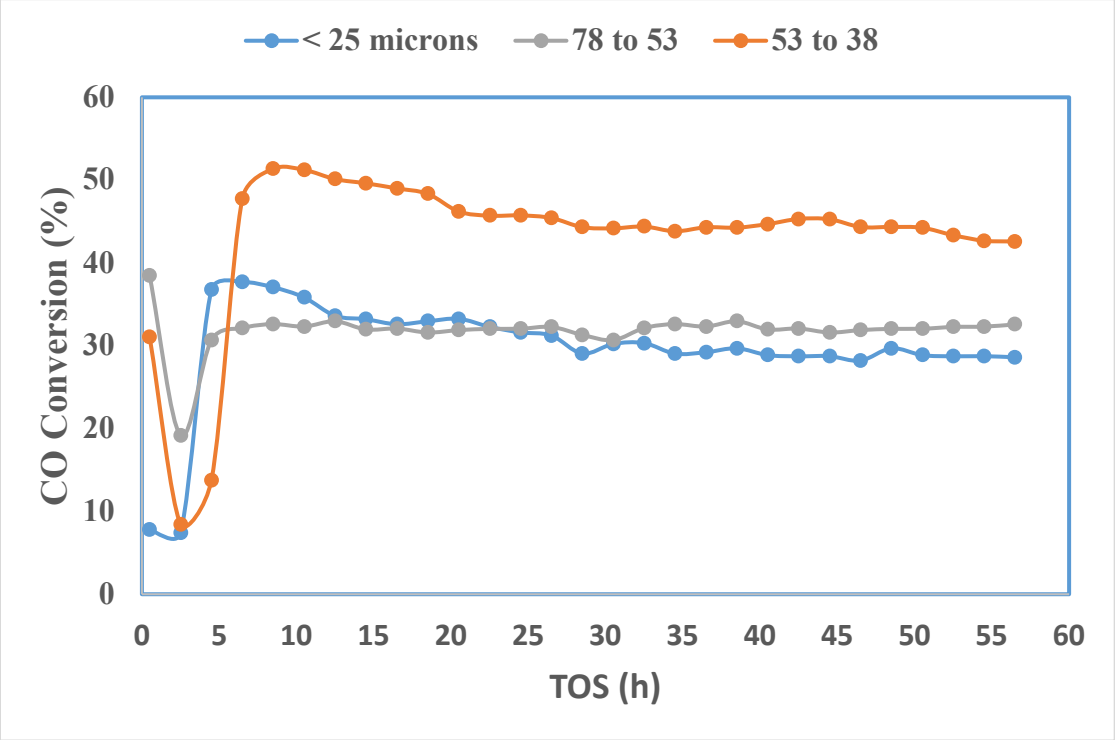

Figure 6.9: CO conversion of cobalt catalysts supported on clinoptilolite particles of different size classes (reaction condition 220 °C, 10.85 bar and 10 mL/min).

With the size class investigated, the CO conversion of these catalysts ranged between 31.29 ±2.90 and 45.87 ±2.56. Higher FT activity was observed for 10wt% Co/Clino (-53 to +38 µm) of 0.0075 $mol_{CO}.g^{-1}{}_{cat}h^{-1}$, which is 26.7 and 36% more than the catalyst with a support particle size of <25 and -78 to +53 µm, respectively. It took all the catalysts about 15 hours to attain a steady state.

Table 6.7: The calculated values for CO conversion, CO rate and cobalt catalyst activity supported on different size of support.

Catalyst name/ size class, µm	FTS Reaction Temperature (°C)	CO Conversion (%)	Activity ($mol_{CO}.g^{-1}_{cat}h^{-1}$)	Conversion CO Rate (mol/s)
10wt% Co/Clino (<25	220	31.29 ±2.90	0.0055	7.64E-07
10wt% Co/Clino (-53 to +38)	220	45.87 ±2.56	0.0075	1.04E-06
10wt% Co/Clino (-78 to +53)	220	32.06 ±0.54	0.0048	6.64E-07

The product selectivity levels obtained for this study are comparable to those published in the literature, which validates the support used. The methane selectivity ranged from 14.95 to 16.97%; the C_2-C_4 selectivity was in the range 14.55 to 19.01%; the C_{5+} selectivity was in the range 66.04 to 70.29%. The study conditions were 220 °C and 10 bar(g) pressure. A comparative examination of the effect of the size of the cobalt crystallites, the experimental conditions and the product selectivity levels are provided in **Table 6.7.** It is significant to note that the product distributions are remarkably similar, regardless of the type of cobalt catalyst used, provided that the co crystallite size and the experimental conditions are very similar.

Research conducted by Song and Li in 2006, at 230 °C and 10 bar(g) of pressure using Co/SiO_2 produced a product distribution with a lower C_2-C_4 selectivity of range 1.8 to -3.8%, a higher C_{5+} selectivity of range 59.9 to 87.2%, and a CH_4 selectivity of range 11-36.4%. The cobalt crystallites measured 9-17 nm (Song & Li, 2006). From this study, it can be determined that cobalt crystallite of 13 and 14.3 nm directed the formation of heavy C_{5+}. However, when the crystallite size increased to 17nm, there was a drop in the amount of C_{5+} detected. Using 9 nm Co crystallites produced a higher CH_4 selectivity and a comparatively lower C_{5+}. In a study done by Saib et al. (2002), 26 nm cobalt crystallite supported on silica resulted in 44% CH_4 in the product stream and

a lower C_{5+} of 32.3%. A 3 nm Co crystallite gave minimal CH_4 selectivity, while 6.9 nm gave the highest C_{5+} selectivity. The literature indicates that crystallite size has been found to have an impact on catalytic activity and product selectivity, and the data in **Table 6.2** supports these conclusions. Larger cobalt particles (> 7 nm) are shown to have a greater favorability for C_{5+} selectivity, while they are less favorable for CH_4 selectivity (Fu et al., 2014). Den Breejen et al. (2009) also reported on the propensity of small Co crystallite (6 nm) to favor strong CH_4 synthesis under FTS conditions. This phenomenon is attributed to increased surface hydrogen coverage.

In another investigation, conducted by Witoon and colleagues (2011) using co crystallite with a diameter of 11.2 nm led to selectivity of 70.2% for C_{5+} and 14.4% for CH_4. This catalyst is quite similar to the 10% Co/Clino catalyst that was employed in the current investigation. The cobalt based catalyst had a co crystallite size of 11.24 nm and a product distribution of 15.16% CH_4 and 70.29% C_{5+}. C_{5+} selectivity decreased as a direct consequence of the decrease in the size of the cobalt crystallites.

This investigation found that the catalyst that was employed performed significantly better than the other catalyst in the literature. (See **Table 6.7**.) Although the performance of the various support particle sizes varied slightly, it was still within the acceptable range in terms of product distribution. In terms of product distribution, no discernible pattern was identified that corresponds with an increase in particle size. Nevertheless, differences in crystallite size do have an effect on product distribution. The observed alpha values for the catalyst used in this study are comparable to those obtained with previous cobalt-based catalysts (as **in Table 6.8**). All the catalysts in **Table 6.8** yielded a higher α value of between 0.81 and 0.88, while C_{5+} selectivity followed the same increasing trend as the alpha values. High C_{5+} selectivity is associated with a high alpha values.

Table 6.8: Comparison of the effect of Co crystallite size, experimental conditions and product selectivity

Catalyst				**mol%**				
	Crystallite size (nm)	Pressure bar (g)	Temp. (oC)	CH_4 Sel. (%)	C_2-C_4 (%)	C_{5+} Sel (%)	Alpha value	References
10wt% Co/Clino (<25mm)	9.24	10	220	14.95	19.01	66.04	0.81	Current study
10wt% Co/Clino (-53 to +38mm)	11.24	10	220	15.16	14.55	70.29	0.88	
10wt% Co/Clino (-78 to +53mm)	8.27	10	220	16.97	16.53	66.50	0.83	
Co/SiO_2 (1)	9	10	230	36.4	3.8	59.9	-	(Song & Li, 2006)
Co/SiO_2 (2)	13	10	230	11	1.8	87.2	-	
Co/SiO_2 (3)	14.3	10	230	11.8	2.3	85.9	-	
Co/SiO_2 (4)	17	10	230	19.3	3.5	77.1	-	
Co/SiO_2-20	26	15	200	44	23.7	32.3	0.72	(Saib et al., 2002)
Co/SiO_2-40	3	15	200	18.7	20.9	60.4	0.77	
Co/SiO_2-60	6.7	15	200	28.5	16.7	54.8	0.81	
Co/SiO_2-100	6.9	15	200	19.2	19	61.8	0.8	
Co/SiO_2-150	8.3	15	200	37.6	18.7	43.7	0.84	

Co/MS-1	6.5	10	220	24.2	22.4	53.4	-	(Witoon et al., 2011)
Co/MS-2	10	10	220	16.1	16.5	67.4	-	
Co/MS-3	11.2	10	220	14.4	15.4	70.2	-	
Co/HS-1	7.1	10	220	20	16.2	63.8	-	
Co/HS-2	11	10	220	17.8	16.5	65.7	-	
Co/HS-3	15.4	10	220	16.1	11	72.9	-	
10Co(N)400/HMS	15	20	270	17.5	27.3	54.3	0.74	(Lira et al., 2008)
20Co(N)400/HMS	16	20	270	19	11.4	65.9	0.77	
10Co(N)400/SiO_2	16	20	270	8.2	12.6	78.6	0.86	
20Co(en)400/HMS	10	20	270	35.4	22.1	41.7	0.82	
20Co(en)400/SiO_2	10	20	270	22.2	30.7	44.8	0.86	
10CoSBA-n	6.2	20	220	28.4	25.3	46.3	0.86	(Martínez et al., 2003)
20CoSBA-n	11.4	20	220	19.5	15.8	64.7	0.87	
30CoSBA-n	13.8	20	220	21.3	15.5	63.2	0.86	
40CoSBA-n	17.6	20	220	18.5	14.8	66.7	0.87	
1Re20CoSBA-n	9.5	20	220	14.1	11.7	74.2	0.87	
2Mn20CoSBA-n	5.9	20	220	19.2	36.6	44.2	0.78	
1Re2Mn20CoSBA-n	6.8	20	220	20.4	35.4	44.2	0.77	
20$CoSiO_2$	14.1	20	220	17.9	19.1	63	0.83	

- indicates information not given.

The pore diameter, composition, pore size and size of the support particle of the catalysts compared in **Table 6.8** varied. However, the product selectivity results are interesting in light of the applied reaction conditions.

6.3.8. Statistical analysis

The statistical significance of the researched parameters was determined using the experimental outcomes. The influence of support particle size on conversion was analyzed statistically to determine if varying the particle size yields statistically distinct outcomes. ANOVA followed by the Bonferroni Post Hoc Test was performed. An alpha of 0.05 was used, which means that the results are 95% correct. In the event that the P value is significantly lower than 0.05 (α-value), it means the difference between these particle size groups exist. Following the application of the Bonferroni correction, the initial alpha value was modified by dividing it by 3 (the number of comparisons). If the P value is less than the corrected alpha value, then the groups are different. The differences between the groups was tested. If the calculated F value is greater than Fcrit, the difference between the groups exists. Also, if the P-value is less than the α-value, there are differences within the groups. Different particle sizes have different effects in conversion.

Tables 6.9 and 6.10 show the statistical analysis of conversion obtained from the three catalysts with different support particle sizes.

The findings of the one-way analysis of variance are summarized in **Table 6.9**, which compares the CO conversion figures that were acquired from the three separate tests. A post-hoc Bonferroni correction test was carried out, and the findings were tabulated in order to make it possible to compare the influence of different particle sizes. The fact that the P values are significantly lower than 0.5, as displayed across all of the ANOVA tables, is compelling evidence that the three different-sized particles reacted in distinctive ways.

Table 6.9: Anova: Single Factor

SUMMARY

Group	Count	Sum	Average	Variance
<25	23	697.542328	30.3279273	3.32630714
-53 to 38	23	1035.33484	45.0145582	6.11765739
-78 to 53	23	737.728756	32.0751633	0.24416855

ANOVA

Source of variation	SS	df	MS	F	P-value	F crit
Between groups	2960.69724	2	1480.34862	458.400583	1.966E-39	3.13591793
Within groups	213.138928	66	3.22937769			
Total	3173.83616	68				

Ss = sum of squares

Df = degrees of freedom

MS = mean squares

Table 6.10: t-Test, Two Sample, assuming Equal Variance

	<25	53 to 38	<25	78 to 53	53 to 38	78 to 53
Mean	30.32792731	45.0145582	30.3279273	32.0751633	45.0145582	32.0751633
Variance	3.326307138	6.11765739	3.32630714	0.24416855	6.11765739	0.24416855
Observations	23	23	23	23	23	23
Pooled variance	4.721982266		1.78523784		3.18091297	
Hypothesized mean difference	0		0		0	
df	44		44		44	
t Stat	-22.9196998		-4.4345795		24.6029392	
P(T<=t) one-tail	2.14603E-26		3.0394E-05		1.184E-27	
t Critical one-tail	1.680229977		1.68022998		1.68022998	
P(T<=t) two-tail	4.29206E-26		6.0788E-05		2.3681E-27	
t Critical two-tail	2.015367574		2.01536757		2.01536757	

Bonferroni adjustment	0.016666667	0.01666667	0.01666667
significant ?	TRUE	TRUE	TRUE

To establish if there is a difference in conversion due to particle size, an ANOVA single factor (CO-conversion) test was performed. The calculated F value (458.400583) was greater than Fcrit (3.13591793), therefore a difference between the groups exists. (See **Table 6.9**.) Also the P-value is less than the α-value of 0.05, which indicates differences within groups. Differently-sized particles have a different effect in conversion.

6.4. Conclusion

A thorough investigation was done of the characteristics of cobalt supported on clinoptilolite particles of different sizes using TPR, XRD, XRF, BET and SEM techniques. It has been demonstrated that these techniques provide insight into the effect of support particle size and could be used as a quality control tool to evaluate the efficacy of the methods used to prepare the catalysts.

The reduction of support size improved the reducibility of cobalt oxide (CoO) and lowered both the reduction temperature and activation energy for Co_3O_4 Significantly. The kinetic investigation substantiates the hypothesis that the interaction between the metal and the support plays a significant part in determining the support's contribution to the overall improvement in catalyst reducibility. The magnitude of the difference between a low heating rate (5°C/min) and a high heating rate is comparatively large; however, the impact of heating rate on the DOR is not definitive. For this particular study, using particles with a diameter of less than 25 μm and performing the reduction at a rate of 5 ^{o}C/min resulted in a low activation energy of 104.14.kJ/mol and a high DOR of 70.57%.

TPR measurements of cobalt supported on clinoptilolite show that more than 60% of the cobalt is decreased at temperatures below 450 ^{o}C, regardless of the size of the particles. Creating a catalyst with a lower reduction temperature that generates acceptable products can reduce the operational expense of an FTS plant significantly. The findings of this study indicate that a particular support size class must be used when making a catalyst. In addition, a sufficient number of experiments must be undertaken to optimize or choose the optimal particle size class and optimal heating rate for use during reduction. The product selectivity results obtained for

this investigation are comparable to those published in the literature, which indicates that the support used was effective. At 220 ºC and 10.85 bar (abs): methane selectivity ranged from 14.95 to 16.97%; C_2-C_4 selectivity ranged from 14.55 to 19.01%; C_{5+} selectivity ranged from 66.04 to 70.29%. Based on the data provided, it appears that changing the PSD of the support material can produce a catalyst with a wide variety of characteristics.

It is worth noting that no clear trend was obtained for any of the BET parameters, although this has been documented. When picking a support from which to create a catalyst, it is crucial to pick a support from a particular size class, in order to ensure that the results can be reproduced accurately. There are issues with reproducibility in the FT method, and this is one of the potential contributing factors that has to be investigated. The compounding of errors is something that needs to be cut down.

References

Bao, A., Liew, K., & Li, J. (2009). Fischer-Tropsch synthesis on CaO-promoted Co/Al2O3 catalysts. *Journal of Molecular Catalysis A: Chemical*, *304*(1–2), 47–51. https://doi.org/10.1016/j.molcata.2009.01.022

Bezemer, G. L., Bitter, J. H., Kuipers, H. P. C. E., Oosterbeek, H., Holewijn, J. E., Xu, X., Kapteijn, F., Van Diilen, A. J., & De Jong, K. P. (2006). Cobalt particle size effects in the Fischer-Tropsch reaction studied with carbon nanofiber supported catalysts. *Journal of the American Chemical Society*, *128*(12), 3956–3964. https://doi.org/10.1021/ja058282w

Bish, D. L., & Ming, D. W. (1955). Natural zeoloites: Ocurrence, properties, applications, *Journal* (Vol. 45).

Borg, Ø., Eri, S., Blekkan, E. A., Storsæter, S., Wigum, H., Rytter, E., & Holmen, A. (2007). Fischer-Tropsch synthesis over γ-alumina-supported cobalt catalysts: Effect of support variables. *Journal of Catalysis*, *248*(1), 89–100. https://doi.org/10.1016/j.jcat.2007.03.008

Bowen, P. (2002). Particle size distribution measurement from millimeters to nanometers and from rods to platelets. *Journal of Dispersion Science and Technology*, *23*(5), 631–662. https://doi.org/10.1081/DIS-120015368

Cahyono, R. B., Mufrodi, Z., Hidayat, A., & Budiman, A. (2016). Acetylation of glycerol for triacetin production using Zr-natural zeolite catalyst. *ARPN Journal of Engineering and Applied Sciences*, *11*(8), 5194–5197.

Cheng, Q., Tian, Y., Lyu, S., Zhao, N., Ma, K., Ding, T., Jiang, Z., Wang, L., Zhang, J., Zheng, L., Gao, F., Dong, L., Tsubaki, N., & Li, X. (2018). Confined small-sized cobalt catalysts stimulate carbon-chain growth reversely by modifying ASF law of Fischer–Tropsch synthesis. *Nature Communications*, *9*(1), 1–9. https://doi.org/10.1038/s41467-018-05755-8

De Klerk, A. (2008). Hydroprocessing peculiarities of Fischer –Tropsch syncrude. *Catalysis Today*, *130*, 439–445. https://doi.org/10.1016/j.cattod.2007.10.006

Den Breejen, J. P., Radstake, P. B., Bezemer, G. L., Bitter, J. H., Frøseth, V., Holmen, A., & De Jong, K. P. (2009). On the origin of the cobalt particle size effects in Fischer-Tropsch

catalysis. *Journal of the American Chemical Society*, *131*(20), 7197–7203. https://doi.org/10.1021/ja901006x

Dietz, W. A. (1967). Response factors for gas chromatographic analyses. *Journal of Chromatographic Science*, *5*(2), 68–71. https://doi.org/10.1093/chromsci/5.2.68

Eroglu, N., Emekci, M., & Athanassiou, C. G. (2017). Applications of natural zeolites on agriculture and food production. *Journal of the Science of Food and Agriculture*, *97*(11), 3487–3499. https://doi.org/10.1002/jsfa.8312

Fisher, P., Aumann, C., Chia, K., O'Halloran, N., & Chandra, S. (2017). Adequacy of laser diffraction for soil particle size analysis. *PLoS ONE*, *12*(5), 1–20. https://doi.org/10.1371/journal.pone.0176510

Fu, T., Lv, J., & Li, Z. (2014). Effect of carbon porosity and cobalt particle size on the catalytic performance of carbon supported cobalt Fischer-Tropsch catalysts. *Industrial and Engineering Chemistry Research*, *53*(4), 1342–1350. https://doi.org/10.1021/ie402128y

Gazi, M. Y., Apu, S. I., Sharmili, N., & Rahman, M. Z. (2021). Origin and characterization of clay deposits in the Dupi Tila Formation of the Bengal Basin, Bangladesh. *Solid Earth Sciences*, *6*(3), 313–327. https://doi.org/10.1016/j.sesci.2021.07.001

Gorimbo, J. (2011). *Effect of the Homoionic Form of Clinoptilolite on Ni 2 + Adsorption Isotherms: A Thermodynamic Study*. Incomplete.

Gorimbo, J. (2016). *An Experimental and Thermodynamic Study of Iron Catalyst Activation and Deactivation during Fischer Tropsch Synthesis*. University of the Witwatersrand.

Gorimbo, J, Muvhiiwa, R., Llane, E., & Hildebrandt, D. (2020). Cobalt Catalyst Reduction Thermodynamics in Fischer Tropsch: An Attainable Region Approach. *Reactions*, *1*(2), 115–129. https://doi.org/10.3390/reactions1020010

Gorimbo, J., Taenzana, B., Kapanji, K., & Jewell, L. L. (2014). Equilibrium ion exchange studies of Ni2+ on homoionic forms of clinoptilolite. *South African Journal of Science*, *110*(5–6), 1–7. https://doi.org/10.1590/sajs.2014/20120027

Javed, M., Cheng, S., Zhang, G., Amoo, C. C., Wang, J., Lu, P., Lu, C., Xing, C., Sun, J., & Tsubaki, N. (2020). A facile solvent-free synthesis strategy for Co-imbedded zeolite-based Fischer-Tropsch catalysts for direct gasoline production. *Chinese Journal of Catalysis*, *41*(4), 604–612. https://doi.org/10.1016/S1872-2067(19)63436-4

Kang, S. H., Bae, J. W., Prasad, P. S. S., & Jun, K. W. (2008). Fischer-Tropsch synthesis using zeolite-supported iron catalysts for the production of light hydrocarbons. *Catalysis Letters*, *125*(3–4), 264–270. https://doi.org/10.1007/s10562-008-9586-2

Khodakov, A. Y., Lynch, J., Bazin, D., Rebours, B., Zanier, N., Moisson, B., & Chaumette, P. (1997). Reducibility of cobalt species in silica-supported Fischer-Tropsch catalysts. *Journal of Catalysis*, *168*(1), 16–25. https://doi.org/10.1006/jcat.1997.1573

Kristiani, A., Sudiyarmanto, S., Aulia, F., Nurul Hidayati, L., & Abimanyu, H. (2017). Metal supported on natural zeolite as catalysts for conversion of ethanol to gasoline. *MATEC Web of Conferences*, *101*. https://doi.org/10.1051/matecconf/201710101001

Kusuma, R. I., Hadinoto, J. P., Ayucitra, A., Soetaredjo, F. E., & Ismadji, S. (2013). Natural zeolite from Pacitan Indonesia, as catalyst support for transesterification of palm oil. *Applied Clay Science*, *74*, 121–126. https://doi.org/10.1016/j.clay.2012.04.021

Li, Y., & Yu, J. (2021). Emerging applications of zeolites in catalysis, separation and host–guest assembly. *Nature Reviews Materials*, *6*(12), 1156–1174. https://doi.org/10.1038/s41578-021-00347-3

Lin, H. Y., & Chen, Y. W. (2004). The mechanism of reduction of cobalt by hydrogen. *Materials Chemistry and Physics*, *85*(1), 171–175. https://doi.org/10.1016/j.matchemphys.2003.12.028

Lira, E., López, C. M., Oropeza, F., Bartolini, M., Alvarez, J., Goldwasser, M., Linares, F. L., Lamonier, J. F., & Pérez Zurita, M. J. (2008). HMS mesoporous silica as cobalt support for the Fischer-Tropsch Synthesis: Pretreatment, cobalt loading and particle size effects. *Journal of Molecular Catalysis A: Chemical*, *281*(1–2), 146–153. https://doi.org/10.1016/j.molcata.2007.11.014

Lu, X. (2011). Fischer Tropsch Synthesis : Towards understanding. In *Dissertation*. University of the Witwatersrand.

Mandić, M., Todić, B., Živanić, L., Nikačević, N., & Bukur, D. B. (2017). Effects of catalyst activity, particle size and shape, and process conditions on catalyst effectiveness and methane selectivity for Fischer-Tropsch reaction: A modeling study. *Industrial and Engineering Chemistry Research*, *56*(10), 2733–2745. https://doi.org/10.1021/acs.iecr.7b00053

Marantos, I., Christidis, G. E., & Ulmanu, M. (2012). Zeolite formation and deposits. In *Handbook of Zeolites* (pp. 28–51).

Martínez, A., López, C., Márquez, F., & Díaz, I. (2003). Fischer-Tropsch synthesis of hydrocarbons over mesoporous Co/SBA-15 catalysts: The influence of metal loading, cobalt precursor, and promoters. *Journal of Catalysis*, *220*(2), 486–499. https://doi.org/10.1016/S0021-9517(03)00289-6

Martínez, A., Rollán, J., Arribas, M. A., Cerqueira, H. S., Costa, A. F., & Eduardo, E. F. (2007). A detailed study of the activity and deactivation of zeolites in hybrid Co/SiO2-zeolite Fischer-Tropsch catalysts. *Journal of Catalysis*, *249*(2), 162–173. https://doi.org/10.1016/j.jcat.2007.04.012

Mokoena, E. M. (2005). Synthesis and use of silica materials as supports for the Fischer-Tropsch reaction. *PhD Thesis, University of the Witwatersrand*.

Olusola, O. J., & Sudip, M. (2016). Temperature programme reduction (TPR) studies of cobalt phases in -alumina supported cobalt catalysts. *Journal of Petroleum Technology and Alternative Fuels*, *7*(1), 1–12. https://doi.org/10.5897/jptaf2015.0122

Phadi, T. T. (2012). Titanium dioxide-carbon spheres composites for use as supports in cobalt Fischer-Tropsch Synthesi*s*. Incomplete.

Prieto, G., Martínez, A., Concepción, P., & Moreno-Tost, R. (2009). Cobalt particle size effects in Fischer-Tropsch synthesis: Structural and in situ spectroscopic characterisation on reverse micelle-synthesised Co/ITQ-2 model catalysts. *Journal of Catalysis*, *266*(1), 129–144. https://doi.org/10.1016/j.jcat.2009.06.001

Saib, A. M., Claeys, M., & Van Steen, E. (2002). Silica supported cobalt Fischer-Tropsch catalysts: Effect of pore diameter of support. *Catalysis Today*, *71*(3–4), 395–402. https://doi.org/10.1016/S0920-5861(01)00466-7

Song, D., & Li, J. (2006). Effect of catalyst pore size on the catalytic performance of silica supported cobalt Fischer-Tropsch catalysts. *Journal of Molecular Catalysis A: Chemical*, *247*(1–2), 206–212. https://doi.org/10.1016/j.molcata.2005.11.021

Van Steen, E., & Town, C. (2008). *Fischer-Tropsch catalysts for the biomass-to-liquid process*. *2*(5), 655–666. https://doi.org/10.1002/ceat.200800067

Vo, D. V. N., Nguyen, T. H., Kennedy, E. M., Dlugogorski, B. Z., & Adesina, A. A. (2011).

Fischer-Tropsch synthesis: Effect of promoter type on alumina-supported Mo carbide catalysts. *Catalysis Today*, *175*(1), 450–459. https://doi.org/10.1016/j.cattod.2011.04.045

Vrbková, E., Šímová, A., Vyskočilová, E., Lhotka, M., & Červený, L. (2021). Acid treated montmorillonite—Eco-friendly clay as catalyst in carvone isomerization to carvacrol. *Reactions*, *2*(4), 486–498. https://doi.org/10.3390/reactions2040031

Wahono, S. K., Stalin, J., Addai-Mensah, J., Skinner, W., Vinu, A., & Vasilev, K. (2020). Physico-chemical modification of natural mordenite-clinoptilolite zeolites and their enhanced CO2 adsorption capacity. *Microporous and Mesoporous Materials*, *294*, 109871. https://doi.org/10.1016/j.micromeso.2019.109871

Witoon, T., Chareonpanich, M., & Limtrakul, J. (2011). Effect of hierarchical meso-macroporous silica supports on Fischer-Tropsch synthesis using cobalt catalyst. *Fuel Processing Technology*, *92*(8), 1498–1505. https://doi.org/10.1016/j.fuproc.2011.03.011

Yao, Y. (2011). Fischer-Tropsch Synthesis using CO_2 -Containing Syngas Mixtures over Cobalt and Iron Based Catalysts. In *University of the Witwatersrand*.

Chapter 7: Optimization and screening of iron-supported on clinoptilolite as a low-temperature Fischer-Tropsch synthesis catalyst

This work has been prepared in the form of a paper for future publication.

Abstract: Modelling fuel production systems allows organizations to investigate the most effective aspects, while operating under optimal conditions. As a result, an innovative data simulation technique based on response surface methodology (RSM) is proposed as part of the design of experiments (DOE) to thoroughly investigate the effect of the various operating conditions. DOE is a statistical strategy that is used to improve a process plan, so that the comprehensive understanding of the mechanism that is gained can be used to optimise the process with the fewest possible series of experiments. It can be used to focus on the impact of different components simultaneously, as well as on the dynamic interaction between them, in a methodical manner. The aims of this paper were to explore the components that influence the production of olefins and paraffin wax in the Fischer-Tropsch (FT) process and then optimise the key components using factorial design and RSM. The parameters evaluated were: hydrogen to carbon monoxide (H_2:CO) ratio; reaction temperature; reaction pressure; gas speed GHSV. By employing multivariate DOE, the effect and the probable synergistic effect of these components were investigated simultaneously. Single and multicentre parameter optimisation was performed, and it was found that the maximum heavy hydrocarbon selectivity (C_{5+} - C∞) and the least amount of methane selectivity (CH4) can be obtained under the following conditions: H_2:CO = 1.9; T=241°C P=17,9 bar; GHSV=1241h-1.

7.1. Introduction

The increasing demand for energy and the finite nature of fossil energy resources have pushed society to explore alternative energy sources. Due to the depletion of conventional sources of oil and gas, alternative techniques for extracting oil and gas products that are based on renewable energy are being explored. As a result, scientists are interested in developing non-fossil-based fuels, and oil and gas derivatives.

The Fischer-Tropsch (FT) process, which synthesizes liquid hydrocarbons, is an ideal pathway for indirect liquefaction of solid or gaseous carbon-based energy sources (fossil fuel) into transportable liquid fuels. Transition metals like cobalt (Co), iron (Fe) and nickel (Ni) are used as catalysts during the FT synthesis process. FT-derived products have various advantages over crude-oil-derived products, including the absence of sulphur (S) and nitrogen (N_2,) and a low aromatic concentration. Synthesis gas, which is the gas used in the FT process, is a mixture of CO and H_2 that is converted into environmentally-friendly fuel and valuable chemicals, with a stoichiometric ratio (H_2:CO) ranging from 1 to 2, depending on the feed and technique. This feed ratio influences the overall products. The FT process produces a plethora of products, the most popular of which are olefins and paraffin, and oxygenate fractions are produced. Substantial quantities of by-products are also produced (Paterson et al., 2017; Tsakoumis et al., 2012).

Equations 7.1- 7.4 represent the key reactions in FT synthesis:

$$Alkanes \qquad nCO + (2n+1)H_2 \rightarrow C_nH_{2n+2} + nH_2O \qquad (7.1)$$

$$Alkenes \qquad nCO + 2nH_2 \rightarrow C_nH_{2n} + nH_2O \qquad (7.2)$$

$$WGS \qquad CO + H_2O \rightarrow CO_2 + H_2 \qquad (7.3)$$

$$Side\ reaction \qquad nCO + 2nH_2 \rightarrow h(-CH_2-)OH + (n-1)H_2O \qquad (7.4)$$

Both the high temperature Fischer-Tropsch (HTFT) and the low temperature Fischer-Tropsch (LTFT) methods of operation are possible in the FT process (Elbashir et al., 2009; Velasco et al., 2010; Wood et al., 2012). The primary distinctions are in the operating conditions, as indicated in **Table 7.1.**

Table 7.1: Comparison of FT process parameters

FT Process	Temperature/ °C	Pressure/ Bar	H_2:CO
HTFT	300-350	20-40	<2
LTFT	200-240	20-45	1.7-2.15

The operating conditions are significant in determining the output product of the FT process. To optimise the process, screening of insignificant factors is crucial. Therefore, two areas of focus were chosen for this study: screening and optimisation. For screening, the multivariate

method referred to as design of experiments (DOE) was applied, and experiments were designed using a two-stage fractional factorial resolution design to identify the statistically significant design variables that have a greater impact on the measured response (yield of C_{5+}-C_{∞} components). Then, the significantly influential factors were further investigated using the response surface methodology (RSM) to determine their optimal points (optimisation). When using a fitted quadratic polynomial model of the experimental findings, RSM is a popular technique for identifying the ideal conditions. It is used after the screening step (Montgomery, 2013).

When calculating selectivity, **equations 7.5 - 7.8** can be used to measure hydrocarbon selectivity, based on carbon.

$$CO\ Conversion\ (\%) = \frac{moles\ of\ CO_{in} - moles\ of\ CO_{\ out}}{moles\ of\ CO_{in}} * 100 \quad (7.5)$$

$$CH_4\ Conversion\ (\%) = \frac{mCH_4}{mCH_4 + \sum_{n=2}^{4} mC_nH_{2n+1} + \sum_{n=5}^{\infty} mC_nH_{2n+1}} * 100 \quad (7.6)$$

$$C_2 - C_4\ Conversion\ (\%) = \frac{\sum_{n=2}^{4} mC_nH_{2n+1}}{mCH_4 + \sum_{n=2}^{4} mC_nH_{2n+1} + \sum_{n=5}^{\infty} mC_nH_{2n+1}} * 100 \quad (7.7)$$

$$C_5 - C_{\infty}\ Conversion\ (\%) = \frac{\sum_{n=5}^{\infty} mC_nH_{2n+1}}{mCH_4 + \sum_{n=2}^{4} mC_nH_{2n+1} + \sum_{n=5}^{\infty} mC_nH_{2n+1}} * 100 \quad (7.8)$$

This study focused on using a combination of two-level fractional factorial design and the RSM in conjunction with the optimal design to identify and optimize factors that affect the hydrocarbons yield from FT processing of synthesis gas. While CO_2 selectivity can be used as a descriptive term for WGS, it was not included in the calculations, because the main purpose was to find out how clinoptilolite zeolite and Fe interact.

7.1.1. Iron-based catalyst

As a result of the low cost and high availability, iron-based catalysts are used in many chemical reactions. According to reports, iron is the most plentiful metal on Earth, constituting some 80% of the Earth's inner and outer core (Keyvanloo et al., 2018). This plentiful supply of iron provided the impetus for the researcher to develop an iron catalyst supported on cheap, naturally-occurring zeolites. Iron catalysts are selective for paraffins when using a lower temperature, while selectivity changes towards olefins as the temperature increases. Due to

their higher WGS activity and lower methane selectivity, iron-based catalysts are preferred over cobalt when coal or biomass is used as the feedstock for the FT process.

Due to the naturally low H_2/CO ratio of syngas produced from coal or biomass, WGS activity is required for internal generation of H_2 during FT (Pardo-Tarifa, 2017). Catalysed iron-based reactions require the use of promoter to promote the production of certain products. This is one of the options offered by iron-based reactions. The operating conditions of the reaction and the additives play a role in influencing output product, as summarised in **Table 7.2.**

Thermally fused iron-based catalysts and impregnated iron-based catalysts are the two main types of iron-based catalysts. They can be further divided into two types: supported and self-supporting catalysts. Although iron catalysts are usually self-supporting, they are often supported in order to improve thermal and mechanical stability (Dry, 2002). Zeolites are widely considered to be one of the most effective supports.

Incipient wetness impregnation (IWP) is a popular production method used for FT catalysts. According to the research done by Wang et al. (2007), Fe catalysts that are based on zeolite faujasite exhibit much greater selectivity for C_{5+} hydrocarbons than Fe catalysts supported on other microporous and mesoporous materials. Further research into the use of lithium as a promoter revealed that the lithium-exchanged zeolite faujasite is the most effective support for iron catalysts to create C_{5+} hydrocarbon fuels through FT synthesis (Wang et al., 2007). However, the position of the iron species in the catalyst is essential to achieving good selectivity for C_{5+} hydrocarbons.

According to Liu et al. (2020), in FT experiments done, Na boosted the catalyst's surface basicity, which increased the selectivity towards olefins from 11% over Fe/H-ZSM-5 to 29.4% over Fe/Na-ZSM-5. According to Kang et al. (2008), ZSM-5 appears to be the most suitable of the three zeolites used as supports for impregnating the FeCuK combination because it retains the physical structure and allows for better reduction of iron species. Wet impregnation of proton-type zeolites was employed by Kang et al. (2008) to manufacture the Fe-based catalysts for FTS from synthesis gas. These proton-type zeolites include ZSM-5 (a Si/Al ratio of 25 and a surface area of 425 m^2g^{-1}), mordenite (a comparatively lower Si/Al ratio of 6 and a surface area of 420 m^2g^{-1}), and beta zeolite (a Si/Al ratio of 12.5 and a surface area of 680 m^2g^{-1}). Mordenite and beta zeolite both undergo morphological transformation as a result of the process (Kang et al. 2008).

Di et al. (2019) developed a catalyst to produce light olefins from syngas. The primary Fe catalyst was responsible for the production of the characteristic FT heavy hydrocarbons. These long-chain hydrocarbons were then hydrocracked into light olefins when they diffused through the SAPO-34 zeolite shell and came into contact with the active acid sites of the SAPO-34. The SAPO-34 zeolite shell boosted the selectivity of light olefins considerably. Da Silva et al. (2018) investigated the catalytic activity of iron and cobalt-supported zeolite catalysts. It was revealed that an increase in the amount of Fe loading led to higher conversion but a decrease in the number of carbon atoms.

The research done by Baranak et al. (2013) showed that the catalyst production procedure, iron loading and reaction temperature changed the catalytic activity of all catalysts considerably. Catalyst activity increased as the catalyst's iron content and reaction temperature increased.

Mierczynski et al. (2019) investigated the physicochemical and catalytic properties of a variety of support materials that are used in FT synthesis. By hydrogenating CO at a pressure of 30 atmosphere and 280 ^{o}C, it was shown that this process had high selectivity for linear hydrocarbons. This selectivity was shown by experimentation. The 40% Fe/zeolite H catalyst exhibited extremely high selectivity for linear hydrocarbons (94,8%), which makes it ideal for producing the gasoline component. The iron catalyst on the Na version of zeolite BEA produced more diesel, but had the lowest selectivity for linear hydrocarbons (66%).

Table 7.2: Comparative analysis of research conducted using Fe and zeolites

Active Metal	**Promoter**	**Synthesis Method**	**H_2/CO ratio**	**Pressure** / Bar	**Temperature** / °C	**CO Conversion** / %	C_{5+}-C_{∞} / %	**Reference**
Fe	-	Incipient wetness impregnation	2	2	270	0-27	11-42	(Wang et al., 2007)
	Na					3-49	19-48	
	K					75	33	
	Cs					91	30	
	Li					40	69	
	Li	Conventional wet impregnation				35	37	
	Li	Mechanical mix				47	30	
Fe	Cu/K	Wet impregnation	2	1	300	63.9-88.1	17.7-40.6	(Kang et al., 2008)
Fe	Co and Al	Step impregnation	2	2	210-250	41.7-73.1		(Alkhimov et al., 2013)
Fe	Cu and K	Incipient wetness impregnation	2	19	279-284	22.6-72.4	41.2-78.2	(Baranak et al., 2013)
		Sequential impregnation				97	29.6	
		Physical admixing				22.7/43	46.5/48	

		Dealumination with oxalic				40.2/19.3	59.4/63.8	
Fe	-	Impregnation Mechanical mixing	1	1	300	57.6 63.6	62.7 54.1	(Xing et al., 2015)
Fe		Incipient wetness impregnation		20	270	19-32	56-60	(Da Silva et al., 2018)
Fe		Incipient wetness impregnation	2	1	260	-	61.4	(Javed et al., 2019)
		Hydrothermal synthesis					57.4-60.8	
Fe	- Na	Impregnation	1	3	280	75,7 65.2	76 58.3	(Mierczynski et al., 2019)
Fe	Na	Impregnation Simple mixing	1	1	325	55.4 64.1	10 15	(Di et al., 2019)
Fe	Na - Na - -	In situ crystallization	2	3	300		6.3 3.3 3.7 59.3 46 52.2	(Amoo et al., 2020)

Fe	H Na	Incipient wetness impregnation	2	21	300-350	14.4-21.8 9.5-16.3	8.3-12.7 11.1-14.4	(Liu et al., 2020)
Fe and Zn	Na Na/Li Na/K Na/Rb	Impregnation	0.5-2	1-3	200-340	87.6-95.4 50.2 49.9 53.5	29-55.8 35.6 36.7 37.2	(Hou et al., 2020)

The isoparaffin selectivity of the Fe/silica/SZ microcapsule catalyst synthesised by Xing et al. (2015) via in situ crystallisation was 46.5%, which shows that in situ crystallisation is a viable synthesis alternative to impregnation approaches. In support of this claim, Amoo et al. (2020) reported that zeolite-coated metal nanoparticles (NPs) showed exceptional performance and ultrastability in heterogeneous catalysis. The charcoal precursor used by Amoo et al. (2020) and the ambient pressure conditions reportedly prevented the migration of Fe NP throughout the in-situ crystallisation process and resulted in catalysts with tiny Fe NPs embedded in zeolite Y crystals. Compared to impregnation, the newly-developed catalyst series showed low activity for high C_{5+} hydrocarbons at FT, which means that in situ crystallisation is an inferior option.

Promoters are also used in conjunction with a support to improve functionality. The type and concentration of promoter used has a crucial impact on the selectivity of FT catalysts. The choice and concentration of promoters has a strong influence on the selectivity of methane and hydrocarbons. Alkaline promoters are typically used to increase basicity, which is associated with a change in selectivity, with a correlation seen between an increase in olefin selectivity and a decrease in methane selectivity (Shafer et al., 2019). For example, commercial iron catalysts all contain up to 3% (wt.%) potassium, which acts as a chemical promoter to enhance the electron donor effect of the iron active sites (Steynberg & Dry, 2004) and to increase the dissociation rate of CO (Shafer et al., 2019).

The use of potassium by Baranak et al. (2013), Hou et al. (2020) and Kang et al. (2008) showed an increase in the production of C_{5+} hydrocarbons. Copper is another metal that is used extensively as a promoter of iron-based catalysts to enhance the reduction of iron oxide in the reduction stage of the catalyst (Luk et al., 2019; Steynberg & Dry, 2004). Ruthenium is also well-suited to enhancing activity. It works at the lowest reaction temperatures and produces high molecular weight hydrocarbons (Abrokwah et al., 2019; Shafer et al., 2019).

This work focussed on LTFT operation and the LTFT iron-based catalyst supported on a clinoptilolite support.

7.2. Experimental

7.2.1. Catalyst Preparation

The incipient wetness impregnation method is a technique for imbuing a substance with water and is explained in the relevant body of scholarly work (Baranak et al., 2013; Javed et al., 2019;

Keyvanloo et al., 2018). It was used to deposit an iron precursor component onto the clinoptilolite support matrix to create the clinoptilolite supported iron catalyst. Prior to air drying at 120°C for an hour, the zeolite support underwent pre-treatment by blending it with distilled water (1:1). Calcination at 400°C for 16 hours was then carried out. Material that had been calcined was ground into particles ranging from 0.5 to 1 mm in size. To achieve a 10% iron metal loading by mass, a $Fe(NO_3)_3$. $9H_2O$ solution was impregnated into the treated support. The finished product was then dried in air for 16 hours at 120 °C, before it was calcined again for 6 hours at 400 °C.

7.2.2. Catalyst Characterization

A Rigaku XRD instrument with a scintillation counter detector was employed to characterize the X-ray diffraction (XRD) patterns. Powdered samples were scanned at a rate of 0.2°/min in the 0°–75° 2 range. A K-beta filter was added to the XRD apparatus equipped with a rhodium tube. The average size of the crystallites was calculated using the diffraction peaks. The physicochemical characteristics of the catalyst were examined using the Brunauer-Emmett-Teller (BET) and XRD analytical techniques. Other studies have used similar strategies for purposes of characterization.

Before analysis, 8 hours of degassing under vacuum at 190°C was done to remove moisture. The specific surface area and pore volume of the iron catalyst were determined using BET analysis. A TriStar II Micromeritics - Surface Area and Porosity analyser was used to determine the catalyst surface area and porosity. Hydrogen temperature-programmed reduction (H_2 -TPR) was utilized to assess the reducibility of the catalyst. The calcined catalysts were investigated using a Micromeritics Autochem ll 2920 machine. 50mg of samples were put into a quartz U-tube. To eliminate impurities and moisture, the catalyst was flushed with argon, while the temperature was increased to 150°C at a rate of 10°C /min; it was maintained at that temperature for 30 minutes. After the sample adjusted to the temperature of the surrounding air, with flowing argon being used, the gas was changed to a 10% H_2 in the argon mixture. The temperature was increased to 950°C at a 10°C /min ramp rate. The variations in the thermal conductivity between the inlet and the exhaust gases was used to monitor H_2 consumption using TCD during the experiment. X-ray fluorescence (XRF) analysis of the clinoptilolite support and 10% Fe/Clino catalyst was done using a Malvern Panalytical MagiX PRO, which is a

wavelength-dispersive device. After 30 minutes at 930°C in air, the loss on ignition (LOI) of the samples was determined; XRF analysis of the principal elements was conducted after borate fusion.

7.2.3. Catalytic testing

For the FT reaction and catalyst reduction, mass flow controllers were used to feed synthesis gas with H_2:CO:N_2 = 6:3:1 and reducing gases to a stainless-steel fixed bed reactor. Within the reactor, the synthesis gas input composition corresponded to a varying partial pressure of P_{H_2}, P_{CO} and P_{N_2} = 0.2 bar. Figure 7.1 is a schematic illustration of the catalyst test setup.

One gram of Fe-Clino catalyst was added to the reactor. The catalyst was dried under nitrogen flow at a temperature of 120 °C for 2 hours at ambient pressure. This was carried out in order to eliminate any moisture that may have accrued when loading the catalyst.

The catalyst was then reduced under similar conditions as those used in the drying process, but at an elevated reactor temperature of 440°C, at a rate of 10°C/min. The reduction temperature for the iron-based catalysts was set at 440°C, based on the H_2-TPR characterization results. The catalyst was reduced using H_2. The system was fed synthesis gas for the remainder of the investigation during the FT reaction. After reduction, the FT reaction began when the reactor pressure was elevated from atmospheric pressure, while the feed continued to flow through the system. the FT tests were conducted in Design Expert for 450 hours on stream, using the reaction parameters listed in **Table 7.3.** The DOE section deals with the results generated by these FT runs.

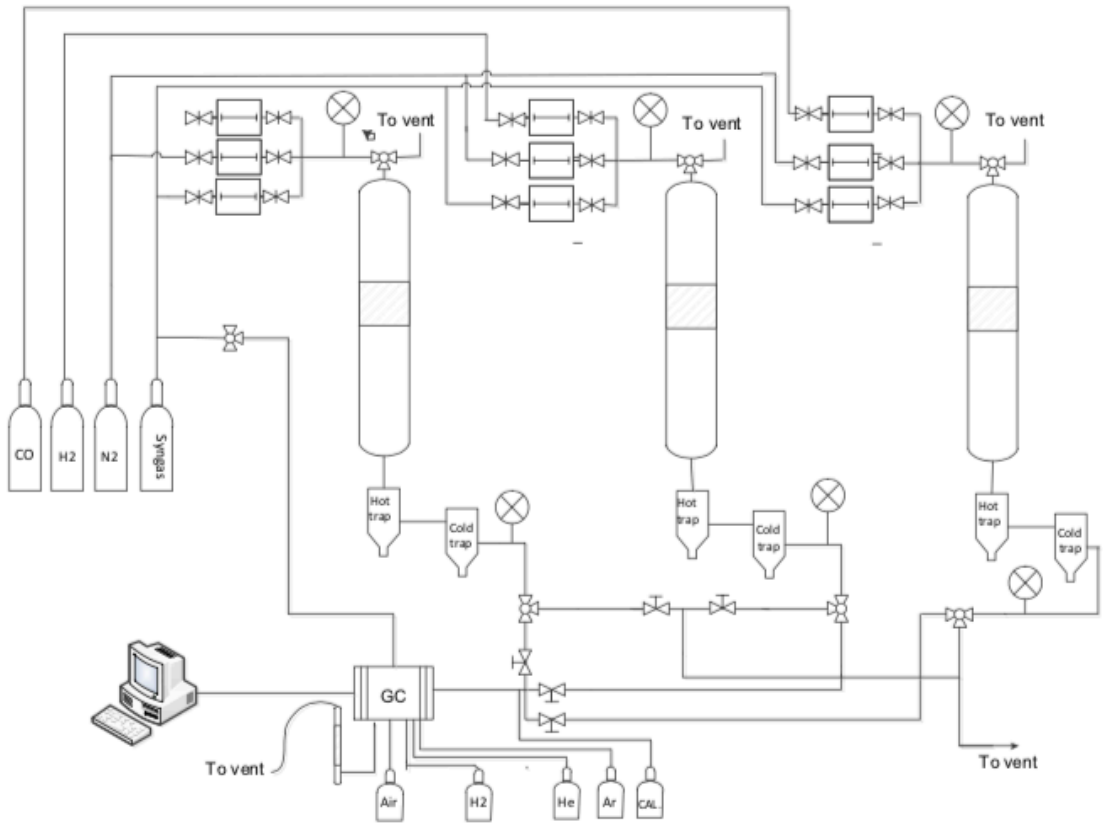

Figure 7.1: Flow scheme of the FT rig with a fixed bed reactor (only one reactor used)



Fixed bed reactor

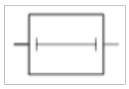

Mass flow controller
Brooks SLA5850



3-way valve
Swagelok



Back pressure regulator



2-way valve
Swagelok

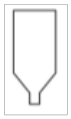

Knock out pots



Non return valve
Swagelok

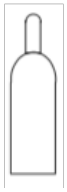

Gas Cylinder

7.2.4. Design of experiment using RSM

Hydrocarbon production from synthesis gas over an iron-impregnated clinoptilolite support catalyst was optimised using RSM. The reaction pressure, reaction temperature, gas rate and H_2:CO molar ratio were assessed as the explanatory variables; the molar CO conversion, the methane yield (CH_4), the yield of light hydrocarbons (C_2-C_4) and the heavy hydrocarbons yield (C_{5+}-C_∞) were the response variables. Even though the reaction temperature was difficult to control, due to the narrow temperature range, the component was investigated. **Table 7.3** details the various explanatory variables used for the FT process.

Table 7.3: DOE reaction parameters and limits

Factor	Name	Minimum	Maximum
1	H_2/CO	1	2.2
2	Temperature	225	300
3	Pressure	8	19
4	Gas speed	700	2800

Twenty distinct test sets were developed. As illustrated in **equation 7.9**, each FT response was used to develop a mathematical model that uses a second-order polynomial equation to relate hydrocarbon production to the independent reaction variables (Li et al., 2021; Montgomery, 2013):

$$f = a_0 + \sum_{i=1}^{m} a_i Z_i + \sum_{i=1}^{m} a_{ii} Z_i^2 + \sum_{i<j}^{m} a_{ij} Z_i Z_j \qquad (7.9)$$

Where: f is the anticipated response value; 0, I ii and ij denote the constant term and coefficient in the derived model equation for linear, quadratic and interaction terms, respectively.

The number of independent process variables used for process optimization was taken into consideration. Furthermore, ANOVA was conducted to evaluate the optimization outcomes. Design Expert software was used to generate the expected values. The analysis of variance test, the significance of variance test, and the first-order coefficient significance test regression

equation are all shown in the ANOVA data analysis. The dependability of the model was then put to the test.

7.2.5. Descriptive statistics and model fitting

Design Expert software version 13 was used to perform regression analysis on the experimental data to ensure it matched the equations. The (R^2) value of the correlation coefficient can be used to gauge the validity of a statistical model when assessing it. Analysis of variance can be used to assess the applicability of the ANOVA-established equations.

7.3. Results and Discussion

In order to minimize CH_4 and maximize C_{5+}- C_∞ conversion, the findings and discussion explore the aforementioned operating settings (temperature, pressure, GHSV, and H_2:CO molar ratio) in order to determine the ideal operating state.

The matrix for the different experimental conditions is given in **Table 7.4** with a total of 20 experimental series having been set up. **Table 7.4** shows the experimental and predicted values for the different experimental conditions. External studentised residuals were used to assess the regression assumptions and to map all the different normal distributions onto a single standard normal distribution, which made it easier to look for problems during analysis. **Figure 7.2** provides the normal probability plots that indicate whether the residuals followed a normal distribution or not.

Table 7.4: Experimental responses and predicted responses using RSM

Run	Factor 1 H_2/CO	Factor 2 Temperature	Factor 3 Pressure	Factor 4 Gas speed	Response 3 CH_4		Response 4 C_2-C_4		Response 5 C_{5+}-C_∞	
	mol/mol	°C	bar	h^{-1}	Predicted	Actual	Predicted	Actual	Predicted	Actual
1	2	225	13	2100	6.6669	6.85	16.2435	16.69	54.1958	51.9
2	1.5	281	19	1400	7.73483	7.8	18.84	19	35.0466	35.5
3	2	263	13	2100	5.5273	5.33	13.4641	12.98	51.2519	54.4
4	2.5	281	19	2800	6.87471	7.36	16.7478	17.93	52.3973	51.1
5	2.5	281	8	2800	8.332	8.36	20.2926	20.36	51.1071	53.3
6	2.7	244	8	1400	4.67775	5.51	11.3941	13.42	51.9773	54.3
7	1.5	281	8	1400	7.23675	7.87	17.6297	19.17	43.6113	44.1

8	2	263	13	2100	5.5273	5.75	13.4641	14.01	51.2519	52.1
9	2.5	281	13	1400	7.57479	7.43	18.452	18.1	54.3018	47.1
10	2	263	8	700	6.2495	5.83	15.2205	14.2	62.3906	62.3
11	1.5	244	8	2800	7.06139	6.87	17.1962	16.73	60.7504	63.7
12	2	263	13	2100	5.5273	5.68	13.4641	13.84	51.2519	50.3
13	2	300	19	2100	7.10198	6.49	17.3005	15.81	46.4016	48.2
14	1.5	281	8	2800	7.33156	7.2	17.859	17.54	57.6093	55.8
15	1.5	281	19	2800	7.82964	7.9	19.0693	19.24	49.0446	48.8
16	2	263	19	2100	6.14157	5.48	14.9625	13.35	49.268	47.9
17	2.5	244	13	1400	4.74502	3.96	11.5626	9.65	56.8936	57.1
18	1.5	244	19	1400	3.85255	4.13	9.38484	10.06	69.3914	69.9
19	2	263	13	2100	5.5273	5.28	13.4641	12.86	51.2519	46.4
20	2.5	281	19	1400	6.7799	7.22	16.5185	17.59	55.0056	60.2

7.3.1. Normal probability plot of effects

The process of screening (finding statistically significant factors) in which replicated factorial design was applied, occasionally yielded high order interactions. A normal probability plot was constructed (based on the coefficient of effects) to estimate the most important effects - degrees and growing probability (Filliben, 1975; Shapiro & Wilk, 1965). A normal probability plot depicts the relationship between real value evaluations and the accumulative normal probability (Montgomery, 2013). The normal probability of the residuals of carbon efficiency and wax production are shown in **Figure 7.2**. The normal probability plots have a straight line of best fit, which means that the hypothesis is correct: the models are adequate. Another indication of the adequacy of the models is the pattern of residual and projected value shown in **Figure 7.3,** which, although not limited in accuracy, is still within the limiting constraints.

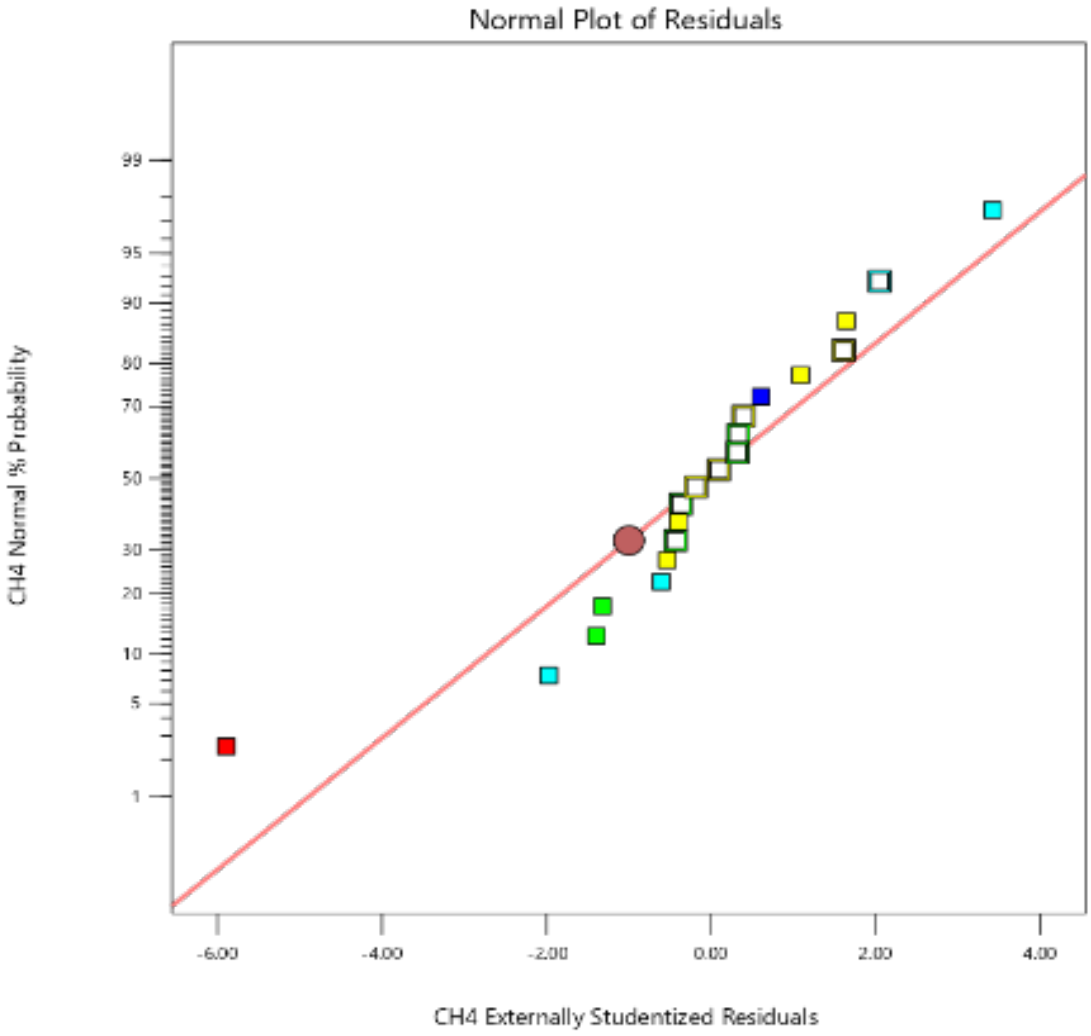
Normal Plot of Residuals
CH4 Normal % Probability
99
95
90
80
70
50
30
20
10
5
1
-6.00
-4.00
-2.00
0.00
2.00
4.00
CH4 Externally Studentized Residuals

(a)

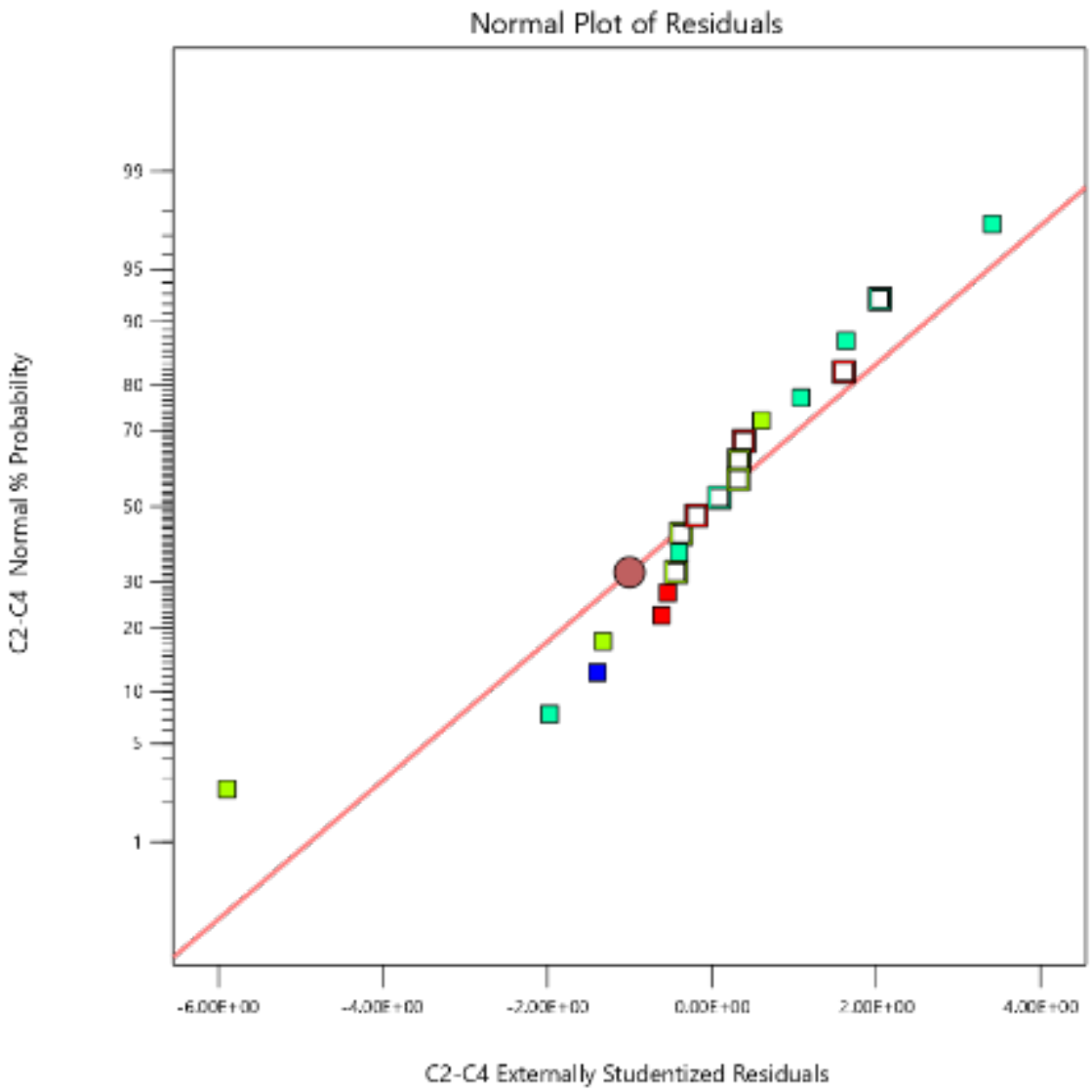
Normal Plot of Residuals
C2-C4 Normal % Probability
99
95
90
80
70
50
30
20
10
5
1
-6.00E+00
-4.00E+00
-2.00E+00
0.00E+00
2.00E+00
4.00E+00
C2-C4 Externally Studentized Residuals

(b)

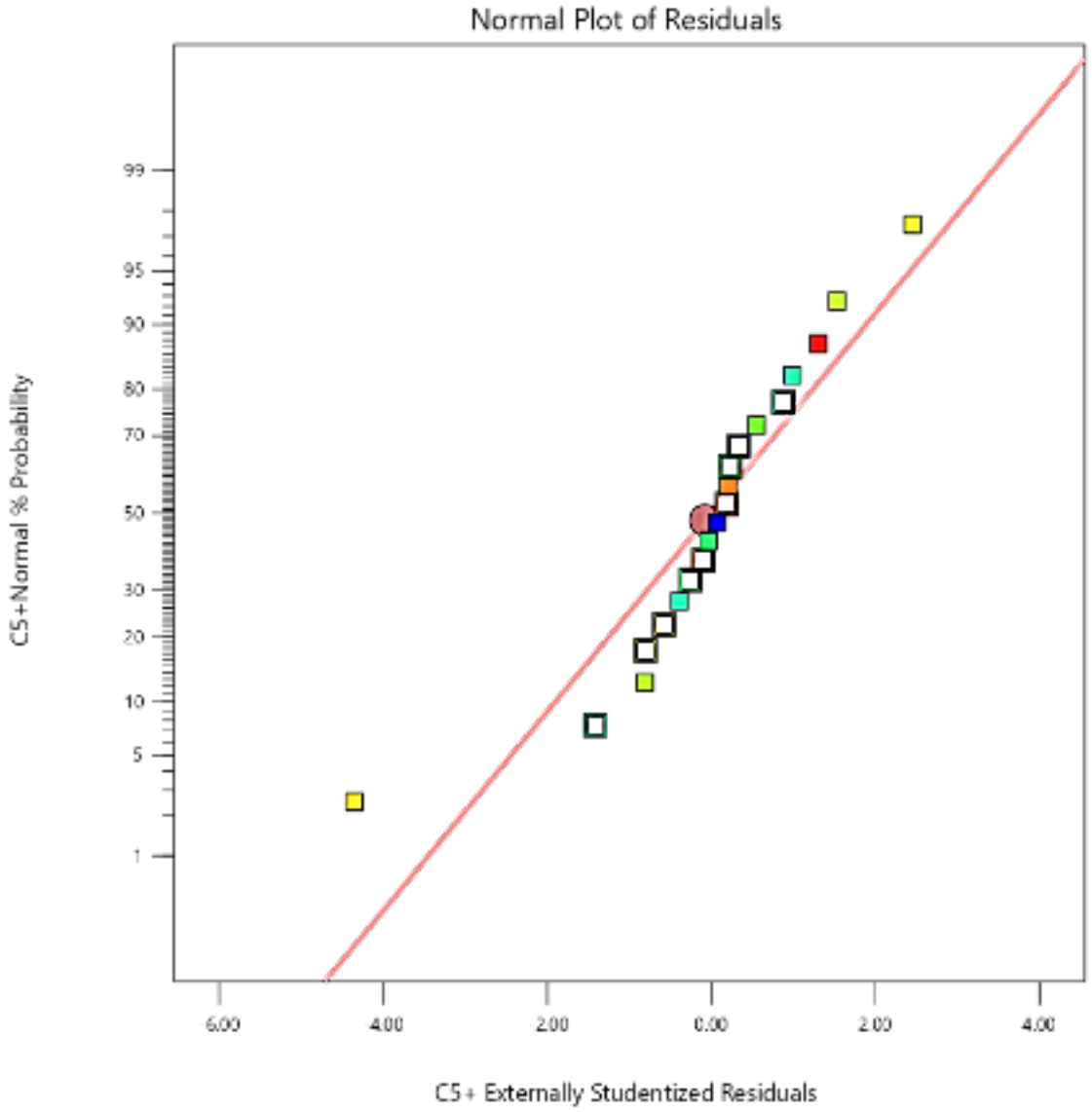

(c)

Figure 7.2: Normal probability residual plot: (a) CH_4 selectivity; (b) C_2-C_4 selectivity; (c) C_{5+}-C∞ selectivity

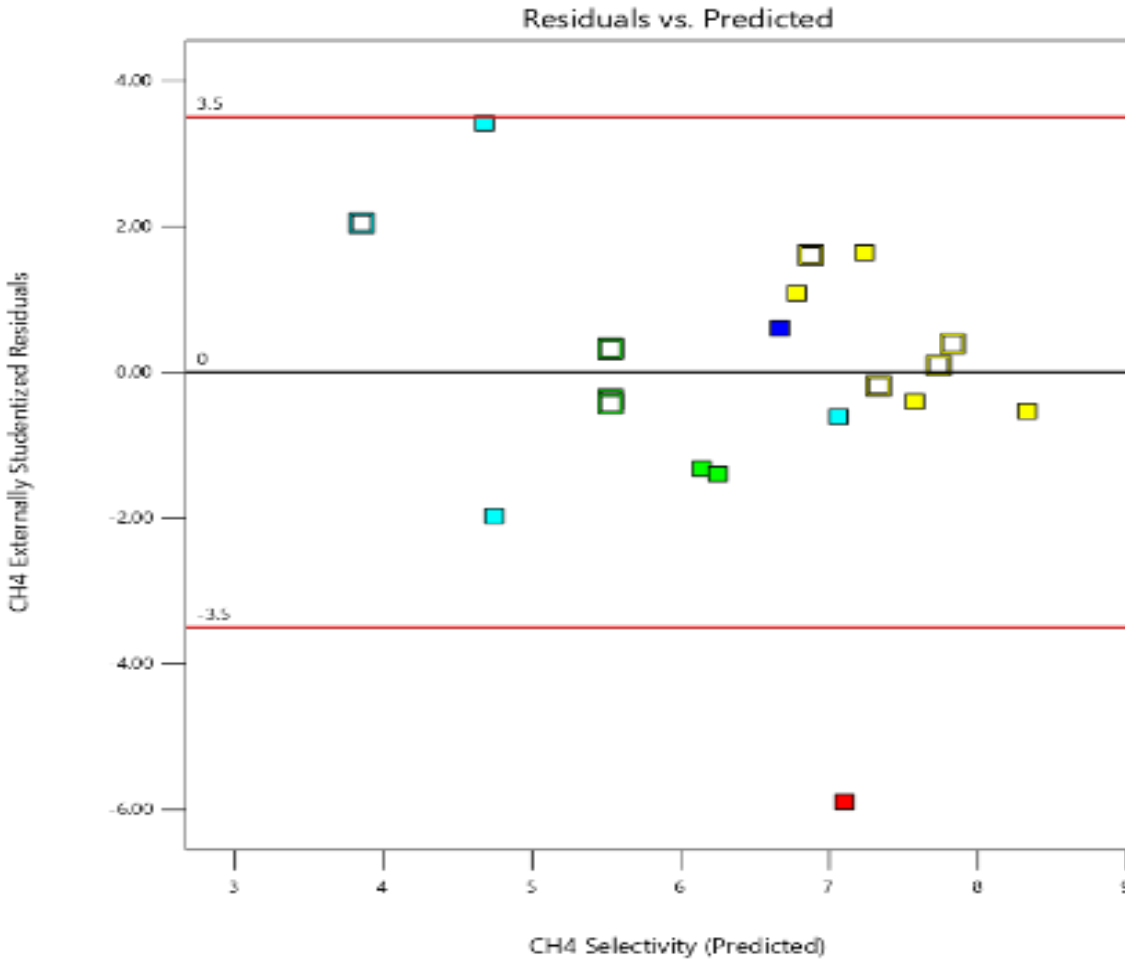
Residuals vs. Predicted
CH4 Externally Studentized Residuals
CH4 Selectivity (Predicted)
4.00
2.00
0.00
-2.00
-4.00
-6.00
3.5
0
-3.5
3
4
5
6
7
8

(a)

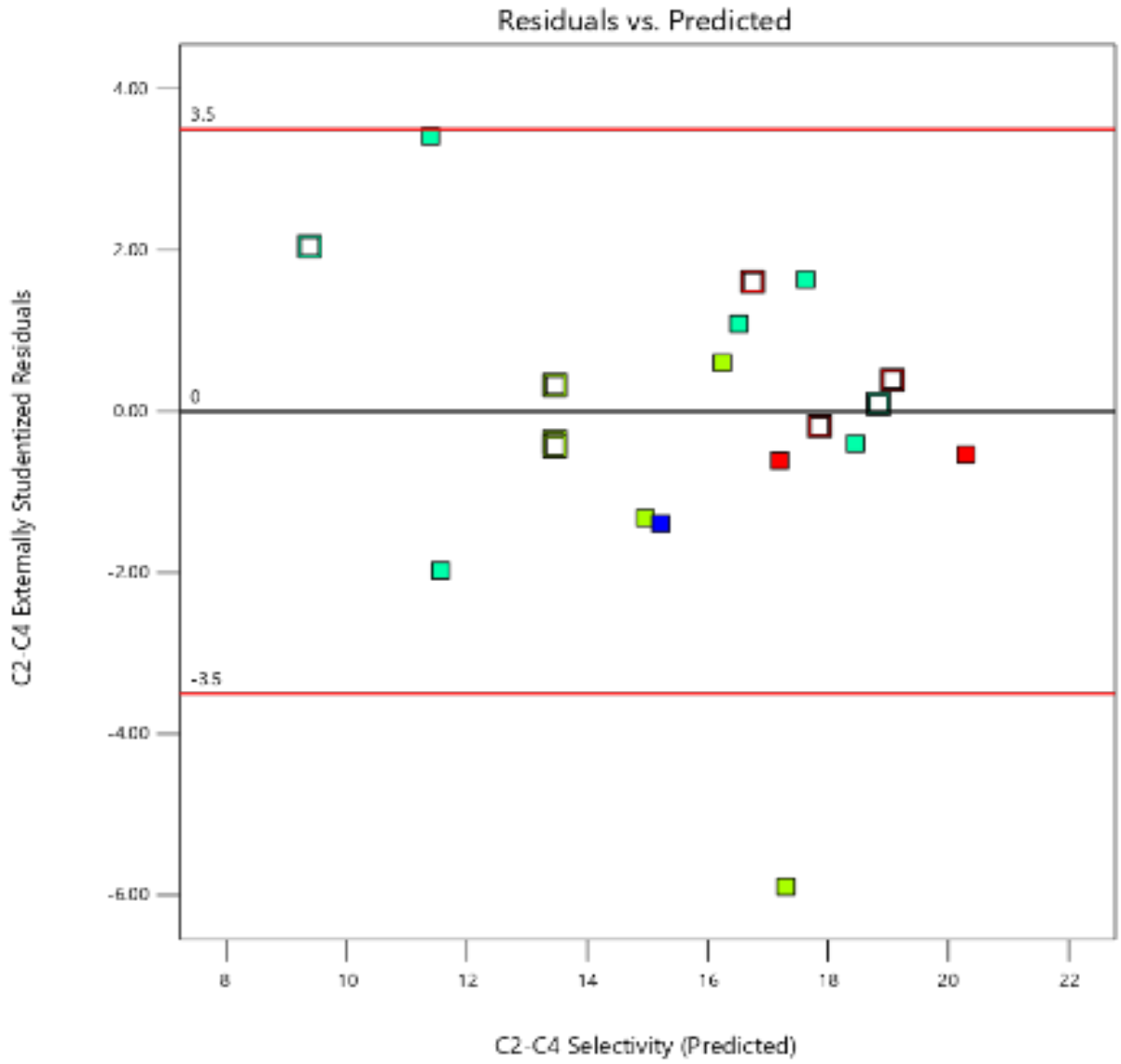
Residuals vs. Predicted
C2-C4 Externally Studentized Residuals
C2-C4 Selectivity (Predicted)
4.00
2.00
0.00
-2.00
-4.00
-6.00
3.5
0
-3.5
8
10
12
14
16
18
20
22

(b)

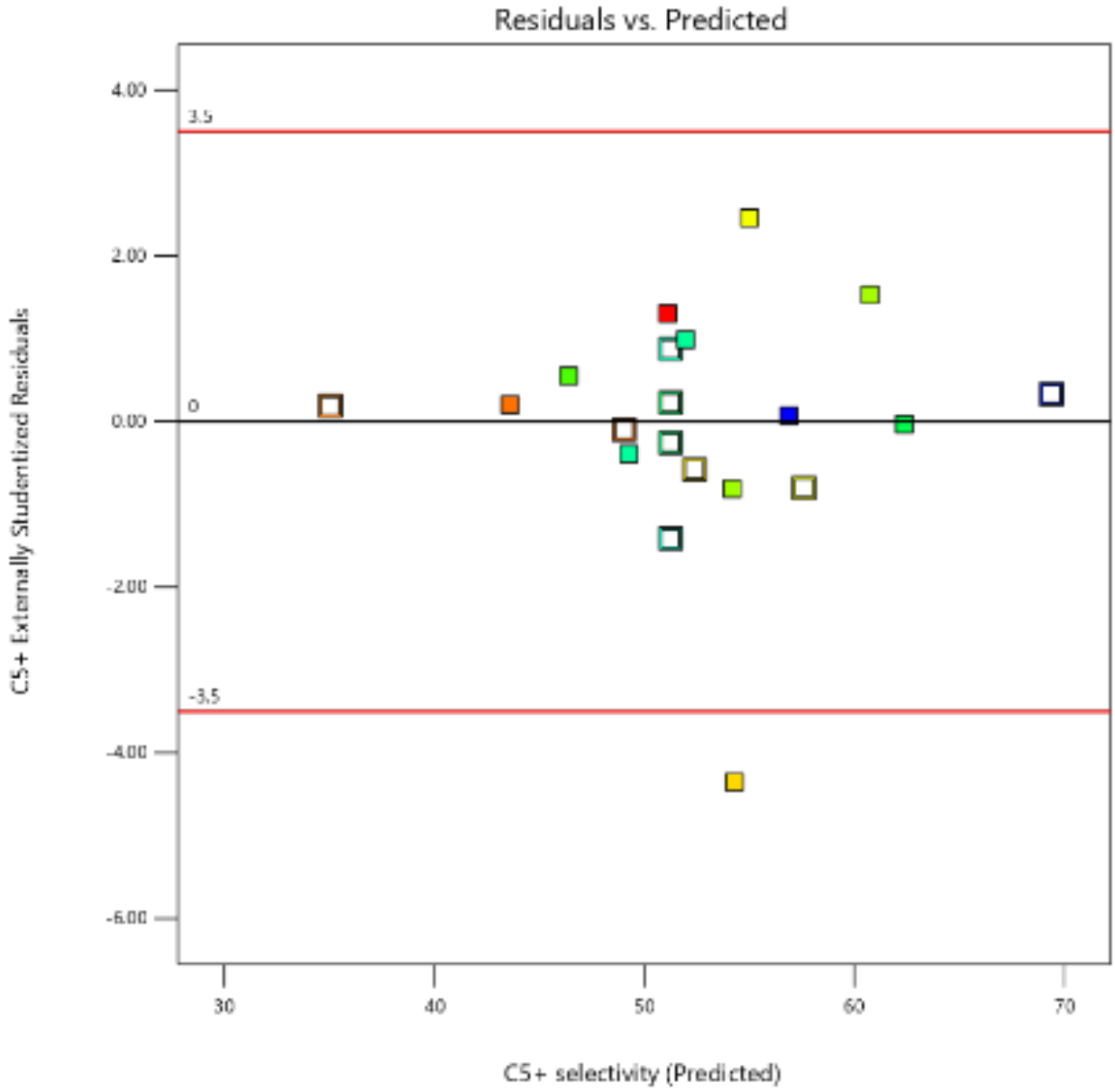

(c)

Figure 7.3: Residual versus predicted value: (a) CH_4 selectivity; (b) C_2-C_4 selectivity; (c) C_{5+}-C∞ selectivity

7.4. Effect of operational parameters (H_2/CO, temperature, pressure and GHSV)

This study looked into the effect on product distribution of various operating conditions. By altering the operating conditions, the distribution of FT products can be altered across a wide range of parameters (Keyvanloo et al., 2018; Mena Subiranas & Schaub, 2007; Xu et al., 2020). Synthesis of hydrocarbons is related to changes in the temperature, H_2:CO, pressure and

GHSV, which causes the main products of the reaction to undergo subsequent hydrogenation and results in hydrocarbons with a large molecular size and different carbon numbers.

7.4.1. Effect of H_2:CO on hydrocarbon selectivity

Figure 7.4 illustrates the influence of synthesis gas composition on FT for the H_2/CO inlet molar ratios studied. These results show that increasing the H_2/CO inlet ratio from 0.5 to 2 increases hydrocarbon production. For light hydrocarbons, this was significant; for heavy hydrocarbons, there was an inverse relationship: as the H_2/CO inlet ratio increased, the selectivity of C_5- C∞ decreased from 89% to 69%. A low H_2:CO ratio led to the production of low CH_4 and C_2-C_4 hydrocarbons, and high C_5-C_∞ hydrocarbons when H_2/CO = 0.5. The C_5-C∞ content decreased when the H_2/CO ratio increased to 2, while CH_4 and C_2-C_4 increased H_2 is responsible for the formation of paraffins from hydrocarbon chains. Consequently, an increase in the H_2/CO feed ratio increases the partial pressure of H_2 in the reactor, which increases the termination rate to paraffins and decreases the proportion of C_5-C_∞ hydrocarbons produced (Dry, 2002; Keyvanloo et al., 2018).

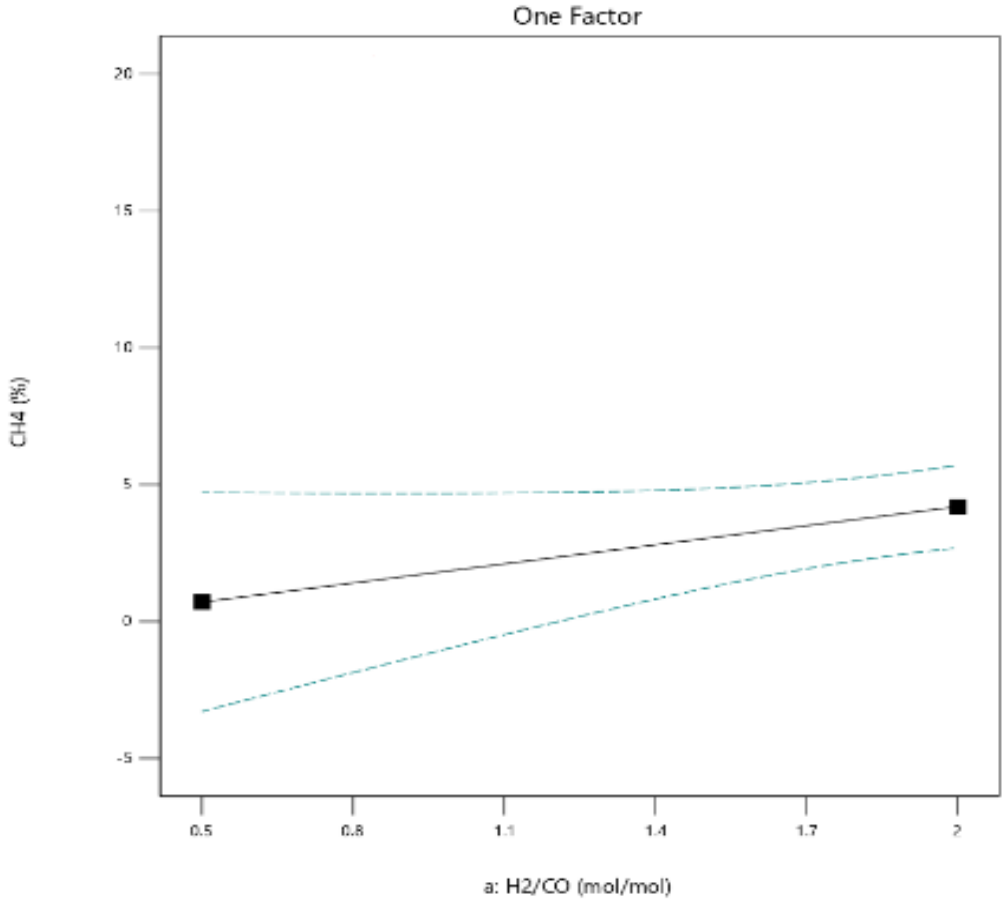

(a)

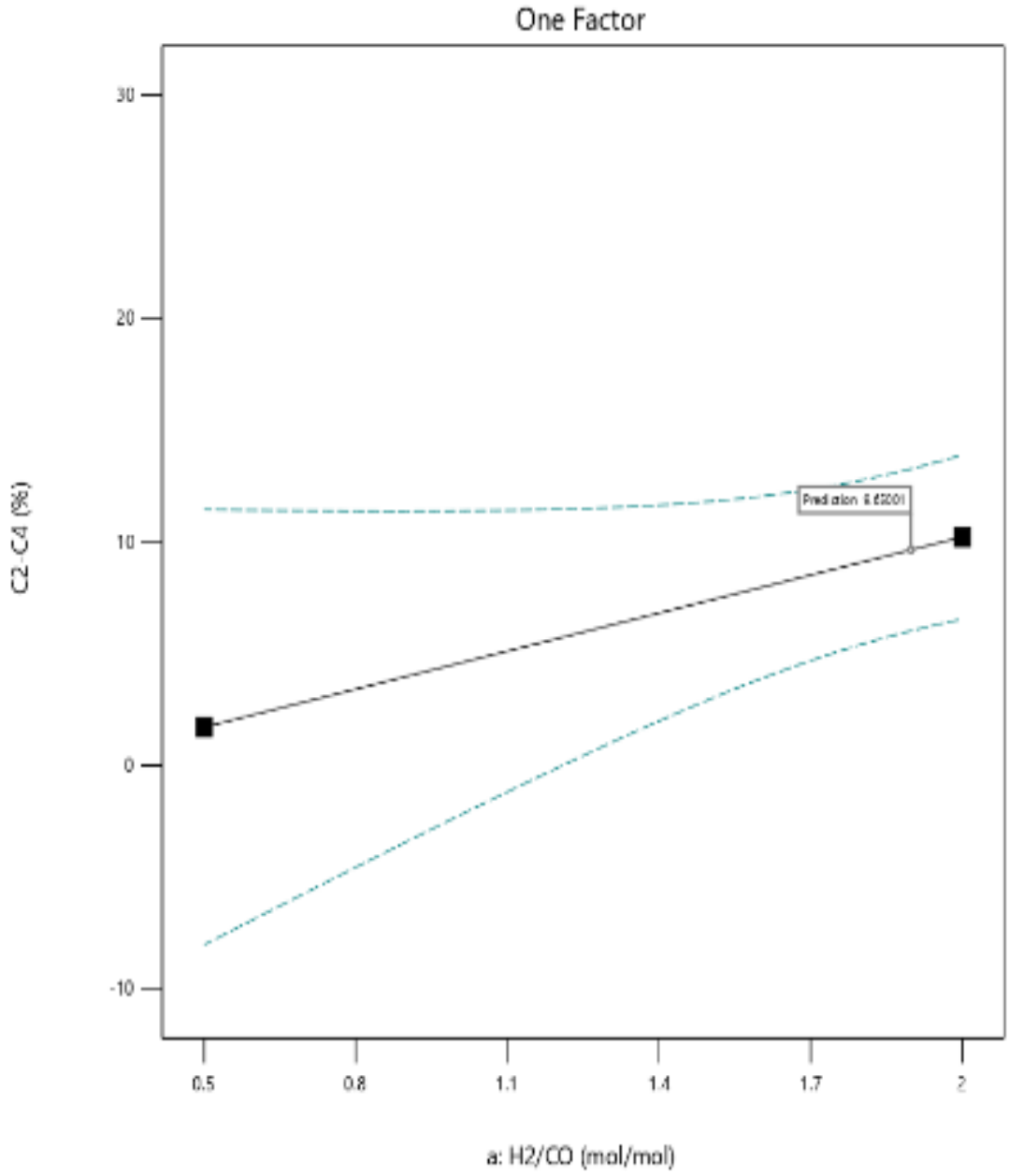

(b)

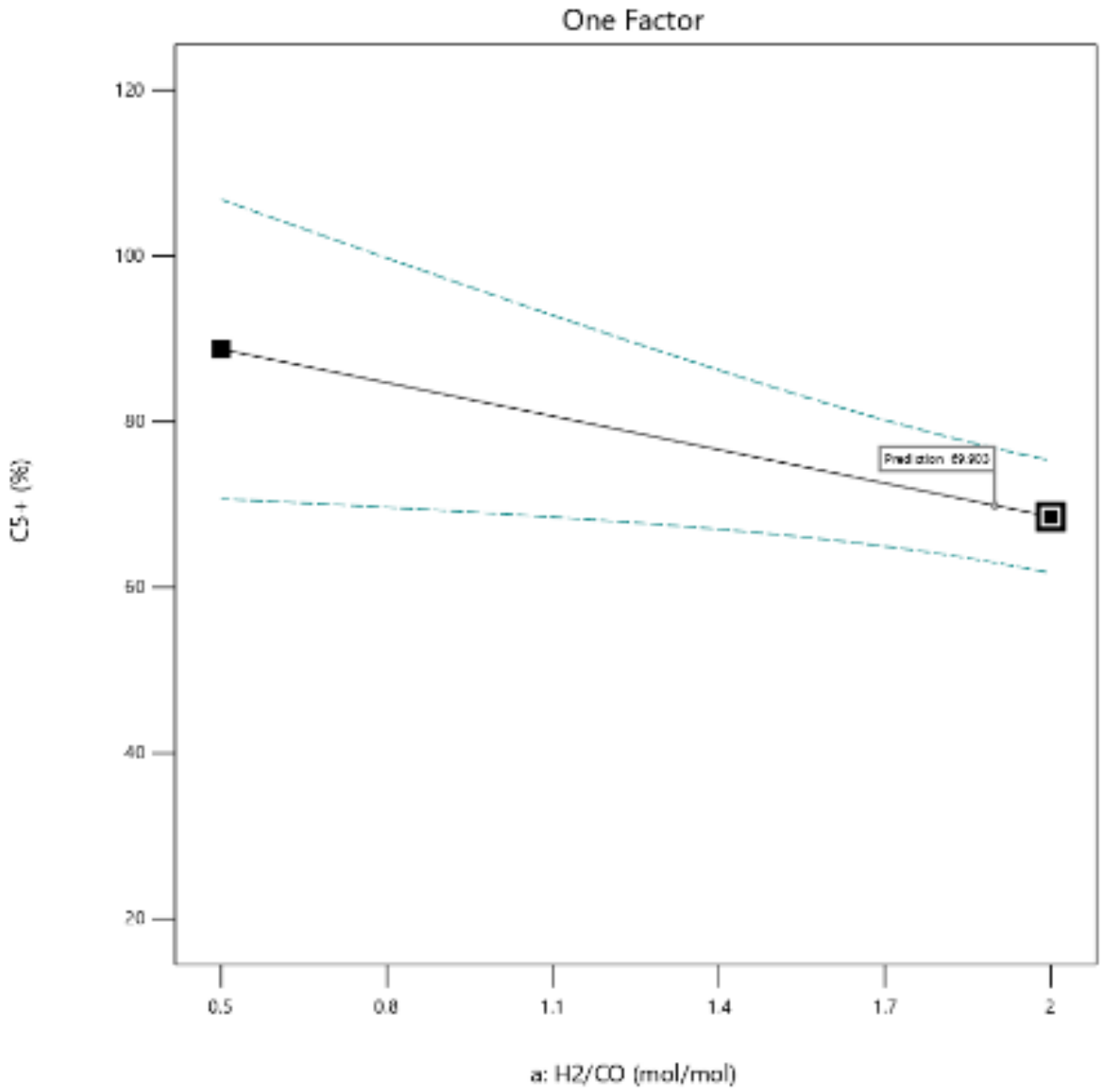

(c)

Figure 7.4: Effect of H_2:CO on hydrocarbon selectivity: (a) CH_4 selectivity; (b) C_2-C_4 selectivity; (c) C_{5+}-C∞ selectivity

As a result, the change of the H_2/CO inlet molar ratio affected the corresponding product distributions, and the best condition for the H_2/CO inlet is 1.90.

7.4.2. Effect of temperature on hydrocarbon selectivity

A higher reaction temperature was seen to have a significant effect on the hydrocarbon formation rate.

Hydrogenation was prevalent at a low temperature. As the reaction temperature increased, hydrogenation reduced and light hydrocarbon selectivity increased. An increase in temperature increased the selectivity of CH_4 and C_2-C_4, while the selectivity of C_{5+}-C_∞ dropped. Increasing the temperature of the FT process boosted selectivity for lighter hydrocarbons by a large margin. The influence of temperature on the FT process is shown in **Figure 7.5**.

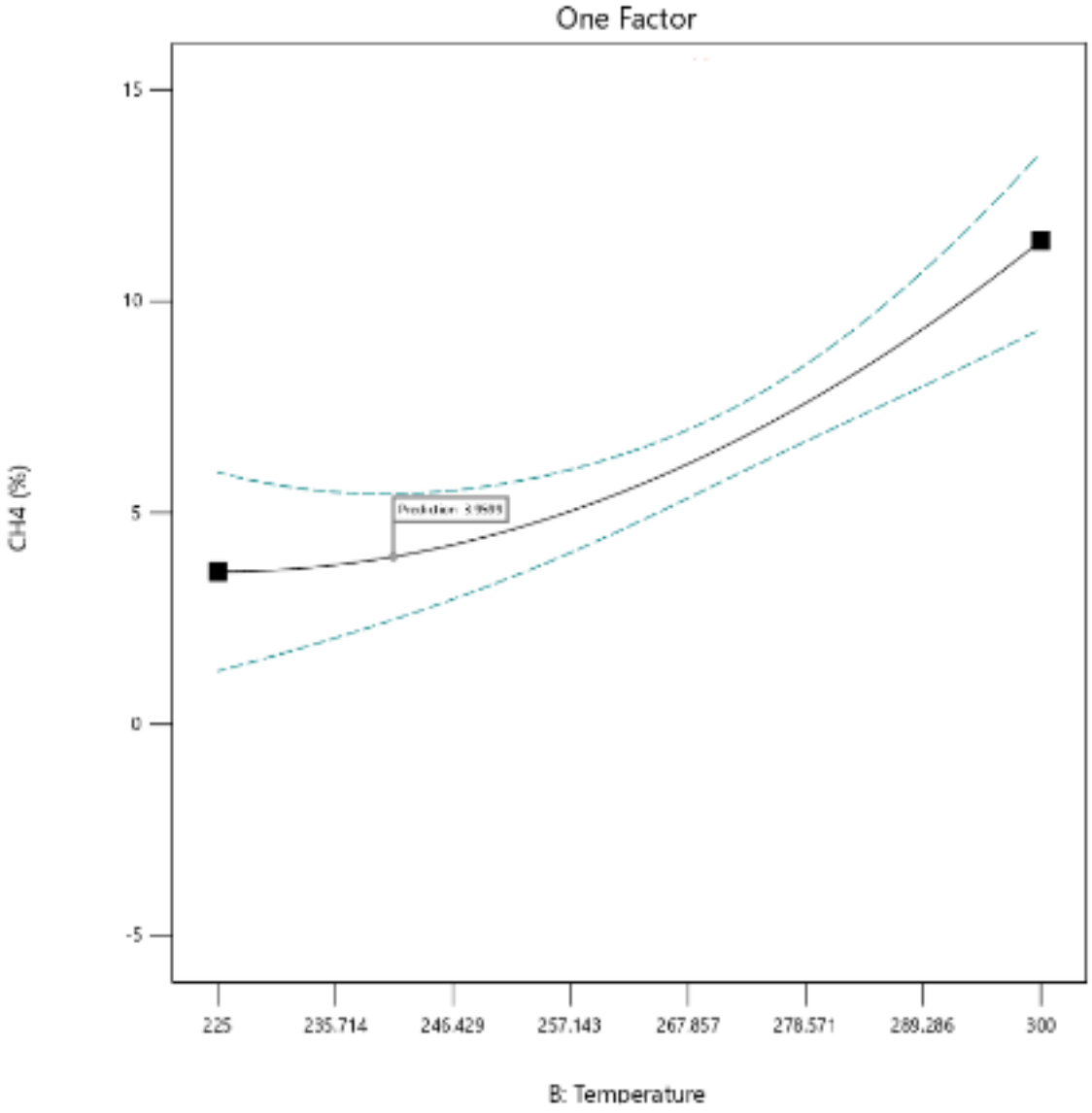

(a)

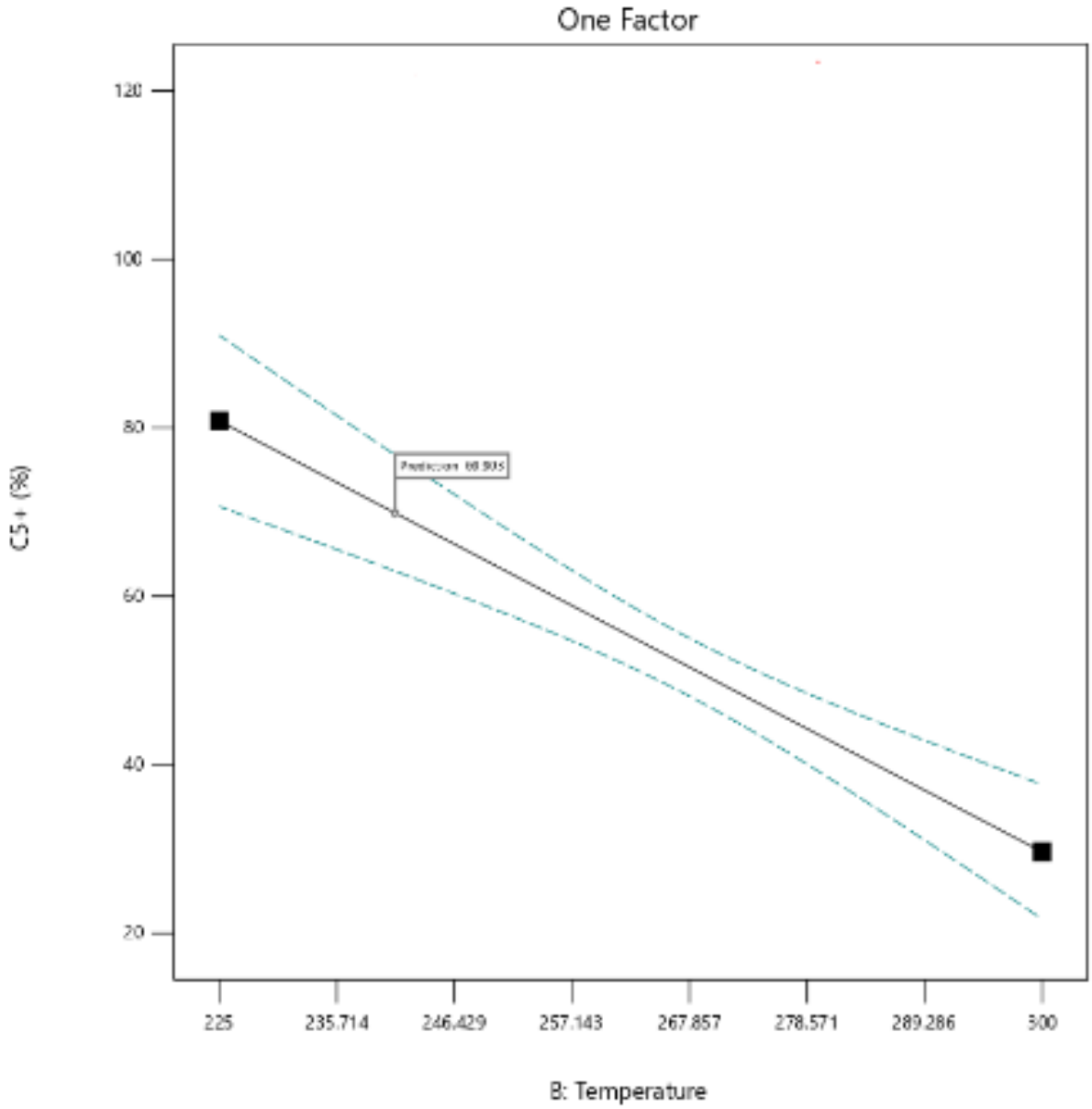
One Factor
120
100
80
60
40
20
C5+ (%)
225
235.714
246.429
257.143
267.857
278.571
289.286
300
B: Temperature

(b)

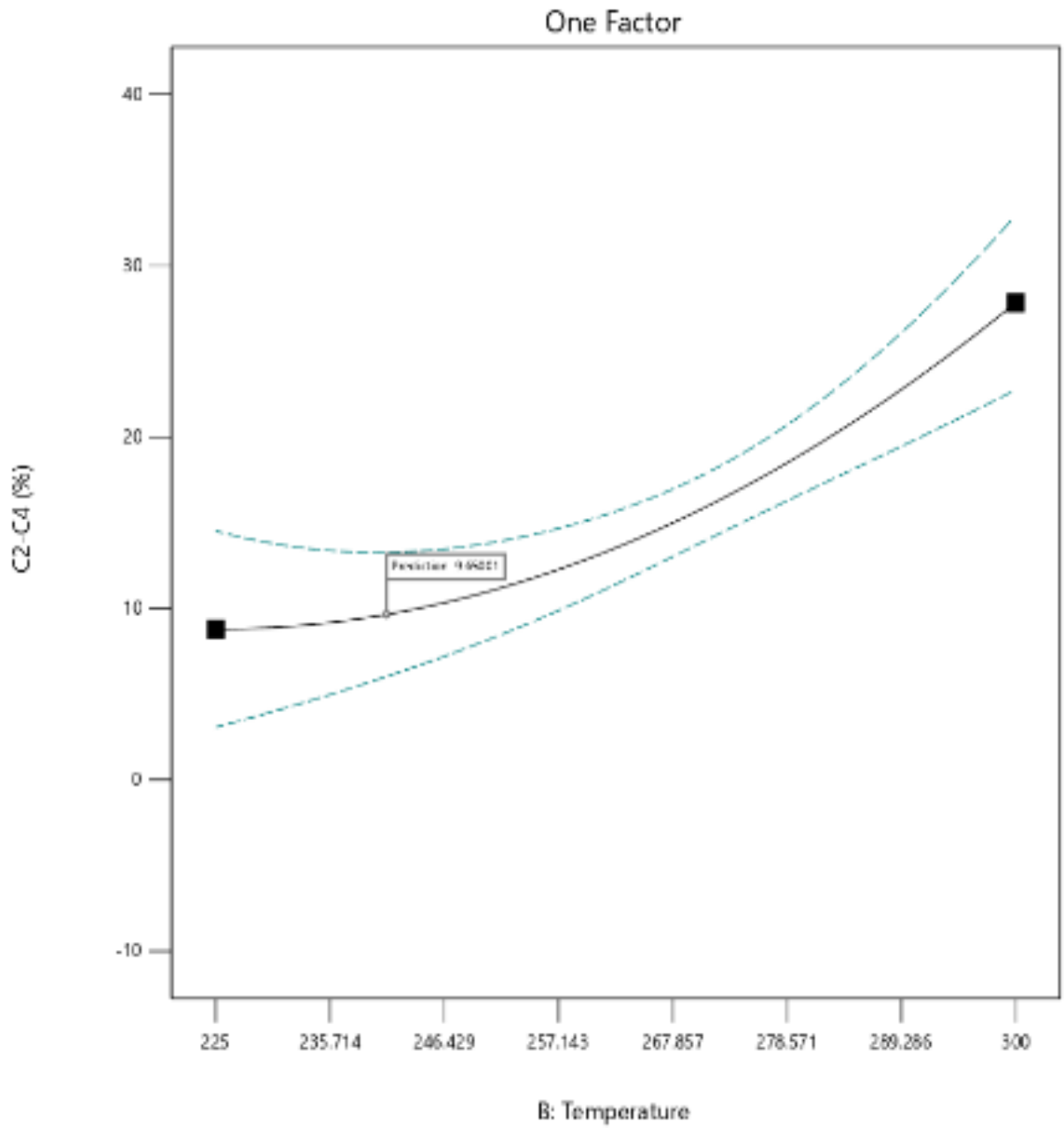

(c)

Figure 7.5: Effect of temperature on hydrocarbon selectivity: (a) CH_4 selectivity; (b) C_2-C_4 selectivity; (c) C_{5+}-C∞ selectivity.

Temperature is the most important variable in the FT process, as the FT reaction is often exothermic.

The temperature range for operating iron is in the LTFT range, which is between 200 and 250°C. However, iron-based catalysts can be used in the HTFT temperature range, which is between 300 and 350 °C, depending on the pre-treatment and formulation, as shown in the studies listed in **Table 7.2**. It is always observed that a higher reaction temperature promotes a

higher rate of CH_4 generation, due to a higher H_2/CO ratio in the reactor and lower chain growth probability (Baranak et al., 2013; Yao et al., 2011). Therefore, raising the temperature from 225°C to 300°C will result in selectivity for C_{5+}-C_∞ decreasing from 81% to 28%, and increasing exponentially for CH_4 and C_2-C_4 from 2.5% to 12% and from 8% to 28%, respectively.

7.4.3. Effect of pressure on hydrocarbon selectivity

In order to investigate the effect that pressure has on the FT process, several injection pressure levels were used, while the other operating conditions were kept constant. As can be seen in **Figure 7.6**, as total pressure increased, the CH_4 and C_2-C_4 conversion rates increased steadily, i.e. from 1% to 4% and from 2% to 10%, respectively, at a pressure of between 8 bar and 19 bar.

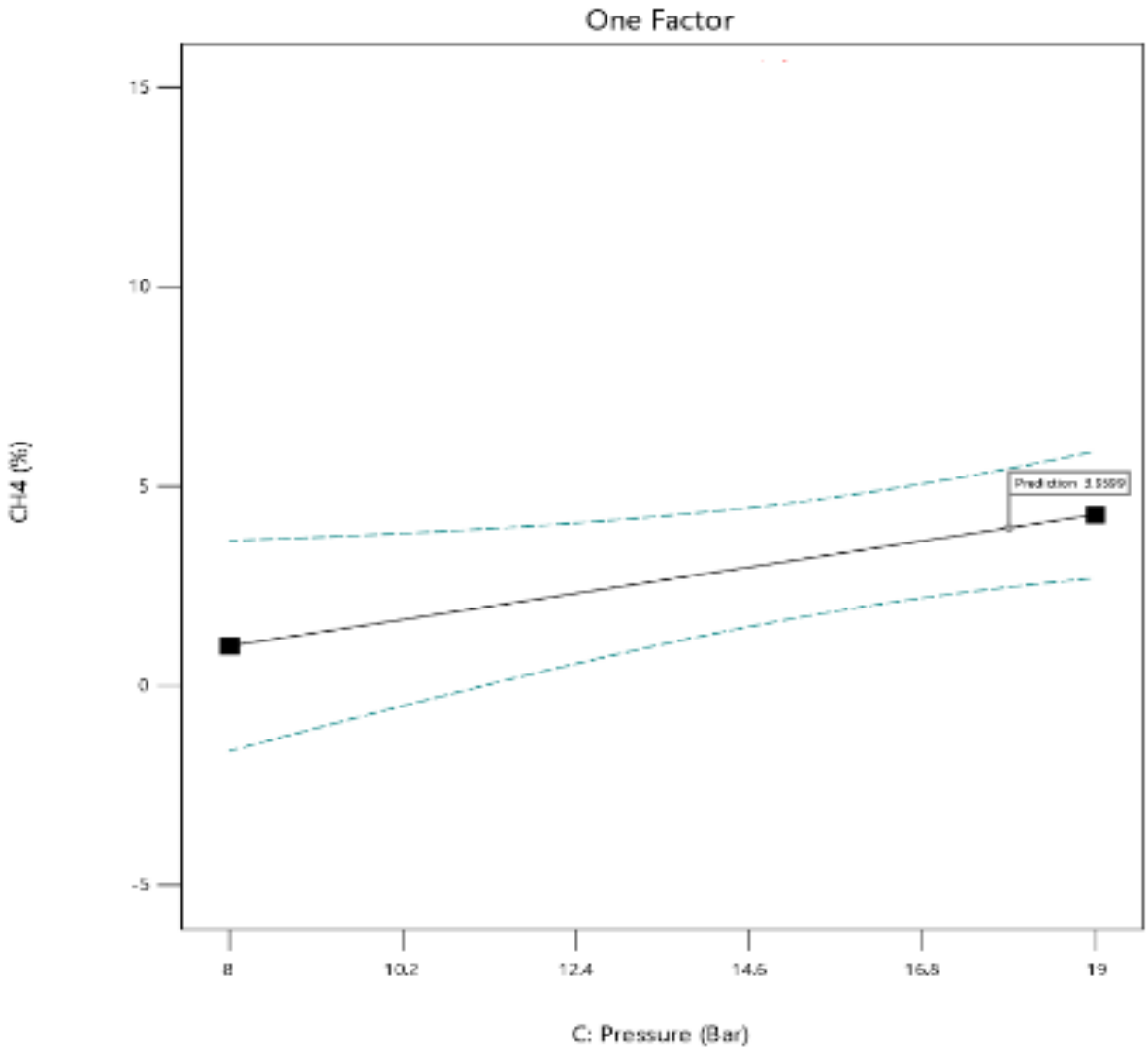

(a)

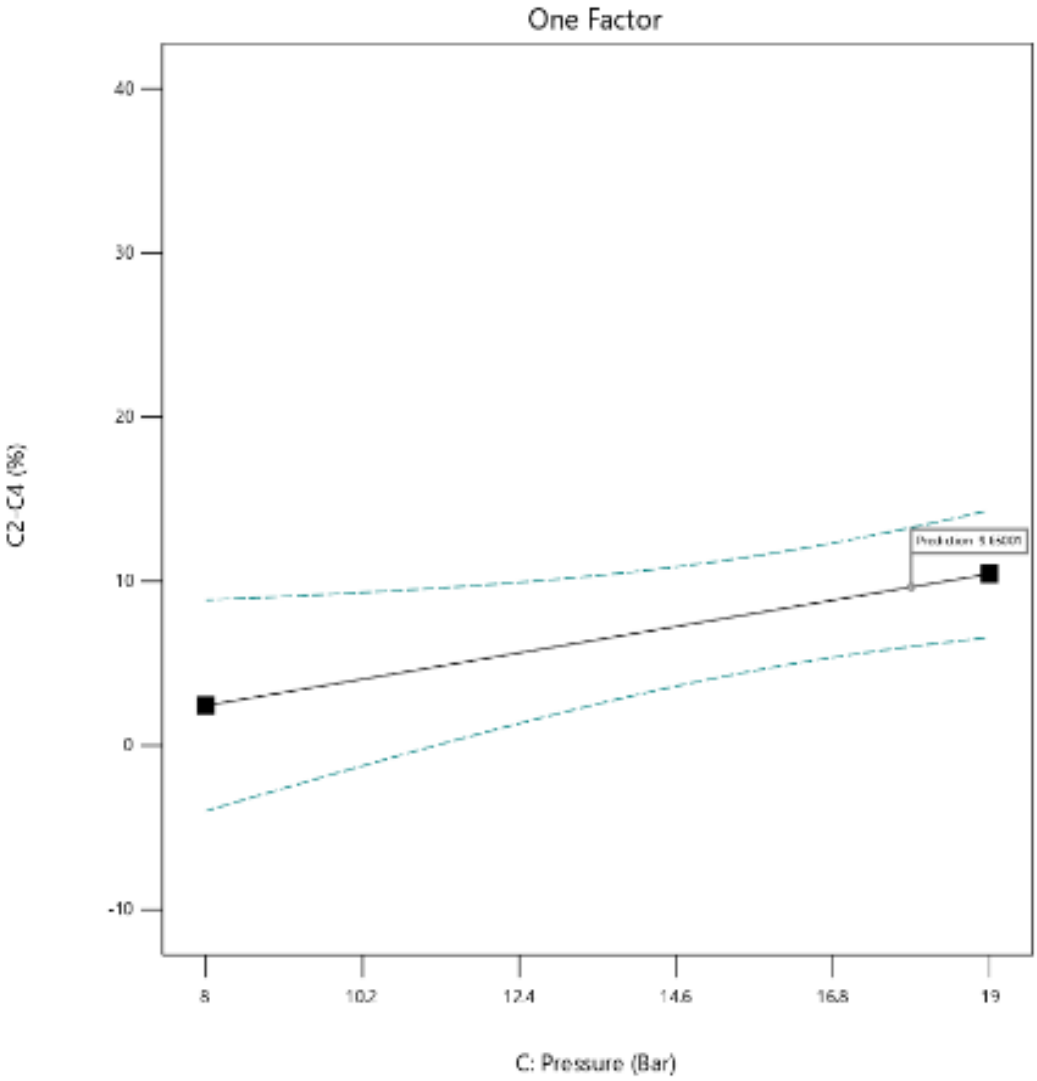
One Factor
C2 C4 (%)
40
30
20
10
0
-10
8
10.2
12.4
14.6
16.8
19
C: Pressure (Bar)

(b)

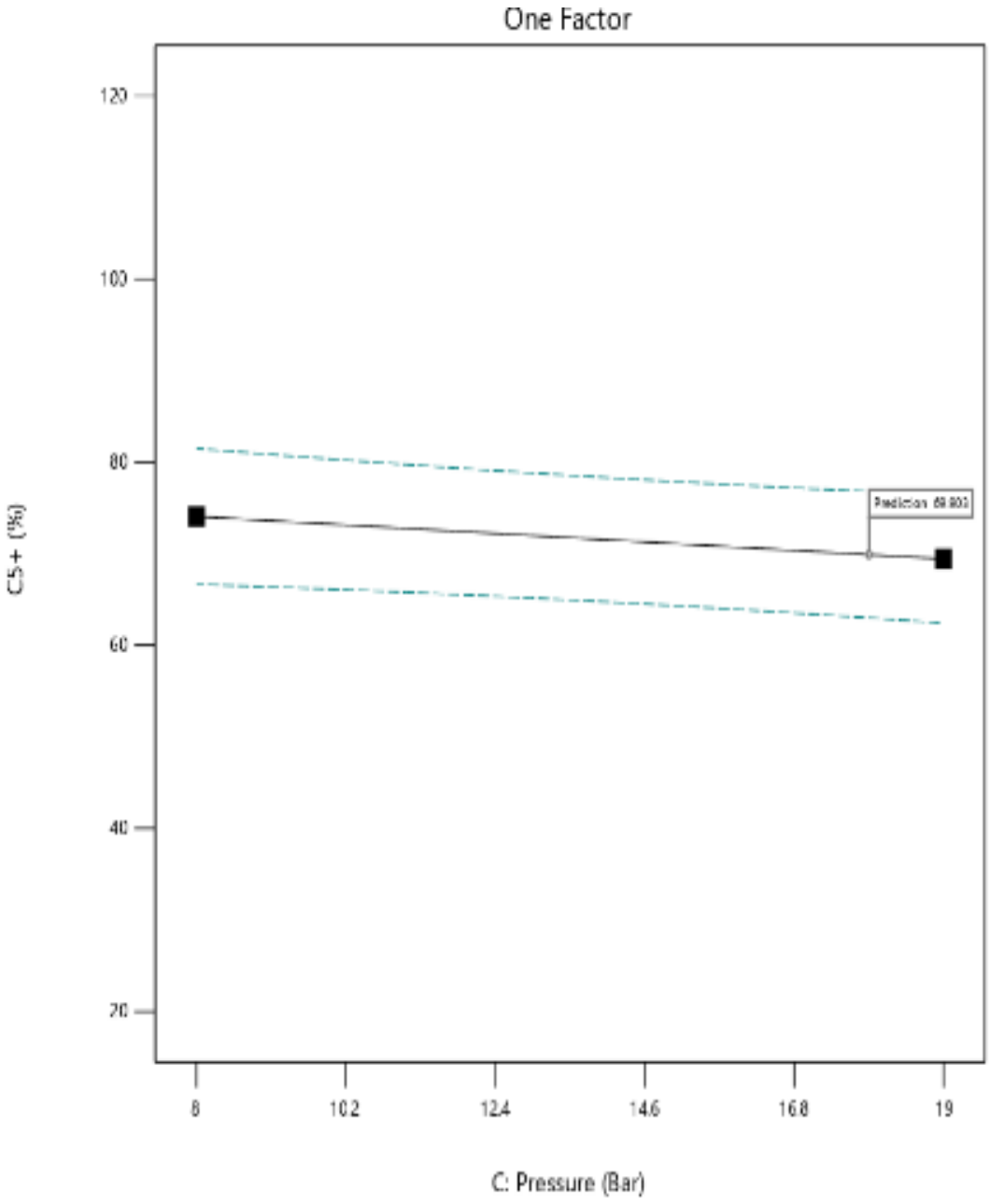

(c)

Figure 7.6: Effect of pressure on hydrocarbon selectivity: (a) CH_4 selectivity; (b) C_2-C_4 selectivity; (c) C_{5+}-C∞ selectivity.

Additionally, as the pressure is raised, selectivity to the heavier hydrocarbons drops from 74% to 64%. The availability of single CH_2- units on the catalyst surface at high pressure promotes chain growth, and may be the cause of the poorer selectivity to light products at a low pressure (Ngwenya et al., 2005; Ojeda et al., n.d.; Sari et al., 2009).

Under operational conditions, a very thin layer of the process end products coats the catalyst particles (Méndez & Ancheyta, 2019). Therefore, reactants must diffuse through this layer in order to reach the catalyst surface, whereas reaction products must do the same in the opposite direction in order to be desorbed (Van der Laan & Beenackers, 2011).

7.4.4. Effect of GHSV on hydrocarbon selectivity

The effect of gas velocity on the FT process is shown in **Figure 7.7**. When the space velocity was increased from 797 h^{-1} to 2500 h^{-1}, the C_{5+}-C_{∞} selectivity decreased from 78% to 44%. However, as the gas velocity increased, the selectivity of CH_4 and C_2-C_4 increased exponentially. With an increase in velocity, the residence time of the reactants and products decreased, which led to a decrease in CO conversion.

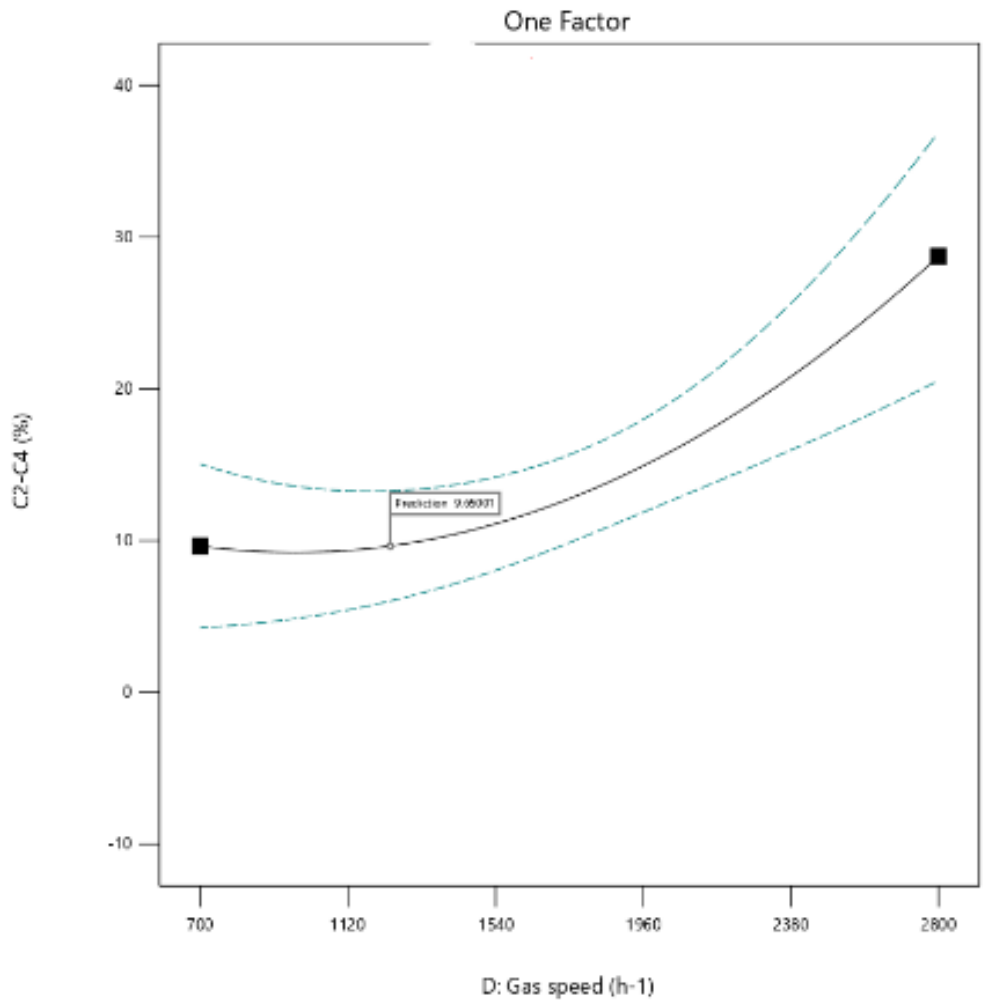

(a)

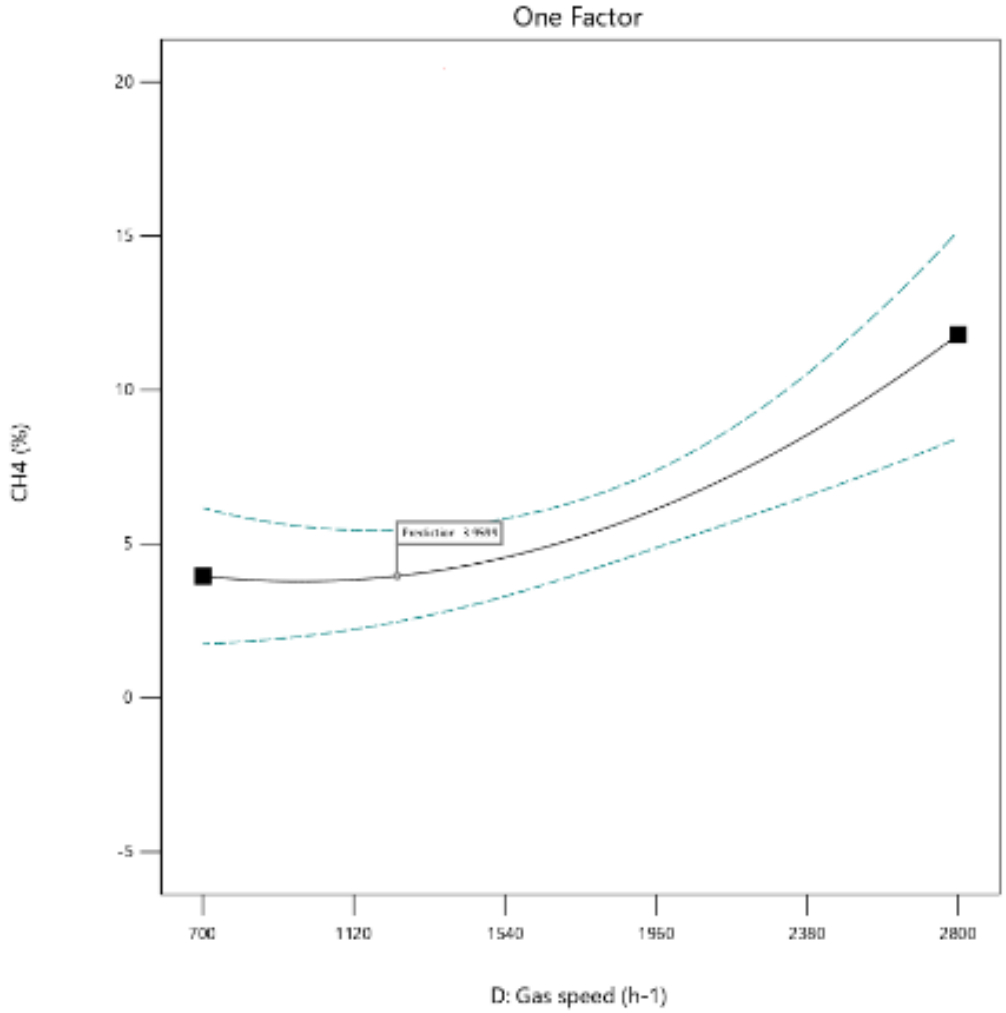
One Factor
20
15
10
5
0
-5
CH4 (%)
700
1120
1540
1960
2380
2800
D: Gas speed (h-1)

(b)

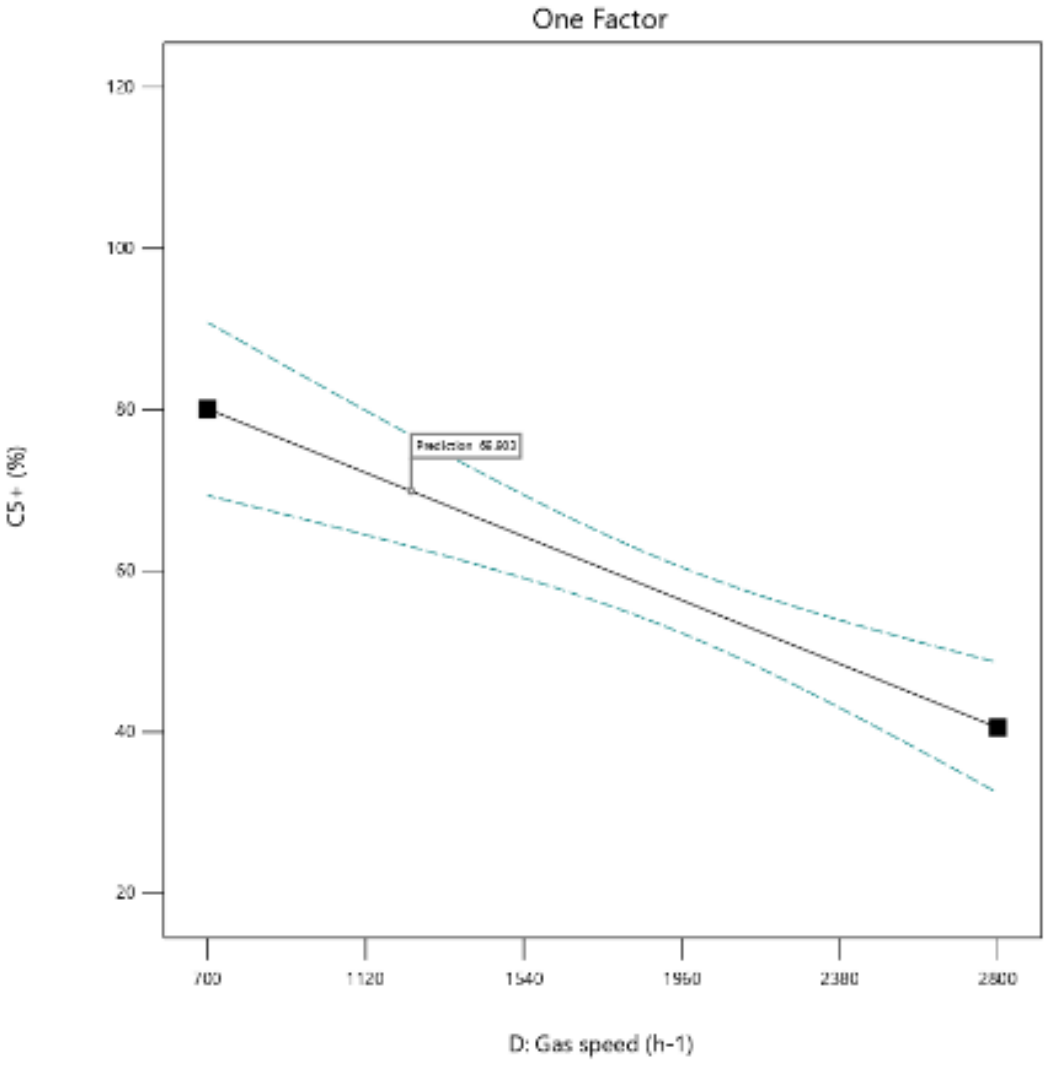

(c)

Figure 7.7: GHSV effect on hydrocarbon selectivity: (a) CH_4 selectivity; (b) C_2-C_4 selectivity; (c) C_{5+}-C∞ selectivity

The effect of velocity on hydrocarbon selectivity is complicated and various results are reported in the literature. It is assumed that a higher velocity reduces retention time, and a short retention time slows down the rate at which the temperature rises in the catalyst bed, which benefits chain growth (Dry, 2002). If diffusion effects are found to play a substantial role in removing hydrocarbons from the surface of the catalyst, then the constraints on mass transfer can be overcome at high gas velocity (Sari et al., 2009). In FT synthesis, the reactants carbon monoxide (CO) and hydrogen (H_2) should be added early during the process, in order to promote the formation of the hydrocarbon chain before the initial product methane detaches from the catalyst surface.

7.4.5. Adequacy of the model developed

The fit of the fitted model was evaluated using analysis of variance (ANOVA), F-value, P-value, and coefficient of determination at a confidence level of 95% (R^2). **Table 7.5** provides the outcomes of an ANOVA for the fitted model. At this level of confidence, a probability value (P-value) of less than 0.05 denotes the significance of the model terms, whereas a value above 0.100 indicates that the components used in the model are not significant. The fitted regression model was seen to be significant, but the significance was not apparent until all results were subjected to the simplified quadratic model procedure.

Table 7.5: ANOVA for the fitted models of responses

	CH_4			C_2-C_4			C_5-C_∞		
Model	**F-value**	**p-value**		**F-value**	**p-value**		**F-value**	**p-value**	
Sub-plot	**5.66**	**0.0267**	**Significant**	**5.65**	**0.0268**	**Significant**	**8.86**	**0.0008**	**Significant**
a	6.36	0.0359		6.37	0.0358		29.91	0.0002	
b	6.85	0.0285		6.86	0.0284		15.57	0.0023	
c	1.94	0.2015		1.95	0.2004		1.61	0.2309	
d	18.63	0.0032		18.62	0.0032		35.72	9.23	
ab	5.99	0.0388		5.99	0.0387		36.64	$8.28*10^{-5}$	
ac	4.28	0.076		4.26	0.0764		3.36	0.0939	
ad	-	-		-	-		12.11	0.0052	
bc	8.47	0.0244		8.48	0.0243		-	-	
bd	20.51	0.0024		20.5	0.0024		28.44	0.0002	
b2	11.43	0.0111		11.44	0.0111		-	-	
d2	17.38	0.0042		17.36	0.0042		-	-	

Where:

a- Hydrogen to carbon monoxide (H_2:CO) ratio

b- Reaction temperature (T)

c- Reaction pressure (P)

d- Gas speed (GHSV)

The summary of statistical fit and the ANOVA table with high R^2 and adjusted R^2 values show that the models are statistically likely to accurately describe the performance of the

experimental system. The experimental data and the anticipated values delivered by the fitted models are displayed in **Table 7.6**. The anticipated values and experimental values were equivalent when using a linear correlation coefficient. According to statistics, this indicates that the independent variables are able to account for 95% of the variation in the sample. As a result, the design process can be directed by this model.

Table 7.6: Significance of predicted models

Model	**Term df**	**Error df**	**F-value**	**p-value**	**R^2**	**Adjusted R^2**
CH_4	10	5.63	5.66	0.0267	0.8917	0.7061
C_2-C_4	10	5.62	5.65	0.0268	0.8917	0.7059
C_5-C_∞	8	11	8.86	0.0008	0.8656	0.7163

7.3.7 Model of selectivity for CH4

The effective parameters of the H_2/CO molar ratio, temperature and pressure, and how they relate are shown in Figure 8. It shows that as H_2:CO increases at temperatures between 250°C and 225°C, the selectivity of methane decreases. The selectivity of methene increases with an increase in both temperature and H_2:CO, as shown in **Figure 7.8(a). Figure 7.8(b)** shows that elevated methane selectivity can be achieved at increased pressure levels and increased H_2:CO, even though the impact is low. Moreover, methane selectivity increases with a high gas velocity. This is evidence that low methane selectivity is favourable at a low temperature.

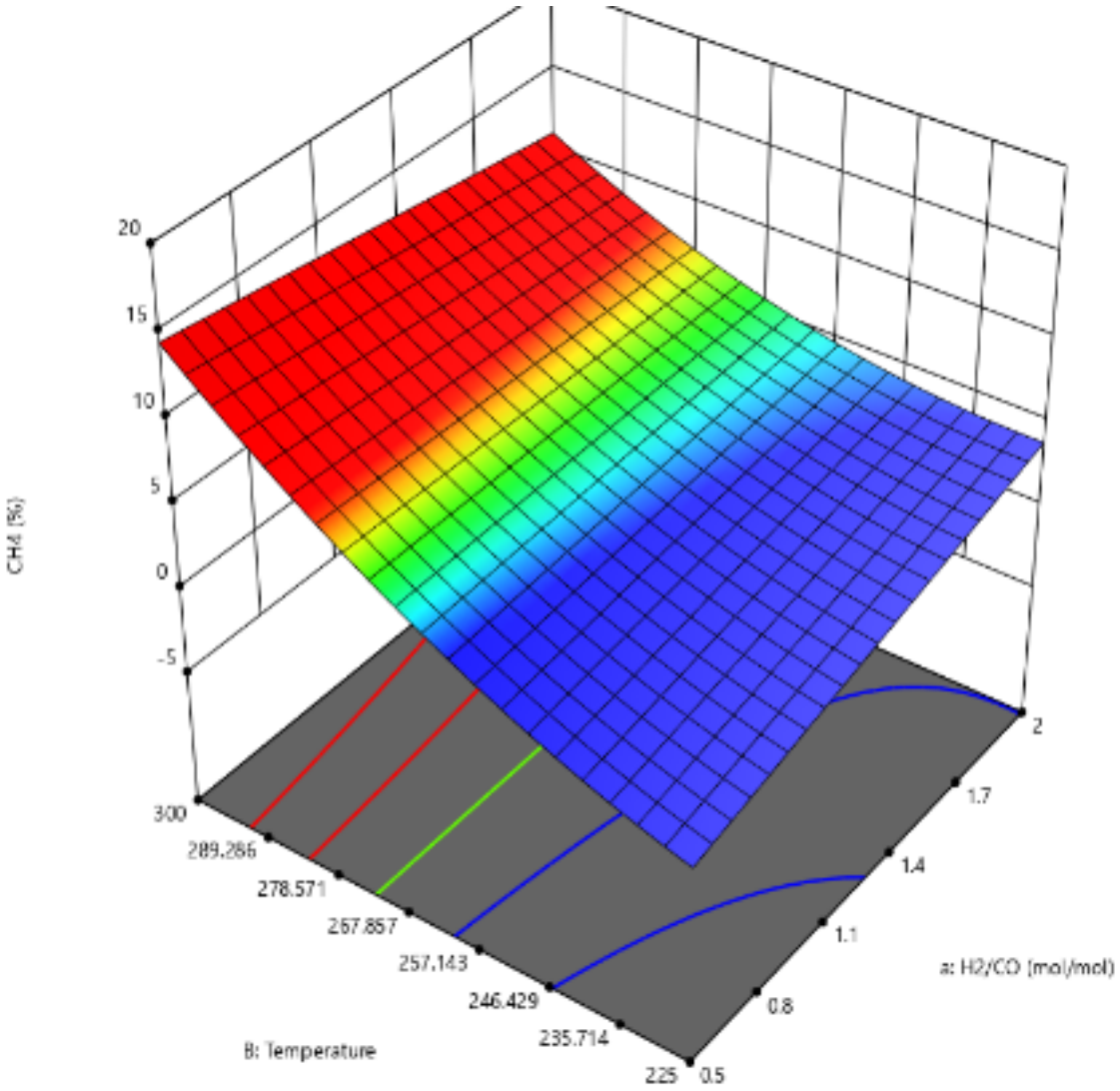
CH4 (%)
20
15
10
5
0
-5
300
289.286
278.571
267.857
257.143
246.429
235.714
225
B: Temperature
0.5
0.8
1.1
1.4
1.7
2
a: H2/CO (mol/mol)

(a)

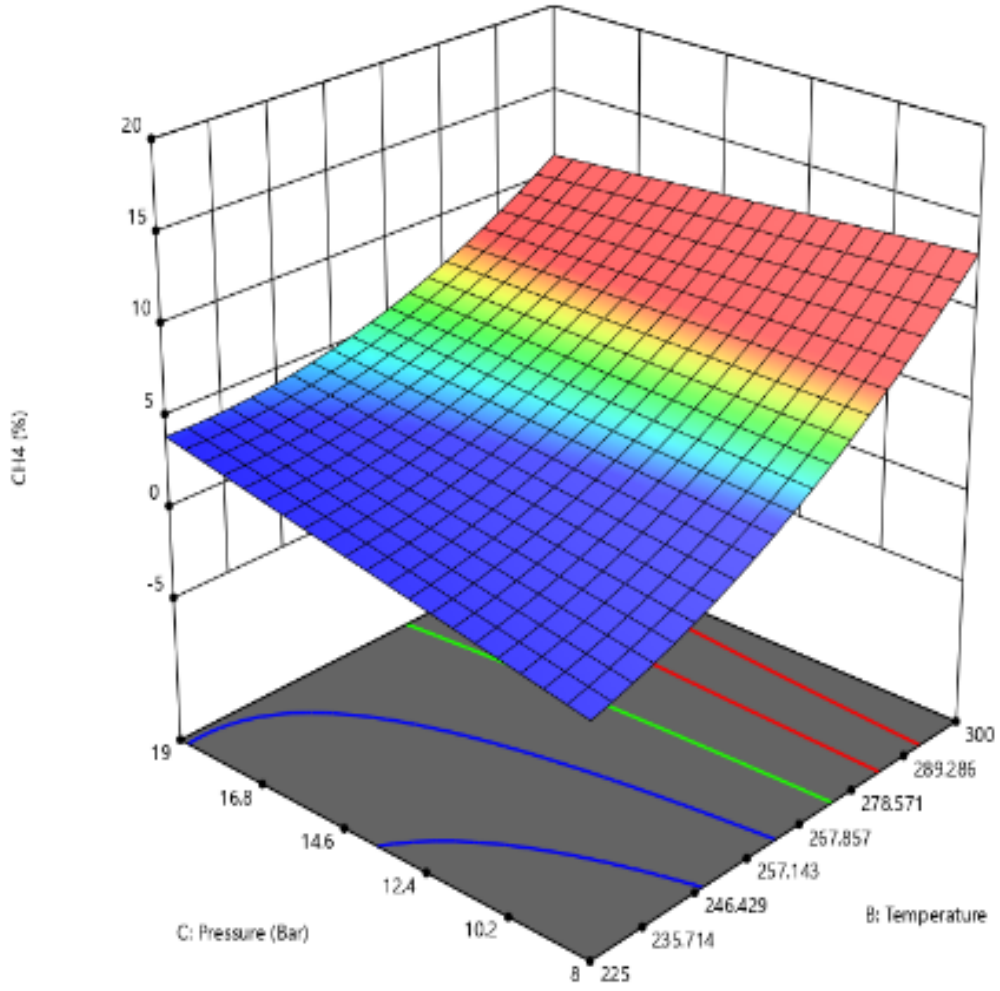
CH4 (%)
20
15
10
5
0
-5
19
16.8
14.6
12.4
10.2
8
C: Pressure (Bar)
225
235.714
246.429
257.143
257.857
278.571
289.286
300
B: Temperature

(b)

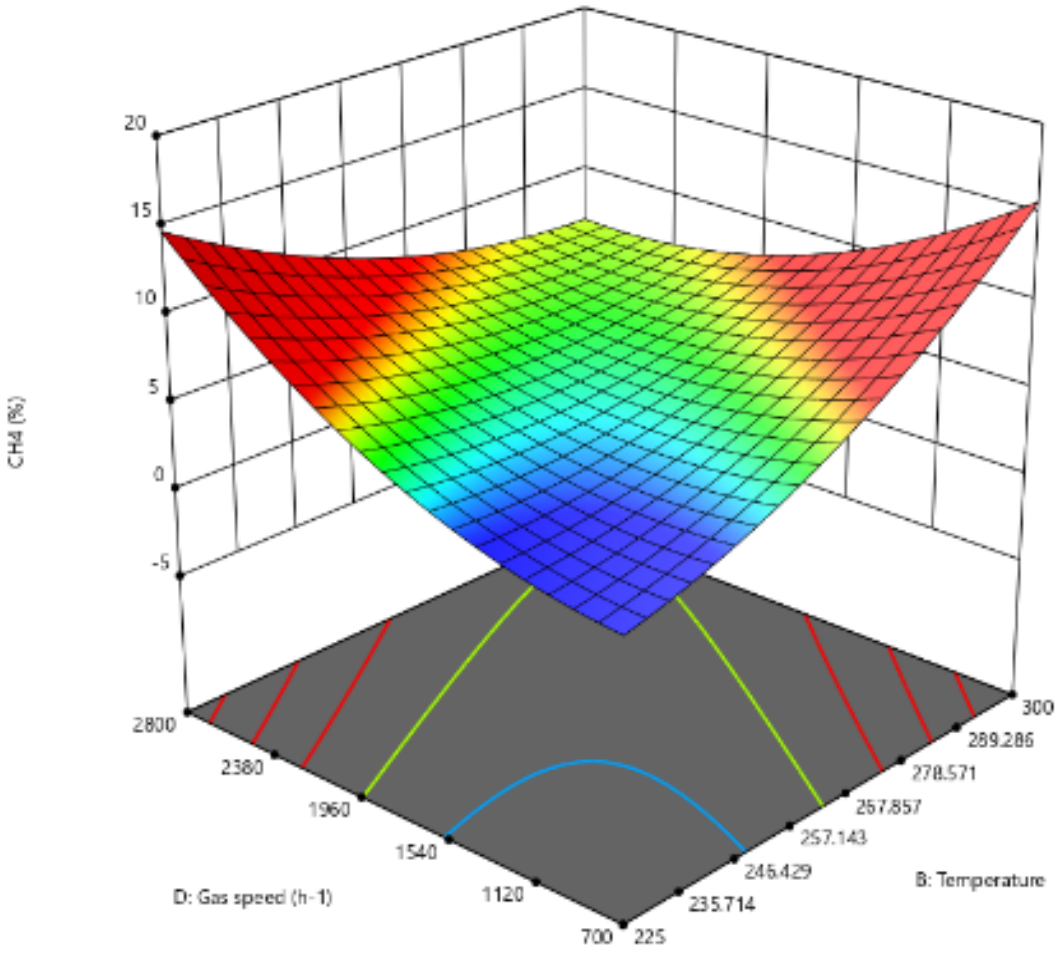

(c)

Figure 7.8: RSM representation of CH_4 selectivity vs reaction parameters

If there are several non-significant model terms (apart from those needed to support the hierarchy), a model reduction was used to improve your model.

A P-value below 0.0500 implies that the model terms are statistically significant. In this instance, the model terms a, B, D, aB, BC, BD, B^2 and D^2 are significant. The model terms are not significant if their value exceeds 0.1000. If the model has a large number of terms that are statistically insignificant (other than those essential to maintaining the hierarchy), a model reduction process is applied to improve it. The proposed coded model of selectivity for CH_4 is given in **equation 7.10** below:

$$S_{CH_4} = \begin{matrix} +14.25 + 14.69a - 41.35b + 4.97c + 11.91d - 38.46ab - 6.44ac \\ - 23.46bc - 39.92bd - 55.51b^2 + 5.38d^2 \end{matrix} \quad (7.10)$$

Where:

e- Hydrogen to carbon monoxide (H_2:CO) ratio

f- Reaction temperature (T)

g- Reaction pressure (P)

h- Gas speed (GHSV)

7.4.6. Model of selectivity for C_2-C_4

Figure 7.9 shows the changes in C_2-C_4 selectivity seen with variations in temperature, pressure and H_2/CO molar ratio. As is evident in **Figure 7.9**, low C_2-C_4 selectivity is favourable at a low temperature with increasing H_2/CO; high selectivity is observed with an increasing temperature and H_2/CO ratio. Similarly, an increasing gas velocity with a decreasing temperature and a low gas velocity with an increasing temperature results in increased C_2-C_4 selectivity. A decrease in H_2:CO with an increase in temperature confirms the increase in C_2-C_4 selectivity.

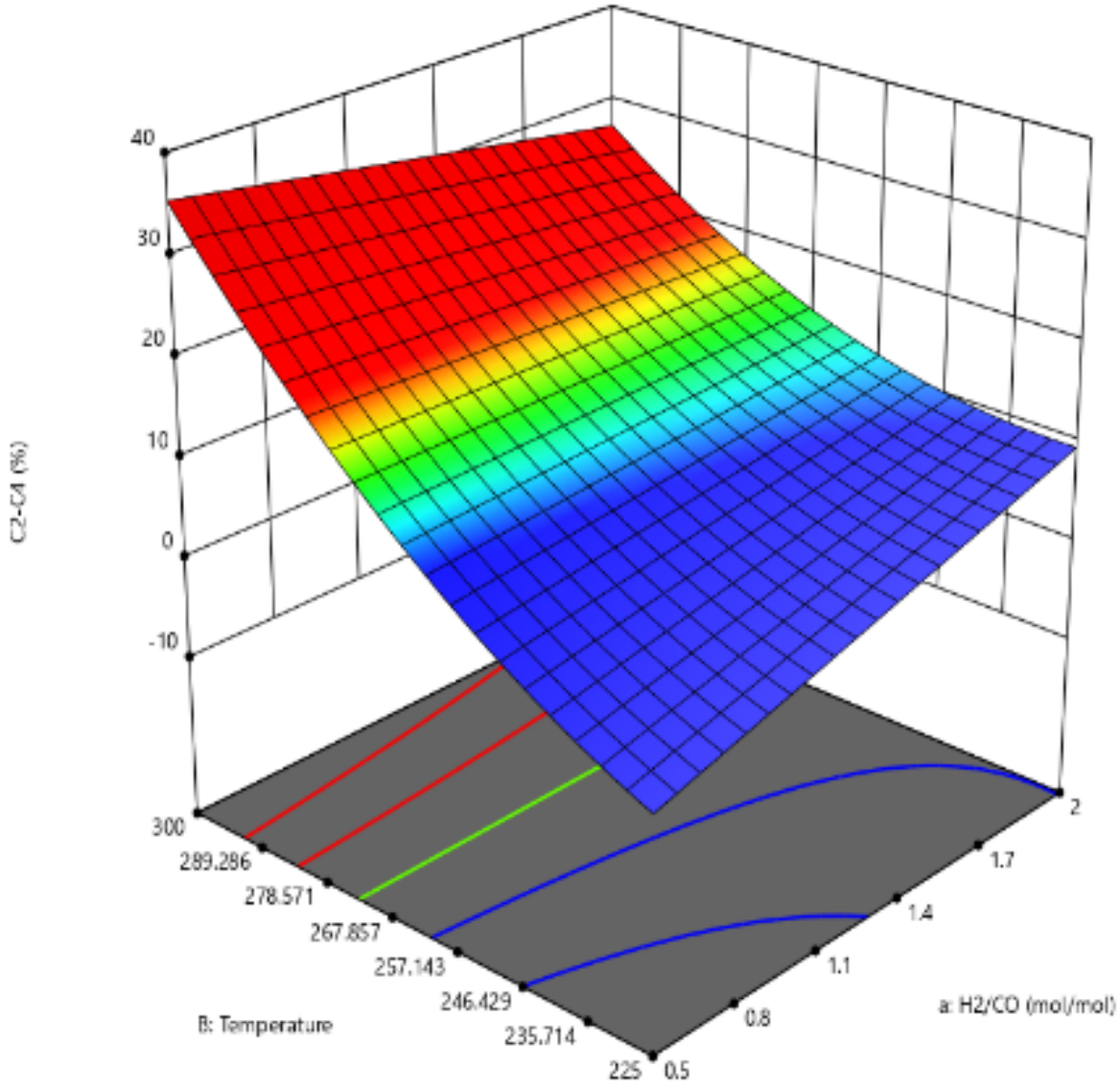
C2-C4 (%)
40
30
20
10
0
-10
300
289.286
278.571
267.857
257.143
246.429
235.714
225
B: Temperature
0.5
0.8
1.1
1.4
1.7
2
a: H2/CO (mol/mol)

(a)

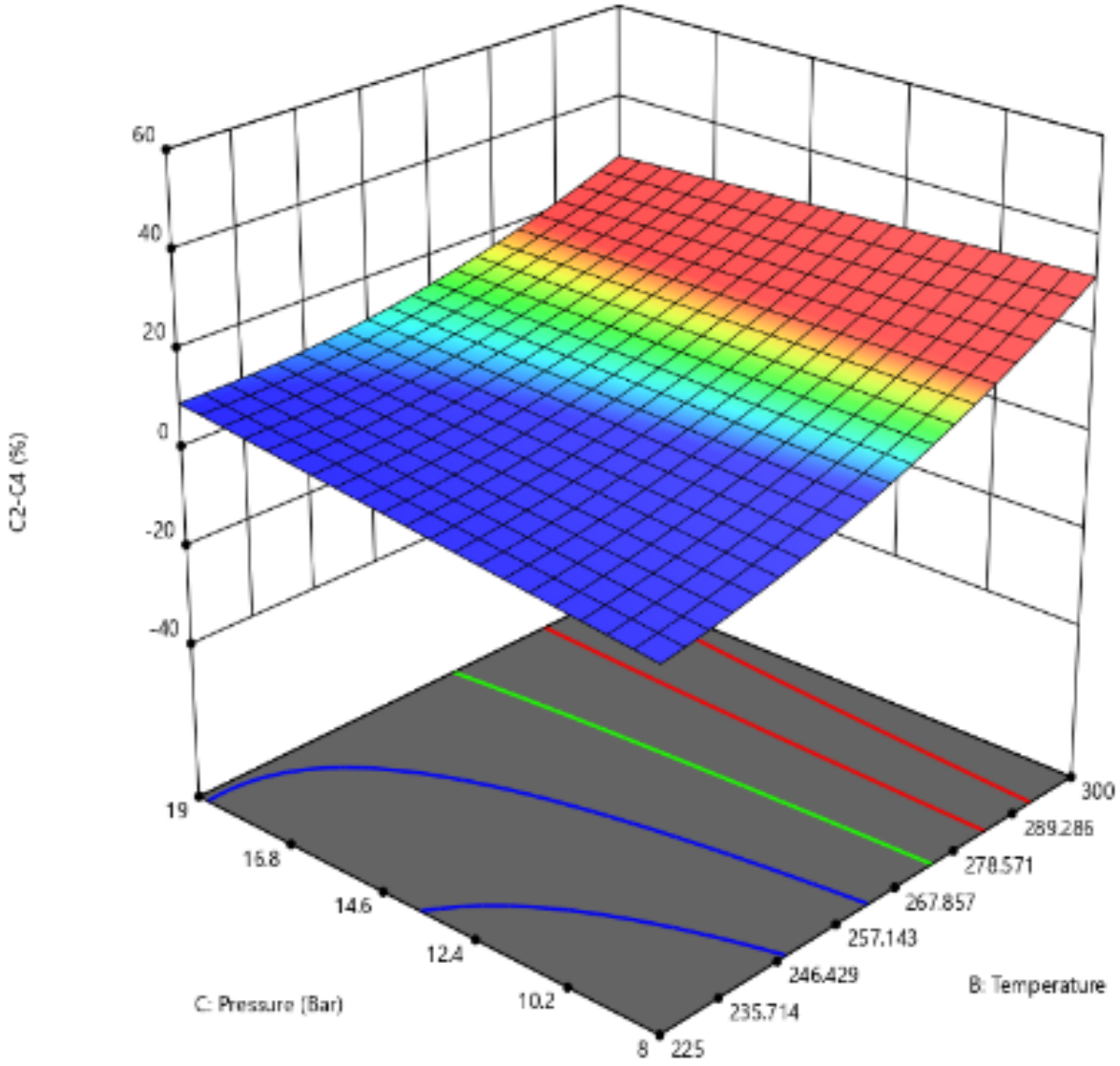
C2-C4 (%)
60
40
20
0
-20
-40
19
16.8
14.6
12.4
10.2
8
C: Pressure (Bar)
225
235.714
246.429
257.143
267.857
278.571
289.286
300
B: Temperature

(b)

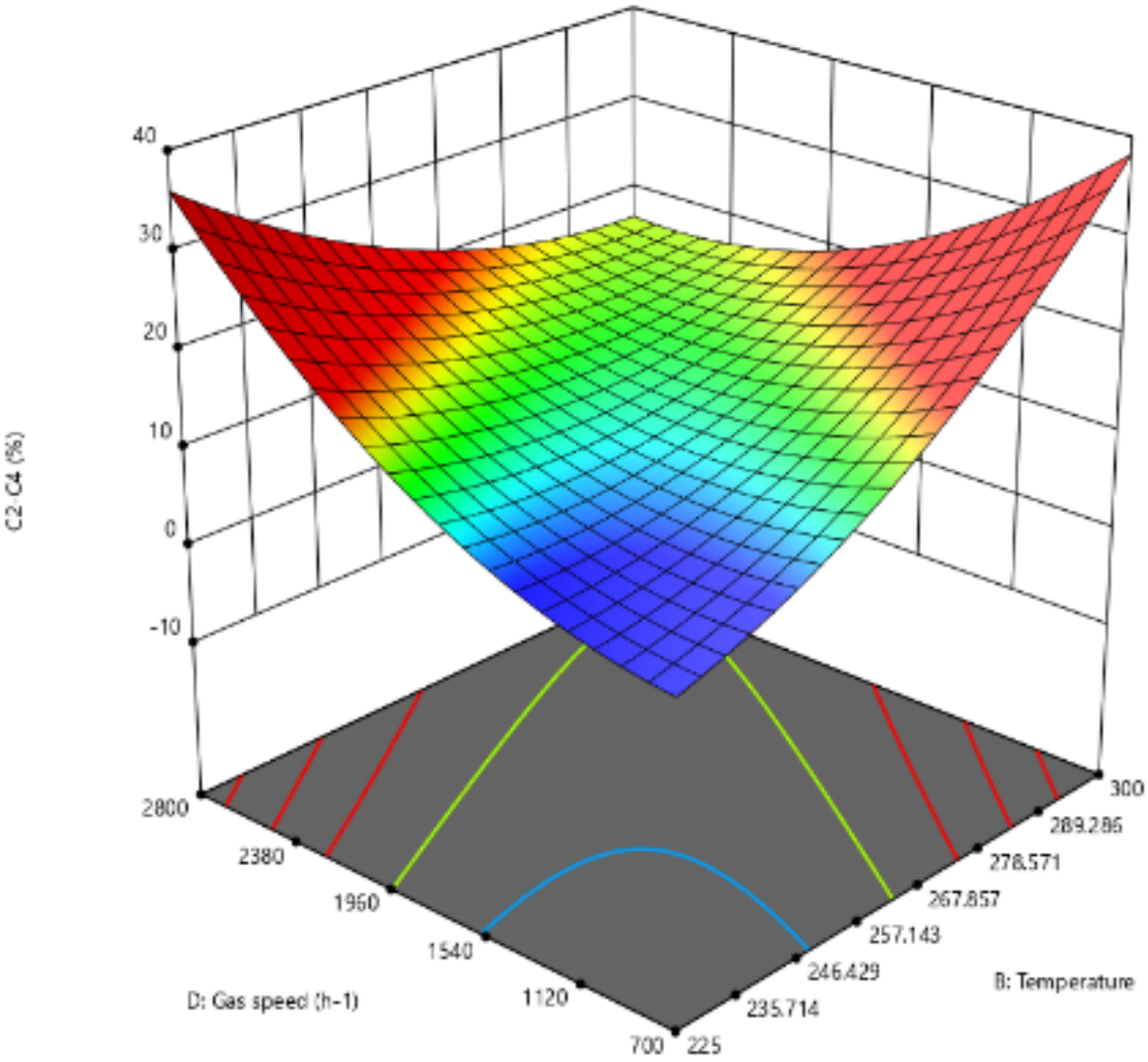

(c)

Figure 7.9: RSM representation of C_2-C_4 selectivity in terms of various reaction parameters

Significant model terms have a P-value less than 0.0500. a, B, D, aB, BC, BD, B^2 and D^2 are essential model terms in this instance. The selectivity model for C_2-C_4 can be formulated as per **equation 7.11**:

$$S_{C_2-C_4} = \begin{matrix} +41.53 + 70.95a - 87.60b + 10.91c + 34.91d - 77.57ab \\ - 14.73ac - 4.41ad - 56.25bc - 100.03bd + 3.09cd \\ + 35.49a^2 + 129.85b^2 + 1.02c^2 + 10.24d^2 \end{matrix} \quad (7.11)$$

Where:

a- Hydrogen to carbon monoxide (H_2:CO) ratio
b- Reaction temperature (T)
c- Reaction pressure (P)
d- Gas speed (GHSV)

7.4.7. Model of selectivity for C_{5+}-C_{∞}

The effect of temperature, gas and H_2: CO on C_{5+}-C_{∞} selectivity is shown in **Figure 7.10.** High selectivity to C_{5+} is evident at a low temperature. A low gas velocity and low temperature favours high C_{5+}-C_{∞} selectivity, as shown. Increasing pressure and a low temperature also have a positive impact on maximum C_{5+}-C_{∞}. **Figure 7.10** shows that a low gas velocity and a low temperature result in high C_{5+} selectivity. It is clear from the analysis that a low temperature has a significant impact on high C_{5+}-C_{∞} production.

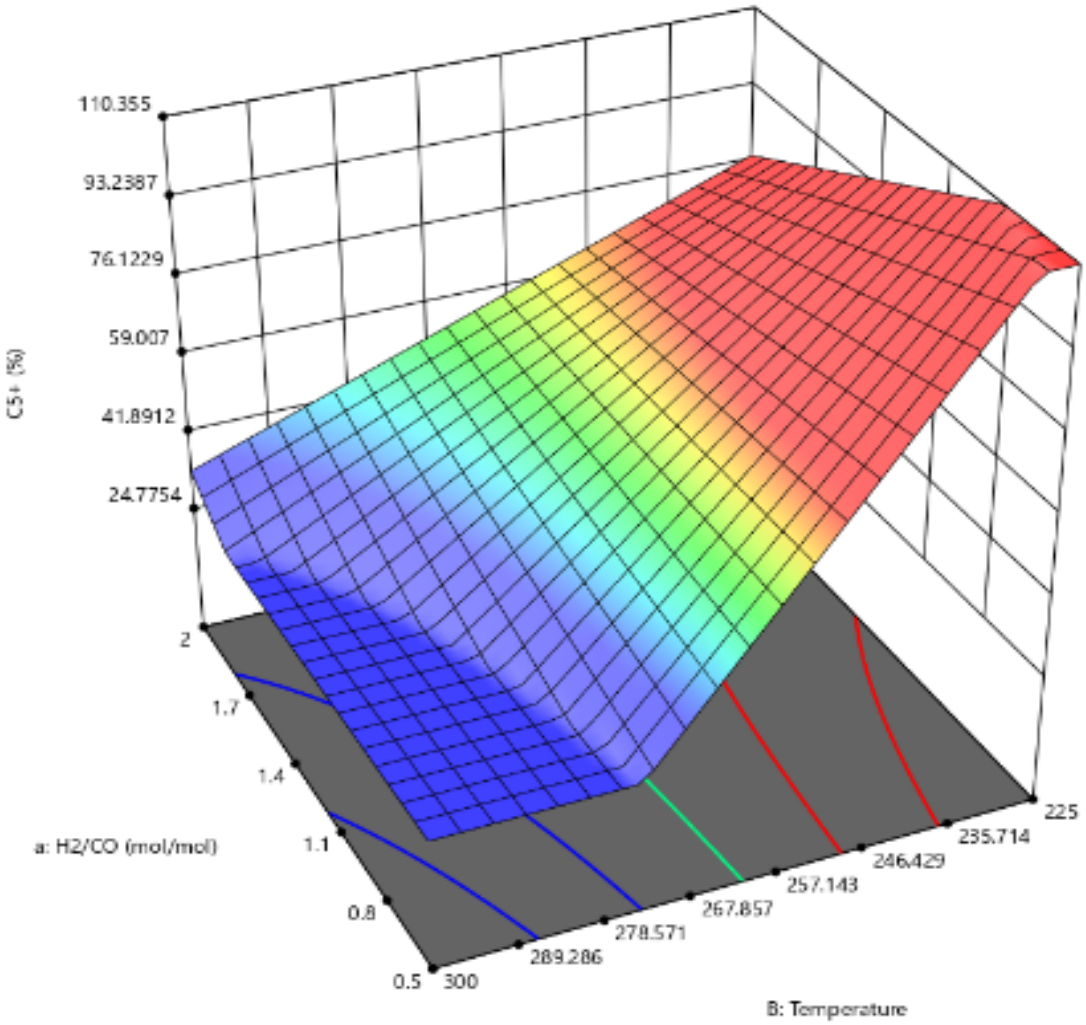

(a)

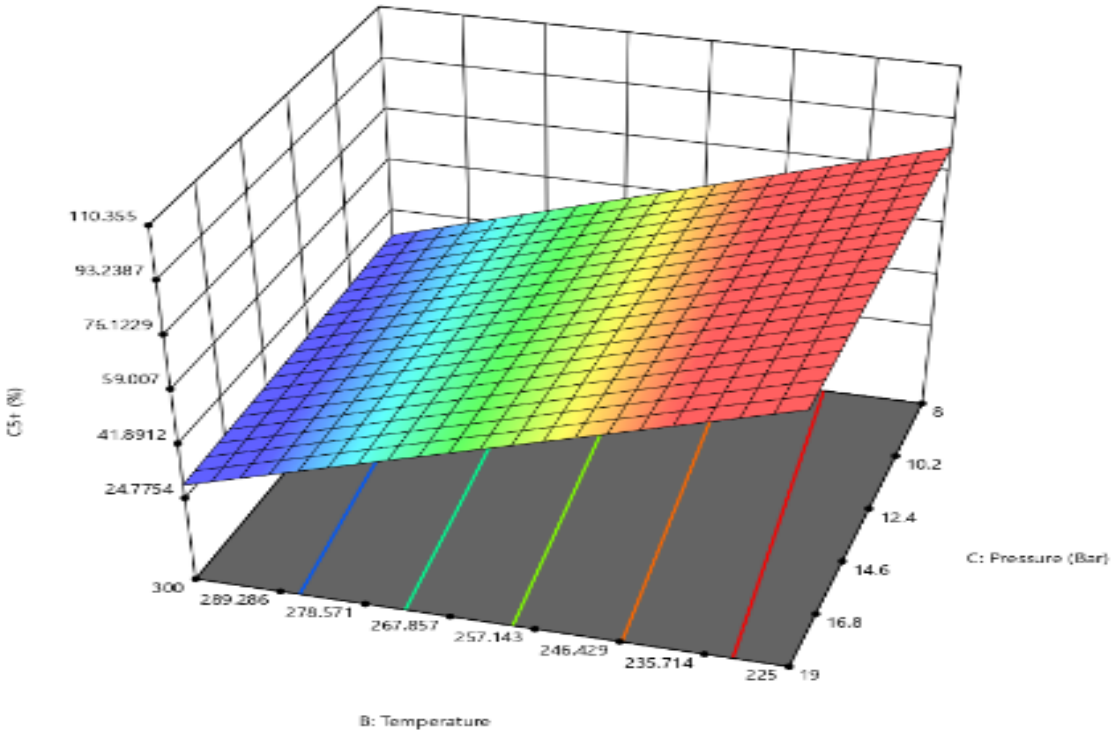
110.355
93.2387
76.1229
59.007
41.8912
24.7754
C5 (%)
300
289.286
278.571
267.857
257.143
246.429
235.714
225
B: Temperature
8
10.2
12.4
14.6
16.8
19
C: Pressure (Bar)

(b)

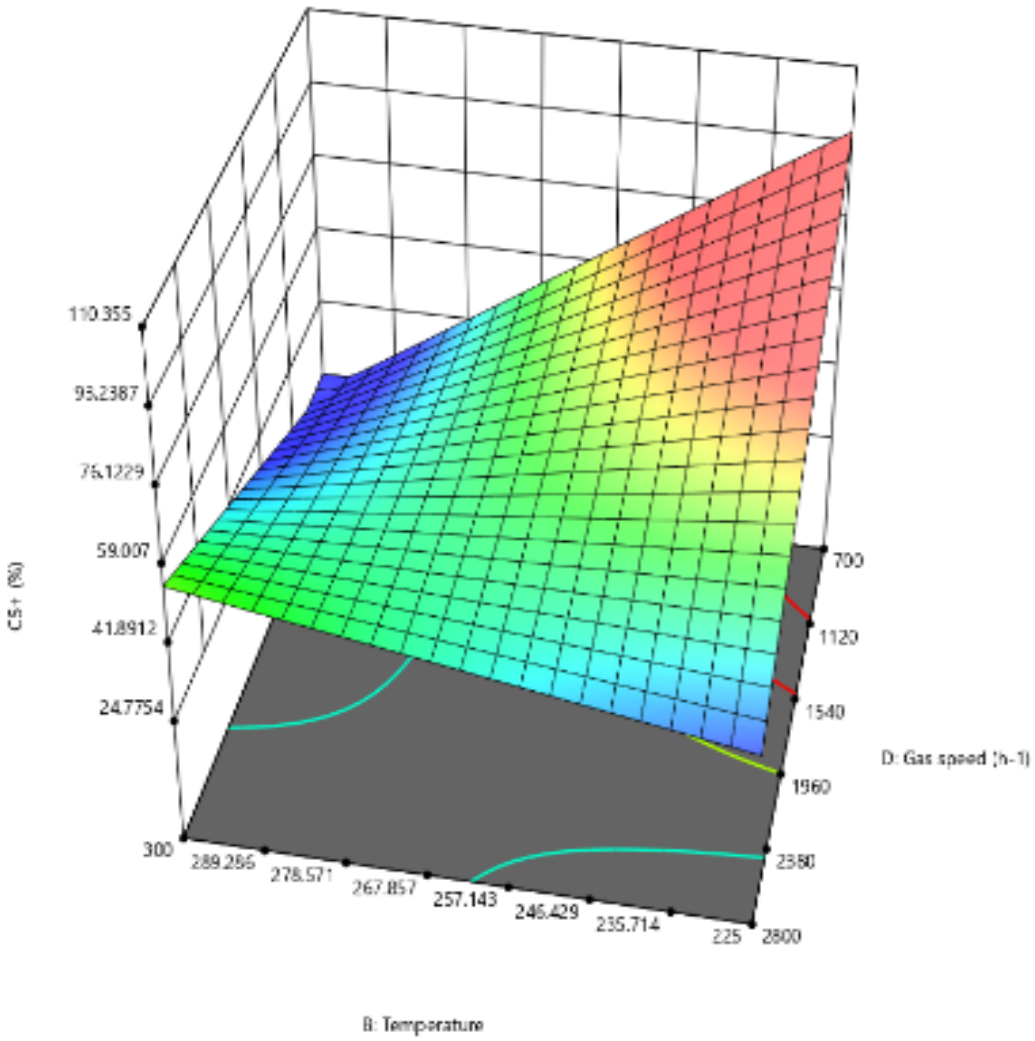

(c)

Figure 7.10: RSM representation of C_{5+}-C∞ selectivity for various reaction parameters

Model terms are statistically significant when the p-value is less than 0.0500. Significant model terms in this scenario include a, B, D, aB, aD and BD. If the value of a variable used in the model is greater than 0.1000, it is not important in the model. **Equation 7.12** can be used to suggest a model for selectivity for C5+:

$$S_{CH_4} = \begin{matrix} +1.72 + 133.63a - 169.31b + 14.69c + 93.29d - 428.02ab \\ - 32.48ac - 44.47ad - 180.20bd \end{matrix} \quad (7.12)$$

Where:

a- Hydrogen to carbon monoxide (H_2:CO) ratio

b- Reaction temperature (T)

c- Reaction pressure (P)

d- Gas speed (GHSV)

7.4.8. Determining optimum conditions

The main purpose of this endeavour was to determine the settings that minimize CH_4 selectivity while increasing C_{5+}-C_{∞} selectivity. After the fitted model had been evaluated for compatibility in the region defined by the design coordinates, and was found to be acceptable, it was used to estimate the coordinates of the stationary point (Kleijnen, 2018). A desirability level of one was considered the ideal scenario for implementing the FT process. Design Expert provides the option of displaying the results in the form shown in **Figure 7.11**. The acceptability of each variable and response, and the overall desirability is shown in the ramp view. These graphs can be created for each optimum point achieved. Minimum and maximum values of variables and the results are shown in the ramp chart, as well as the optimal points, so as to compare the optimal point with the level used.

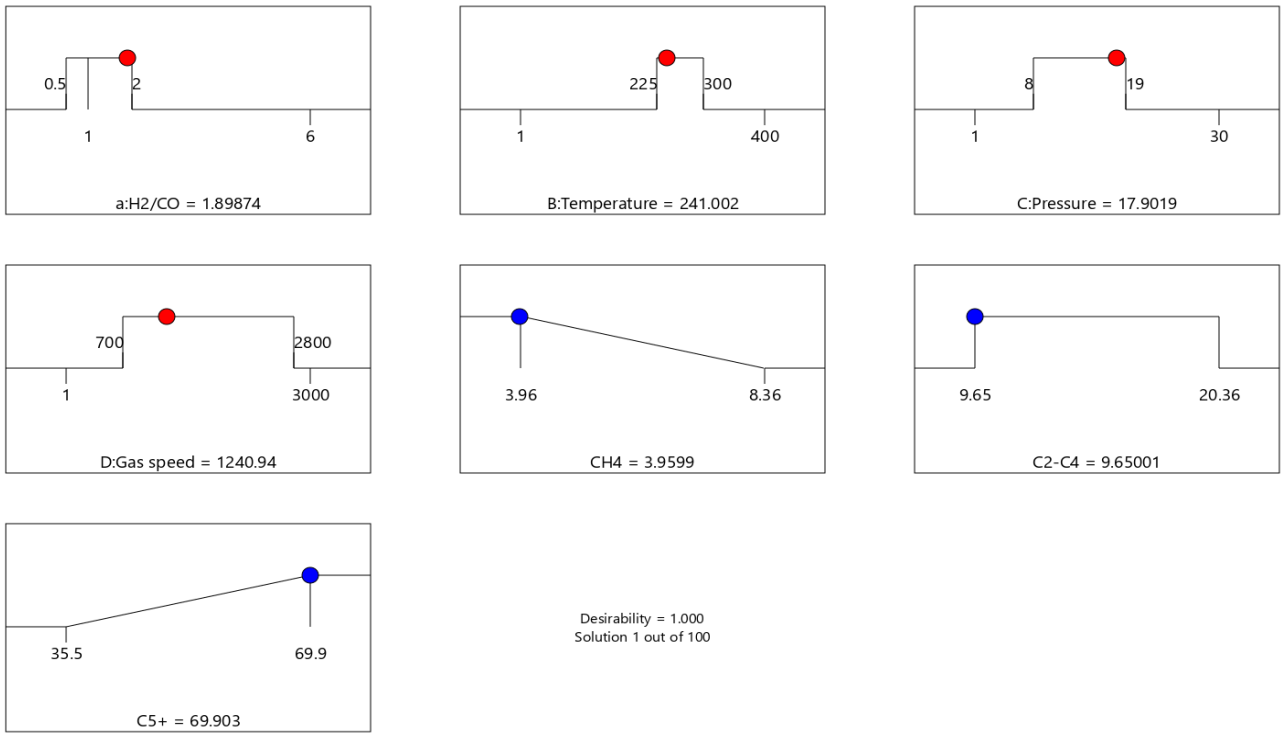

Figure 7.11: Optimized design parameters for the proposed FT process

The models created are dependable, as all the findings were in satisfactory agreement with the predictions. Incorporating DOE resulted in an overall improvement in the yield and the selectivity of the FT process. Alterations made to the temperature, the ratio of hydrogen to carbon monoxide and the flow rate of the gas all contributed to an improvement in the final product distribution. This modification has the potential to increase the productivity of FT systems.

7.5. Conclusion

The purpose of this research was to provide an overall account of the product distribution using a clinoptilolite zeolite that was subjected to incipient Fe impregnation and then used in the FT process. A simple examination of the output of DOE in relation to the design constraints was done, which revealed the possibility of changing the design to provide the desired products. The DOE experiment was carried out with two goals: increasing the effectiveness of the Fe-based FT catalyst; preserving the equilibrium between CO, H_2 and the precursors for chain development.

Synthesis of heavy hydrocarbons via the FT process using synthesis gas as feedstock is an important aspect of design. When the operating settings were adjusted, there was a discernible shift in the selectivity. As the parameters were altered, there was a corresponding shift in the average carbon number of the hydrocarbon derivatives. The H_2/CO ratio, temperature and gas velocity were found to have a strong effect on the production of low CH_4, optimal C_2-C_4 and high heavy hydrocarbon products, whereas pressure was statistically negligible and had no discernible impact.

The experimental results of the importance of the parameters under study were illustrated using probability graphs. Optimal Design and RSM were used to alter the significant factors used, in order to identify the ideal experimental conditions. The selectivity to C_{5+} - C_{∞} hydrocarbons was strongly favored by lower design parameters for temperature, a high H_2/CO ratio, and gas speed.

According to the constraints set, H_2/CO = 1.90, temperature = 241 ^{o}C, pressure = 17.9 bar_g and velocity =1240.9 provided were the optimal design parameters under the experimental conditions evaluated. To verify this, the actual values were compared with the predicted values, and it was found that the models fitted the experimental data well.

The following conclusions were drawn from the results:

- The experimental design technique and statistical methods used were able to distinguish between the components under examination that were statistically significant and those that were not.
- A high R^2 value shows that the developed model can deliver a reassuringly accurate response estimate for the system in the area under study.
- Statistical analysis of the normal probability plot showed the significant influence of the parameters and their distribution.
- Under the experimental conditions outlined, the model fits the experimental data well. It can be adapted to fit light hydrocarbons, which were discovered during development, but were not studied in this work.

References

Abrokwah, R. Y., Rahman, M. M., Deshmane, V. G., & Kuila, D. (2019). Effect of titania support on Fischer-Tropsch synthesis using cobalt, iron, and ruthenium catalysts in silicon-microchannel microreactor. *Molecular Catalysis*, *478*. https://doi.org/10.1016/j.mcat.2019.110566

Alkhimov, S. A., Grigor´ev, D. A., & Mikhailov, M. N. (2013). Nature of active sites in hybrid metal-zeolite catalysts for the Fischer-Tropsch synthesis. In *Izvestiya Akademii Nauk. Seriya Khimicheskaya* (Vol. 62, Issue 5).

Amoo, C. C., Li, M., Noreen, A., Fu, Y., Maturura, E., Du, C., Yang, R., Gao, X., Xing, C., & Tsubaki, N. (2020). Fabricating Fe nanoparticles embedded in zeolite y microcrystals as active catalysts for Fischer-Tropsch Synthesis. *ACS Applied Nano Materials*, *3*(8), 8096–8103. https://doi.org/10.1021/acsanm.0c01515

Baranak, M., Gürünlü, B., Sarioğlan, A., Ataç, Ö., & Atakül, H. (2013). Low acidity ZSM-5 supported iron catalysts for Fischer-Tropsch synthesis. *Catalysis Today*, *207*, 57–64. https://doi.org/10.1016/j.cattod.2012.04.013

Da Silva, J. F., Bragança, L. F. F. P. G., & Da Silva, M. I. P. (2018). Catalytic performance of KL zeolite-supported iron and cobalt catalysts for the Fischer–Tropsch synthesis. *Reaction Kinetics, Mechanisms and Catalysis*, *124*(2), 563–574. https://doi.org/10.1007/s11144-018-1388-y

Di, Z., Zhao, T., Feng, X., & Luo, M. (2019). A newly designed core-shell-like zeolite capsule catalyst for synthesis of light olefins from syngas via Fischer–Tropsch Synthesis reaction. *Catalysis Letters*, *149*(2), 441–448. https://doi.org/10.1007/s10562-018-2624-9

Dry, M. E. (2002). The Fischer–Tropsch process: 1950–2000. *Catalysis Today*, *71*(3–4), 227–241. https://doi.org/10.1016/S0920-5861(01)00453-9

Elbashir, N. O., Bao, B., & El-Halwagi, M. M. (2009). An approach to the design of advanced Fischer-Tropsch reactor for operation in near-critical and supercritical phase media. *Proceedings of the 1st Annual Gas Processing Symposium*, 423–433. https://doi.org/10.1016/B978-0-444-53292-3.50051-1

Filliben, J. J. (1975). The probability plot correlation coefficient test for normality. *Technometrics*, *17*(1), 111. https://doi.org/10.2307/1268008

Hou, Y., Li, J., Qing, M., Liu, C. L., & Dong, W. S. (2020). Direct synthesis of lower olefins from syngas via Fischer–Tropsch synthesis catalyzed by a dual-bed catalyst. *Molecular Catalysis*, *485*. https://doi.org/10.1016/j.mcat.2020.110824

Javed, M., Zhang, G., Gao, W., Cao, Y., Dai, P., Ji, X., Lu, C., Yang, R., Xing, C., & Sun, J. (2019). From hydrophilic to hydrophobic: A promising approach to tackle high CO2 selectivity of Fe-based Fischer-Tropsch microcapsule catalysts. *Catalysis Today*, 39–45. https://doi.org/10.1016/j.cattod.2018.08.010

Kang, S. H., Bae, J. W., Prasad, P. S. S., & Jun, K. W. (2008). Fischer-Tropsch synthesis using zeolite-supported iron catalysts for the production of light hydrocarbons. *Catalysis Letters*, *125*(3–4), 264–270. https://doi.org/10.1007/s10562-008-9586-2

Keyvanloo, K., Huang, B., Okeson, T., Hamdeh, H. H., & Hecker, W. C. (2018). Effect of support pretreatment temperature on the performance of an iron Fischer-Tropsch catalyst supported on silica-stabilized alumina. *Catalysts*, *8*(2). https://doi.org/10.3390/catal8020077

Kleijnen, J. P. C. (2018). Design and analysis of simulation experiments: Tutorial. *SSRN Electronic Journal*. https://doi.org/10.2139/SSRN.2941492

Li, L., Zheng, Y., Xu, B., Xu, Y., & Liu, Z. (2021). Wax separated effectively from Fischer-Tropsch wax residue by solvent desorption: Thermodynamic and kinetic analysis. *Applied Sciences (Switzerland)*, *11*(16). https://doi.org/10.3390/APP11167745

Liu, R., Ma, Z., Sears, J. D., Juneau, M., Neidig, M. L., & Porosoff, M. D. (2020). Identifying correlations in Fischer-Tropsch synthesis and CO2 hydrogenation over Fe-based ZSM-5 catalysts. *Journal of CO2 Utilization*, *41*. https://doi.org/10.1016/j.jcou.2020.101290

Luk, H. T., Mondelli, C., Mitchell, S., Curulla Ferré, D., Stewart, J. A., & Pérez-Ramírez, J. (2019). Impact of carrier acidity on the conversion of syngas to higher alcohols over zeolite-supported copper-iron catalysts. *Journal of Catalysis*, *371*, 116–125. https://doi.org/10.1016/j.jcat.2019.01.021

Mena Subiranas, A., & Schaub, G. (2007). Combining Fischer-Tropsch (FT) and hydrocarbon reactions under FT reaction conditions - Catalyst and reactor studies with Co or Fe and Pt/ZSM-5. *International Journal of Chemical Reactor Engineering*, *5*(1). https://doi.org/10.2202/1542-6580.1522/MACHINEREADABLECITATION/RIS

Méndez, C. I., & Ancheyta, J. (2019). Dynamic one-dimensional pseudo homogeneous model for Fischer-Tropsch fixed-bed reactors. *Fuel*, *252*, 371–392. https://doi.org/10.1016/J.FUEL.2019.04.100

Mierczynski, P., Dawid, B., Chalupka, K., Maniukiewicz, W., Witoska, I., Vasilev, K., & Szynkowska, M. I. (2019). Comparative studies of Fischer-Tropsch synthesis on iron catalysts supported on Al2O3-Cr2O3 (2:1), multi-walled carbon nanotubes or BEA zeolite systems. *Catalysts*, *9*(7). https://doi.org/10.3390/catal9070605

Montgomery, D. C. (2013). *Design and Analysis of Experiments, Eighth Edition*. www.wiley.com/go/permissions.

Ngwenya, T., Glasser, D., Hildebrandt, D., Coville, N., & Mukoma, P. (2005). Fischer−Tropsch results and their analysis for reactor synthesis. *Industrial and Engineering Chemistry Research*, *44*(16), 5987–5994. https://doi.org/10.1021/IE0493199

Ojeda, M., Ishikawa, A., Nabar, R., Nilekar, A. U., Mavrikakis, M., & Iglesia, E. (n.d.). *Fischer-Tropsch Synthesis Catalysis: Low-Temperature Fe Catalysts and the Mechanism for CO Dissociation on Fe and Co*.

Pardo-Tarifa, F. (2017). *Cobalt catalyst supports for Fischer-Tropsch synthesis*.

Paterson, J., Peacock, M., Ferguson, E., Ojeda, M., & Clarkson, J. (2017). In situ X-ray diffraction of Fischer-Tropsch catalysts—Effect of water on the reduction of cobalt oxides. *Applied Catalysis A: General*, *546*, 103–110. https://doi.org/10.1016/j.apcata.2017.08.017

Sari, A., Zamani, Y., & Taheri, S. A. (2009). Intrinsic kinetics of Fischer–Tropsch reactions over an industrial Co–Ru/γ-Al2O3 catalyst in slurry phase reactor. *Fuel Processing Technology*, *90*(10), 1305–1313. https://doi.org/10.1016/J.FUPROC.2009.06.024

Shafer, W. D., Gnanamani, M. K., Graham, U. M., Yang, J., Masuku, C. M., Jacobs, G., & Davis, B. H. (2019). Fischer–Tropsch: Product selectivity–the fingerprint of synthetic fuels. *Catalysts 2019, Vol. 9, Page 259*, *9*(3), 259. https://doi.org/10.3390/CATAL9030259

Shapiro, S. S., & Wilk, M. B. (1965). An analysis of variance test for normality (complete samples). *Biometrika*, *52*(3/4), 591. https://doi.org/10.2307/2333709

Steynberg, A., & Dry, Mark. (2004). *Fischer-Tropsch technology*. 700.

Tsakoumis, N. E., Voronov, A., Ronning, M., Beek, W. Van Borg, O., Rytter, E., & Holmen, A. (2012). Fischer-Tropsch synthesis: An XAS/XRPD combined in situ study from catalyst activation to deactivation. *Journal of Catalysis*, *291*, 138–148. https://doi.org/10.1016/j.jcat.2012.04.018

Van der Laan, G. P., & Beenackers, A. A. C. M. (2011). Kinetics and selectivity of the Fischer–Tropsch Synthesis: A literature review. *Http://Dx.Doi.Org/10.1081/CR-100101170*, *41*(3–4), 255–318. https://doi.org/10.1081/CR-100101170

Velasco, J. A., Lopez, L., Velásquez, M., Boutonnet, M., Cabrera, S., & Järås, S. (2010). Gas to liquids: A technology for natural gas industrialization in Bolivia. *Journal of Natural Gas Science and Engineering*, *2*(5), 222–228. https://doi.org/10.1016/J.JNGSE.2010.10.001

Wang, P., Kang, J., Zhang, Q., & Wang, Y. (2007). Lithium ion-exchanged zeolite faujasite as support of iron catalyst for Fischer-Tropsch synthesis. *Catalysis Letters*, *114*(3–4), 178–184. https://doi.org/10.1007/s10562-007-9062-4

Wood, D. A., Nwaoha, C., & Towler, B. F. (2012). Gas-to-liquids (GTL): A review of an industry offering several routes for monetizing natural gas. *Journal of Natural Gas Science and Engineering*, *9*, 196–208. https://doi.org/10.1016/J.JNGSE.2012.07.001

Xing, C., Sun, J., Chen, Q., Yang, G., Muranaka, N., Lu, P., Shen, W., Zhu, P., Wei, Q., Li, J., Mao, J., Yang, R., & Tsubaki, N. (2015). Tunable isoparaffin and olefin yields in Fischer-Tropsch synthesis achieved by a novel iron-based micro-capsule catalyst. *Catalysis Today*, *251*, 41–46. https://doi.org/10.1016/j.cattod.2014.10.022

Xu, Y., Wang, T., Shi, C., Liu, B., Jiang, F., & Liu, X. (2020). Experimental investigation on the two-sided effect of acidic HZSM-5 on the catalytic performance of composite Fe-based Fischer-Tropsch catalysts and HZSM-5 zeolite in the production of aromatics from CO2/H2. *Industrial*

and Engineering Chemistry Research, *59*(18), 8581–8591. https://doi.org/10.1021/acs.iecr.0c00992

Yao, Y., Hildebrandt, D., Glasser, D., & Liu, X. (2011). A study of low temperature Fischer-Tropsch synthesis by switching between CO2/H2/N2 and CO/H2/N2 syngases over a cobalt-based catalyst. *11AIChE - 2011 AIChE Spring Meeting and 7th Global Congress on Process Safety, Conference Proceedings*.

Yao, Y., Liu, X., Hildebrandt, D., & Glasser, D. (2011). Fischer-Tropsch synthesis using H 2/CO/CO 2 syngas mixtures over an iron catalyst. *Industrial and Engineering Chemistry Research*, *50*(19), 11002–11012. https://doi.org/10.1021/IE200690Y

Chapter 8: Conclusion and recommendations

8.1. Conclusion

To advance knowledge on the possibilities of simplifying the FT process and to validate the operating conditions that yield favorable product distribution was the primary objective of the research that was carried out for this thesis. The usage of naturally occurring clinoptilolite was the secondary objective because it has been discovered that when employed as a support, it behaves almost exactly like the convectional supports utilized in Fischer-Tropsch synthesis. This chapter provides a concise overview of the key findings and insights from the research conducted, drawing on the results and comments offered in the preceding chapters (Chapters 2-7).

8.1.1. Debunking the effect of crystallite / particle size in cobalt-based Fisher-Tropsch synthesis

The literature review investigates the relationship between the distribution of FTS products and the size of cobalt crystallites on various supports. According to data gleaned from the literature, the ideal range for the average cobalt crystallite diameter should be between 6 and 8 nm, and changing these diameters of cobalt crystallite has an impact on the frequency of carbon monoxide turnover as well as the product distribution, specifically the selectivity of CH_4, C_2-C_4 and C_{5+}.

In addition, the research suggests that the morphology and size of the support particles should be carefully monitored and changed in order to establish a consistent catalyst. It would be optimal for experimental repeatability in FTS applications if catalyst particles have evenly sized support particles and crystallites. The techniques for measuring crystallite size were also investigated. Based on the review of the relevant literature, it has been concluded that there is insufficient evidence to warrant rejecting the comparability of XRD, H_2-Chemisoption, and TEM particle size analysis data. It should be noted that though XRD is widely used in FT to determine particle size, it is generally insensitive to small metal particles that are <3 nm (Mustard & Bartholomew, 1981).

The diameter of the cobalt crystallite appears to be a significant factor in cobalt crystallite oxidation, and the thermodynamics of cobalt reduction and oxidation are also computed and reported. By making the appropriate adjustments to the hydrogen and water partial pressures in the FT reactor, it is possible to reduce the amount of oxidation that occurs on cobalt particles with a diameter of less than 6 nm. Controlling the speciation of the cobalt catalyst through oxidation appears to be dependent on a number of factors, one of which is the cobalt crystallite diameter. Design-Expert optimization of existing literature data resulted in the optimal conditions for enhancing the major target product of FTS, C_{5+} selectivity..

8.1.2. Experimental section

The laboratory-scale experiments that were conducted to gather the data that formed the basis of the discussions in later chapters are thoroughly explained by the author in this chapter. The experimental setup, used gases and catalysts, and selected reactors for this investigation are all summarized in the first section of the chapter. The procedures for operating the Fischer Tropsch (FT) system, gathering the data, and using gas chromatography (GC) equipment to analyze the data are described. The study's main focus was on light hydrocarbons, while wax and liquid hydrocarbons were also examined. The conversion of hydrogen is not mentioned because of analytical limitations.

A significantly larger source of error is found during FTS, which makes it difficult to duplicate the results of an FTS experiment. One of the factors that the author looked at is the impact that the different support particle sizes have. A support that has a particle size distribution that is consistent throughout can aid to keep metal loading uniform and can also assist in mantaining the size of the metal crystallites that develop on its surface. It is important for the catalyst that goes into the reactor to be an accurate representation of the bulk. It should be able to reproduce the distribution characteristics of the entire batch, whether it be in terms of the size of the particles, the shape of the particles, or the loading on the particles. The majority of the time, problems that occurred during sampling or manufacturing of the catalyst are to blame for an inability to repeat FTS data. Even with precise product analysis, these errors may accumulate and become impossible to correct.

8.1.3. Clinoptilolite-supported cobalt crystallite as Fischer-Tropsch catalyst: Effect of support particle size

Techniques such as TPR, XRD, XRF, BET, and SEM were utilized in order to conduct an in-depth examination of the properties of cobalt that was supported on clinoptilolite particles of varying sizes. It has been demonstrated that these techniques provide insight on the effect of the particle size of the support, and this could be used as a quality control tool to evaluate the efficacy of the preparation method (Fisker et al., 2000; Gavrilović et al., 2018; Nanosains, 2008; Xiong et al., 2005).

According to the findings of the study, decreasing the size of the support increased the reducibility of cobalt oxide (Co_3O_4), which resulted in a considerable decrease in both the reduction temperature and the activation energy required for Co_3O_4. The kinetic investigation provided evidence that the interaction between the catalyst and the support plays a significant part in the critical role played by the support in enhancing the reducibility of the catalyst. The DOR went down when the particle sizes went from -212 to +150 μm; -150 to +106 μm; -106 to +75 μm; -75 to +53 μm; -53 to +38 μm; -38 to +25 μm; -25 μm to Pan. This was true for all heating rates.

The impact of heating rate on the DOR is also not conclusive, despite the fact that the size of the difference between a low heating rate (5 ^oC/min) and a high heating rate is very substantial. There is little difference between 10^oC/min and 15^oC/min in terms of DOR. TPR tests of cobalt supported on clinoptlilolite demonstrate that more than 60 % of the cobalt is reduced below 450 ^oC. This decline occurs regardless of the particle size. It would appear, on the basis of the data that was presented, that modifying the PSD of the support material can result in the production of a catalyst with a wide variety of properties. When testing the reducibility of cobalt while utilizing clinoptilolite as a support, researchers found that using particles with sizes ranging from 212 to +150 mm produced the greatest results.

These observations show that the required temperature for reduction varies according to the particle size of the substance being lowered. It is essential for the manufacturing industry to get these temperatures down, as doing so will dramatically cut the cost of the input energy that is required for reduction. It is important to note that there was not a discernible pattern produced for any of the BET parameters that were evaluated; nonetheless, the disparities within were noted. According to the findings of this research thesis, the development of a catalyst requires the use of a particular particle size class. Additionally, a sufficient amount of testing must be carried out in order to select the suitable particle size class and reduction heating rate. In addition, when selecting a support from which to develop a catalyst, it is absolutely necessary to select a support from a particular size class. Doing so is the only way to guarantee that the results described here can be replicated precisely. When utilizing the FTS method, there are problems with reproducibility, and this is one of the possible variables that lead to errors and needs to be studied. The other aspects that contribute to errors also need to be looked into. The issue of compounding of errors needs to be reduced.

8.1.4. Optimization and evaluation of the distribution of Fischer-Tropsch products over a cobalt-based catalyst utilizing design expert software

The DOE was carried out with the goals of maximizing the efficiency of the cobalt-based FT catalyst and ensuring that the product groups stayed within the acceptable range throughout the entire experiment. The final product's chemical make-up is partially determined by a number of factors, including the size of the crystallite, the temperature, and the pressure at which the FT reaction is carried out. Using RSM and estimated distribution models, analyses of product distribution and yield expressed as a percentage of total hydrocarbons were conducted, respectively. Thus, the effect of system settings and model parameters on the predicted product distribution was determined, and it was determined that this distribution is a function of the operating conditions. Plotting the experiment's results into probability distributions helped identify the experiment's parameters' importance. The operating settings changed selectively. The number of carbon atoms in hydrocarbon derivatives changed as the parameters were changed.

The cobalt crystallite size, temperature and pressure were all found to be statistically significant parameters that have a significant impact on the formation of C_1 optimum, C_2-C_4 and C_{5+}.

However, pressure was statistically inconsequential and had no significant impact on the formation of C_1 optimum, C_2-C_4 and C_{5+}. The significant factors were optimized using RSM, so as to identify the best experimental conditions. The parameters of crystallite size = 11nm, pressure = 10 Bar and temperature = 220 °C provided the best product distribution under the experimental conditions considered. In order to confirm this, confirmatory tests were conducted using almost identical settings. Optimum conditions were obtained based on the preference of the author, which was maximum C_{5+} output.

8.1.5. Effect on support particle size in Fischer-Tropsch Synthesis: The use of natural clinoptilolite as support

Reducing the size of the support increased the reducibility of cobalt oxide (CoO) and decreased the reduction temperature and activation energy for Co_3O_4. The kinetic analysis confirms that the interaction between the metal and the support plays a key role in determining the contribution of the support to the overall improvement in catalyst reducibility. The difference between a low heating rate (5 ^oC/min) and a high heating rate (5 ^oC/min) is rather substantial; yet, the effect of heating rate on the DOR is inconclusive. Using particles with a diameter of less than 25 microns and reducing at a pace of 5 ^oC/min resulted in a low activation energy of 104.14 kJ/mol and a high DOR of 70.57 % in this investigation.

Fischer Tropsch synthesis was run at 220 ^oC and 10.85 bar (abs) only for the catalyst with support particle sizes of -75 to +53 μm; -53 to +38 μm; and -25 μm to Pan. The product distribution observed from the three reactors had methane selectivity which ranged from 14.95 to 16.97%; C_2-C_4 selectivity ranged from 14.55 to 19.01%; C_{5+} selectivity ranged from 66.04 to 70.29%. The results of this study reveal that a specific support size class must be utilized while developing a catalyst. Moreover, a significant number of trials must be conducted in order to optimize or choose the optimal particle size class and optimal heating rate for use during reduction. This experiment yielded equivalent product selectivity results to those reported in the literature (Den Breejen et al., 2009; Saib et al., 2002), indicating that the support employed was acceptable.

8.1.6. Optimization and screening of Iron supported on Clinoptilolite as a low-temperature Fischer- Tropsch synthesis catalyst

This research was conducted with the intention of providing a comparison study that utilized a different metal that was supported on clinoptilolite. The purpose of the DOE experiment that was carried out was to find ways to improve the performance of the FT catalyst that was based on iron. There was a perceptible shift in the selectivity after the operating conditions were adjusted, and the case was quite similar to the one with the cobalt supported on clinoptilolite.

For the purpose of this research, the H_2/CO ratio, temperature, and gas velocity were investigated, and it was discovered that all three variables have a significant impact on the production of low CH_4, optimal C_2-C_4, and high heavy hydrocarbon products. On the other hand, the researchers discovered that the effect of pressure was statistically insignificant and had no discernible effect. The selectivity to C_{5+} - C_∞ hydrocarbons were strongly favored by lower design parameters for temperature, a high H_2/CO ratio, and gas speed. According to the constraints set, H_2/CO = 1.90, temperature = 241 ^oC, pressure = 17.9 bar_g and velocity =1240.9 provided an optimal design under the experimental conditions evaluated. To verify this, the actual values were compared with the predicted values, and it was found that the models fitted the experimental data quite well. Experiments carried out with iron supported on clinoptilolite produced results that were, on the whole, equivalent to those produced by conventional supports.

8.2. Recommendations

In this thesis, the conclusions of this research are presented, demonstrating great progress in the development of innovative, less expensive catalyst supports for FTS. The chemical composition of clinoptilolite, which is used as a support, consists mainly of silica, alumina, and titania (Gorimbo, 2011), which are the three supports utilized in FTS to the greatest extent. As a result of this study, we now understand that clinoptilolite can serve as an effective support in FTS. Because clinoptilolite is a mined mineral, the clinoptilolite rock needs to be milled before it can be utilized. As a result, this study also investigated the effects of varying the particle size of the clinoptilolite. As a result, the recommendations state that, in order to ensure the repeatability of tests, a particle

size class that is uniform should be used. The researcher also anticipates that the impact of particle sizes outside the range examined in this thesis will be looked into.

On recommendation, employing clinoptilolite in the future necessitates further exhaustive examination of the effect of adding promoters because other metal oxides (in its chemical makeup) could operate as promoters if they are not situated in inaccessible areas in the zeolite framework. Additionally, it is essential to carry out comparable study on all of the factors that were examined in this thesis by making use of a reactor that is constantly agitated (continuously stirred-tank reactor (CSTR). Design of Experiments (DOE) is also recommended since it enables researchers to study the most efficient aspects under optimal conditions.

References

Den Breejen, J. P., Radstake, P. B., Bezemer, G. L., Bitter, J. H., Frøseth, V., Holmen, A., & De Jong, K. P. (2009). On the origin of the cobalt particle size effects in Fischer-Tropsch catalysis. *Journal of the American Chemical Society*, *131*(20), 7197–7203. https://doi.org/10.1021/ja901006x

Fisker, R., Carstensen, J. M., Hansen, M. F., Bødker, F., & Mørup, S. (2000). Estimation of nanoparticle size distributions by image analysis. *Journal of Nanoparticle Research*, *2*(3), 267–277. https://doi.org/10.1023/A:1010023316775

Gavrilović, L., Brandin, J., Holmen, A., Venvik, H. J., Myrstad, R., & Blekkan, E. A. (2018). Fischer-Tropsch synthesis—Investigation of the deactivation of a Co catalyst by exposure to aerosol particles of potassium salt. *Applied Catalysis B: Environmental*, *230*(September 2017), 203–209. https://doi.org/10.1016/j.apcatb.2018.02.048

Gorimbo, J. (2011). *Effect of the homoionic form of clinoptilolite on Ni2+ adsorption isotherms: A thermodynamic study, Msc dissertation, University of the Witwatersrand.*

Mustard, D. G., & Bartholomew, C. H. (1981). Determination of metal crystallite size and morphology in supported nickel catalysts. *Journal of Catalysis*, *67*(1), 186–206. https://doi.org/10.1016/0021-9517(81)90271-2

Nanosains, J. (2008). Derivation of Scherrer Relation Using an Approach in Basic Physics Course. *Nano*, *1*(1), 28–32.

Saib, A. M., Claeys, M., & Van Steen, E. (2002). Silica supported cobalt Fischer-Tropsch catalysts: Effect of pore diameter of support. *Catalysis Today*, *71*(3–4), 395–402. https://doi.org/10.1016/S0920-5861(01)00466-7

Xiong, H., Zhang, Y., Wang, S., & Li, J. (2005). Fischer-Tropsch synthesis: The effect of Al2O3 porosity on the performance of Co/Al2O3 catalyst. *Catalysis Communications*, *6*(8), 512–516. https://doi.org/10.1016/j.catcom.2005.04.018

APPENDIX A

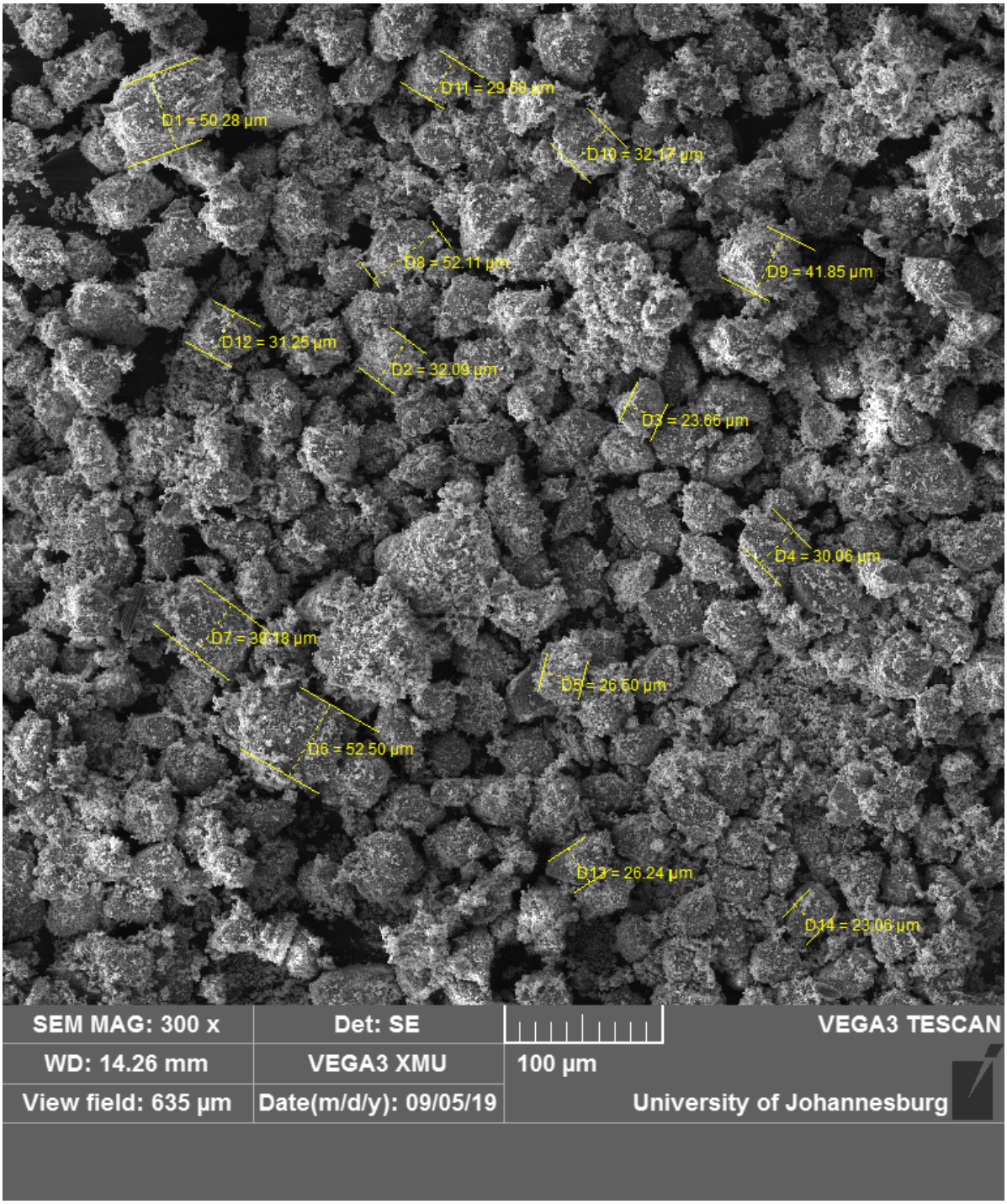

Appendix A-1: SEM micrograph of particles in the range -38 to +25 µm

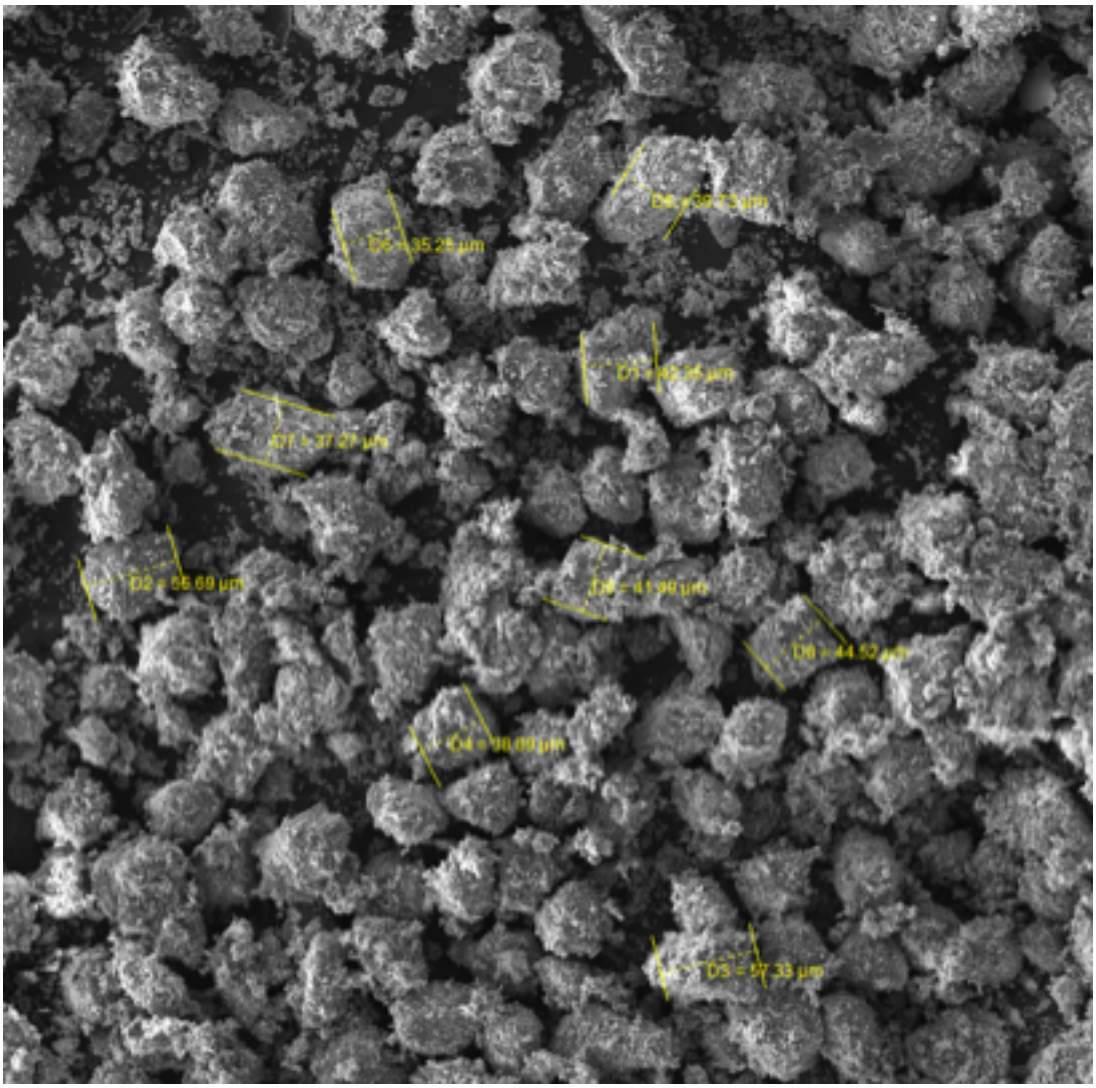

Appendix A-2: SEM micrograph of particles in the range -53 to +38mm

A micrograph taken with a SEM displaying clinoptilolite particles at a magnification of 300x. The image depicts particles of varying shapes and sizes that fall within the dimensions specified for the particle size range.

Appendix B: Anova Single factor analysis done to establish if there is a significant difference between SEM measure particles

Anova: Single Factor

SUMMARY

Groups	*Count*	*Sum*	*Average*	*Variance*
25 micron	44	589.31	13.39341	24.22222
38 to25	46	1719.28	37.37565	62.30329
53 to 38	30	1243.64	41.45467	120.4675
75 to 53	32	1904.59	59.51844	211.3367

ANOVA

Source of Variation	*SS*	*df*	*MS*	*F*	*P-value*	*F crit*
Between Groups	41164.43	3	13721.48	146.2023	4.66E-44	2.665729
Within Groups	13890.2	148	93.8527			
Total	55054.63	151				

t-Test: Two-Sample Assuming Equal Variances

	25 micron	*38 to25*
Mean	13.39341	37.37565
Variance	24.22222	62.30329
Observations	44	46
Pooled variance	43.6955	
Hypothesized mean difference	0	
df	88	
t Stat	-17.205	
P(T<=t) one-tail	3.38E-30	
t Critical one-tail	1.662354	
P(T<=t) two-tail	6.75E-30	
t Critical two-tail	1.98729	

Appendix B contains the statistical analysis results to evaluate if SEM particles are significantly different. As demonstrated in Figure 4.2 (the malven result), most particles lie within the prescribed range, although SEM and Malvern measurements indicated particles outside the ranges, raising the possibility of overlap. We conducted an Anova single factor to test if these particles differ statistically, and the findings demonstrate they do. The computed F value (146.2023) is higher than the Fcrit (2.665729) The 4.66 X 10-44 P-value is less than 0.05, indicating group differences.